

MAPPING URBAN FOREST EXTENT AND MODELING SEQUESTERED
CARBON ACROSS CHATTANOOGA, TN USING
GIS AND REMOTE SENSING

By

Will Stuart

A.K.M. Azad Hossain
Associate Professor of Geology
(Chair)

Nyssa Hunt
Research Associate/GIS Analyst
(Committee Member)

Hong Qin
Professor of Computer Science
(Committee Member)

MAPPING URBAN FOREST EXTENT AND MODELING SEQUESTERED
CARBON ACROSS CHATTANOOGA, TN USING
GIS AND REMOTE SENSING

By

Will Stuart

A Thesis Submitted to the Faculty of the University of
Tennessee at Chattanooga in Partial
Fulfillment of the Requirements of the Degree
of Master of Science: Environmental Science

The University of Tennessee at Chattanooga
Chattanooga, Tennessee

May 2023

ABSTRACT

Chattanooga, Tennessee is among many cities experiencing rapid urbanization and subsequent losses to urban forest area. Using remote sensing and digital image processing, this research 1) applied supervised hybrid classification across Landsat imagery that quantified the extent of urban forest loss across Chattanooga between 1984 and 2021, 2) modeled the carbon sequestered in the biomass of Chattanooga's urban trees using field data and vegetation indices, and finally 3) developed the first city-wide high-resolution land cover map across Chattanooga using SkySat imagery and object-based classification. Results found that Chattanooga has lost up to 43% of its urban tree canopy and gained up to 134% of urban land area. Additionally, a methodology for modeling sequestered carbon across urban forests was identified. Finally, using high-resolution imagery and the object-based workflow as described here, it is capable of producing accurate maps of urban tree canopy distribution with overall accuracy quantified in excess of 93%.

ACKNOWLEDGEMENTS

I would like to thank the European Space Agency (ESA), the National Aeronautics and Space Administration (NASA), and the United States Geological Survey (USGS) for providing this research with pre-processed multispectral imagery free of charge, the Lyndhurst foundation for funding the acquisition of high resolution SkySat imagery acquired by Planet Labs, the City of Chattanooga, Tennessee, and Green|Spaces for also providing financial support and for seeing the value of this research, Department of Biology, Geology, and Environmental Science at the University of Tennessee at Chattanooga (UTC) for providing the research opportunities to make this work possible, UTC's Interdisciplinary Geospatial Technology (IGT) Lab staff for always offering critical thinking assistance, advice, and support, and the Multidisciplinary Research Center (SimCenter) for creating the distributed processing environments that made this research possible. A special thanks is due to:

- Dr. Azad Hossain, for accepting me as a research student under his supervision, sparking my passion for Earth systems monitoring, allowing me the flexibility to choose my own specific research interests, always keeping me grounded and tasked, and for all the wisdom you have imparted.
- Nyssa Hunt for being an amazing friend, editor, technical support guru, my graduate school mentor, and literal life coach throughout this research. Your confidence, optimism, and seamlessly never ending patience was much appreciated.

- Dr. Hong Qin for the valuable input and insights that contributed to the success of this research and served to improve the quality of the obtained results.
- Charlie Mix for all your advice, for the instrumental role you played in helping to turn an idea into a physical project, and for the instrumental communications that allowed my access to UTC distributed processing environment for SkySat imagery processing.
- Peter Stewart, for never turning down an opportunity to help answer questions and assist during critical thinking, and for connecting me with Dr. Eric Wiseman, whose comprehensive reports were valuable sources during the field sampling conducted in this research.
- Dr. Shannon McCarragher, for the passion, patience, and belief in me, which started this long, strange trip. I cannot thank you enough.
- McKenzie Whitten, for sticking around through the good and the bad, never losing faith in me, and most of all for keeping my mind from straying too far away from my passions.
- And finally, for all of my friends and family for the endless support you provided throughout.

- *To each of you, I offer my most sincere thanks.* -

TABLE OF CONTENTS

ABSTRACT.....	iii
ACKNOWLEDGEMENTS.....	iv
LIST OF TABLES	x
LIST OF FIGURES	xii
LIST OF ABBREVIATIONS.....	xvi
LIST OF SYMBOLS	xix
CHAPTER	
1. INTRODUCTION	1
Background	1
Problem Statement	2
Objectives	3
2. LITERATURE REVIEW	4
Forests and Carbon Sequestration.....	4
Earth’s Biogeochemical Cycles and Carbon Sequestration.....	4
Sequestration of Atmospheric CO ₂ and the Geologic Carbon Cycle	4
Sequestration of Atmospheric CO ₂ and the Biologic Carbon Cycle	5
Photosynthesis: Light-Dependent Reactions	5
Photosynthesis: Light-Independent Reactions.....	5
Forest Carbon Reservoir	6
Human Impact on Temperate Forests	7
Historic Uses of Temperate Forests	7
Current Status of Temperate Forests.....	8
Urban Forests	9
Remote Sensing of Forestry and Carbon Sequestration	11
Advantages of Remote Sensing	11
Sensor Platform.....	12
Airborne Sensors.....	12
Spaceborne Sensors	13

Sensor Type	14
Active Sensors	14
Radar	14
LiDAR.....	15
Passive Sensors	15
Spatial Resolution	16
Course Spatial Resolution.....	16
Moderate Spatial Resolution.....	16
Fine Spatial Resolution.....	17
Spatial Resolution and Machine Learning-Based Image Classification.....	19
Coarse and Moderate Resolution Imagery.....	19
Fine Resolution Imagery.....	19
Spectral Resolution	22
Analyzing Forest Extent and Sequestered Carbon Using Remote Sensing.....	23
Allometric Equations	23
Remote Sensing Applications	23
Modeling Forest Carbon Using Field Data and Remote Sensing.....	25
Literature Review Summary	27
Restatement of the Research Objectives.....	28
 3. APPLICATION OF LANDSAT IMAGERY	 29
Study Site.....	29
Data Collection	31
Methods.....	33
Image Pre-Processing and Enhancement	33
Feature Extraction.....	34
Supervised Classification.....	34
Unsupervised Classification.....	36
Image Post-Processing	37
Image Reclassification	37
Creating the Final Land Cover Datasets	38
Accuracy Assessment	40
Results.....	42
Confusion Matrices	42
Assessment of Spatiotemporal Trends.....	45
 4. APPLICATION OF PLANETSCOPE AND SENTINEL IMAGERY	 48
Study Site.....	48
Data Collection	50
Methods.....	52
Image Pre-Processing.....	52
Image Enhancements	52
Feature Extraction.....	57
Field Data Collection	57

Modeling Sequestered Carbon	59
Preparing the Independent Variables	59
Preparing the Dependent Variable	60
Simple Linear Regression	62
Results.....	63
Correlation Coefficient	63
Linear Regression Analysis	63
5. APPLICATION OF SKYSAT IMAGERY	72
Study Site	72
Data Collection	74
Methods.....	77
Image Pre-Processing.....	77
Data Storage and Backup.....	77
QAQC	77
Feature Extraction.....	78
Image Segmentation.....	78
Training Sample Collection	81
Image Classification.....	83
Image Post-Processing	85
Refining the High Resolution Land Cover Dataset	85
Accuracy Assessment	86
Results.....	88
Accuracy Assessment Results.....	89
6. DISCUSSION	91
Objectives of the Study	91
Application of Landsat Imagery	91
Application of Planet Scope and Sentinel Imagery	93
Application of SkySat Imagery	96
Segmenting High Resolution Multispectral Imagery	96
Using ArcGIS Pro's Pixel Editor to Refine Classified Results	98
Training Sample Collection and Imagery Classification	98
Documented Challenges	99
Schema Changes Not Preserved	99
Error 999999: Unexpected Errors	99
Error 003436: No Training Samples Found.....	100
7. FUTURE DIRECTIONS AND CONCLUSIONS	102
Future Directions	102
Conclusions.....	105
REFERENCES	107

APPENDIX

A. APPLICATION OF LANDSAT IMAGERY	119
B. APPLICATION OF SKYSAT IMAGERY	180
VITA	190

LIST OF TABLES

3.1 Landsat 5 TM and Landsat 8 OLI sensor specifications.....	31
3.2 Acquired Landsat 5 TM and Landsat 8 OLI imagery	32
3.3 Final thematic land cover dataset class names and descriptions.....	39
3.4 Confusion matrices derived from the accuracy assessment of 1984 – 2021 final land cover datasets	42
3.5 Area and relative percentage of land cover classes quantified across the 10 final land cover datasets (Non-Forest Vegetation = NF)	45
3.6 Land cover class area percent change between imagery acquisition dates.....	47
4.1 Master field sampling dataset, consisting of sampled tree common name, sample site ID, field measured DBH (in), calculated dry weight biomass (lbs), and finally sequestered carbon (lbs)	61
4.2 Allometric equations used to derive biomass estimations from field measured DBH [121]	61
4.3 Pearson’s correlation and linear regression analysis results from each tested independent variable derived from PlanetScope and Sentinel-2a imagery	64
4.4 Obtained linear regression equation for each tested independent variable derived from PlanetScope and Sentinel-2a imagery	66
5.1 Description of acquired multispectral SkySat imagery	75
5.2 Unique spectral and spatial detail parameters for each SkySat image used in the configuration of the “Segment Mean Shift” geoprocessing tool with ArcGIS Pro.....	80
5.3 Confusion matrix derived from the accuracy assessment of the unrefined land cover dataset.....	90

5.4 Confusion matrix derived from the accuracy assessment of the refined land cover dataset.....	90
--	----

LIST OF FIGURES

1.1 (A) Landsat 5 TM image of east Chattanooga, Tennessee captured June 27th, 1984; (B) Landsat 8 OLI image of east Chattanooga, Tennessee captured July 3rd, 2021	2
2.1 Effects of deforestation in Colorado in 1915 [34]	7
2.2 Global temperate forest distribution [37].....	8
2.3 Comparison of pixel-based (middle) and object-based (right) classification outputs [101]	20
2.4 Visualization of the impact of chlorophyll abundance on NDVI [117].....	25
3.1 Study site map for Landsat research and the City of Chattanooga, Tennessee’s boundary	30
3.2 True color Landsat 8 OLI image acquired July 3, 2021 over the City of Chattanooga, TN	33
3.3 (A) Distribution of training samples used for supervised classification shown on the true color 2021 Landsat 8 OLI imagery; (B) 3 class thematic land cover dataset derived from the supervised classification of the 2021 Landsat 8 OLI imagery	35
3.4 Land cover output consisting of 10 spectrally distinct classes of previous pixels following unsupervised classification (2021 Landsat 8 OLI imagery displayed).....	36
3.5 Reclassification of 10 spectrally distinct classes of previous pixels into a new 2 class thematic raster consisting of Non-Forest Vegetation and Forest Vegetation (2021 Landsat 8 OLI imagery displayed).....	38
3.6 Final supervised hybrid thematic 4-class land cover raster	39
3.7 Example of the polygons digitized using Google Earth’s historic imagery to conduct the accuracy assessment across each of the 10 supervised hybrid land cover datasets (Images not to scale)	41

3.8 Land cover class area in acres for the 10 final land cover datasets	46
4.1 Study site map for Planet Scope and Sentinel-2a research representing the campus of the University of Tennessee at Chattanooga (UTC)	49
4.2 Acquired multispectral imagery (viewed in false color to highlight the presence of vegetation in red) to model urban tree canopy across the campus of the University of Tennessee at Chattanooga (UTC); (A) Sentinal2-a visible and NIR bands have a resolution of 10 meters; (B) PlanetScope imagery has a resolution of 3 meters; (C) NAIP imagery has a resolution of 1 meter	51
4.3 First order PCA conducted on NAIP imagery to help delineate shadows, colored in bright green	53
4.4 Digital surface model (DSM) generated using the data obtained from USGS [126]	53
4.5 (A) NDVI generated from Sentinel-2a imagery (30m); (B) NDVI generated from PlanetScope imagery (3m)	56
4.6 Urban tree canopy polygons hand digitized across UTC from NAIP imagery	58
4.7 Modeling approach for developing the predictive carbon model using simple linear regression	62
4.8 Plotted distribution of pounds of sequestered carbon per square meter (y) and mean GNDVI values extracted from PlanetScope imagery (x) using the digitized urban tree canopy polygons	67
4.9 Plotted distribution of pounds of sequestered carbon per square meter (y) and mean NDVI values extracted from PlanetScope imagery (x) using the digitized urban tree canopy polygons	67
4.10 Plotted distribution of pounds of sequestered carbon per square meter (y) and mean SAVI values extracted from PlanetScope imagery (x) using the digitized urban tree canopy polygons	68
4.11 Plotted distribution of pounds of sequestered carbon per square meter (y) and mean GNDVI values extracted from Sentinel-2a imagery (x) using the digitized urban tree canopy polygons	68
4.12 Plotted distribution of pounds of sequestered carbon per square meter (y) and the maximum NDVI values extracted from Sentinel-2a imagery (x) using the digitized urban tree canopy polygons.....	69

4.13 Plotted distribution of pounds of sequestered carbon per square meter (y) and the maximum RENDVI1 values extracted from Sentinel-2a imagery (x) using the digitized urban tree canopy polygons	69
4.14 Plotted distribution of pounds of sequestered carbon per square meter (y) and the maximum RENDVI2 values extracted from Sentinel-2a imagery (x) using the digitized urban tree canopy polygons	70
4.15 Plotted distribution of pounds of sequestered carbon per square meter (y) and the maximum SAVI values extracted from Sentinel-2a imagery (x) using the digitized urban tree canopy polygons.....	70
4.16 Final map of sequestered carbon for the trees of UTC’s campus derived from PlanetScope GNDVI	71
5.1 Study site map for SkySat research, representing the City of Chattanooga, Tennessee’s boundary	73
5.2 Fine resolution (50 cm) orthorectified mosaic of tasked SkySat imagery clipped to the study site boundary	73
5.3 Footprint of acquired multispectral SkySat imagery	75
5.4 Footprint boundary and true color SkySat imagery acquired	76
5.5 Over- and under-segmentation within an object-based classification workflow	78
5.6 Footprint boundary, study site boundary, and segmented true color SkySat rasters	80
5.7 Training samples collected across segmented SkySat imagery to support object-based classification	82
5.8 Final unrefined high resolution (50 cm) land cover dataset derived from SkySat imagery	84
5.9 Final refined high resolution (50 cm) land cover dataset derived from SkySat imagery	85
5.10 500 randomly distributed points used for the accuracy assessment of the final unrefined high resolution land cover dataset.....	86
5.11 500 randomly distributed points used for the accuracy assessment of the final refined high resolution land cover dataset.....	87

5.12 Subsets showcasing the true color SkySat imagery (top), refined land cover dataset (bottom) over Coolidge Park / North Shore (left), and the Chattanooga National Cemetery (right).....	88
--	----

LIST OF ABBREVIATIONS

ATP, Adenosine Triphosphate

AVHRR, Advanced Very High Resolution Radiometer

B, Blue

BCC, Biologic Carbon Cycle

CHM, Canopy Height Model

CO₂, Carbon Dioxide

DBH, Diameter at Breast Height

DSM, Digital Surface Model

DTM, Digital Terrain Model

EMR, Electromagnetic Radiation

EMS, Electromagnetic Spectrum

Esri, Environmental Science Research Institute

ESA, European Space Agency

EVI, Enhanced Vegetation Index

G, Green

GCC, Geologic Carbon Cycle

GIS, Geographic Information Systems

GLAS, Geoscience Laser Altimeter System

GNDVI, Green Normalized Difference Vegetation Index

GNSS, Global Navigation Satellite System

G3P, Glyceraldehyde 3-Phosphate

ICW, Image Classification Wizard

INS, Inertial Navigation System

IFOV, Instantaneous Field of View

LAD, Leaf Area Density

LAI, Leaf Area Index

LiDAR, Light Detection and Ranging

MODIS, Moderate Resolution Imaging Spectroradiometer

MSI, Moisture Vegetation Index

NADPH, Nicotinamide Adenine Dinucleotide\

NAIP, National Agricultural Imagery Program

NASA, National Aeronautics and Space Administration

NDVI, Normalized Difference Vegetation Index

NIR, Near Infrared

NLCD, National Landcover Dataset

OLI, Operational Land Imagery

PCA, Principal Component Analysis

PPK, Post-Processed Kinematic

R, Red

Radar, Radio Detection and Ranging

RENDVI1, Red Edge Normalized Difference Vegetation Index 1

RENDVI2, Red Edge Normalized Difference Vegetation Index 2

RMSE, Root Mean Square Error

RPK, Real-time Processing Kinematic

SAVI, Soil Adjusted Vegetation Index

SR, Simple Ratio

TIRS, Thermal Infrared Scanner

TM, Thematic Mapper

UAV, Unmanned Aerial Vehicles

USDA, United States Department of Agriculture

USFS, United States Forest Service

USGS, United States Geologic Survey

UTC, University of Tennessee at Chattanooga

3DEP, 3D Elevation Program

3-PGA, 3-Phosphoglycerate

LIST OF SYMBOLS

aa, alder/willow

cl, cedar/larch

mh, mixed hardwood

mo, maple/oak/hickory/beech

pi, pine

e , Euler's number

κ , Cohen's Kappa coefficient

\ln , natural logarithm

L , soil brightness correction factor

r , Pearson's Product-Moment Correlation Coefficient

R^2 , coefficient of determination

μm , micrometers

ρ , surface reflectance

ρNIR , near infrared surface reflectance

ρR , red surface reflectance

ρG , green surface reflectance

ρRE1 , red-edge 1 surface reflectance

ρRE2 , red-edge 2 surface reflectance

CHAPTER 1

INTRODUCTION

Background

As metropolitan areas across the United States, Europe, and East Asia grow ever larger, more and more of Earth's unique temperate forest ecosystems, places of enormous ecological, recreational, and cultural significance in the southeastern United States, are destroyed to make way for new urban development. Urbanization, or the conversion of natural, pervious surfaces to developed spaces, often involves the destruction of the bulk of extant plant communities in a given area, resulting in habitat loss and fragmentation, which in turn contributes to the rapid declines currently observed in global biodiversity [1, 2]. Converting natural, undeveloped landscapes to impervious, urbanized spaces can have a significant negative impact on local surface water quality [3, 4]. Urbanization has also been connected with increased surface and air temperatures in urban spaces, a phenomena referred to as urban heat island effect [5]. Additionally, once destructively removed from a landscape, the bulk of the carbon collectively sequestered in the biomass of the extracted vegetation will be released back to the atmosphere as carbon dioxide (CO₂), thereby reducing the total carbon sequestration potential of the urbanized land area [6, 7].

Because of their proximity to human development, urban forests in particular possess an increased risk of being impacted by or converted to urban landscape [7-9]. Here, an urban forest or urban tree canopy is defined as all continuous or fragmented undeveloped landscapes dominated by trees within and surrounding a city, whether planted or naturally seeded [10].

Problem Statement

Since 1984, Chattanooga, Tennessee's urban land area has increased rapidly. It is well understood that this conversion of undeveloped temperate forest to urban spaces across Chattanooga has resulted in an overall decrease in surface water quality and increases in surface and air temperatures [3, 4]. Aside from the inventory of coordinates of street trees located in the heart of downtown, no current or historic assessment of the distribution of Chattanooga's urban tree canopy has ever been conducted. Additionally, a predictive model capable of estimating the dry weight of above ground sequestered carbon per unit area of urban tree canopy from field sampled tree measurements and imagery-derived spectral indices has never been created for the City of Chattanooga.

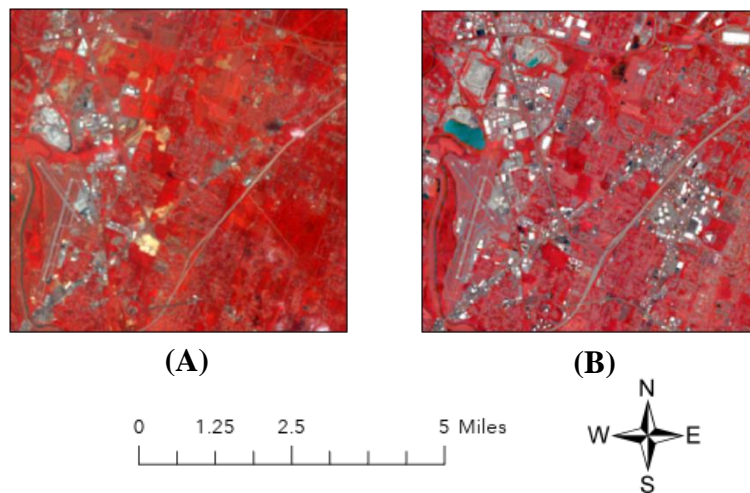


Figure 1.1 (A) Landsat 5 TM image of east Chattanooga, Tennessee captured June 27th, 1984;
(B) Landsat 8 OLI image of east Chattanooga, Tennessee captured July 3rd, 2021

In recent decades, remote sensing has proven to be a powerful and cost-efficient tool for assessing a city's urban tree canopy [11-13]. Furthermore, using free satellite imagery and field measured biophysical variables, such as diameter at breast height (DBH), it is possible to create predictive models capable of estimating the carbon sequestered in the biomass of trees across smaller study areas with acceptable accuracy [12, 14, 15]. However, a diverse array of sensors, each with unique advantages and disadvantages have been used with variable levels of accuracy [13]. For each of these data sources, there are complexities and nuances associated with accessing and manipulating the acquired data that should initially be considered.

Objectives

In order to assist future forestry research across the city, to better inform urban planning decisions into the future, and to help enhance the inherent value of trees in the eyes of local government and the community, this research uses remote sensing and digital image processing techniques to answer the following three questions:

1. How has the extent of Chattanooga's urban tree canopy changed between 1984 and 2021?
2. How can the carbon sequestered in the biomass of urban forest trees be predictively modeled at little to no cost and without a significant time investment?
3. What is the current extent of Chattanooga's urban tree canopy?

CHAPTER 2

LITERATURE REVIEW

Forests and Carbon Sequestration

Earth's Biogeochemical Cycles and Carbon Sequestration

Earth's biogeochemical cycles represent the various routes taken by major elements, like nitrogen and carbon, and neutral compounds, such as water, through the biotic and abiotic components of Earth's atmosphere, biosphere, hydrosphere, and lithosphere. These biogeochemical cycles are essential systems that altogether contribute to sustain life on Earth [16].

Within the carbon cycle, any mechanism that results in the removal and storage of CO₂ from the atmosphere is referred to as a carbon sink [6]. The storage of carbon in any sink is referred to as carbon sequestration [17]. CO₂ is sequestered from the atmosphere via the carbon cycle at two different scales: the geologic carbon cycle (GCC), driven by geologic forces, and the biologic carbon cycle (BCC), driven by biologic forces [6, 18].

Sequestration of Atmospheric CO₂ and the Geologic Carbon Cycle

The GCC deals with both the dissolution of CO₂ from the atmosphere into the surface water of Earth's oceans, as well as the anaerobic burial of organic matter its subsequent transformation into carbon-rich fossil fuel deposits [18]. CO₂ is sequestered through its dissolution into the surface water of Earth's oceans and its eventual mixing into the waters of the deep ocean.

Under the intense pressure of the deep ocean, dissolved CO₂ will ultimately be incorporated into carbonate rocks, such as limestone, as constituents in the mineral lattice of calcite crystals [19]. Carbon stored here can remain stable for vast expanses of time.

Sequestration of Atmospheric CO₂ and the Biologic Carbon Cycle

The sequestration of atmospheric carbon in the BCC involves the conversion of water, CO₂, and electromagnetic radiation (EMR) from the sun by plants into sugars with which they use to grow and reproduce. This process is collectively referred to as photosynthesis. To better understand its mechanisms, we can break down the processes of photosynthesis into a series of light-dependent and light-independent biochemical reactions occurring inside the chloroplasts of plant cells.

Photosynthesis: Light-Dependent Reactions

The purpose of the light-dependent reactions of photosynthesis is to generate chemical energy in the form of adenosine triphosphate (ATP) and nicotinamide adenine dinucleotide (NADPH) from CO₂, water, and EMR from the sun, with wavelengths in the blue range (400-475 nm) and the orange-red range (650-700 nm) being the optimal wavelength absorption range for chlorophyll-a [20, 21].

Photosynthesis: Light-Independent Reactions

Once chemical energy becomes available, provided by the light-dependent reactions, the plant can now begin the light-independent process of photosynthesis. This process ultimately results in the creation of the carbon-containing glucose molecule that the plant will use to form its biomass [21]. Named after the pioneers that discovered this critical step in plant biomass assimilation and carbon sequestration, the light-independent photosynthetic reactions are often

referred to collectively as the Calvin-Benson cycle [21]. The cycle begins with carbon fixation, in which inorganic CO₂ in the atmosphere is absorbed through plant stomata and in a series of reactions is incorporated into a 3-carbon molecule called 3-phosphoglycerate (3-PGA) [21]. The 3-PGA molecule is subsequently reduced to form a 3-carbon sugar, glyceraldehyde 3-phosphate (G3P). Every 3 CO₂ molecules absorbed result in the net production of one G3P molecule. After 6 cycles, 6 G3P molecules are rearranged to form a 6-carbon sugar, glucose, which the plant will use to form its biomass [21].

Forest Carbon Reservoir

Today, 30% of Earth's surface is composed of forest ecosystems [22]. In addition to the myriad of human and animal communities composing their structure and ecologic function support, the trees of Earth's forests represent a staggering 80% of the total biomass on Earth [6, 23, 24]. In fact, the global forest carbon reservoir alone has incorporated more atmospheric carbon in its biomass and soils than currently exists in the entire atmosphere [24].

Forests are characterized in part by the dominance of woody tree species. Though not as permanent as the carbon stored in the GCC, the carbon stored within their woody biomass can remain sequestered until the end of that tree's life cycle [25].

Therefore, the trees of Earth's forests represent a prodigious carbon sink in the global carbon cycle [26-29]. However, compared to that stored via the GCC, due to natural disturbance events and anthropogenic pressures, the carbon making up the biomass of tree is under a greater threat of being released back to the atmosphere before the end of the tree's natural life cycle [30].

Human Impact on Temperate Forests

Historic Uses of Temperate Forests

Humans have directly impacted the health and integrity of temperate forests more than any other forest type [31, 32]. The current global extent of temperate forests is now estimated to be between 40% to 50% of its historic expanse. Furthermore, 99% of all temperate forests have been harmfully impacted by agriculture, logging, urbanization, or another human activity resulting in deforestation or the harmful disturbance of the composition, structure, or overall function of temperate forest [31, 33].



Figure 2.1 Effects of deforestation in Colorado in 1915 [34]

By as early as 1100 BC, temperate forest area in Europe had already been reduced to 30% of its original extent as a result of increased demand for fuel wood and agricultural land area by early human civilizations [32, 35, 36]. During the American Industrial Revolution, the rapid clearing of forests for timber harvest and agricultural land conversion cleared 35% of the continent's temperate forests. [36].

Current Status of Temperate Forests

Today, temperate forests cover about 10.4 million km² (Figure 2.2.), representing a quarter of the world's forest cover today. North America contains roughly 60% of total global temperate forests; Europe contains 24%; and eastern Asia, combined with other areas in the Southern Hemisphere, contain the remaining 16% [36].

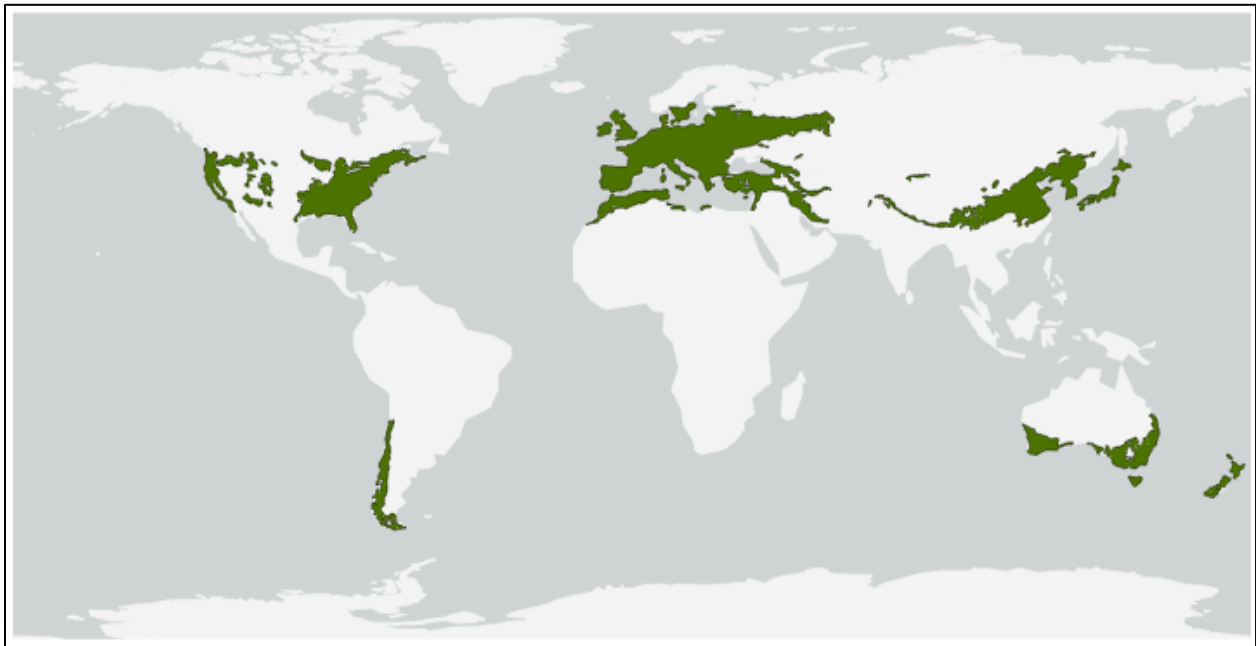


Figure 2.2 Global temperate forest distribution [37]

Despite the overexploitation of temperate forests to fuel growing timber markets during the pre- and post-industrialization stages of emergent nations, temperate forest land area is slowly increasing as successional communities begin to reestablish themselves in areas historically used for timber harvest or agricultural production that are no longer in operation [24, 36]. However, in the same way the overexploitation of timber in the industrial revolution threatened forest habitat, rapid urban development and the associated habitat loss is threatening the global extent of temperate forests (Figure 2.2.) once again, now at an unprecedented rate, scale, and intensity [38, 39].

Urban Forests

As urban centers in the United States, Europe, and eastern Asia grow ever larger to accommodate swelling populations, temperate forests are cut, bare earth is paved, and buildings are constructed. This generalized process of land cover change is collectively referred to as urbanization [4, 40]. Due to their proximity to human infrastructure and population centers, urban forests, or forested areas within or adjacent to a metropolitan center, are often the best option for developers [7-9]. The urban forest of a given city includes forested fragments, greenways, riparian zones, wetlands, urban parks, residential trees, street trees and working forests [10]. The US Forest Service reports that approximately 127 million acres of forest in the US is in immediate proximity to metropolitan areas, and therefore can be classified as urban forest [9]. However, as stated previously, when forest habitat is closer in proximity to human development, it runs a higher risk of being negatively impacted or destroyed [30, 41].

Therefore, due to the collective burden of natural disturbances (forest fires and extreme weather events) and anthropogenic pressures (losses in habitat and habitat connectivity (fragmentation) resulting from land cover changes, associated decreases in biodiversity, invasive species proliferation, and any unanticipated indirect and/or synergistic reactions between the aforementioned pressures), the composition, structure, and function of urban forests are at an extreme risk of deterioration.

Urban forests are critically relied upon by wildlife. Following the urbanization of a landscape, the remaining interspersed fragments of urban forest serve as functional islands which provides extant species with some level of shelter from human impacts [8]. Urban forests are relied upon by humans as well. Urban forests play a significant role in the establishment of one's sense of place, which can be passed down through generations [42]. Therefore, forests are often known to possess great cultural value [43, 44]. Additionally, urban forests provide metropolitan areas with a number of ecosystem services, such as mitigating a potential urban heat island effect through the cooling of surface and air temperatures via evapotranspiration, reducing the volume and rate of flow of a runoff event via stormwater uptake, filtering city air, and reducing urban noise [45].

Contrary to what has been observed in tropical forests, recent research is suggesting that the trees along the edges of temperate forest fragments, adjacent to urban areas, are sequestering carbon dioxide in biomass and soils at an accelerated rate [46-48]. A study conducted by Morreale et al. (2021) found that trees along the edges of temperate forest fragments adjacent to urban areas grow up to 36% faster and sequester 24% more carbon than trees within the forest interior [48]. Separate research conducted by Garvey et al. (2022) found that in urban areas, respiration rates and associated carbon loss rates of soil along the edges of urban forest fragments are up to 25% lower compared to trees within the forest interior [47].

In support of maintaining these critical services urban forest provide to metropolitan areas into the foreseeable future, as urbanization continues, understanding the distribution of a metropolitan area's urban tree canopy relative to other land cover types, such as impervious surfaces, exposed soil, and water, will be increasingly useful [8, 10, 12, 43, 45].

Remote Sensing of Forestry and Carbon Sequestration

Advantages of Remote Sensing

Objects selectively absorb and reflect EMR due to subtle differences in the molecular composition of their surfaces [20]. Remote sensing can be defined as the utilization of EMR to detect objects on Earth's surface based on that object's interaction with and subsequent reflection of visible, infrared, and microwave portions of incident EMR [20].

Due to the considerable amount of time needed to visit and document a statistically viable sample of urban tree canopy sites across an entire city recent decades, the utilization of remote sensing techniques alongside computer-based geographic information systems (GIS) have proven to be powerful, cost-efficient tools with a wide variety of applications, including land use and land cover change studies, meteorological studies, emergency response planning, urban heat island monitoring and mitigation, water quality monitoring, forest carbon and biomass estimation, vegetation biophysical measurement estimation, and the management of urban forest vegetation [3-5, 11, 49-56].

To understand how remote sensing can be utilized to both assess urban tree canopy extent, and to predictively model sequestered carbon across urban forest biomass, some specific advantages and disadvantages associated with remote sensor platform, type, and resolution will be discussed respectively in the following section.

Sensor Platform

Airborne Sensors

Airborne platforms commonly utilized to map forest extent and to model sequestered carbon include airplanes and unmanned aerial vehicles (UAV) [13, 57, 58]. Airborne platforms are capable of carrying passive sensors, such as multispectral or hyperspectral sensors, and active sensors, like radio detection and ranging (radar) and light detection and ranging (LiDAR) systems. However, unlike spaceborne sensors, the flight altitude of a given airborne sensor is much lower than that of a spaceborne sensor. Therefore, the spatial resolution of airborne sensors can be very fine [20]. This very fine resolution supports the accurate detection of individual tree crowns and other parameters of forest structure [59].

Airborne platforms give researchers freedom to determine when the best time to acquire imagery might be. To keep the influence of tree canopy shadow artifacts and cloud pollution to a minimum, a manned or unmanned acquisition of aerial imagery could be scheduled on a clear day around noon, when the solar zenith angle is near 90° . However, the data provided by plane-mounted sensors is inherently limited by the cost of fueling and operating the airborne platform [57, 60]. UAV platforms can avoid potential cloud cover issues by flying just a few hundred feet above the ground, capturing imagery with spatial resolution measured in millimeters.

One caveat of the ultra-fine resolution of UAVs is a small instantaneous field of view (IFOV), or the ground area observed by the sensor at a given altitude and a given time. As a result, UAV data is often broken up into many relatively small chunks which require complex processing techniques before it is ready to be used in analysis.

Spaceborne Sensors

Spaceborne satellites are the most commonly utilized remote sensor platform, with many research applications including land use and land cover change studies, sequestered carbon modeling, and urban forest management [49, 51-54, 56]. Spaceborne sensors typically run continuously, collecting data along defined orbital paths, thereby creating large volumes of reliable data in a short amount of time [20]. Additionally, spaceborne sensors provide a synoptic view of Earth, allowing researchers to obtain data virtually anywhere on the Earth's surface in an instant without the need to charter an aircraft fitted with remote sensing equipment or scheduling a UAV flight [61, 62]. However, because of their predefined orbital paths, spaceborne sensors commonly collect data containing cloud pollution. Additionally, a majority of the data sources offering fine resolution spaceborne imagery are expensive.

On the other hand, a number of moderate resolution spaceborne data sources offer inexpensive or free data to researchers [61, 62]. Additionally, a few moderate resolution spaceborne data sources offer publicly available, low-cost, historical datasets. For example, the Landsat missions provide researchers with free moderate resolution multispectral imagery of Earth's surface dating back to 1972. Other remote sensors that provide comprehensive temporal datasets include NASA's Moderate Resolution Imaging Spectroradiometer (MODIS) and ESA's Sentinel-2 mission [63, 64].

Sensor Type

Active Sensors

Active remote sensors emit and detect their own EMR across a landscape in the form of visible, infrared, and/or microwave radiation [20]. Active sensors are commonly fixed to airborne and ground-based platforms. The sensors are largely represented by radar and LiDAR systems.

Radar

Radar systems detect the backscatter of emitted radio and microwaves to measure the surface roughness of objects within a given area [20, 65]. Smooth surfaces, such as a still water body, express very low surface roughness, as a majority of the emitted micro- and radio waves are being reflected on the smooth surface. Conversely, rough surfaces, such as urban tree canopy, scatter the emitted micro- and radio waves such that only the scattered light incident to urban tree canopy is reflected and subsequently detected by the radar sensor [66].

Because radar uses longer wavelengths of EMR, these sensors are capable of detecting objects obscured by cloud cover, which facilitates its application in military operations and emergency response [67]. However, some regions of the electromagnetic spectrum (EMS) which radar sensors operate in may not be useful in the mapping of vegetation or the modeling of sequestered carbon [68]. Additionally, because radar systems are side looking, large trees or undulating terrain that blocks other adjacent smaller trees create voids in the radar data [69]. For these reasons, radar systems are not commonly utilized to assess urban tree canopy extent or predictively model the carbon sequestered therein.

LiDAR

Like radar, LiDAR systems emit pulses of EMR and measure the amount of time it takes to detect the reflected energy [20, 58]. While radar systems use radio and microwaves, LiDAR uses more narrow wavelengths of EMR, such as visible and infrared light [20]. By continuously measuring the range between the sensor and objects on the ground, LiDAR systems create outputs of dense, 3-dimensional point clouds, where each point represents a location at which the emitted energy from the LiDAR sensor was reflected from some object in the field.

However, a few drawbacks hinder the application of LiDAR data to map urban tree canopy extent. Spaceborne LiDAR systems such as the Geoscience Laser Altimeter System (GLAS), are still in preliminary stages; the low point density of spaceborne LiDAR systems currently hinder their utility in the modeling of a complex forest canopy structure. Airborne LiDAR offers higher point densities; however, these data sources are limited and obtaining data is expensive. Finally, utilizing ground-based systems to assess urban tree canopy extent across a city's full extent is impractical, as the processing required to model urban tree canopy extent from ground-based sensors is complex and ground-based LiDAR scanners capable of mapping forest extent across an urban space are expensive. Therefore, unless low-cost airborne LiDAR data is accessible, researchers should consider other sources of remotely sensed data.

Passive Sensors

Passive sensors, also referred to as optical sensors, detect EMR emitted from the sun following its subsequent reflection off objects exposed on Earth's surface [20]. Like active sensors, passive sensors can be fixed to both spaceborne and airborne platforms. Defined as a remote sensor's specific characteristics and resolving power, sensor resolution can be further broken down

into the following components: spatial, spectral, temporal and radiometric resolution [20]. This section offers a brief discussion on a few advantages and disadvantages of the spatial and spectral resolution of common passive remote sensors.

Spatial Resolution

Spatial resolution is defined as the area of ground observable within a passive remote sensor's IFOV, or the specific ground area represented by a single pixel, at a given moment [20]. Because the altitude and the solid angle by which a given passive remote sensor is capable of detecting EMR is different from sensor to sensor, the spatial resolution of different remote sensors is variable [20].

Coarse Spatial Resolution

Coarse resolution sensors have spatial resolutions ranging from 40 meters to several kilometers. Therefore, coarse resolution data captured by Earth imaging sensors such as MODIS, Advanced Very High Resolution Radiometer (AVHRR), and Geostationary Operational Environmental Satellite (GOES) is typically used to map forest extent or model sequestered typically constrained to regional and global studies [64, 70-72].

Moderate Spatial Resolution

Moderate resolution remote sensors have spatial resolutions ranging between 10 and 30 meters. Of the host of moderate remote sensors used to monitor forest vegetation, no other remote sensor has been as influential as the optical sensors of the Landsat program [37, 49, 56, 62, 63, 73-80]. Landsat's temporal data archive provides continuous data from 1972 to current day, making it the single earliest and longest continuous archive of global multispectral remote imagery

source [81, 82]. Additionally, since 2008, researchers can freely view and download raw and processed data from Landsat's extensive temporal archive [4, 83]. Because of this accessibility, combined with its unparalleled archive of historical imagery, the Landsat program is one of the most heavily relied upon sources of remote sensing data on Earth [81].

Sentinel-2a is another moderate resolution multispectral data source used in forestry applications [51, 63, 75, 84-86]. Aside from it being another source of free multispectral data, Sentinel-2a imagery offers four moderate spatial resolution (20 meters) red-edge bands specifically sensitive to different regions of strong visible red absorption and (near-infrared radiation) NIR reflection of healthy vegetation at 705, 740, 783, and 865 nm respectively. However, as discussed by Cohen et al. (2003), when conducting studies across an intermittent urban tree canopy, it can be difficult to accurately model forest structural parameters using moderate resolution remote sensing data, as many pixels containing the spectral signature of forest canopy will be polluted by spectral signatures from other adjacent land cover types [73].

Fine Spatial Resolution

Fine resolution remote sensors are characterized by spatial resolutions smaller than 5 meters. Unlike the free moderate resolution multispectral imagery offered by Landsat and Sentinel-2a, the fine resolution multispectral imagery captured by satellites such as QuickBird, IKONOS, and the SkySat constellation requires significant financial investment. However, when seeking to map urban tree canopy using remotely sensed imagery, the ability to functionally delineate individual tree crown pixels from adjacent non-tree crown pixels across an urbanized landscape with any accuracy is only possible with fine resolution imagery [87-89].

A few low cost sources of fine resolution multispectral imagery are available to researchers. Among these sources is the United States Department of Agriculture's (USDA)

National Agricultural Imagery Program (NAIP). With a spatial resolution of ~1 meter or less, NAIP imagery is a suitable data source for vegetation mapping [90]. However, this data source has a lengthy temporal resolution of three years. Researchers using this source to model forest extent or structural parameters might consider planning research around known acquisition times.

PlanetScope is another low-cost fine resolution multispectral data source. PlanetScope consists of a constellation of over 180 small cube satellites, or Doves, that continuously image Earth's surface. By applying to Planet's Education and Research Program, individuals affiliated with a university can download up to ~1,900 square miles of 4 and 8 band multispectral imagery with a spatial resolution of 3 meters and a daily revisit time free of charge. Many studies have shown that due to its temporal resolution and near-fine spatial resolution, PlanetScope is a superior data source for vegetation mapping [91, 92].

One last fine resolution data source is SkySat. Planet's SkySat constellation consists of 21 fine resolution Earth imaging multispectral satellites. SkySat imagery has 5 bands (red, green, blue, NIR, and panchromatic) and a spatial resolution of 50 centimeters. One drawback of SkySat is that unlike PlanetScope data, SkySat data must be tasked, which comes at a steep cost. However, SkySat's sub-meter spatial resolution and approximately 3.6 mile wide swath width merges the advantages of a spatial resolution comparable to that of airborne platforms with the image size of spaceborne platforms. For this reason, SkySat is a preeminent data source for mapping urban tree canopy extent and modeling forest structural parameters.

Spatial Resolution and Machine Learning-Based Image Classification

Coarse and Moderate Resolution Imagery

When attempting to classify imagery using a machine learning algorithm, supervised classification is a commonly utilized method [93]. Supervised classification is a machine learning technique that works to identify distinct patterns in a dataset based on user-provided training data [94]. When dealing with coarse or moderate resolution imagery however, it can be very difficult to visually differentiate objects, such as tree canopies, apart from other types of vegetation or land cover types when collecting pure training samples with which to train a machine learning algorithm for supervised classification. In these situations, unsupervised classification workflows can be applied. Like supervised classification, unsupervised classification is a machine learning technique that works to identify distinct patterns in a dataset, however no training data is required [95].

One commonly utilized unsupervised classification method is iso cluster [95-97]. Isocluster works by randomly selecting clusters in a dataset and iteratively sorting data to the nearest cluster [95]. After each iteration, cluster centers are redefined based on the average of the assigned data values. This process continues until clusters stabilize, or until a user-defined iteration convergence threshold is reached. By setting an appropriate iteration convergence threshold you prevent potential overfitting of the classified results [95].

Fine Resolution Imagery

One specific advantage of fine resolution imagery is the ability to utilize an object-based image classification approach. When classifying fine resolution imagery, object-based classification has been found to offer accuracy advantages over traditional pixel-based classification methodologies [87, 88]. Because an individual pixel within moderate or course

resolution imagery is not exclusive to a single object, object-based classification is not typically employed in conjunction with these data sources.

Unlike traditional pixel-based classification methods, object-based classification considers the spectral, geometric, and topological characteristics of pixel clusters [98]. As a result, when applied to fine resolution datasets, object-based classification approaches are capable of yielding smoother, more interpretable land cover datasets compared to that of pixel-based approaches [99].

Following an object-based classification approach, different clusters of pixels representing various objects across an image are segmented based on the spectral signature, shape, length, and adjacency characteristics of homogeneous pixel clusters prior to classification [100].

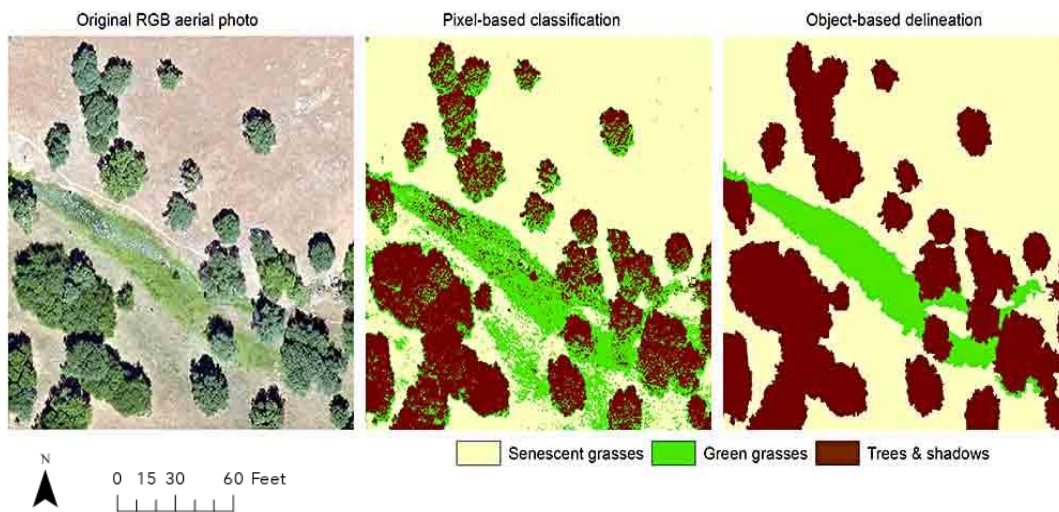


Figure 2.3 Comparison of pixel-based (middle) and object-based (right) classification outputs [101]

Using ArcGIS Pro, there are a few methods to segment imagery. One such method employs an algorithm known as mean shift. Mean shift segmentation works by selecting a pixel within the input imagery and creating a window around the selected pixel. The algorithm then calculates the average value for all pixels in that window. Then, the window is shifted in the direction of

increasing pixel values, until it reaches a maximum. Next, the algorithm effectively outlines the region represented by all pixels of similar value within the window. This process continues iteratively until all pixels have been outlined or segmented [102-104].

For each of the desired classes within the land cover dataset, training samples are collected by selecting image segments representative of the land class/object you are attempting to classify. For example, segmented tree crown segments are collected from the segmented image as training samples and fed into a machine learning algorithm to inform the identification and classification of tree canopy segments across the image based on the spectral, geometric, and topological characteristics of the segment [105].

Following Esri's object-based image classification workflow as directed by ArcGIS Pro's Image Classification Wizard, during image classification, the machine learning classifier will specifically be looking for the spectral, geometric, and topologic segment characteristics transferred from the segmented layer to the training samples as attributes during sample collection. If samples derived purely from the multispectral image were selected as training data and not samples derived from the segmented layer, then the spectral and spatial characteristics needed to classify the image are not successfully transferred to the training samples [125].

With recent updates to the Environmental Science Research Institute's (Esri) flagship software, ArcGIS Pro, objects-based image classification workflows are now easily accessible via user friendly, ready-to-use software packages. However, the segmentation and classification processes can be time consuming, especially performed at the scale of larger municipality geographies [106].

Spectral Resolution

In the same way that fine resolution imagery is needed to effectively map urban tree canopy extent, when modeling sequestered carbon using passive remote sensors, spectral resolution should be considered, as the spectral signature expressed by healthy chlorophyll commonly serves as the basis for the independent variable of predictive model [107].

While some passive spaceborne sensors are fitted with only a few channels capable of detecting a relatively broad range of wavelengths (multispectral), others are fitted with hundreds of narrow band channels which can differentiate minute variations in the wavelength of reflected energy (hyperspectral) associated with differences in the molecular composition of objects at the surface of the Earth [20]. Multispectral imagery is well suited for the mapping of forest extent across a heterogeneous urban landscape. However, when modeling carbon using optical sensor data, especially when the independent variable selected is proxy for chlorophyll concentration, it is recommended that researchers obtain data with relatively narrow bands in the red (650-700 nm) and NIR (700-1000 nm) region of the EMS, corresponding to the strong absorption of visible red light and the strong reflection of NIR by chlorophyll [20]. Sentinel-2a's four narrow red edge bands are specifically sensitive to these regions of the EMS. Integrating these narrow red-edge bands into multispectral sensors merges the spectral power of hyperspectral sensors with the accessibility of moderate resolution sensors.

Analyzing Forest Extent and Sequestered Carbon Using Remote Sensing

Allometric Equations

The modeling of sequestered carbon across an urban tree canopy typically includes the utilization of allometric equations and biomass expansion factors [108-111]. Allometric equations are statistical formulas that can estimate sequestered carbon through analysis of a combination of biophysical variables measured in the field, such as DBH and tree height [111]. Because the sequestered carbon of a tree increases proportionally with biophysical variables such as height and DBH, allometric equations can provide accurate estimations of sequestered carbon without the need to destructively harvest vegetation. Allometric equations can be developed for a single species or a regionally specific community assemblages. Additionally, separate equations to model biomass and sequestered carbon across urban forests have been developed by the US Forest Service [112, 113].

Remote Sensing Applications

Because the internal and external structure of plants have evolved to facilitate photosynthesis, these structures, and their interaction with incident EMR, have a direct influence on how leaves and the canopies of trees appear when analyzed by optical remote sensors [20]. Healthy vegetation expresses strong absorption of EMR between 650-700 nm (visible red light), and strong reflection of EMR between 700-1000 nm (NIR) [20]. This sharp change in reflectance values for vegetation is known as the red edge, where the slope of this red edge is strongly influenced by chlorophyll concentration [114].

Additionally, because of healthy green vegetation's strong absorption of red wavelengths and strong reflection of near-infrared wavelengths, in a composite image with red and NIR bands, it is possible to generate a single normalized value, oftentimes ranging from 0 to 1, for each pixel, where each value represents the relative abundance of healthy green vegetation at that pixel. This is the concept for vegetation indices [20, 114, 115].

$$\mathbf{NDVI} = \frac{(\rho_{NIR} - \rho_R)}{(\rho_{NIR} + \rho_R)} \quad (1)$$

Vegetation indices such as the normalized differential vegetation index (NDVI), seen in Equation 1, are based upon this concept, where ρ_{NIR} is the reflectance values of the NIR band, ρ_R is the reflectance values of the red band [115]. Similar to structural predictors such as canopy height and basal area, vegetation indices, like NDVI, can be effectively utilized as a spectral predictor variable to estimate sequestered carbon [62, 84-86]. Similar to NDVI, many other vegetation indices, such as GNDVI, have been created, each with advantages and disadvantages. GNDVI for example was created with the idea that the integration of the green band in place of the red band would allow the derived index to be more sensitive to variation in chlorophyll content than compared to NDVI, where ρ_{NIR} is the reflectance values of the NIR band, ρ_G is the reflectance values of the green band [116].

$$\mathbf{GNDVI} = \frac{(\rho_{NIR} - \rho_G)}{(\rho_{NIR} + \rho_G)} \quad (2)$$

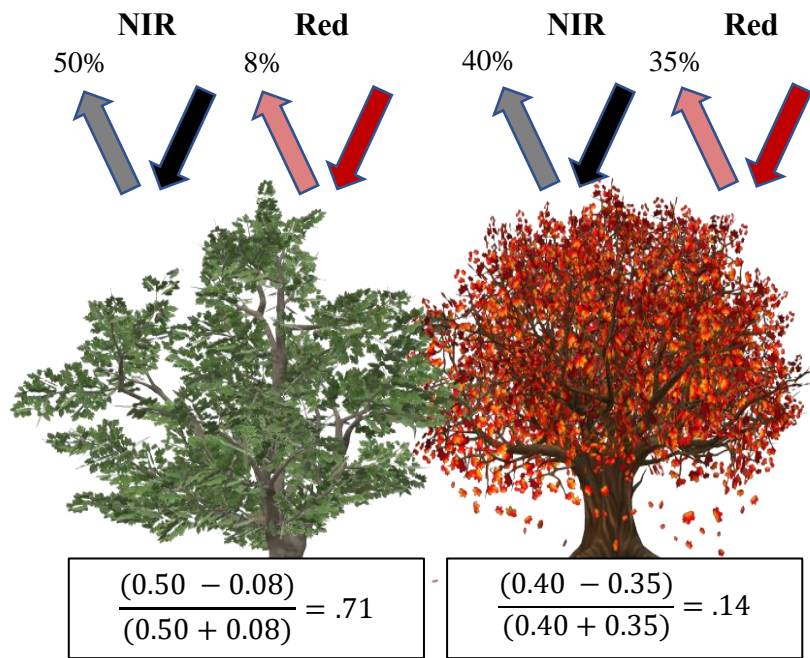


Figure 2.4 Visualization of the impact of chlorophyll abundance on NDVI [117]

Modeling Forest Carbon Using Field Data and Remote Sensing

In developing predictive models via regression analysis, two specific variables are identified by the researcher: the dependent variable, otherwise known as the response variable, and the independent variable, otherwise known as the predictor variable. The response variable in this case would be sequestered carbon values sampled in the field using allometric equations. Predictor variables used to model sequestered carbon are variable, and can generally be broken into biophysical measurements, such as DBH and stem volume, or spectral characteristics of remote sensing data [57, 58]. Common structural predictor variables used in the predictive modeling of sequestered carbon include diameter at stump height, DBH, canopy height, crown volume, crown area, leaf area index (LAI), and leaf area density (LAD) [73, 112, 118-121].

Using spectral predictor variables to model sequestered carbon often involves the creation of vegetation indices [20]. Vegetation indices take advantage of chlorophyll's strong reflection and absorption of NIR and red wavelengths respectively [20, 114, 115]. Some of the most common vegetation indices are: NDVI, enhanced vegetation index (EVI), soil adjusted vegetation index (SAVI), simple ratio vegetation index (SR), moisture vegetation index (MSI), and green normalized vegetation index (GNDVI) [122]. Using vegetation indices like NDVI, relative chlorophyll concentration has been found to be an acceptable proxy for sequestered carbon when utilizing remote sensing techniques [56, 62, 115, 122, 123]. Additionally, some studies utilizing spectral predictor variables take advantage of the narrow red edge band sensors when creating vegetation indices [74, 75, 85, 86, 114, 122].

To effectively model sequestered carbon across an urban tree canopy using vegetation indices as the predictor variable, it is recommended that all source imagery be acquired during late spring to early summer, when the levels of chlorophyll within tree leaves are at peak concentrations, as it is this variation in chlorophyll concentration that that predictive model is based on [20]. Additionally, any predictive model derived using vegetation indices or other spectral information as the predictor variable should only be applied within the specific geographic location represented by the source imagery from which the predictor variable was derived [62].

Literature Review Summary

As the urbanization of metropolitan areas continues into the future, compared to the carbon stored via the GCC, carbon sequestered in the biomass of Earth's forests is under a greater threat of being released back to the atmosphere as CO₂ [30]. Due to their proximity to human development, the composition, structure, and function of urban forests in particular possess an enhanced risk of deterioration overtime [30, 41]. In support of maintaining the critical services urban forest provide to metropolitan areas into the foreseeable future, as urbanization continues, understanding the distribution of a metropolitan area's urban tree canopy relative to other land cover types, such as impervious surfaces, exposed soil, and water, will be increasingly useful [8, 10, 12, 43, 45].

Remote sensing techniques and geographic information systems offer researchers with streamlined methods to quickly assess the distribution of land cover types, including urban tree canopy, across a city [20]. Following a review of peer reviewed literature, Landsat's historic imagery archive is the choice imagery source when seeking a historic imagery source across the full extent of a city's urban tree canopy [81, 82].

When mapping the current extent of urban tree canopy at the city-level, fine resolution multispectral imagery with a sufficiently large swath size was found to be the ideal data characteristic. Similarly, when developing predictive models to estimate sequestered carbon from satellite imagery, fine resolution multispectral imagery is superior, however it can be expensive to obtain. PlanetScope imagery is a great low cost option for researchers seeking higher resolution imagery in the development of predictive carbon models from satellite imagery.

Additionally, though Sentinel-2a is not a fine resolution sensor, considering its data comes with four narrow red edge bands and the fact that its imagery is free to download, Sentinel-2a data is a great data source for vegetation mapping. However, if seeking to obtain the highest resolution imagery possible across mid-sized or large metropolitan areas, and assuming financial resources are not limited, researchers might consider acquiring SkySat imagery. Its 50 cm resolution and 3.6 mile wide swath width make SkySat a preeminent data source for mapping urban tree canopy at the city-level.

Restatement of the Research Objectives

Over the next three chapters presented here, this research works to identify practical methodologies using remote sensing and digital image processing to answer each of the following three questions:

- CHAPTER 3. How has the extent of Chattanooga's urban tree canopy changed between 1984 and 2021?
- CHAPTER 4. How can the carbon sequestered in the biomass of urban forest trees be predictively modeled at little to no cost and without a significant time investment?
- CHAPTER 5. What is the current extent of Chattanooga's urban tree canopy?

CHAPTER 3

APPLICATION OF LANDSAT IMAGERY

The objective of this chapter is to map the extent of Chattanooga's urban forest canopy between 1984 and 2021 using historic satellite imagery. Because of the Landsat program's unparalleled continuity, this section of research employs 30m Landsat 5 Thematic Mapper (TM) and 30m Landsat8 Operational Land Imager (OLI) to conduct all spatial analyses.

Study Site

The study site for this research was the City of Chattanooga, Tennessee. Research recently conducted at the University of Tennessee at Chattanooga has confirmed Chattanooga's urban land areas have increased rapidly since 1986 [4, 124]. Previous research also confirmed that the conversion of forest to developed areas in the City of Chattanooga can be directly associated with impacts to surface water quality, increased surface and air temperatures, and decreased canopy cover resulting from the extraction of vegetation [3, 4, 83, 124, 125]. Analyzing the multidecade spatiotemporal impact of urbanization on forest canopy in Chattanooga could help direct sustainable development efforts towards areas urbanizing at an above-average rate. To date, no published research has identified the historic extent of Chattanooga's urban tree canopy.



Figure 3.1 Study site map for Landsat research and the City of Chattanooga, Tennessee's boundary

Data Collection

For this research, Landsat 5 Thematic Mapper (TM) and Landsat 8 Operational Land Imager (OLI) data were obtained from USGS's Earth Explorer data hub, seen in Figure 3.2. Landsat data can be obtained from Earth Explorer as a Level-1 or a Level-2 product, where Level-1 data are provided as digital numbers without atmospheric corrections conducted, and Level-2 data are provided as calibrated surface reflectance values. For this research, Level-2 data were obtained. Downloaded from Earth Explorer as Level-2 products, Landsat 8 OLI imagery consisted of 9 bands, while Landsat 5 TM imagery consisted of 7 bands, shown in Table 3.1.

Table 3.1 Landsat 5 TM and Landsat 8 OLI sensor specifications

	Bands	Description	Wavelength (μm)	Spatial resolution (m)	Temporal Resolution
Landsat 5	TM 1	Blue	0.45 - 0.52	30	16 Days
	TM 2	Green	0.52 - 0.60	30	
	TM 3	Red	0.63 - 0.69	30	
	TM 4	Near-Infrared	0.76 - 0.90	30	
	TM 5	Near-Infrared	1.55 - 1.75	30	
	TM 6	Thermal-Infrared	10.40 - 12.50	120	
	TM 7	Mid-Infrared	2.08 - 2.35	30	
Landsat 8	OLI 1	Coastal Aerosol	0.43 - 0.45	30	16 Days
	OLI 2	Blue	0.45 - 0.51	30	
	OLI 3	Green	0.53 - 0.59	30	
	OLI 4	Red	0.64 - 0.67	30	
	OLI 5	Near-Infrared	0.85 - 0.88	30	
	OLI 6	Shortwave-Infrared	1.57 - 1.65	30	
	OLI 7	Shortwave-Infrared	2.11 - 2.29	30	
	OLI 8	Panchromatic	0.50 - 0.68	15	
	OLI 9	Cirrus	1.36 - 1.38	30	

In order to understand how forest canopy coverage was impacted by urbanization between 1984 and 2021, imagery was obtained along a defined interval, where the years between imagery acquisition (referred to in Table 3.2. as “Acquisition Gap”) was equal to or less than 5 years. A 5-year interval was selected by the researchers in order to effectively observe urban growth and canopy loss through time without obtaining an excessive number of Landsat scenes. In this research a total of 10 scenes were obtained representing 37 years of urbanization in the City of Chattanooga, TN. All Landsat scenes were obtained during the months of June and July to account for any seasonal variation in canopy coverage. In some cases when cloud coverage was an issue, imagery was acquired before the defined 5-year interval. In one case however, the acquisition period between scenes was greater than the defined 5-year interval. This was due to excessive cloud coverage above Chattanooga, TN between the months of June and July from 2014 to 2020. For this reason, the acquisition gap between scenes 8 and 9 was 6 years instead of 5 years.

Table 3.2 Acquired Landsat 5 TM and Landsat 8 OLI imagery

Scene ID	Year	Month and Day	Acquisition Gap	Satellite - Sensor	RGB
1	1984	June 27	0	Landsat 5 - TM	321
2	1988	July 8	4		321
3	1990	June 28	2		321
4	1995	July 12	5		321
5	2000	June 23	5		321
6	2004	July 20	4		321
7	2009	June 16	5		321
8	2014	June 14	5	Landsat 8 - OLI	432
9	2019	August 31	6		432
10	2021	July 3	1		432

Methods

Image Pre-Processing and Enhancement

Using the Composite Band geoprocessing tool in ArcGIS Pro, the individual bands for each of the downloaded scenes, as shown in Table 3.1., were stacked to create 10 composite multispectral images. Next, using the Clip Raster geoprocessing tool within ArcGIS Pro, each of the 10 composite images were clipped to the City of Chattanooga's boundary. Landsat true color imagery is seen in Figure 3.2. and Appendix Figures A1-A10. For Landsat 5 scenes 1 – 7, the band combination for RGB true color was 321. For Landsat scenes 8 – 10, the band combination for RGB was 432. The images were stretched using either “percent clip” or “standard deviation”.



Figure 3.2 True color Landsat 8 OLI image acquired July 3, 2021 over the City of Chattanooga, TN

Feature Extraction

The final step in image processing was classifying each image to obtain a thematic land cover map visualizing the following classes: developed areas, forest canopy, non-forest vegetation, and water. To do this, both pixel-based supervised classification and pixel-based unsupervised classification were utilized. This is commonly referred to as a supervised hybrid classification strategy. For reasons related to Landsat's 30 m spatial resolution, pixel-based supervised hybrid classification was ultimately selected.

Supervised Classification

To conduct supervised pixel-based classification, ArcGIS Pro's "Image Classification Wizard" (ICW) was utilized. On the "Configure" pane of the ICW, "supervised" and "pixel-based" were selected. ArcGIS Pro's default classification schema was selected. In the next pane of the ICW, ("Training Samples Manager") a new 3-class schema was created consisting of pervious surfaces, impervious surfaces, and water. This 3-class schema was then used to collect 10 separate training sample datasets which would be used to train the classification of the 10 obtained Landsat images (Figure 3.3.A.; Appendix Figures A11-A20). In the next pane of the ICW, ("Train") support vector machine was selected as the machine learning classifier for supervised classification. The default maximum number of samples per class were used. However, if a greater number of samples are collected in a single class than the default value, this value should instead be set to 0 so that the classifier considers all collected training samples. The output data obtained from supervised classification was 10 raster datasets consisting each of 3 land cover classes: pervious surfaces, impervious surfaces, and water (Figure 3.3.B.; Appendix Figures A21-A30).

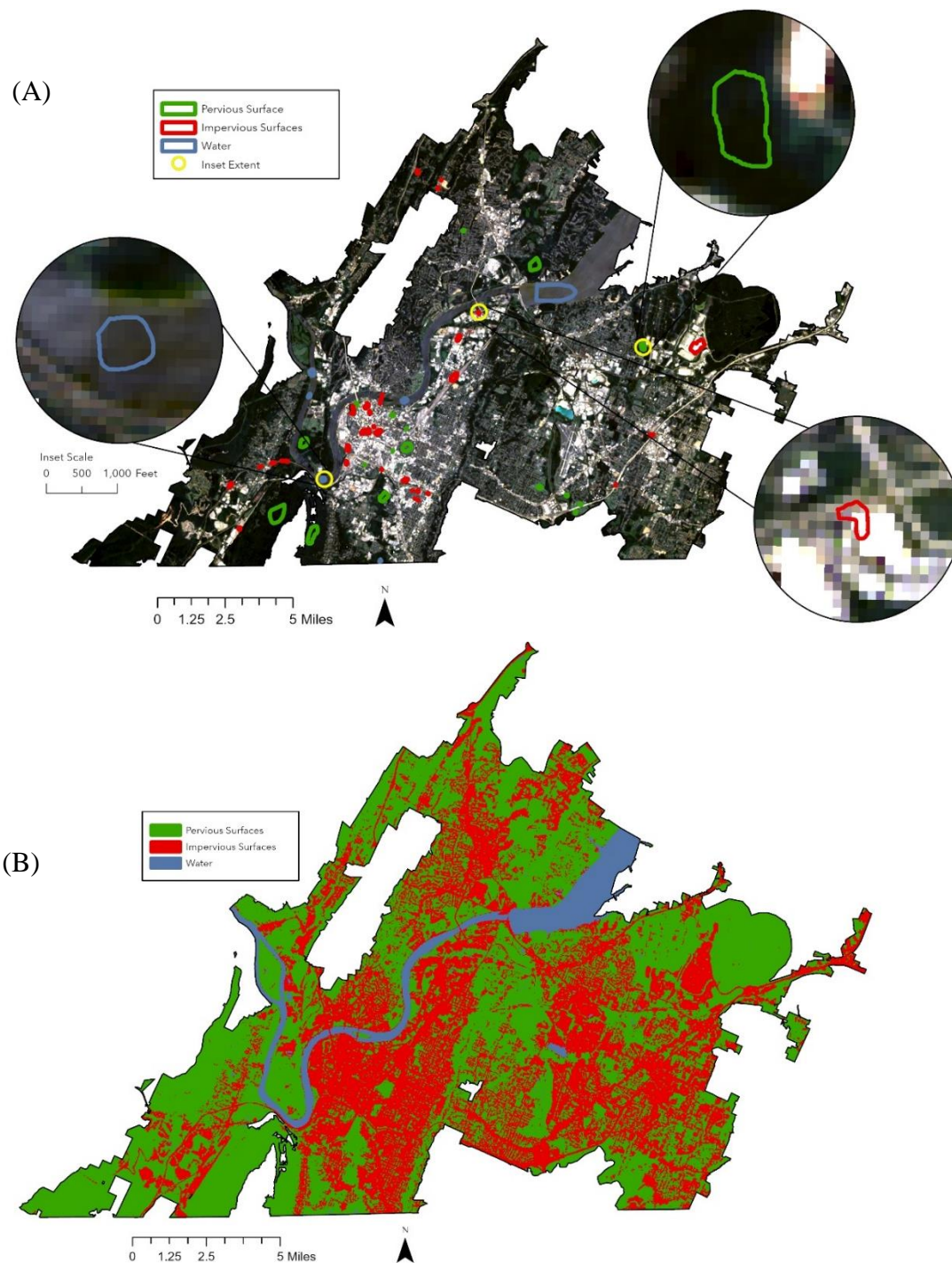


Figure 3.3 (A) Distribution of training samples used for supervised classification shown on the true color 2021 Landsat 8 OLI imagery; (B) 3 class thematic land cover dataset derived from the supervised classification of the 2021 Landsat 8 OLI imagery

Unsupervised Classification

Next, using ArcGIS Pro's Extract By Mask geoprocessing tool, pixels from the original multispectral Landsat images coincident with the pervious surfaces class from the output of supervised classification were extracted. Using these extracted pervious pixels from all obtained Landsat scenes, unsupervised classification was employed to classify the extracted multispectral pervious pixels into 10 spectrally distinct classes.

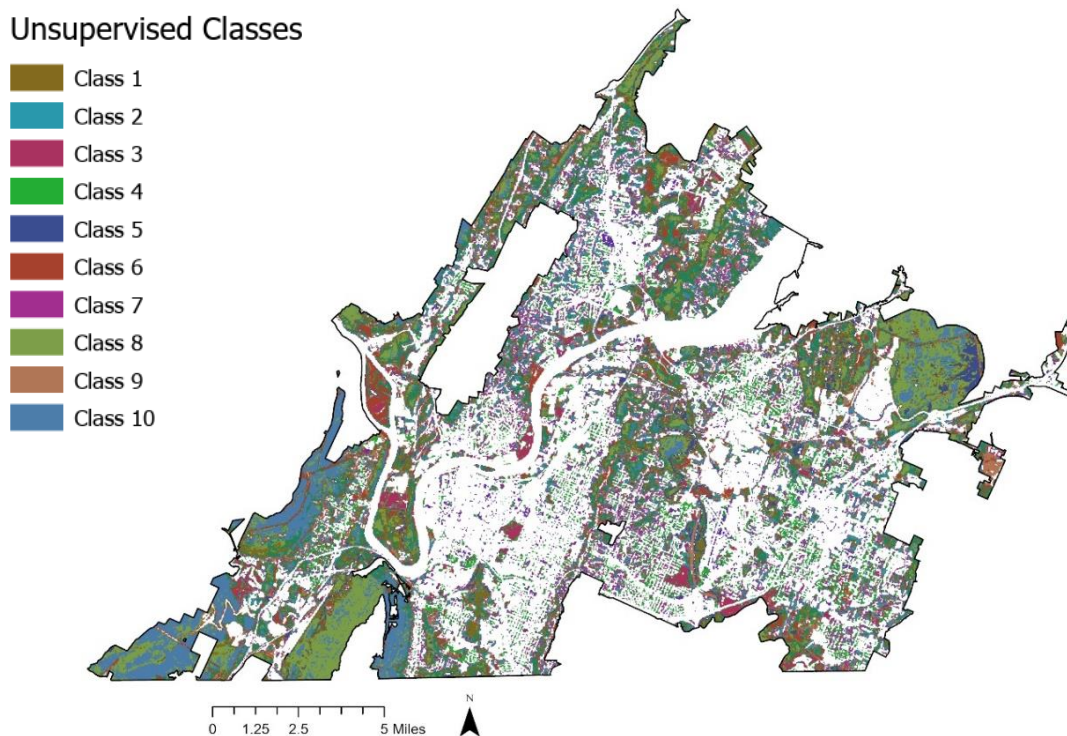


Figure 3.4 Land cover output consisting of 10 spectrally distinct classes of pervious pixels following unsupervised classification (2021 Landsat 8 OLI imagery displayed)

Unsupervised classification was selected to identify forest canopy pixels apart from other non-forest vegetation pixels. This step was conducted within ArcGIS Pro's ICW. On the "Configure" pane of the ICW, "Unsupervised" and "Pixel based" were selected.

ArcGIS Pro's default classification schema was selected. In the next pane of the ICW ("Train"), iso cluster was selected as the classifier for unsupervised classification. The maximum number of classes was set to 10. Unsupervised classification within ArcGIS Pro was configured with an appropriate iteration convergence threshold. All other parameters were left at default values. The output data obtained from unsupervised classification was 10 raster datasets, each consisting of 10 spectrally distinct classes of previous pixels (Figure 3.4.; Appendix Figures A31-A40).

Image Post-Processing

Image Reclassification

Next, the unsupervised outputs needed to be reclassified into 2-class rasters consisting of forest canopy and non-forest vegetation. This was accomplished using a true color reference to inspect each of the 10 classes of previous pixels for all unsupervised outputs. After determining whether each class of the unsupervised outputs belonged to the forest canopy class or the non-forest vegetation class, the unsupervised output was reclassified using ArcGIS Pro's Reclassify geoprocessing tool. The output obtained from the reclassification of unsupervised data was 10 raster datasets, each consisting of forest canopy and non-forest vegetation (Figure 3.5.; Appendix Figures A41-A50).

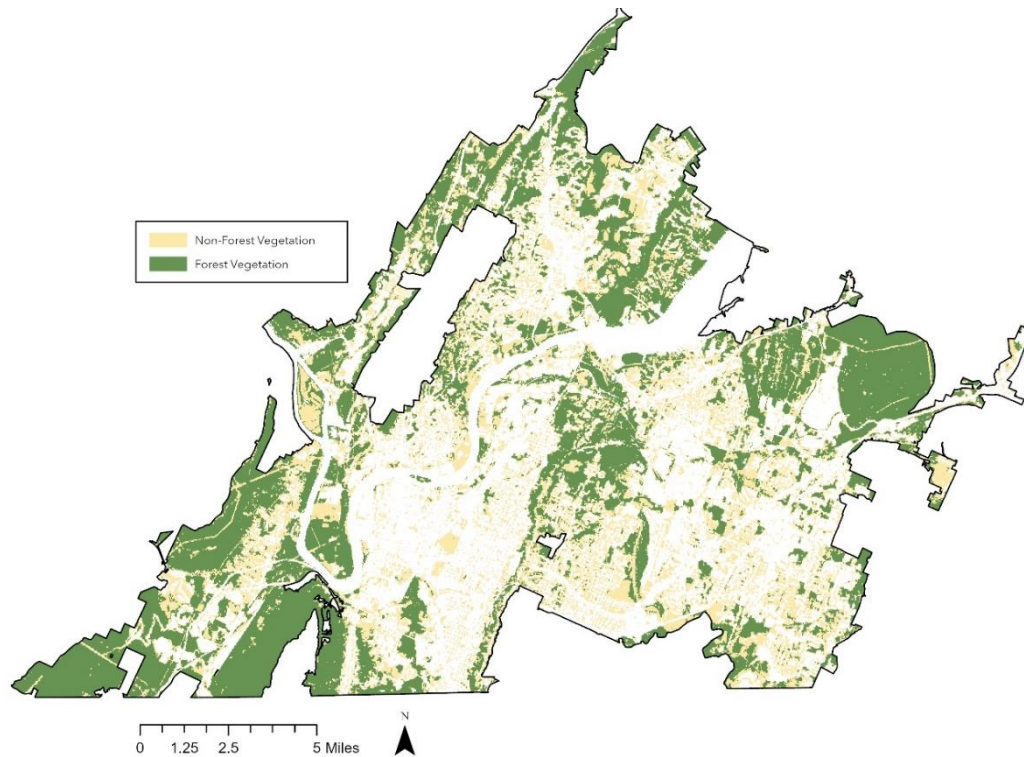


Figure 3.5 Reclassification of 10 spectrally distinct classes of previous pixels into a new 2 class thematic raster consisting of Non-Forest Vegetation and Forest Vegetation (2021 Landsat 8 OLI imagery displayed)

Creating the Final Land Cover Datasets

Finally, to obtain the desired 4-class land cover map, the outputs from the reclassification of pervious pixels and supervised classification needed to be combined. From each of the supervised classification outputs, all pervious pixels were reclassified to “NoData” using ArcGIS Pro’s Reclassify geoprocessing tool. Next, using ArcGIS Pro’s Merge raster function, the developed and water classes from supervised classification and the forest and non-forest vegetation classes from unsupervised classification were combined. The final output data obtained was 10 raster datasets, each consisting of 4 classes: developed areas, forest canopy, non-forest vegetation, and water (Figure 3.6.; Appendix Figures A51-A60).

Table 3.3 Final thematic land cover dataset class names and descriptions

Land Class	Class Code	Class Description
Impervious Surfaces	1	Buildings, Roads, Cars, Parking Lots, Artificial Turf, etc.
Non-Forest Vegetation	2	Grasses, Scrubs, Shrubs, Crops, Ornamental Plants, etc.
Urban Forest Canopy	3	All tree canopy within the study area.
Water	4	Flooded Wetlands, Rivers, Streams, Man-Made Retention Ponds, etc.

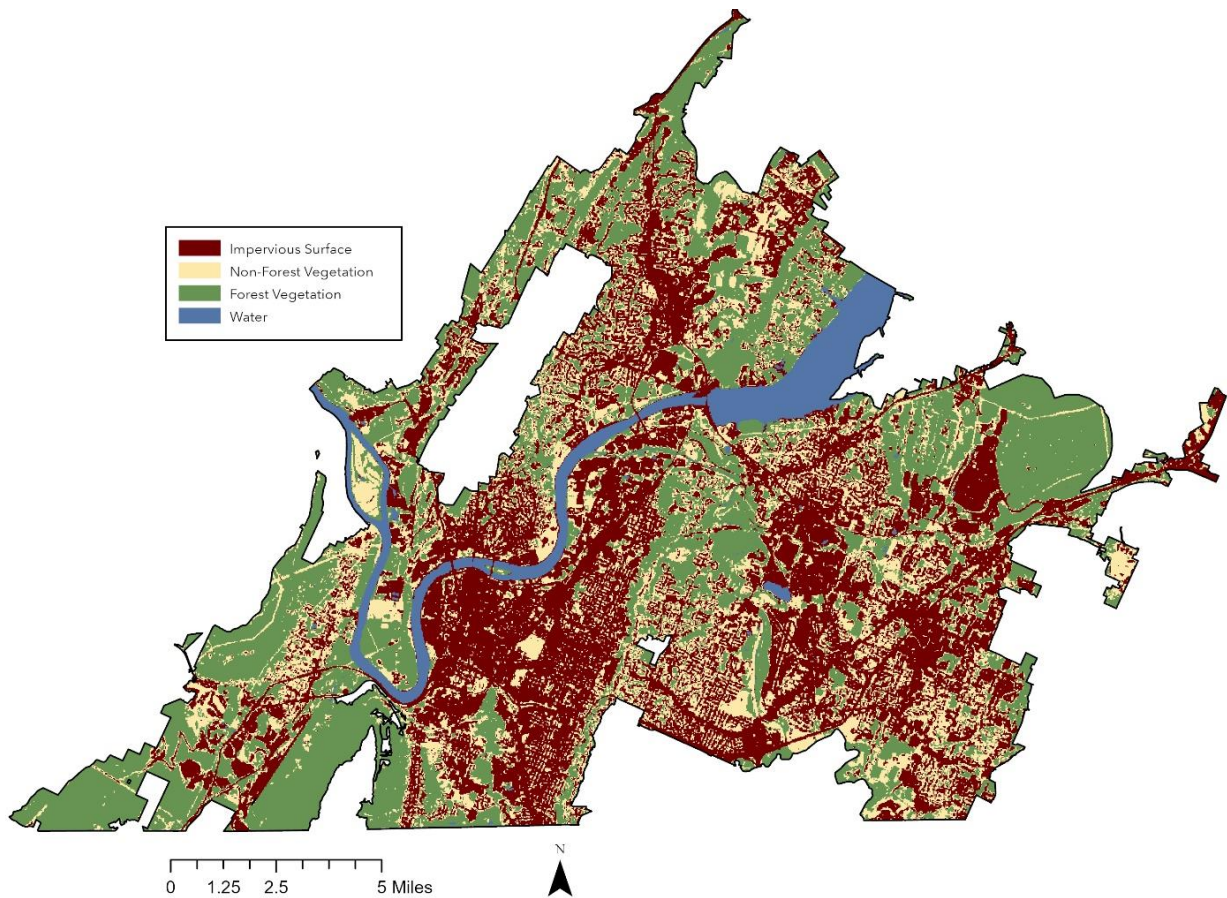


Figure 3.6 Final supervised hybrid thematic 4-class land cover raster

Accuracy Assessment

Typically, accuracy assessments of spatial analyses incorporate ground-truth data to reference the derived land cover dataset. However, this is generally not possible when dealing with temporal datasets. Therefore, to conduct an accuracy assessment of the spatiotemporal analysis conducted across Chattanooga's forest canopy, Google Earth's historic imagery archive was utilized. For each year of acquisition for the Landsat imagery obtained in this research, polygons representing pure samples of the 4 classes derived in the final output of this analysis were collected using random stratified sampling across the imagery and saved as separate kml files. The files were then uploaded to ArcGIS Pro and saved as feature classes. Finally, using ArcGIS Pro's Tabulate Area geoprocessing tool, an analysis of user accuracy was preformed (Table 3.4.).

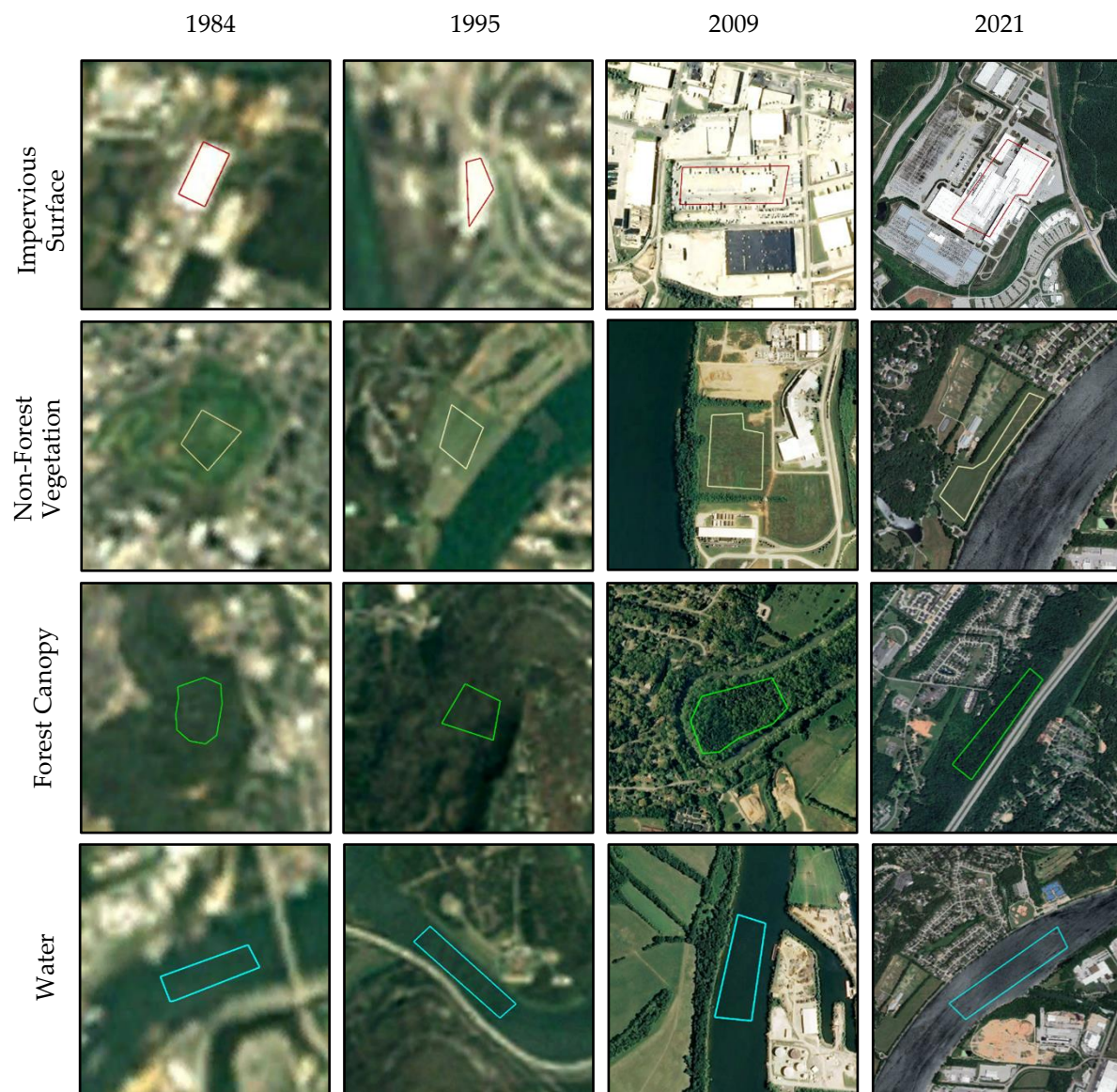


Figure 3.7 Example of the polygons digitized using Google Earth's historic imagery to conduct the accuracy assessment across each of the 10 supervised hybrid land cover datasets (Images not to scale)

Results

Confusion Matrices

For each of the classified land cover datasets, a confusion matrix was generated and provided in Table 3.4. Based on the results of the accuracy assessments conducted across each of the ten land cover datasets, overall accuracy ranged from 92.97% to 99.71%. Scene 10 (2021) yielded the highest overall accuracy, while Scene 1 (1984) produced the lowest. Results across all ten accuracy assessments suggest the most common error of commission (Type I error / false-positive) was the erroneous classification of Non-Forest Vegetation pixels into the Impervious Surface and Forest Canopy land classes, while the most common error of omission (Type II error / false-negative) was the erroneous classification of Impervious Surface pixels into the Non-Forest Vegetation and Forest Canopy land classes.

Table 3.4 Confusion matrices derived from the accuracy assessment of 1984 – 2021 final land cover datasets

1984	Classified Pixels	Developed	Non-Forest Vegetation	Forest	Water	Total	User's Accuracy
	Developed Pixels	413	18	2	0	433	95.38%
	Non-Forest Vegetation Pixels	166	206	135	0	507	40.63%
	Forest Pixels	0	0	1026	0	1026	100.00%
	Water Pixels	0	0	0	2599	2599	100.00%
	Total	579	224	1163	2599	4565	
	Producer's Accuracy	71.33%	91.96%	88.22%	100.00%		Overall = 92.97%
1988	Classified Pixels	Developed	Non-Forest Vegetation	Forest	Water	Total	User's Accuracy
	Developed Pixels	214	3	3	0	220	97.27%
	Non-Forest Vegetation Pixels	66	172	60	0	298	57.72%
	Forest Pixels	22	28	709	0	759	93.41%
	Water Pixels	0	0	0	2599	2599	100.00%
	Total	302	203	772	2599	3876	
	Producer's Accuracy	70.86%	84.73%	91.84%	100.00%		Overall = 95.30%

1990	Classified Pixels	Developed	Non-Forest Vegetation	Forest	Water	Total	User's Accuracy
	Developed Pixels	206	0	0	0	206	100.00%
	Non-Forest Vegetation Pixels	102	263	6	0	371	70.89%
	Forest Pixels	0	0	802	0	802	100.00%
	Water Pixels	0	1	1	2597	2599	99.92%
	Total	308	264	809	2597	3978	
	Producer's Accuracy	66.88%	99.62%	99.13%	100.00%		Overall = 97.23%
1995	Classified Pixels	Developed	Non-Forest Vegetation	Forest	Water	Total	User's Accuracy
	Developed Pixels	157	0	0	0	157	100.00%
	Non-Forest Vegetation Pixels	2	294	43	0	339	86.73%
	Forest Pixels	0	0	431	0	431	100.00%
	Water Pixels	0	0	0	2599	2599	100.00%
	Total	159	294	474	2599	3526	
	Producer's Accuracy	98.74%	100.00%	90.93%	100.00%		Overall = 98.72%
2000	Classified Pixels	Developed	Non-Forest Vegetation	Forest	Water	Total	User's Accuracy
	Developed Pixels	132	0	0	0	132	100.00%
	Non-Forest Vegetation Pixels	0	164	149	0	313	52.40%
	Forest Pixels	41	0	606	0	647	93.66%
	Water Pixels	0	0	0	2599	2599	100.00%
	Total	173	164	755	2599	3691	
	Producer's Accuracy	76.30%	100.00%	80.26%	100.00%		Overall = 94.85%
2004	Classified Pixels	Developed	Non-Forest Vegetation	Forest	Water	Total	User's Accuracy
	Developed Pixels	125	0	0	0	125	100.00%
	Non-Forest Vegetation Pixels	51	187	0	0	238	78.57%
	Forest Pixels	0	1	417	0	418	99.76%
	Water Pixels	0	0	0	2599	2599	100.00%
	Total	176	188	417	2599	3380	
	Producer's Accuracy	71.02%	99.47%	100.00%	100.00%		Overall = 98.46%
2009	Classified Pixels	Developed	Non-Forest Vegetation	Forest	Water	Total	User's Accuracy
	Developed Pixels	295	0	0	0	295	100.00%
	Non-Forest Vegetation Pixels	24	159	10	0	193	82.38%
	Forest Pixels	0	0	1658	0	1658	100.00%
	Water Pixels	0	0	0	2599	2599	100.00%
	Total	319	159	1668	2599	4745	
	Producer's Accuracy	92.48%	100.00%	99.40%	100.00%		Overall = 99.28%

2014	Classified Pixels	Developed	Non-Forest Vegetation	Forest	Water	Total	User's Accuracy
	Developed Pixels	297	0	0	0	297	100.00%
	Non-Forest Vegetation Pixels	46	161	5	0	212	75.94%
	Forest Pixels	1	0	1190	0	1191	99.92%
	Water Pixels	0	0	0	2599	2599	100.00%
	Total	344	161	1195	2599	4299	
	Producer's Accuracy	86.34%	100.00%	99.58%	100.00%		Overall = 98.79%
2019	Classified Pixels	Developed	Non-Forest Vegetation	Forest	Water	Total	User's Accuracy
	Developed Pixels	253	0	0	0	253	100.00%
	Non-Forest Vegetation Pixels	15	152	6	0	173	87.86%
	Forest Pixels	0	8	1288	0	1296	99.38%
	Water Pixels	0	0	0	2599	2599	100.00%
	Total	268	160	1294	2599	4321	
	Producer's Accuracy	94.40%	95.00%	99.54%	100.00%		Overall = 99.33%
2021	Classified Pixels	Developed	Non-Forest Vegetation	Forest	Water	Total	User's Accuracy
	Developed Pixels	586	1	0	0	587	99.83%
	Non-Forest Vegetation Pixels	3	302	0	0	305	99.02%
	Forest Pixels	0	13	2431	0	2444	99.47%
	Water Pixels	0	0	0	2599	2599	100.00%
	Total	589	316	2431	2599	5935	
	Producer's Accuracy	99.49%	95.57%	100.00%	100.00%		Overall = 99.71%

Assessment of Spatiotemporal Trends

Figure 3.8 displays the area of each land cover class in acres for all ten images in a bar chart. Trendlines were added to both impervious surface and forest canopy classes. Between 1984 and 2021, a negative linear relationship was identified between time (x) and acres of forest canopy (y). Conversely, between 1984 and 2021, a positive linear relationship was identified between time (x) and acres of impervious surface (y). The area in acres and the relative percentage of each land cover class for all images is also provided in Table 3.6.

The percent change in the area of land cover classes between consecutive imagery dates was calculated and provided in Table 3.7. From the final land cover class area estimations, since 1984, Chattanooga has steadily lost forest canopy. In the 37 years analyzed, this study estimates that Chattanooga has lost approximately 36.9 square miles of its urban tree canopy. These losses in forest canopy are complimented by steady gains in impervious surface area. Since 1984 Chattanooga's urban spaces have gained 32.5 square miles, an increase of approximately 134%.

Table 3.5 Area and relative percentage of land cover classes quantified across the 10 final land cover datasets (Non-Forest Vegetation = NF)

	Impervious Surface		NF Vegetation		Forest Canopy		Water	
	Acres	% Area	Acres	% Area	Acres	% Area	Acres	% Area
1984	15526	16.10%	20229	20.97%	55549	57.60%	5140	5.33%
1988	24546	25.45%	18595	19.28%	48325	50.11%	4979	5.16%
1990	23512	24.38%	22976	23.82%	44968	46.63%	4988	5.17%
1995	25875	26.83%	23931	24.81%	41707	43.24%	4931	5.11%
2000	21833	22.64%	26213	27.18%	43356	44.95%	5043	5.23%
2004	22358	23.18%	30393	31.51%	38630	40.05%	5063	5.25%
2009	27485	28.50%	28235	29.28%	35590	36.90%	5134	5.32%
2014	32365	33.56%	24086	24.97%	34857	36.14%	5136	5.33%
2019	31981	33.16%	22188	23.01%	37278	38.65%	4991	5.18%
2021	36316	37.65%	23347	24.21%	31924	33.10%	4857	5.04%

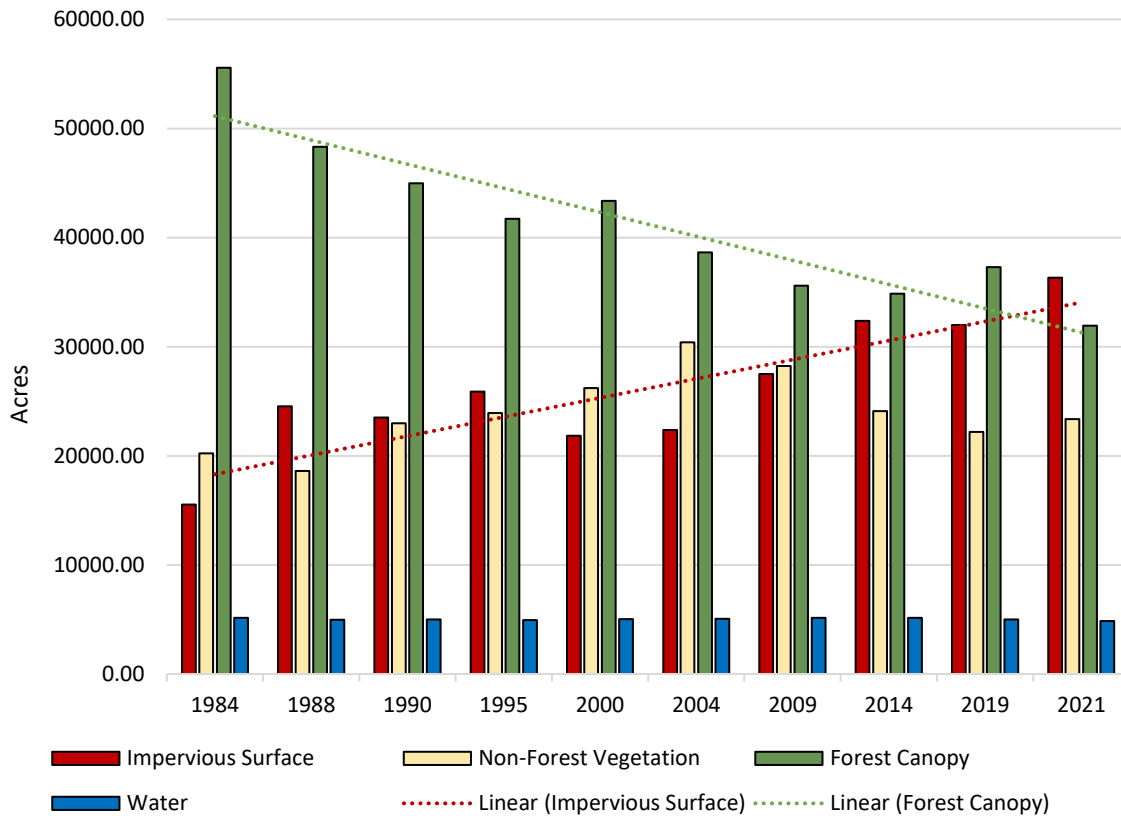


Figure 3.8 Land cover class area in acres for the 10 final land cover datasets

The most significant change in urban tree canopy surface area occurred between 2019 and 2021. During this period, urban forest area decreased by 14%, while impervious surface area increased by 14%. The most significant change in impervious surface area between consecutive images occurred between 1984 and 1988. During this time period, Chattanooga’s urban spaces increased in area by ~14 square miles, an increase of approximately 58%, while urban forest area decreased by ~11 square miles, and non-forest vegetation decreased by ~3 square miles. This rapid increase in impervious surfaces alongside decreases in both forest canopy and non-forest vegetation classes suggests that Chattanooga likely experienced a period of rapid urbanization between 1984 and 1988.

Table 3.6 Land cover class area percent change between imagery acquisition dates

	Impervious Surface	Non-Forest Vegetation	Forest Canopy	Water
1984 - 1988	58.09%	-8.08%	-13.01%	-3.13%
1988 - 1990	-4.21%	23.56%	-6.95%	0.19%
1990 - 1995	10.05%	4.16%	-7.25%	-1.15%
1995 - 2000	-15.62%	9.53%	3.95%	2.27%
2000 - 2004	2.40%	15.95%	-10.90%	0.40%
2004 - 2009	22.93%	-7.10%	-7.87%	1.41%
2009 - 2014	17.75%	-14.69%	-2.06%	0.04%
2014 - 2019	-1.19%	-7.88%	6.94%	-2.83%
2019 - 2021	13.55%	5.23%	-14.36%	-2.68%

In two separate instances, the percent change of urban tree canopy is positive rather than negative, suggesting a net growth in urban tree canopy. The first instance, occurring between 1995 and 2000, reports increases in forest canopy around 4% complimented by an ~10% increase in non-forest vegetation. The second, occurring between 2014 and 2019, found an increase in forest canopy around of ~7% complemented by an ~8% loss in non-forest vegetation and negligible losses in all other classes. In both of these cases, increases in forest canopy can reasonably be explained by the regeneration of forest across recently harvested timber operations.

Based on the results from the accuracy assessments, the methodology utilized in this research is effective when using a spatiotemporal dataset of moderate resolution remote sensing data, such as Landsat 5 TM and Landsat 8 OLI imagery, to classify broad land cover types apart from other broad land cover classes at the city-scale or larger. However, when seeking to obtain more granular information from the resulting landcover data, such as the percent of urban tree canopy across a park within the city itself for example, the utility and effective accuracy of the obtained land cover model would be far less. The inherent limitation of moderate resolution sensors in the mapping of urban tree canopy will be discussed in greater detail in later sections.

CHAPTER 4

APPLICATION OF PLANETSCOPE AND SENTINEL IMAGERY

The objective of this chapter is to develop a methodology to model the carbon sequestered in the biomass of Chattanooga's urban forest trees using field data and different vegetation indices. Because of the limited spatial resolution of Landsat imagery (30 m), this section of research employs PlanetScope (3 m) and Sentinel-2a imagery (10 and 20 m).

Study Site

The study site for this research is a 177-acre portion of the University of Tennessee at Chattanooga (UTC). Covering an approximately 320 acre region within the center of downtown Chattanooga, Tennessee, the UTC campus was selected as a study site for the proof of concept to develop a model to estimate the carbon sequestered in a subset of urban forest biomass before scaling up to the full extent of a mid-sized city like Chattanooga.

Conducting random, city-scale field sampling requires a significant amount of time to generate a statistically viable sample upon which to develop a predictive model. Because the goal of this research was to determine how the carbon sequestered in the biomass of urban forest trees can be predictively modeled at little to no cost and without a significant time investment, a subset of Chattanooga's urban tree canopy bound by UTC's campus was selected as the study site.

Some less-accessible portions of the campus, such as around common areas of on-campus housing, and areas of campus where vegetation is not easily measured by remote sensors, such as trees planted on the perimeter of buildings were exclude from the study site. The resulting study site was a 177 acre subset of UTC's campus.

Aside from mapping urban tree canopy and modeling sequestered carbon across the UTC campus, this research explores various techniques that might be applied to mapping urban tree canopy rapidly across larger areas, such as the City of Chattanooga and the greater Chattanooga region.

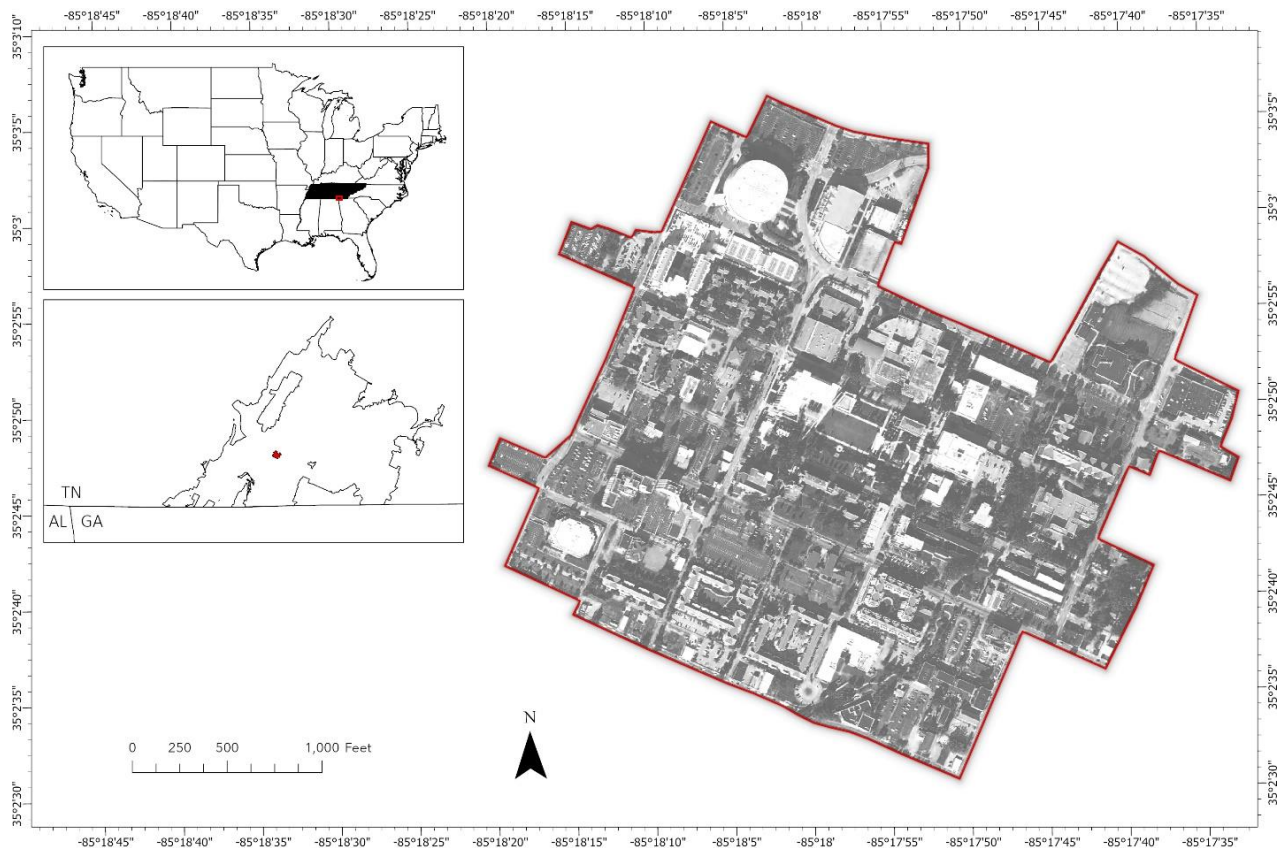


Figure 4.1 Study site map for Planet Scope and Sentinel-2a research representing the campus of the University of Tennessee at Chattanooga (UTC)

Data Collection

For this research, all acquired imagery received geometric, radiometric, atmospheric, and positional accuracy corrections prior to collection. Collected data includes: a 4-band multispectral orthorectified NAIP image captured on November 10th, 2018 at 2:16 P.M.; a 4-band multispectral orthorectified PlanetScope Analytic image product captured on July 26, 2020 at 4:04 P.M.; and an 8-band multispectral orthorectified Sentinel-2a image captured May 9th, 2020 at 3:34 P.M. NAIP imagery was downloaded from USDA's NAIP imagery Dropbox page. PlanetScope data was downloaded from Planet Labs geospatial data portal for academic users. Sentinel-2a imagery was downloaded from the Copernicus Open Data Access Hub.

Because NAIP imagery was acquired far outside the period of peak chlorophyll concentration, as a fine resolution image lacking the spectral information needed to derive a predictive model based on chlorophyll concentration, NAIP imagery was strictly used as reference data for the image-based digitization of urban tree canopy across the study site.

NAIP and PlanetScope Imagery consisted of blue, green, red, and NIR bands, while Sentinel-2a consisted of blue, green, red, NIR, and 4 narrow red-edge bands. The spatial resolution of NAIP imagery is 1 meter, which facilitated the differentiation of individual tree crowns across the urban tree canopy. PlanetScope's spatial resolution is 3 meters, while Sentinel-2a's spatial resolution is 10 meters across blue, red, green, and NIR bands, and 20 meters across the 4 red edge bands. Because the spectral information contained in PlanetScope and Sentinel-2a imagery would be used in analysis, corrected surface reflectance products were obtained. Finally, 2015 USGS 3D Elevation Program (3DEP) LiDAR data was acquired free directly from the Tennessee State Government's GIS data portal.

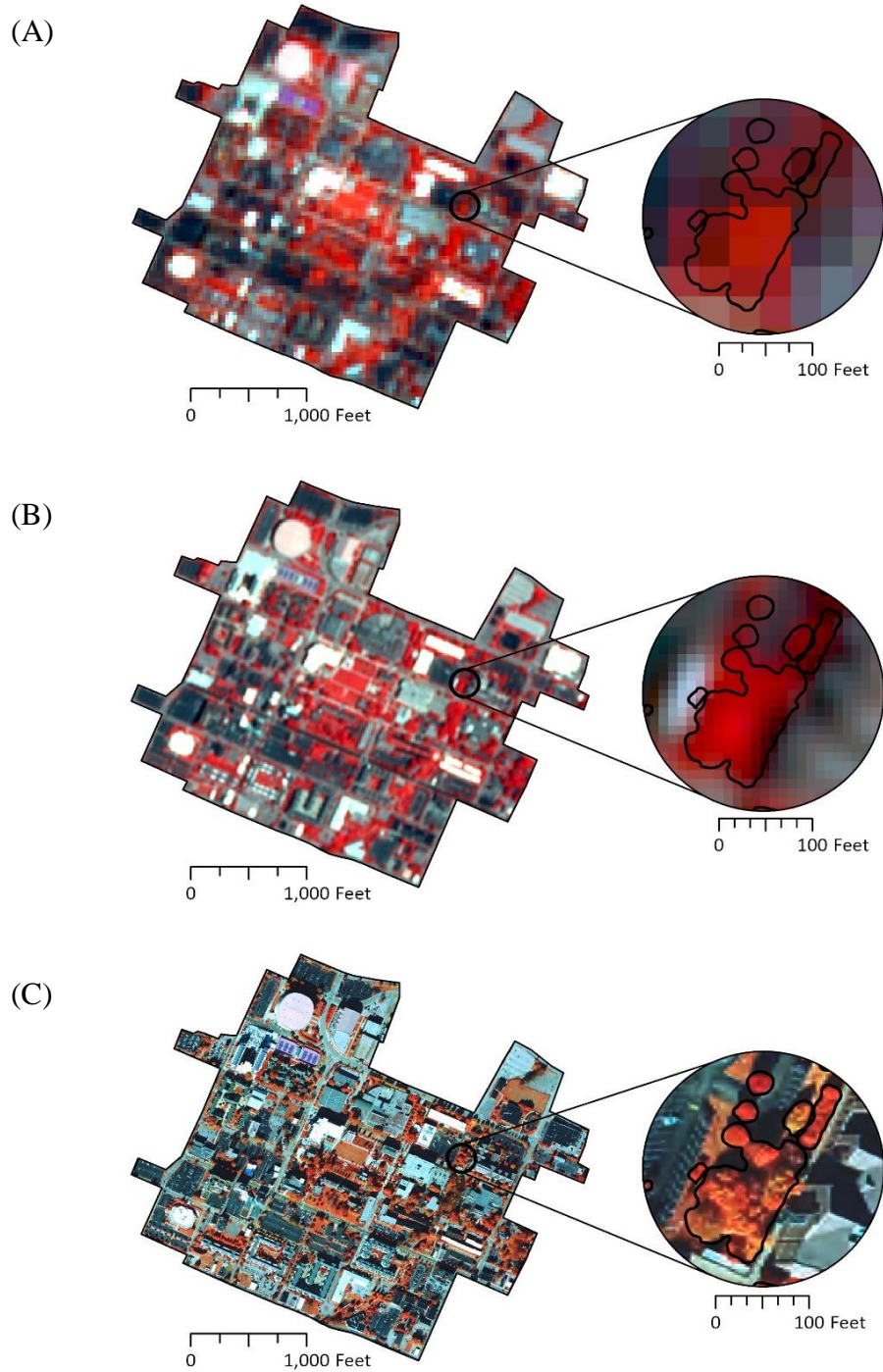


Figure 4.2 Acquired multispectral imagery (viewed in false color to highlight the presence of vegetation in red) to model urban tree canopy across the campus of the University of Tennessee at Chattanooga (UTC); (A) Sentinel2-a visible and NIR bands have a resolution of 10 meters; (B) PlanetScope imagery has a resolution of 3 meters; (C) NAIP imagery has a resolution of 1 meter

Methods

Image Preprocessing

As previously stated, all acquired imagery received geometric, radiometric, atmospheric, and positional accuracy corrections prior to collection. Additionally, because the spectral information contained in PlanetScope and Sentinel-2a imagery would be used in analysis, corrected surface reflectance products were obtained.

The bands of both NAIP and PlanetScope imagery came pre-stacked in composite images. Using the Composite Band geoprocessing tool in ArcGIS Pro, the individual bands of Sentinel-2a were stacked into a composite image (Figure 4.2.) A general quality assessment was conducted across all three multispectral composite imagery sources to determine if cloud coverage and/or missing data might inhibit the extraction of useful data.

Image Enhancements

Using the band combination: Red = PC1, Green = PC2, Blue = PC1, a first order principal component analysis (PCA) was conducted on NAIP imagery using the Principal Components geoprocessing tool in ArcGIS Pro. The PCA was successfully able to detect shadows across the image, seen in Figure 4.3 as bright green regions.

To assist with the digitization of urban tree canopy across the 2018 NAIP reference image, a canopy height model (CHM) was generated from 2015 3DEP LiDAR [126]. A digital surface model (DSM) and a digital terrain model (DTM) were generated by right clicking the .las file and separately selecting Las Filters, then First Return (DSM) and Ground Return (DTM), then selecting Export Raster. By subtracting the DTM from the DSM using Raster Calculator in ArcGIS Pro, a canopy height model was generated.



Figure 4.3 First order PCA conducted on NAIP imagery to help delineate shadows, colored in bright green



Figure 4.4 Digital surface model (DSM) generated using the data obtained from USGS [126]

Next, the vegetation indices to be used as spectral predictor variables in the modeling of sequestered carbon were generated using the Band Arithmetic raster function in ArcGIS Pro. From the Sentinel-2a image, five different vegetation indices were calculated: NDVI shown in Equation 1, Green Normalized Difference Vegetation Index (GNDVI) shown in Equation 2, Soil Adjusted Vegetation Index (SAVI) shown in Equation 3, and two NDVI models derived using Sentinel-2a's red edge bands (RENDVI1 and RENDVI2) shown in Equations 4 and 5 respectively. From the PlanetScope image, three vegetation indices were calculated: NDVI, GNDVI, and SAVI, shown in Equations 1 – 3 respectively. Figure 4.5 shows the NDVI model derived from (a) Sentinel-2a and (b) PlanetScope imagery. It should be mentioned here that Equation 3, SAVI, was derived originally from MODIS imagery to reduce the brightness of bare soil in areas of relatively sparse vegetation [127-129]. However, SAVI has been successfully applied to other imagery sources [127-129]. A generic soil brightness correction factor (L) of 0.5 has been found to be acceptable when applied across a number of imagery sources [130]. Finally, all multispectral imagery, the derived CHM and PCA, and all generated vegetation indices were clipped to the study area using UTC's campus boundary and the Clip Raster geoprocessing tool in ArcGIS Pro.

$$\mathbf{NDVI} = \frac{(\rho_{\text{NIR}} - \rho_{\text{R}})}{(\rho_{\text{NIR}} + \rho_{\text{R}})} \quad (1)$$

$$\mathbf{GNDVI} = \frac{(\rho_{\text{NIR}} - \rho_{\text{G}})}{(\rho_{\text{NIR}} + \rho_{\text{G}})} \quad (2)$$

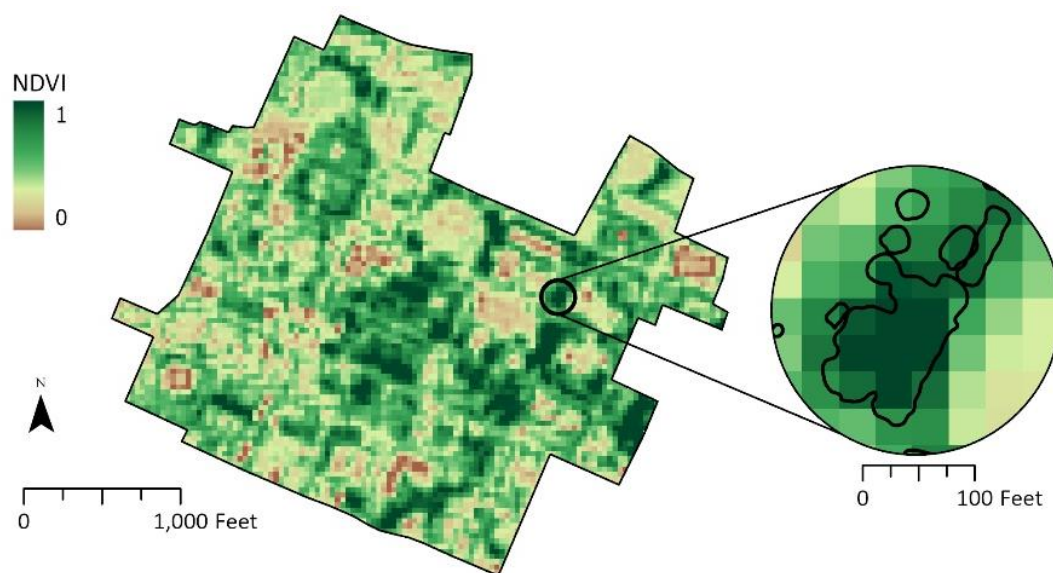
$$\mathbf{SAVI} = \frac{(\rho_{\text{NIR}} - \rho_{\text{R}})}{(\rho_{\text{NIR}} + \rho_{\text{R}} + L)} * (1 * L) \quad (3)$$

$$\mathbf{RE1NDVI} = \frac{(\rho_{\text{NIR}} - \rho_{\text{RE1}})}{(\rho_{\text{NIR}} + \rho_{\text{RE1}})} \quad (4)$$

$$\mathbf{RE2NDVI} = \frac{(\rho_{\text{NIR}} - \rho_{\text{RE2}})}{(\rho_{\text{NIR}} + \rho_{\text{RE2}})} \quad (5)$$

As stated previously, the equations above represent the vegetation indices equations used to derive the separate independent variables in this research, where ρ_{NIR} is the reflectance values of the NIR band, ρ_{R} is the reflectance values of the red band, ρ_{G} is the reflectance values of the green band, ρ_{RE1} is the reflectance values of Sentinel-2a's first red edge band, ρ_{RE2} is the reflectance values of Sentinel-2a's second red edge band, and L is the soil brightness correction factor.

(A)



(B)



Figure 4.5 (A) NDVI generated from Sentinel-2a imagery (30m); (B) NDVI generated from PlanetScope imagery (3m)

Feature Extraction

Next, from the fine spatial resolution NAIP image, 1,057 canopy polygons representing urban tree canopy were hand digitized across the UTC campus using ArcGIS Pro. Trees that were close enough together such that their canopies were difficult to delineate apart from one another in NAIP imagery were drawn as a single canopy zone. To facilitate the digitization process, the PCA model was used to detect shadows, seen as the brightest green regions across the PCA image. In cases where shadows were detected in the PCA image, but no trees were clearly visible in the NAIP image, the CHM served as a reference to confirm the presence or absence of a tree. Vegetation with a clearly visible canopy in the NAIP imagery and CHM, and a visible shadow, symbolized in green in the PCA image, was assumed to be a tree and the boundary of its canopy was hand digitized.

Field Data Collection

To sample DBH across UTC's campus, the Subset Features geoprocessing tool within ArcGIS Pro was used to take a random subset of 10%, or approximately 112 of the 1,057 digitized urban tree canopy zones. However, of the 112 urban tree canopy sample sites, 26 sample sites were removed due to DBH measurements exceeding the minimum DBH threshold that a given allometric equation was calibrated to. The remaining 86 canopy zones, containing roughly 125 individual DBH measurements, can be seen in Figure 4.6. as represented by the red canopy polygons. Each canopy zone was labeled with a unique ID.



Figure 4.6 Urban tree canopy polygons hand digitized across UTC from NAIP imagery

To facilitate navigation between sampling sites, the subset of 86 canopy zones and reference NAIP imagery was uploaded to an ArcGIS Field Maps project and referenced throughout the sampling process. Within each canopy zone visited in the field, the DBH for each tree was measured and recorded using a Forestry Supplies DBH tape. The unique canopy zone ID for each measurement was carefully documented. The positional accuracy needed to verify the canopy zone that each measured tree belonged to was achieved using a global navigation satellite system (GNSS) receiver. Additionally, in order to select the appropriate allometric equation when calculating sequestered carbon, tree species was documented each time DBH was measured using free plant identification applications, such as LeafSnap and PlantNet. All sampling was conducted by the sole researcher over the course of 2 days.

Modeling Sequestered Carbon

Preparing the Independent Variables

Using the subset of 86 sampled canopy zone polygons as a mask, the Extract by Mask geoprocessing tool within ArcGIS Pro was used to create 5 new Sentinel-2a vegetation index rasters and 3 new PlanetScope vegetation index rasters clipped to the 86 sampled urban tree canopy polygons. The Zonal Statistics to Table geoprocessing tool within ArcGIS Pro was then used to extract the maximum and average vegetation index value within all of the 86 sampled canopy zones separately for each of the clipped urban tree canopy vegetation indices, resulting in average and maximum urban tree canopy vegetation index values for each sampled canopy zone. The average and maximum vegetation index value representative of each sampled canopy zone across all 8 derived vegetation indices were tested separately as independent variables.

Preparing the Dependent Variable

Using Microsoft Excel, a master spreadsheet was created consisting of the common name of each tree, the unique polygon ID of each tree, and DBH (cm). For this research, allometric equations were found for all tree species or species groups sampled using the database of allometric equations created by the United States Forest Service (USFS) [112]. The output for all of these allometric equations is dry weight above ground biomass. Jenkins et al. (2003) provides specific allometric equations for common species of tree across the United States [112]. Using these equations and the field sampled DBH values, above ground biomass was calculated for each canopy zoner. Next, sequestered carbon was derived by multiplying the above ground biomass value for each canopy zone by the biomass-carbon conversion factor [131-133]. These sequestered carbon values were then divided by the area of the canopy zone to determine the average carbon sequestered per square meter of each canopy zone. The master spreadsheet, consisting of the common name of each tree, the unique polygon ID of each sample site, field measured DBH (cm), calculated dry weight biomass, and finally sequestered carbon is provided in Table 4.1.

Table 4.1 Master field sampling dataset, consisting of sampled tree common name, sample site ID, field measured DBH (in), calculated dry weight biomass (lbs), and finally sequestered carbon (lbs)

Common Name	Sample Site ID	Formula ID	DBH (in)	Biomass (lbs)	Carbon (lbs)
Paradise Apple	1	mh	6.06	164.24	82.12
American Holly	2	mh	14.55	1444.59	722.30
Sweet Bay Magnolia	3	mh	5.10	107.01	53.51
Willow Oak	5	mo	6.93	317.44	158.72
Red Maple	6	mb	5.39	158.41	79.21
Bald Cypress	7	cl	8.64	309.54	154.77
Bald Cypress	8	cl	6.99	191.58	95.79
Bald Cypress	9	cl	8.38	288.91	144.46
Bald Cypress	10	cl	8.33	285.25	142.62
Eastern Cottonwood	11	aa	14.29	1278.05	639.02
Pen Oak	12	mo	7.64	402.29	201.15
Pen Oak	13	mo	11.48	1084.37	542.19
Sugar Maple	14	mo	6.73	295.10	147.55
Sugar Maple	15	mo	6.16	238.19	119.09
Pen Oak	16	mo	3.58	63.64	31.82
Willow Oak	16	mo	22.34	5479.40	2739.70
American Holly	17	mh	10.54	647.81	323.90
Sweet Bay Magnolia	17	mh	7.02	236.66	118.33
Sour Cherry	18	mh	5.43	125.08	62.54
Sugar Maple	19	mo	18.89	3639.53	1819.77

Table 4.2 Allometric equations used to derive biomass estimations from field measured DBH [134]

Symbol	Species Group	Allometric Equation
mh	Mixed Hardwood	biomass (kg) = $e^{(-2.48 + 2.48 * \ln(DBH))}$
cl	Cedar / Larch	biomass (kg) = $e^{(-2.03 + 2.26 * \ln(DBH))}$
aa	Alder / Willow	biomass (kg) = $e^{(-2.21 + 2.39 * \ln(DBH))}$
mo	Maple / Oak / Hickory / Beech	biomass (kg) = $e^{(-2.01 + 2.43 * \ln(DBH))}$
pi	Pine	biomass (kg) = $e^{(-2.54 + 2.48 * \ln(DBH))}$

Simple Linear Regression

A series of linear regression analyses were run using Microsoft Excel. The independent/predictor variables tested were the maximum and average vegetation index values within sampled canopy zones across each of the 8 vegetation indices, while the dependent/response variable was the pounds of carbon sequestered per meter of each canopy zone. The complete modeling approach is visualized in Figure 4.7.

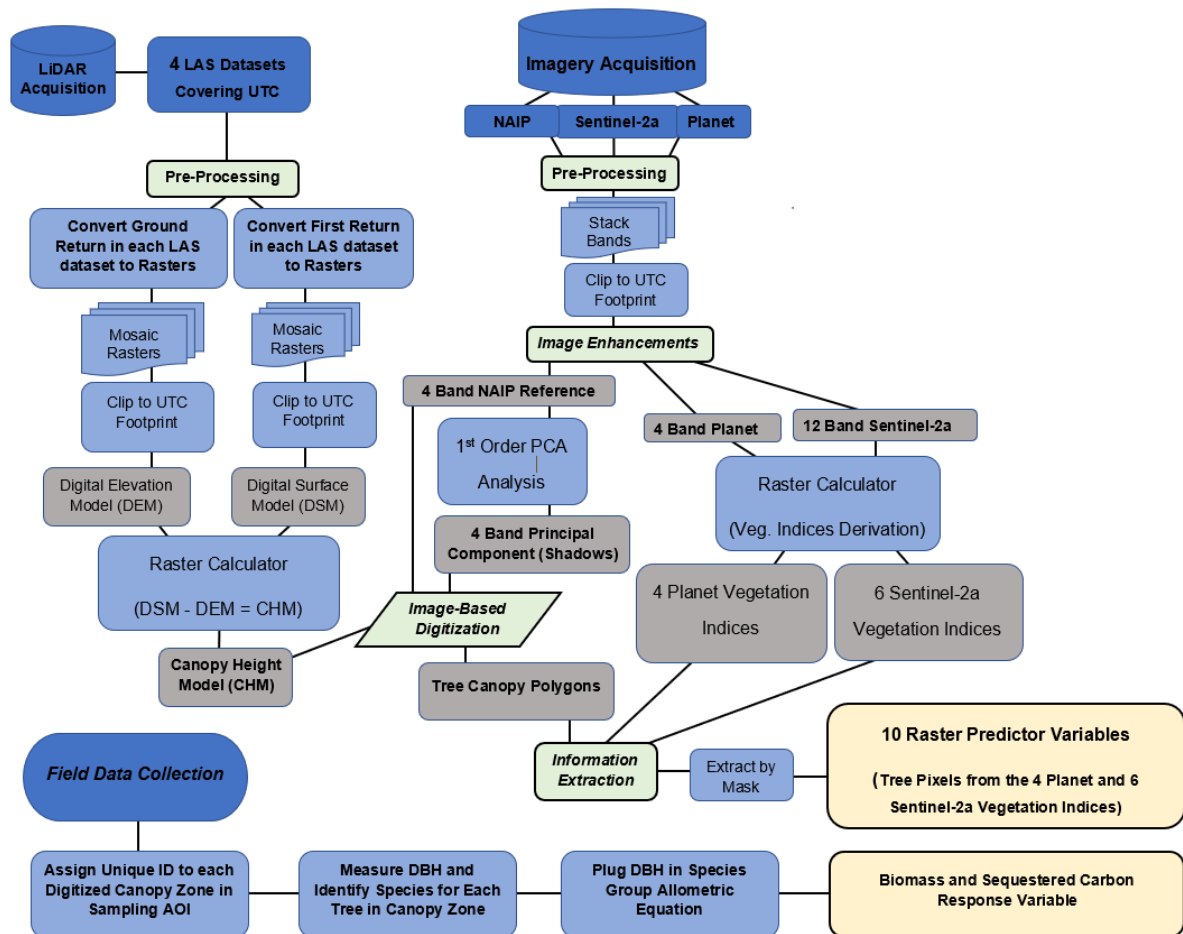


Figure 4.7 Modeling approach for developing the predictive carbon model using simple linear regression

Results

Correlation Coefficient

A Pearson's product-moment correlation coefficient (r) was calculated to identify the presence of a correlation between the derived Planet Scope and Sentinel-2a vegetation index statistics, and the average carbon sequestered per meter of sampled urban tree canopy. Pearson's correlation coefficient is a common way to analyze the linear correlation between two separate variables [135]. Results from this analysis suggest that PlanetScope derived vegetation indices expressed a slight positive correlation ($r = < 0.462$), while Sentinel-2a derived vegetation indices expressed a low positive correlation ($r = < 0.345$). The correlation coefficients for each tested PlanetScope and Sentinel-2a variable is provided in Table 4.3.

Linear Regression Analysis

A linear regression analysis was run on each of the independent variables to determine the coefficient of determination (R^2) which is used to assess the strength of an identified correlation. The results from each linear regression conducted here are provided in Table 4.4. Additionally, for the best performing statistic derived from each vegetation index (average or maximum), a linear regression plot is provided in Figures 4.8. – 4.15.

Table 4.3 Pearson's correlation and linear regression analysis results from each tested independent variable derived from PlanetScope and Sentinel-2a imagery

Data Source	Independent Variable	r	R^2	$RMSE$	p -value
PlanetScope	GNDVImean	0.462	0.213	7.607	0.07
	GNDVImax	0.434	0.189	7.725	0.10
	NDVImean	0.436	0.190	7.717	0.21
	NDVImax	0.394	0.156	7.881	0.33
	SAVImean	0.434	0.188	7.726	0.03
	SAVImax	0.396	0.157	7.874	0.05
Sentinel-2a	GNDVImean	0.345	0.120	7.795	0.41
	GNDVImax	0.336	0.113	7.901	0.34
	NDVImean	0.290	0.084	8.140	0.05
	NDVImax	0.342	0.117	7.994	0.14
	SAVImean	0.290	0.084	8.233	0.73
	SAVImax	0.339	0.115	8.095	0.84
	RENDVImean	0.240	0.058	8.315	0.004
	RENDVImax	0.273	0.075	8.240	0.006
	RENDVI2mean	0.252	0.063	8.336	0.02
	RENDVI2max	0.278	0.078	8.273	0.04

Of the independent variables tested in this research, the average $\text{GNDVI}_{\text{PlanetScope}}$ tree canopy zone pixel values expressed the strongest correlation to field sampled sequestered carbon ($R^2 = 0.213$). The next strongest correlation was expressed by the average $\text{NDVI}_{\text{PlanetScope}}$ tree canopy zone pixel values ($R^2 = 0.190$) followed by the $\text{SAVI}_{\text{PlanetScope}}$ tree canopy zone pixel values ($R^2 = 0.188$). Of the Sentinel-2a derived vegetation indices tested as independent variables, the strongest correlation to field sampled sequestered carbon was expressed by the average $\text{GNDVI}_{\text{Sentinel-2a}}$ tree canopy pixel values ($R^2 = 0.120$), followed by the maximum $\text{NDVI}_{\text{Sentinel-2a}}$ tree canopy pixel values ($R^2 = 0.117$). In a few of the analyses, the removal of extreme outliers had a slight improved the analysis results.

In this research, the three regressions conducted using PlanetScope imagery outperformed all analyses using Sentinel-2a derived vegetation indices. Furthermore, amongst Sentinel-2a derived vegetation indices, RENDVI1 and RENDVI2 had the weakest correlation to field measured sequestered carbon. The significance of these trends in the overall strength of the identified correlations across the predictive models tested in this research is discussed in later sections.

Table 4.4 Obtained linear regression equation for each tested independent variable derived from PlanetScope and Sentinel-2a imagery

Data Source	Independent Variable	Regression Equation
PlanetScope	GNDVImean	$(49.888 * \text{GNDVI}) - 10.282$
	GNDVImax	$(45.471 * \text{GNDVI}) - 10.073$
	NDVImean	$(43.518 * \text{NDVI}) - 6.621$
	NDVImax	$(37.198 * \text{NDVI}) - 5.4106$
	SAVImean	$(48.917 * \text{SAVI}) - 17.176$
	SAVImax	$(48.825 * \text{SAVI}) - 16.590$
Sentinel-2a	GNDVImean	$(25.539 * \text{GNDVI}) + 3.235$
	GNDVImax	$(27.720 * \text{GNDVI}) + 3.6953$
	NDVImean	$(18.164 * \text{NDVI}) + 6.8864$
	NDVImax	$(19.334 * \text{NDVI}) + 5.2217$
	SAVImean	$(21.233 * \text{SAVI}) + 1.8106$
	SAVImax	$(23.820 * \text{SAVI}) - 1.0797$
	RENDVImean	$(15.382 * \text{RENDVI}) + 9.3956$
	RENDVImax	$(15.671 * \text{RENDVI}) + 8.3793$
	RENDVI2mean	$(16.387 * \text{RENDVI2}) + 8.2671$
	RENDVI2max	$(16.636 * \text{RENDVI2}) + 7.2153$

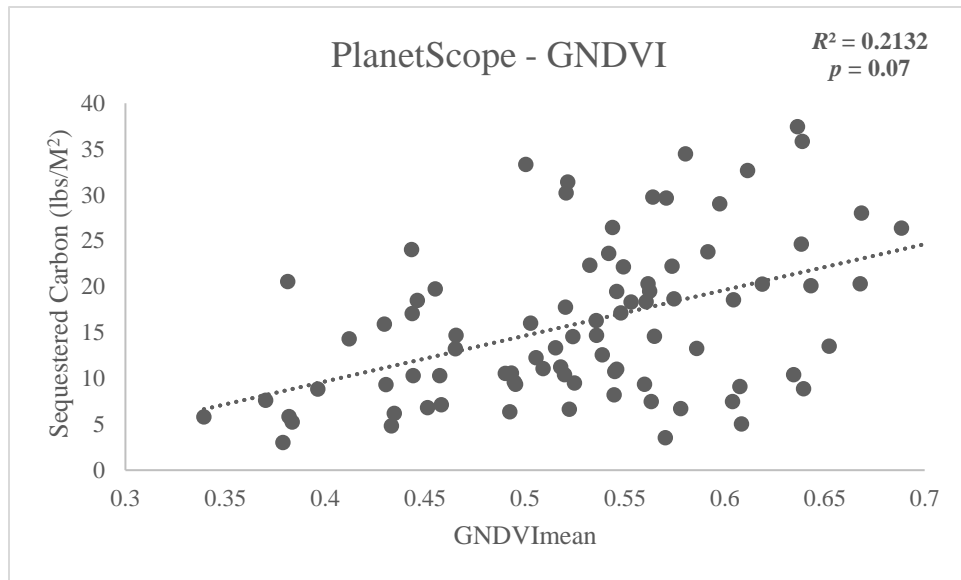


Figure 4.8 Plotted distribution of pounds of sequestered carbon per square meter (y) and mean GNDVI values extracted from PlanetScope imagery (x) using the digitized urban tree canopy polygons

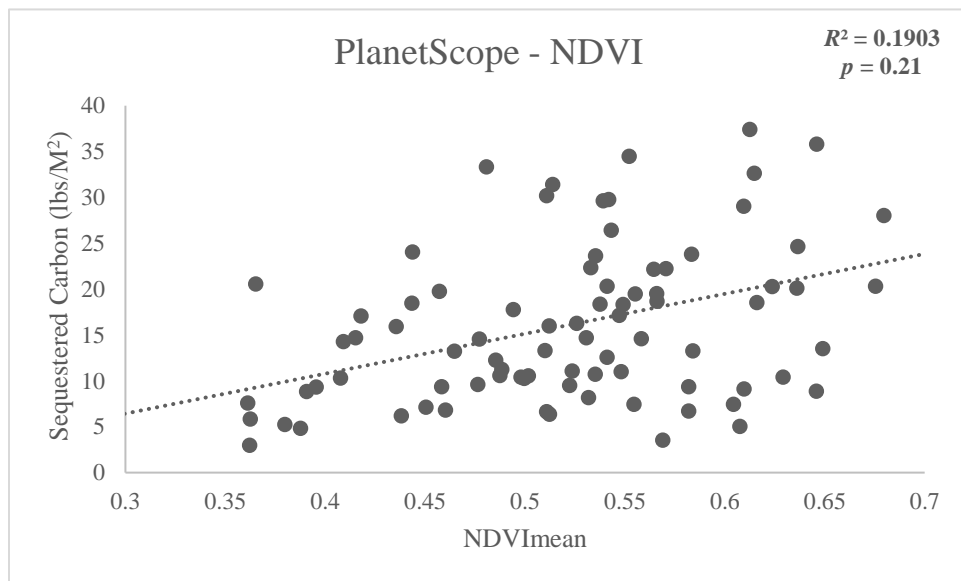


Figure 4.9 Plotted distribution of pounds of sequestered carbon per square meter (y) and mean NDVI values extracted from PlanetScope imagery (x) using the digitized urban tree canopy polygons

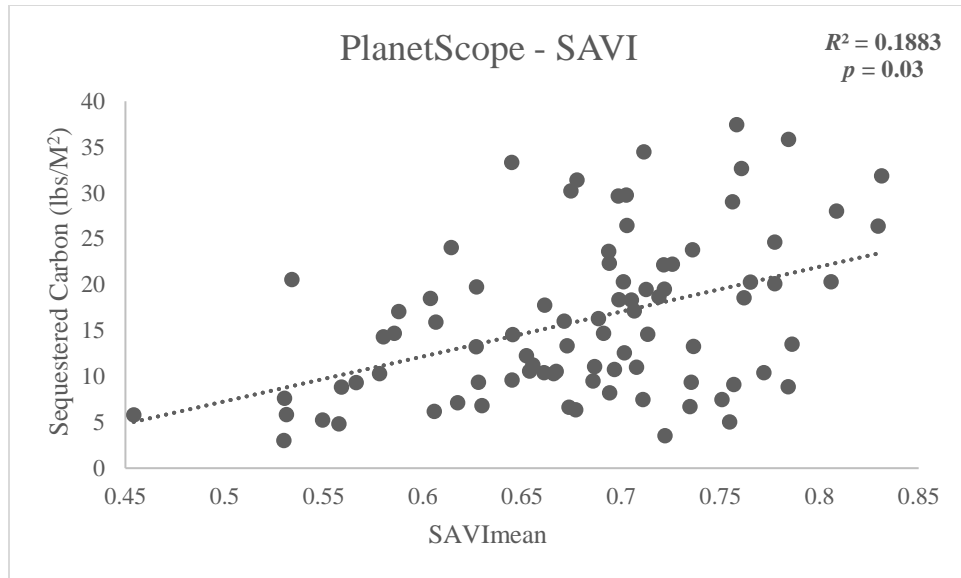


Figure 4.10 Plotted distribution of pounds of sequestered carbon per square meter (y) and mean SAVI values extracted from PlanetScope imagery (x) using the digitized urban tree canopy polygons

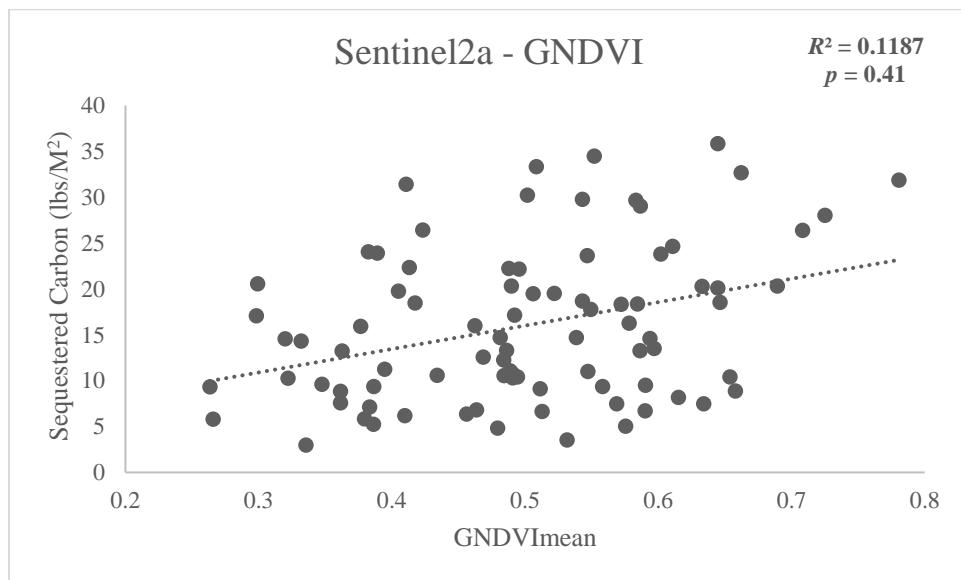


Figure 4.11 Plotted distribution of pounds of sequestered carbon per square meter (y) and mean GNDVI values extracted from Sentinel-2a imagery (x) using the digitized urban tree canopy polygons

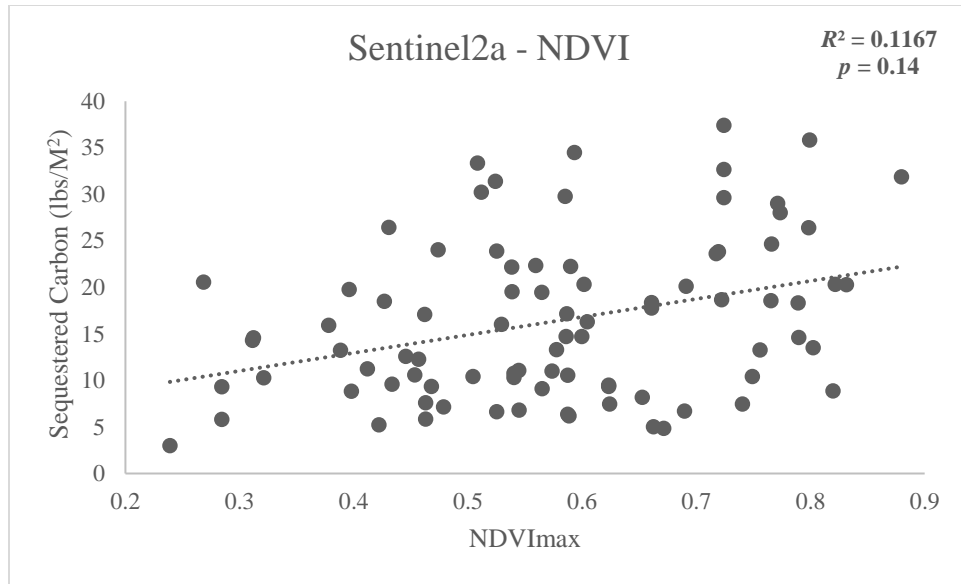


Figure 4.12 Plotted distribution of pounds of sequestered carbon per square meter (y) and the maximum NDVI values extracted from Sentinel-2a imagery (x) using the digitized urban tree canopy polygons

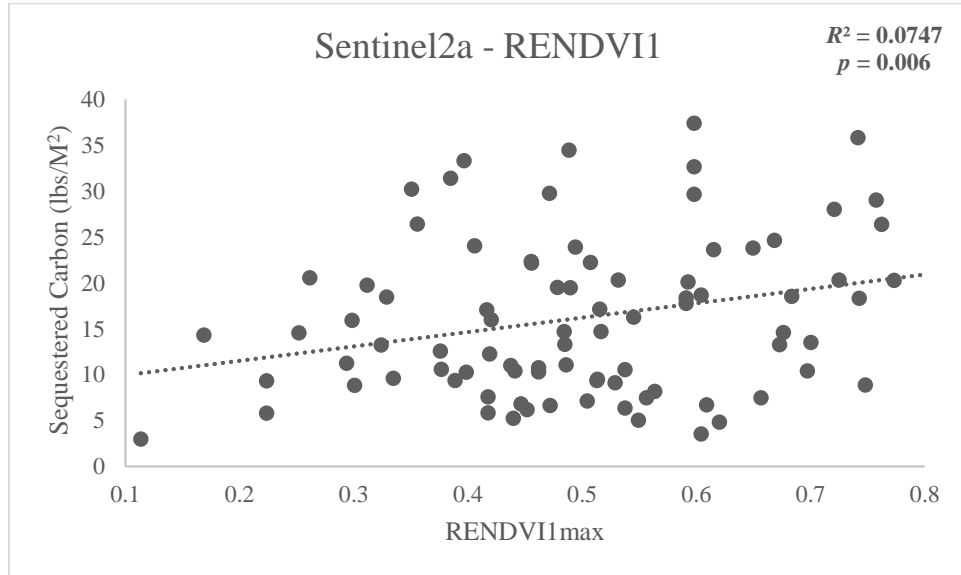


Figure 4.13 Plotted distribution of pounds of sequestered carbon per square meter (y) and the maximum RENDVI1 values extracted from Sentinel-2a imagery (x) using the digitized urban tree canopy polygons

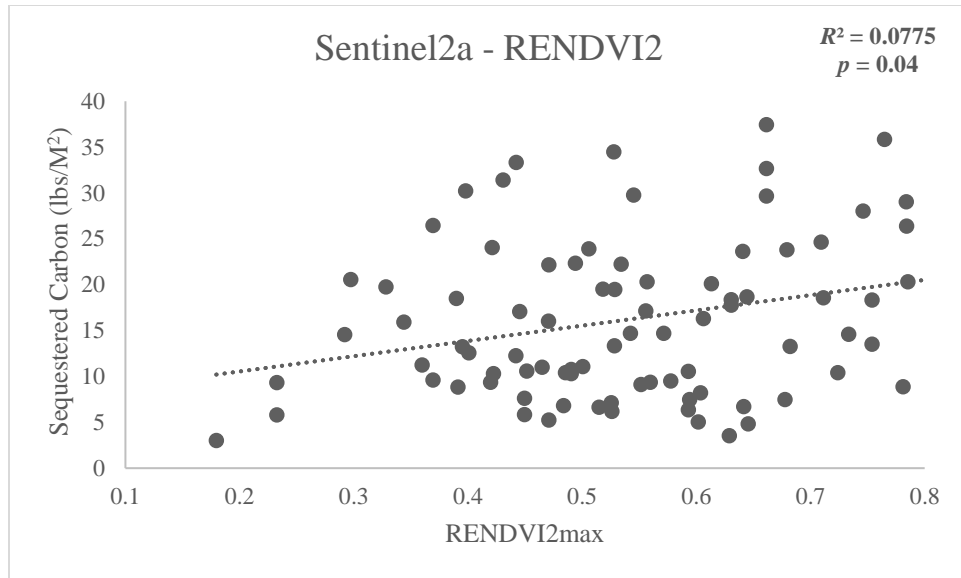


Figure 4.14 Plotted distribution of pounds of sequestered carbon per square meter (y) and the maximum RENDVI2 values extracted from Sentinel-2a imagery (x) using the digitized urban tree canopy polygons

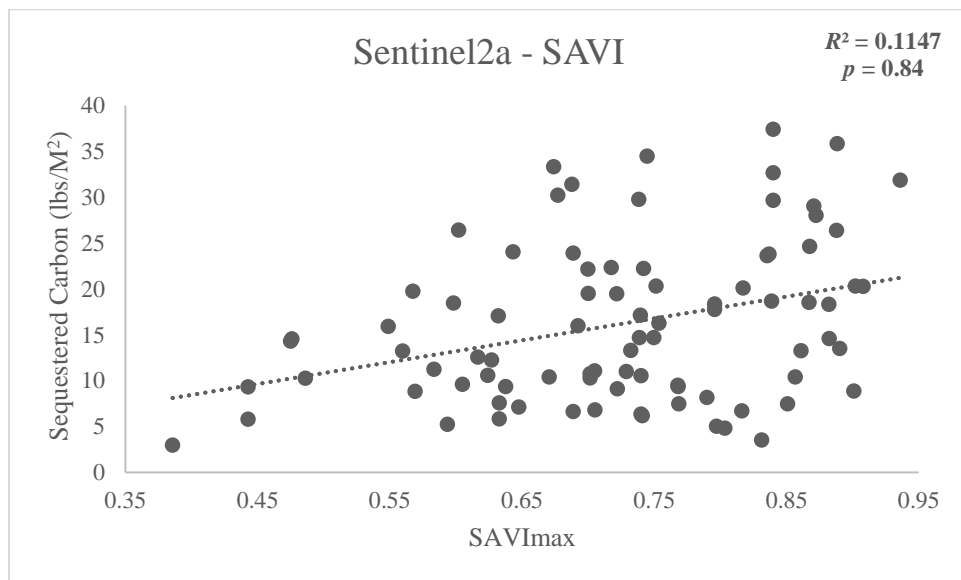


Figure 4.15 Plotted distribution of pounds of sequestered carbon per square meter (y) and the maximum SAVI values extracted from Sentinel-2a imagery (x) using the digitized urban tree canopy polygons

Sequestered Carbon (lbs / m²) = 49.888 * (GNDVI) - 10.282



Figure 4.16 Final map of sequestered carbon for the trees of UTC's campus derived from PlanetScope GNDVI

CHAPTER 5

APPLICATION OF SKYSAT IMAGERY

The objective of Chapter 5 is to map the current extent of Chattanooga's urban tree canopy. Because of the inherent difficulties in classifying urban tree canopy pixels apart from other forms of vegetation in moderate resolution imagery, as discussed in previous chapters, the final section of research presented here employs fine resolution SkySat imagery to map the distribution of Chattanooga's urban tree canopy at a high spatial accuracy.

Study Site

The City of Chattanooga is one of many mid-sized cities in the southeastern United States experiencing rapid urban growth. As a result, forest ecosystems, places of enormous ecological, recreational, and cultural significance in the greater Chattanooga region, are destroyed to make way for new urban development. In order to help conserve Chattanooga's urban forest habitat, mitigate levels of CO₂ released to the atmosphere associated with the extraction of forest biomass, and to help support sustainable development initiatives around the city, the overall goal of this research is to develop a high-resolution land cover dataset utilizing high resolution multispectral SkySat imagery, object-based classification, and machine learning in order to assess the distribution of urban tree canopy across Chattanooga, Tennessee in detail. .

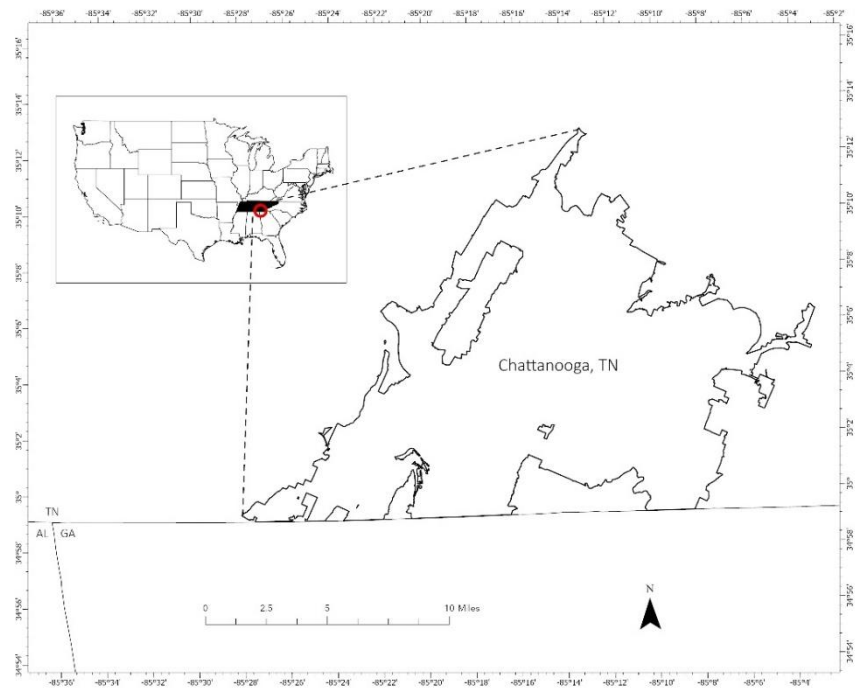


Figure 5.1 Study site map for SkySat research, representing the City of Chattanooga, Tennessee's boundary



Figure 5.2 Fine resolution (50 cm) orthorectified mosaic of tasked SkySat imagery clipped to the study site boundary

Data Collection

For this project, stakeholders requested the most recent and highest resolution multispectral imagery available and within the scope of the project budget. Funding from the Lyndhurst Foundation facilitated the tasking of high spatial resolution, multispectral images of Chattanooga acquired by Planet's SkySat constellation. Over the course of late summer and early fall of 2021, Planet SkySat data was tasked, collecting imagery on cloud free days. The spatial resolution of SkySat is approximately 50 cm.

For convenience, Planet processed their individual images to six mosaiced strips of multispectral imagery covering the full extent of the city, as seen in Table 5.1. and Figure 5.2 (Appendix Figures B2-B3). Two pre-processed imagery products were ultimately downloaded from the six mosaiced strips: orthorectified pansharpened 4-band multispectral imagery and raw 4-band multispectral surface reflectance. The orthorectified pansharpened imagery was used in the object-based classification workflow to generate the high resolution landcover dataset, while the raw surface reflectance values will be used in research stemming from this project. All pre-processing and processing steps were conducted separately for each of the six strips of multispectral SkySat images.

Table 5.1 Description of acquired multispectral SkySat imagery

SkySat Image ID	Satellite ID	Acquisition Date	Acquisition Time
Strip 1	SSC4	October 18, 2021	3:58 pm
Strip 2	SSC4	October 23, 2021	4:04 pm
Strip 3	SSC4	October 18, 2021	3:59 pm
Strip 4	SSC1	September 25, 2021	4:47 pm
Strip 5	SSC6	November 6, 2021	7:24 pm
Strip 6	SSC1	September 25, 2021	4:46 pm

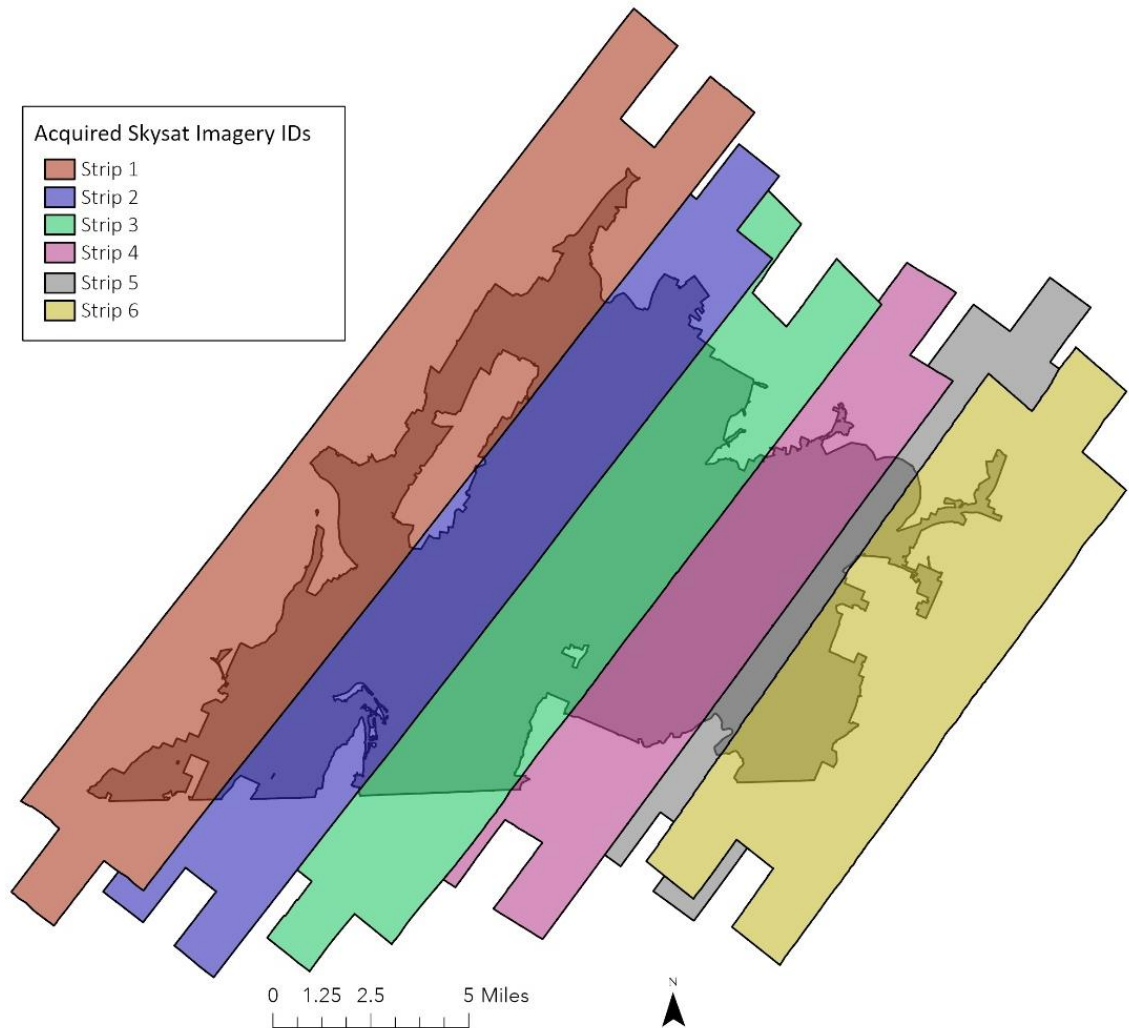


Figure 5.3 Footprint of acquired multispectral SkySat imagery

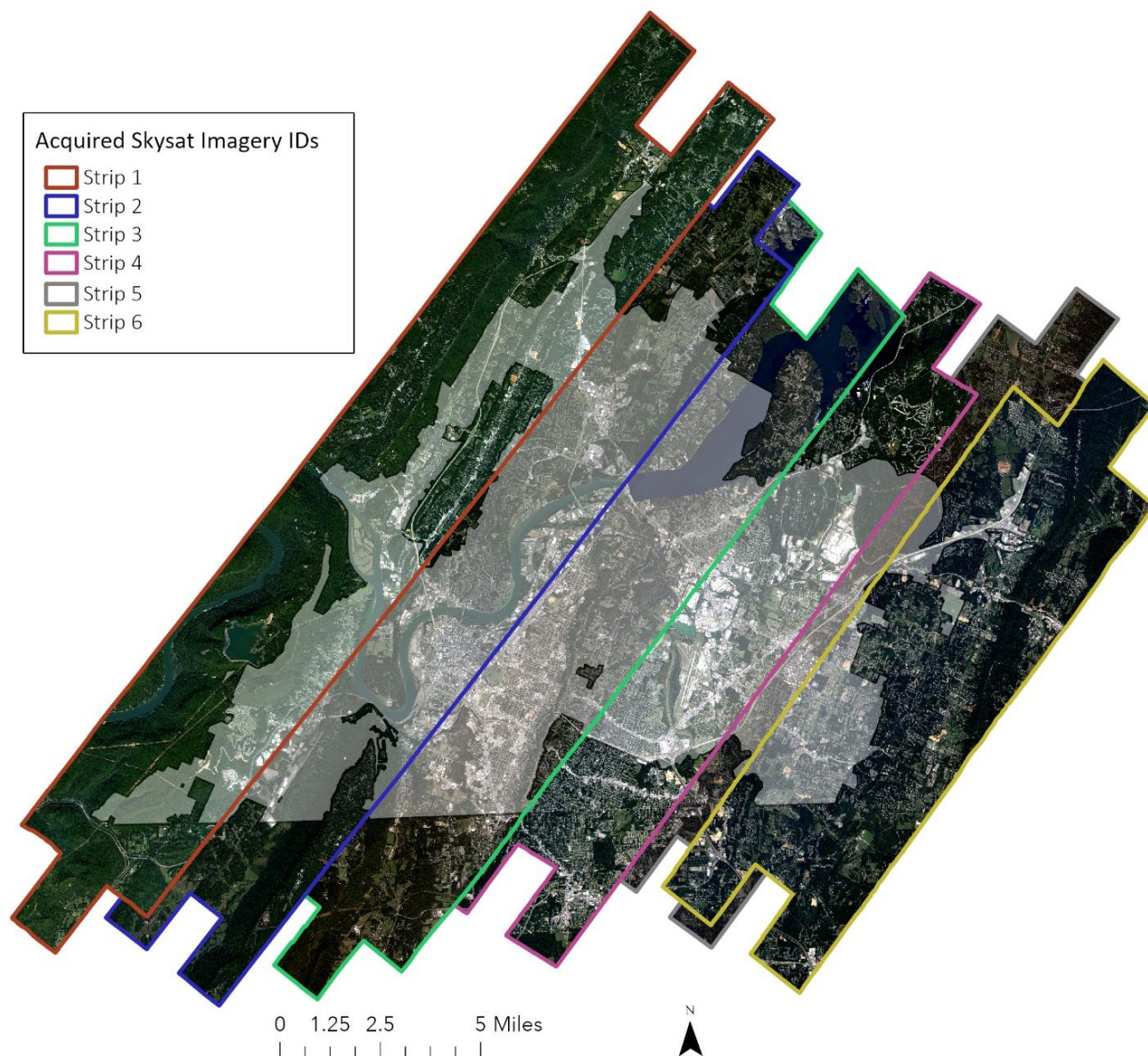


Figure 5.4 Footprint boundary and true color SkySat imagery acquired

Methods

Image Pre-Processing

Data Storage and Backup

After acquiring both the orthorectified pansharpened imagery and surface reflectance imagery products, a few data management steps were made before moving on to processing. First, all raw data was backed up. Due to the size of the raw imagery used in this research, this step is time consuming. Furthermore, because SkySat is a high resolution sensors, and because the study site for this research covered the entire City of Chattanooga, the acquired imagery for this research required a large amount of storage. In general, as spatial resolution increases, the more storage space is needed.

To accommodate storage needs and to facilitate rapid processing of SkySat imagery, all pre-processing and processing was conducted within a powerful distributed processing server system managed and operated by the University of Tennessee at Chattanooga SimCenter to help speed up processing times and to provide large amounts of storage.

Finally, because ArcGIS Pro was utilized exclusively during processing, all image files were imported into a geodatabase. This greatly improves the display speed of the high resolution imagery.

QAQC

Once all imagery was backed up, a final quality check was conducted across all four bands of both the orthorectified pansharpened imagery and surface reflectance imagery products. Potential things to look for which, if found, may warrant communication with the imagery provider regarding re-tasking include high and low altitude clouds, cloud shadows, seam lines,

holes/missing data, distorted data, scan line artifacts, and other artifacts in imagery. This concludes all pre-processing.

Feature Extraction

Image Segmentation

All multispectral imagery was segmented using the “Segment Mean Shift” geoprocessing tool and “Segment Mean Shift” raster function within ArcGIS Pro (Figure 5.6.; Appendix Figure B4). Both versions of “Segment Mean Shift” only accept a 3-band raster with an 8-bit unsigned character pixel depth as the input raster. To do this, the “Extract Bands” raster function was run across each image. For all images, the red, green, and blue bands were used.

A number of segmentation iterations will likely be required before obtaining satisfactory results. Fine-tuning segmentation is a computationally intensive and time consuming process. To save time, raster functions may be utilized to rapidly process temporary files using the computer’s memory for the purpose of exploring the effectiveness of different segmentation parameter configurations [136].

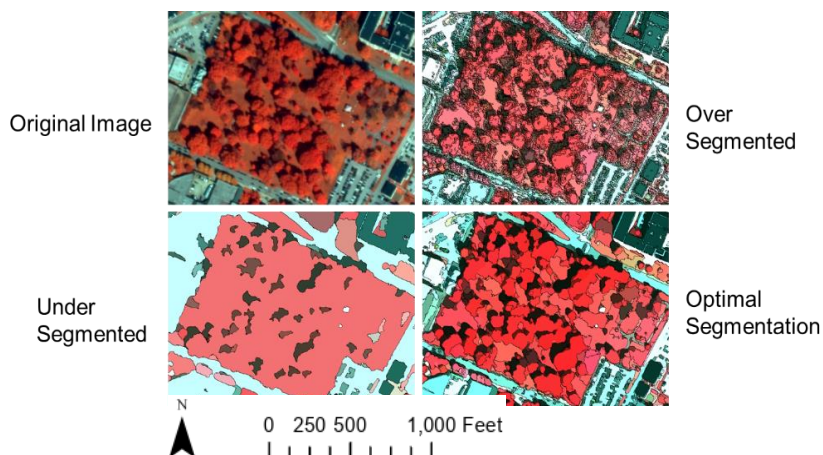


Figure 5.5 Over- and under-segmentation within an object-based classification workflow

The two segmentation parameters to explore and fine-tune within the “Segment Mean Shift” raster function and geoprocessing tool are “Spectral Detail” and “Spatial Detail”. “Spectral Detail” controls how strong variation in spectral signatures will influence the creation of separate segments. It can be set from 1 - 20, where a higher value is best when you have objects you want to classify separately but have more or less similar spectral characteristics [136]. “Spatial Detail” controls how strong variation in distance between objects will influence the creation of separate segments. It is also set between 1 and 20, where a higher value is best when the objects you are trying to classify apart from one another are small and clustered together [136]. There is no specific rational in determining the best “Spectral Detail” and “Spatial Detail” values, as the optimal “Spectral Detail” and “Spatial Detail” values will be unique for a given image, so this process requires careful trial and error.

This research selected the most sensitive configuration and increased the “Spectral Detail” and “Spatial Detail” values iteratively as needed. Keeping documentation on which segmentation parameter configurations have been tested is a helpful practice here.

One thing to keep in mind is that as a raster function output, your segmented layer will process on-the-fly when changing scale. As a result, the topology of your segmented layer will vary at different scales. To resolve this issue, within ArcGIS Pro, select the option to “Zoom to Source Resolution” of the segmented layer. This scale will display the segmented layer as it would appear using the geoprocessing version. For this research the optimal segmentation parameters can be found in Table 5.2.

Once the optimal segmentation parameters are determined using raster functions, the next step is to run the “Segment Mean Shift” geoprocessing tool within ArcGIS Pro using the parameters you determined in the previous step. For this research, a multi-core server at the University of

Tennessee at Chattanooga's Multidisciplinary Research Building was used to complete all segmentation.

Table 5.2 Unique spectral and spatial detail parameters for each SkySat image used in the configuration of the “Segment Mean Shift” geoprocessing tool with ArcGIS Pro

SkySat Image ID	Spectral Detail	Spatial Detail
Strip 1	15.5	2
Strip 2	15.5	2
Strip 3	18	15
Strip 4	18	15
Strip 5	18	2
Strip 6	18	7

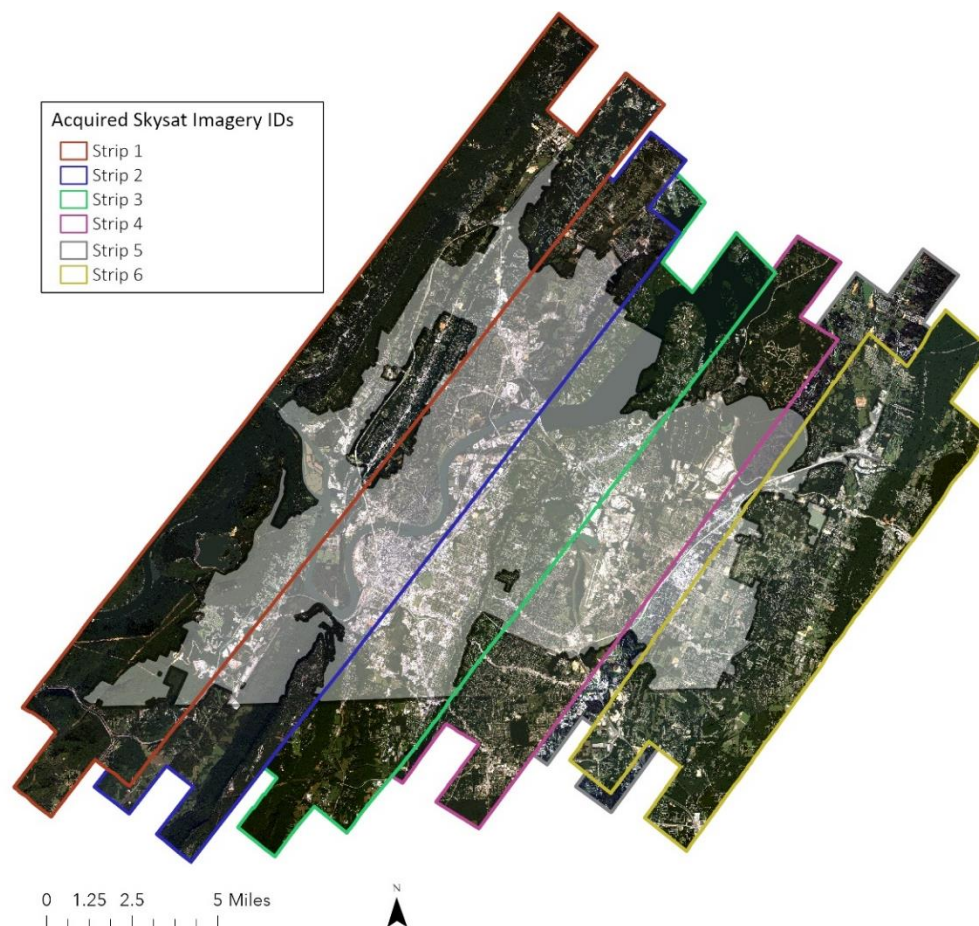


Figure 5.6 Footprint boundary, study site boundary, and segmented true color SkySat rasters

Training Sample Collection

Following imagery segmentation, the next step in the object-based classification workflow is collecting samples with which to train the machine learning classifier using ArcGIS Pro's Training Samples Manager. The collected samples provide the machine learning algorithm with the specific characteristics expressed by each of your classes. These characteristics are then used by the classifier to sort every segment across your image into a specific class [136]. In this research, the collection of training samples and classification of an image was conducted iteratively; multiple rounds of training sample collection and image classification were performed separately for each image.

Next, the schema was updated within "Training Samples Manager" such that each class name and unique class value was correct prior to collecting training samples. A copy of the schema was saved to use later during image classification. Representative samples of each class were then collected via two different methods: selecting directly from the segmented layer from the previous step and by hand-drawing a polygon over the object in the image. More often than not, segments were selected directly in lieu of hand-drawing polygons.

The collection process was started by first selecting the segmented layer in the contents pane and choosing the select segment option in the "Training Sample Manager" interface. Then within the schema, as displayed in the "Training Samples Manager" interface, a class was selected to begin collecting samples. As a note, this research found it useful to save often and utilize file versioning throughout this step of the workflow. Approximately 50 pure samples were collected for Forest Canopy, Non-Forest Vegetation, Developed Surfaces, and Shadows.

For exposed soil and water, ~20 pure samples were collected, as these land cover classes represent a considerably smaller land area than compared to other land cover types across the City of Chattanooga. In general, segments containing multiple image objects should not be sampled. Following this preliminary collection of training samples, the image was classified. Then, according to any apparent misclassification resulting from over- or under classification, additional rounds of training sample collection and image classification were performed until the image was sufficiently classified. For each of the six strips of imagery, between 150 - 350 training samples were collected for each class (Figure 5.7.; Appendix Figure B5) Once training samples were collected, a copy of the final training sample shapefile for each strip of imagery was saved.

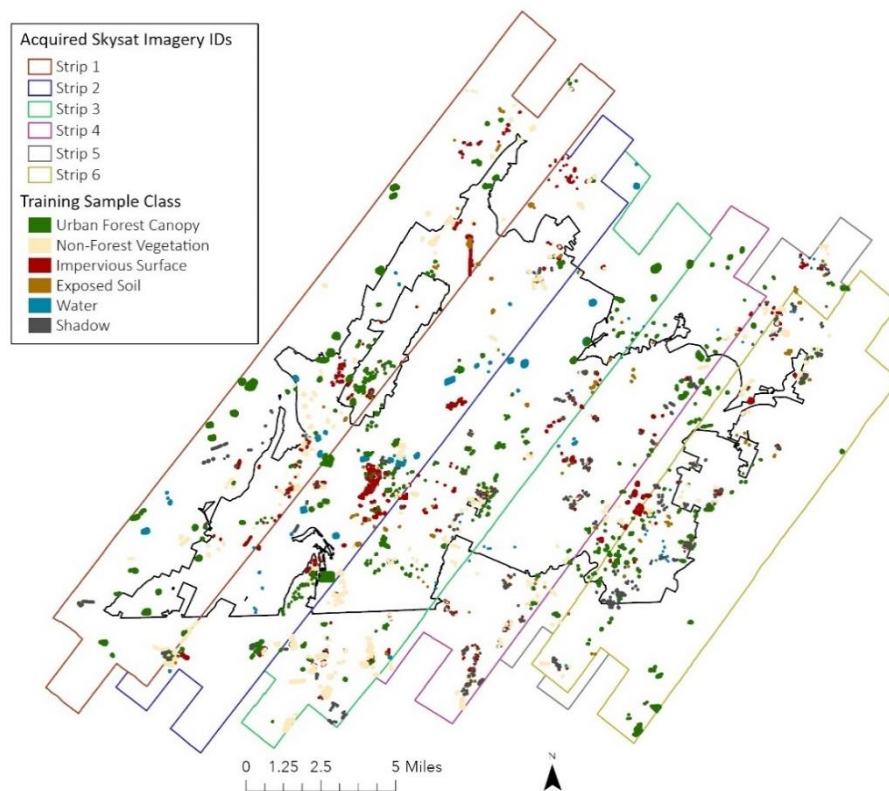


Figure 5.7 Training samples collected across segmented SkySat imagery to support object-based classification

Image Classification

As stated previously, multiple rounds of training sample collection followed by image classification were conducted separately for each image. If classes were visually over-represented or under-represented in the output land cover data, poor quality training samples were reduced or additional pure training samples were added. In each round of classification, supervised classification was selected as the classification method, and the source location for the segmented layer, multispectral imagery, schema file and training sample dataset for a given strip of imagery were added to the configuration window. Next, support vector machine (SVM) was selected as the machine learning algorithm, as it is known to work well with an unbalanced number of classes and/or small sample sizes in a given class [136]. The maximum number of samples per class was kept at the default setting of 500. Following classification, the final, unrefined high resolution land cover dataset (Figure 5.8.; Appendix Figure B6) was obtained.

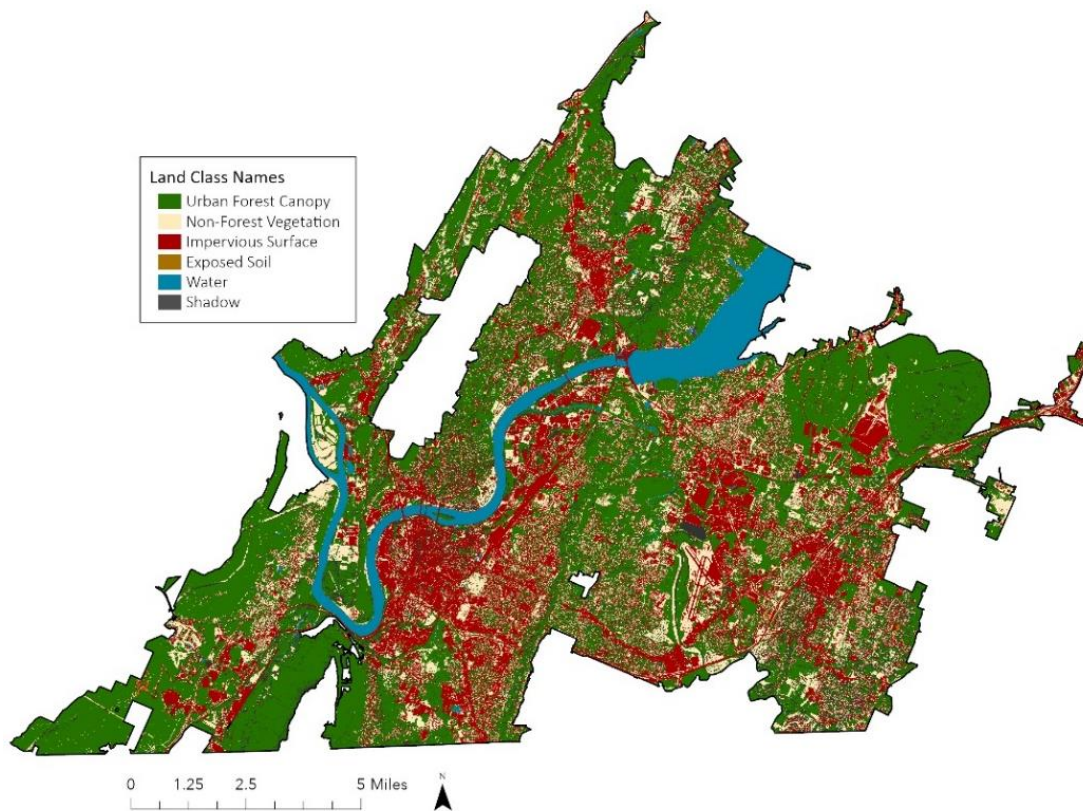


Figure 5.8 Final unrefined high resolution (50 cm) land cover dataset derived from SkySat imagery

Image Post-Processing

Refining the High Resolution Land Cover Dataset

After classifying each of the six strips of SkySat imagery, the next step was refining the land cover dataset, wherein all shadows were removed, and any areas that were misclassified based on visual interpretation were corrected to reduce error across the derived land cover map. First, the land cover dataset was exported as a .tif to a folder saved outside of the software. This folder was then copied to an external hard drive as a backup. Then, a 1000 square meter grid across the full extent of the land cover dataset was generated; the land cover dataset was assessed a cell at a time, with edits performed as needed using “Pixel Editor” within ArcGIS Pro.

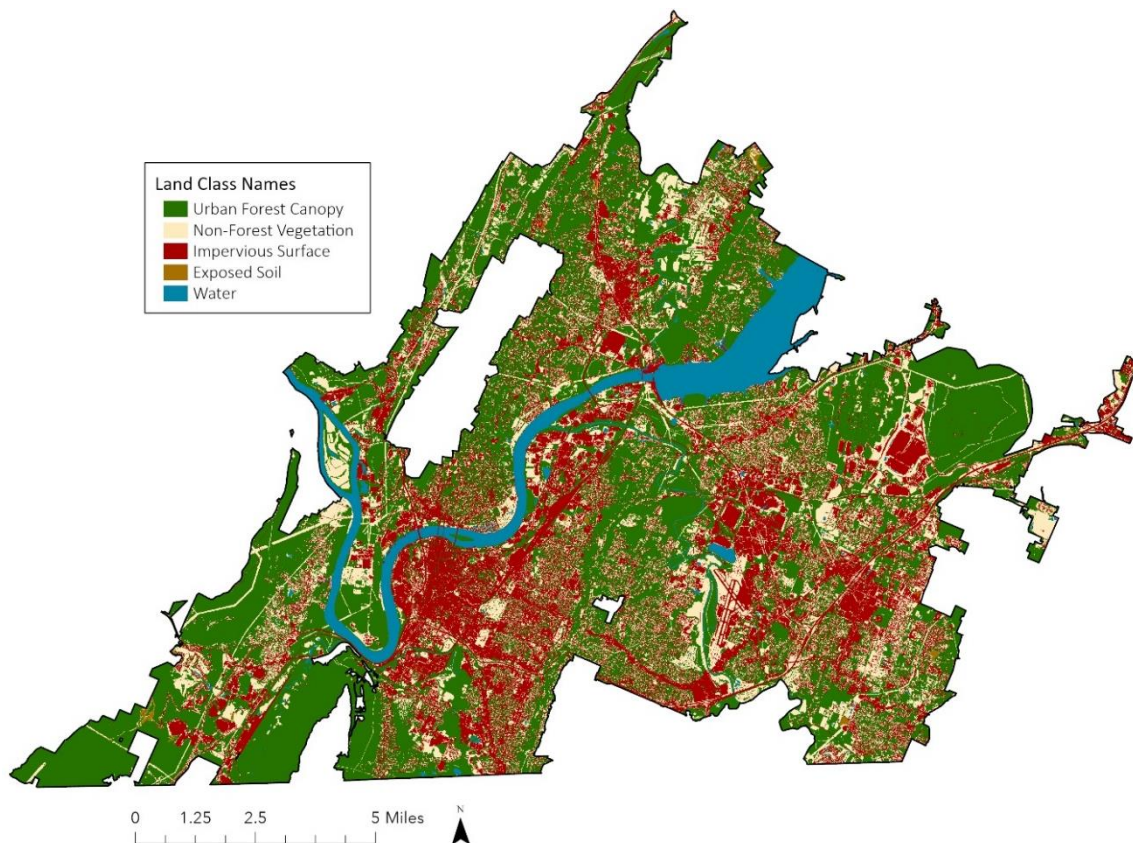


Figure 5.9 Final refined high resolution (50 cm) land cover dataset derived from SkySat imagery

Accuracy Assessment

For both the unrefined and refined landcover accuracy assessments, approximately 500 randomly distributed points were created using the “Create Accuracy Assessment Points” geoprocessing tool within ArcGIS Pro. Each point within the “Create Accuracy Assessment Points” output feature class was visually inspected, and a class code was assigned to the “GrndTruth” field for that point within the feature class’s attribute table. Finally, “Compute Confusion Matrix” geoprocessing tool within ArcGIS Pro was run using the 500 random points as input data. The output confusions matrices are provided in Table 5.3. and 5.4.



Figure 5.10 500 randomly distributed points used for the accuracy assessment of the final unrefined high resolution land cover dataset



Figure 5.11 500 randomly distributed points used for the accuracy assessment of the final refined high resolution land cover dataset

Results

Following image processing and post-processing tasks, an unrefined, 6-class thematic land cover dataset (Figure 5.8.; Appendix Figure B6), consisting of: Forest Canopy, Non-Forest Vegetation, Impervious Surfaces, Exposed Soil, Water, and Shadows; and a refined 5-class thematic land cover dataset (Figure 5.9.; Appendix Figure B7), consisting of: Forest Canopy, Non-Forest Vegetation, Impervious Surfaces, Exposed Soil, and Water was obtained.

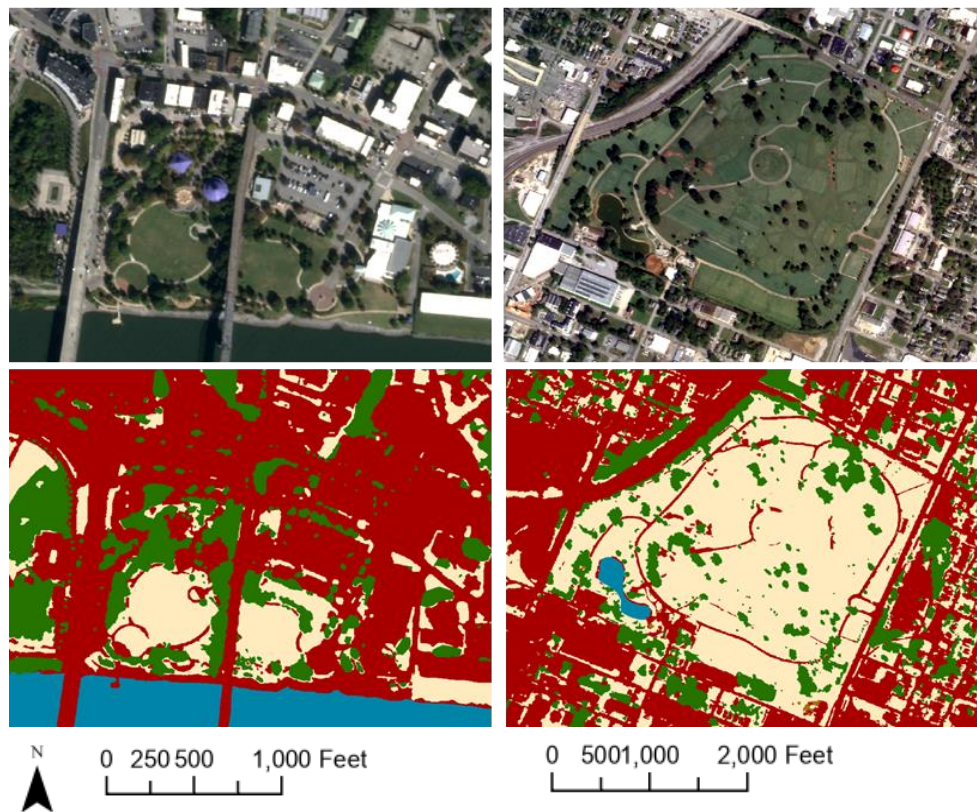


Figure 5.12 Subsets showcasing the true color SkySat imagery (top), refined land cover dataset (bottom) over Coolidge Park / North Shore (left), and the Chattanooga National Cemetery (right)

Accuracy Assessment Results

Accuracy assessments were performed on both the unrefined and refined land cover datasets using geoprocessing tools within ArcGIS Pro (Figures 5.9., 5.10., and 5.11.; Appendix Figures B7, B8, and B9). Results from an accuracy assessment of the unrefined land cover data can be used to determine if any refining is necessary, or if this process can be skipped. Additionally, assessing the accuracy of the refined dataset and comparing the results to the unrefined dataset accuracy assessment can help determine the effectiveness of the entire refining process. Considering the overall accuracy of the 2019 National Landcover Dataset (NLCD) is reportedly between 85% and 90% using 30-meter Landsat imagery, the results from the accuracy assessment of the refined data, as presented in Table 5.4., support the idea that an object-based workflow, compared to a more traditional pixel-based workflow, is well suited to classify large, high resolution multispectral images at a high accuracy.

Results from the accuracy assessment of the unrefined data found an overall accuracy of 87% with a supporting kappa coefficient of 0.82, as seen in Table 5.3. Results from the second accuracy assessment found the overall accuracy of the final refined land cover dataset to be 93% with a supporting kappa coefficient of 0.9, as seen in Table 5.4.

Table 5.3 Confusion matrix derived from the accuracy assessment of the unrefined land cover dataset

Classification	Forest Canopy	Non-Forest Vegetation	Impervious Surface	Exposed Soil	Water	Shadow	Total	User's Accuracy	Kappa
Forest	203	16	1	0	0	18	238	85.29%	
Non Forest Vegetation	5	72	4	0	0	0	81	88.89%	
Impervious	1	3	106	2	0	0	112	94.64%	
Exposed Soil	1	0	0	9	0	0	10	90.00%	
Water	0	0	0	0	26	0	26	100.00%	
Shadow	10	0	2	0	3	27	42	64.29%	
Total	220	91	113	11	29	45	509		
Producer's Accuracy	92.27%	79.12%	93.81%	81.82%	89.66%	60.00%		87.03%	
Kappa									0.8174

Table 5.4 Confusion matrix derived from the accuracy assessment of the refined land cover dataset

Classification	Forest Canopy	Non-Forest Vegetation	Impervious Surface	Exposed Soil	Water	Total	User's Accuracy	Kappa
Forest	232	12	3	0	0	247	93.93%	
Non Forest Vegetation	8	90	1	2	0	101	89.11%	
Impervious	0	3	117	1	0	121	96.69%	
Exposed Soil	0	0	2	8	0	10	80.00%	
Water	1	0	0	0	27	28	96.43%	
Total	241	105	123	11	27	507	0	
Producer's Accuracy	96.27%	85.71%	95.12%	72.73%	100.00%	0	93.49%	
Kappa								0.9023

CHAPTER 6

DISCUSSION

Objectives of the Study

This collection of research sought to: (1) quantify how the extent of Chattanooga's urban tree canopy changed between 1984 and 2021 using Landsat imagery, (2) determine how the carbon sequestered in the biomass of urban forest trees can be predictively modeled at little to no cost and without a significant time investment using PlanetScope and Sentinel-2a imagery, and (3) map the current extent of Chattanooga's urban tree canopy using high resolution SkySat imagery. Throughout this research, a number of obstacles were identified. These obstacles, along with any insight gained throughout the research are discussed below.

Application of Landsat Imagery

The main goal of this research was to identify the historic extent of urban tree canopy across the City of Chattanooga. In conducting this research, Landsat 5 and 8 data were obtained. Landsat 5 and 8 however, are two different systems designed three decades apart. Therefore, image quality between these systems is inherently different. Additionally, variable levels of atmospheric dust, pollen, and water vapor can impact the accuracy of a remote sensor. For this reason, a supervised hybrid classification workflow as described in this research was implemented in lieu of more traditional classification methods to normalize potential variation across classified results.

To accurately classify the extent of forest canopy in each of the images, it was necessary to delineate tree pixels from pixels representing non-tree vegetation. However, because of Landsat's moderate 30 meter spatial resolution, and the spectral similarities between tree pixels and non-tree pixels, it was highly difficult to differentiate between forest canopy and non-forest vegetation, even when viewing the imagery in false color. This was true across large portions of the city, where the forest canopy is highly fragmented and mixed in thoroughly with other fragments of non-forest vegetation and impervious surfaces, all in areas smaller than the spatial resolution of most moderate resolution sensors.

Furthermore, the spectral response of individual features smaller in surface area than the spatial resolution of the sensor that captured the image were not clearly distinguishable or detectable in the obtained imagery. Clusters of multiple small features were visible in imagery, however the structure or form of one individual unit of the cluster of small features were not distinguishable.

As a result, during the creation of both training sample polygons with which to train the machine learning classifier and accuracy assessment polygons with which to assess the obtained results, the primary researcher selected large, pure clusters of clearly identifiable forest and non-forest vegetation as samples. In this way, bias was introduced that potentially influenced the results and accuracy reports of the obtained models. All attempts were made to maintain some sense of diversity in the obtained training and accuracy assessment sample datasets, especially with regards to forest canopy and non-forest vegetation. To these ends, an unsupervised workflow for previous pixel classification was applied, as there was a greater chance for the algorithm to spectrally differentiate between spectrally distinct groups of forest and non-forest vegetation pixels than by a supervised classification with user inputs.

In this sense, the spatiotemporal analysis conducted here may be highly accurate in the classification of larger clusters of forest apart from areas of vegetation that might be forest vegetation or non-forest vegetation. However, due to the limited resolution of moderate sensors, the ability to classify urban tree canopy from other vegetation types with accuracies that can be consistently and objectively quantified is only obtainable using fine resolution imagery.

Finally, when conducting spatiotemporal analyses, one approach was to acquire as much imagery as possible within a defined acquisition period. However, when working with a large multispectral dataset, generating classified outputs that are accurate enough to be compared chronologically without excessive under-classification or over-classification from dataset to dataset is quite difficult. Therefore, it could be helpful to only acquire data around the beginning and end of the defined temporal scope of a research project.

Application of Planet Scope and Sentinel Imagery

In this research, imagery from three separate sensors and their derivative products were correlated to derive a workflow capable of predicting the carbon sequestered in Chattanooga's urban forest. The specific imagery sources acquired were NAIP, PlanetScope, and Sentinel-2a. However, like Landsat 5 and Landsat 8 as used in Chapter 4, each of these imagery sources have unique specifications and characteristics that can make data correlation difficult. This is a well-known and heavily researched area of remote sensing research [137-139].

One specific challenge in correlating imagery from different remote sensors is variable spectral bandwidth [20]. In other words, the range of EM wavelengths detectable by a given sensor's individual bands is different. This can lead to differences in the information collected by each sensor. Providers of remote sensing imagery help work around the issue of variable spectral

bandwidth by configuring remote sensors with broad-width bands, as broad band sensors are more likely to share similarities with other broad width sensors.

Next, different sensors have different radiometric resolution. Radiometric resolution is essentially the ability for a given sensor to interpret between different levels of brightness in an image [20]. Providers of remote sensing data attempt to work around variable radiometric resolution by conducting radiometric calibration, which involve the conversion of raw digital number values into calibrated radiance or surface reflectance values. Last, as discussed in detail throughout this research, different remote sensors have their own unique spatial resolution. Different spatial resolution directly translates to different levels of detail in the obtained results [20]. Image fusion is a technique specifically used to combine imagery sources with different spatial resolutions into a single composite image that embodies the strengths of both sensors [140].

Additionally, in recent years more computationally complex harmonization processes have been employed that work to adjust variable spectral and radiometric resolution, as well as geometric inconsistencies across different sources of imagery [141, 142]. More research could be used here to test the application of these calibration and correction techniques in the context of the research presented here.

In review of the application of PlanetScope and Sentinel-2a derived vegetation indices to model urban forest sequestered carbon, regression analyses results report that across all tested independent variables, at best, a low correlation can be identified between the obtained sample dataset of sequestered carbon per square meter and the extracted tree canopy vegetation index values. These results are in part likely due to an incorrect assumption that was made that the urban forest of UTC's campus was a representative subset of the larger urban forest of the City of Chattanooga.

As was discovered during the collection of field data, like many other colleges across the nation, UTC capitalizes on the presence of any large old growth trees across its campus. Furthermore, UTC's landscaping facilities are often busy with new projects involving tree planting around the campus; there are a high number of small, newly planted trees across campus.

In this way, a large portion of the trees sampled consisted of large, old growth trees, such as the massive oaks found across campus, or smaller trees, representing the younger, relatively new trees planted around campus. In order to obtain a sample dataset more representative of the population, a larger sample size could be considered across a larger, more representative subset of the city. As a result, developing a predictive model from a likely non-normal and under-sampled training dataset is likely to yield insignificant results, which can be improved with further research.

Nonetheless, some valuable findings were in fact obtained from this research. Mean GNDVI pixels derived from PlanetScope imagery had the strongest correlation to the variation in sequestered carbon across the sample dataset ($R^2 = 0.213$). The broad band independent variables derived from Sentinel-2a imagery tested in this research (GNDVI, NDVI, and SAVI) had less correlative strength to field sampled sequestered carbon ($R^2 = < 0.120$) comparatively. Finally, the narrow band independent variables derived from Sentinel-2a imagery tested in this research (RENDVI1 and RENDVI2) had the weakest correlation to field sampled sequestered carbon ($R^2 = < 0.078$).

While the observed correlation and respective strengths reported by the analyses conducted here yielded relatively weak results, a trend between the correlation coefficient intensity and spatial resolution was identified. Organized according to the spatial resolution of each independent variable tested, GNDVI derived from PlanetScope is among the finest resolution imagery products used here (3 m), followed by the broad band independent variables derived from Sentinel-2a

(GNDVI, NDVI, and SAVI; 10 m), and tailed by the narrow band independent variables derived from Sentinel-2a (RENDVI1 and RENDVI2; 20 m).

Based on these results, as the spatial resolution of the source imagery becomes coarser, the ability for the sensor to identify the spectral identity of a single isolated or small cluster of trees across an urban environment quickly decreases. Therefore, for modeling sequestered carbon across an urban tree canopy using remote sensing principles, the finest resolution imagery should be sought.

Application of SkySat Imagery

Research presented in Chapter 5 sought to develop a land cover dataset utilizing high resolution multispectral SkySat imagery, object-based classification, and machine learning in order to assess the distribution of urban tree canopy across the City of Chattanooga, Tennessee in detail. Results suggest object-based classification is a highly effective classification method when combined with high resolution imagery. However, during the analysis, several obstacles were identified. Some insight, and the implications of these obstacles on accuracy assessments conducted are discussed below.

Segmenting High Resolution Multispectral Imagery

The functional goal of segmentation is to generate a boundary, or segment around each object in imagery. However, perfectly segmenting an image such that each object is represented by a singular segment is not realistic. More likely, the segmented image will be slightly over- or under-segmented. In some situations, a few of which being discussed here, some level of over- and under-segmentation in the derived segmented layer can be accepted without a significant impact on the final accuracy of the obtained land cover dataset.

In general, it is better to over-segment than under-segment. Images with objects consisting of multiple segments are over-segmented, whereas images with multiple objects in a segment are under-segmented. In an over-segmented image, most of the image objects have been completely segmented, however rather than being represented by a single segment, image objects consist of multiple segments. Under-segmented images on the other hand are overgeneralized; many image objects have been erroneously included in a single segment [143].

Adjusting the segmentation parameters such that each image object is represented by a single segment, or as few as possible without under-segmenting, is one of, if not the most important parts of the workflow as described in this report. When correctly segmented, the classifier will have an easier time sorting the various image objects (tree canopy, grassy field, building, etc.) into the defined classes that comprise the final land cover dataset. This directly translates to less error requiring revision in the final land cover dataset.

When utilizing an object-based workflow to classify an image, one thing to consider early is the number and identity of the unique classes which will collectively comprise the land cover dataset. When composed of few, very broad land cover classes, such as “Water”, “Soil”, “Impervious Surfaces”, etc., as was the case with this research, some under-segmentation can be accepted without a significant impact on the final accuracy of the obtained land cover dataset as long as all instances of under-segmentation occur within single land cover classes and not across multiple land cover classes. A few examples of acceptable under-segmentation within a single land cover class could be adjacent cars in a parking lot or a clump of trees being erroneously bound by a single segment. A few examples of unacceptable under-segmentation across multiple land cover classes could be a grassy front yard and a sidewalk or a tree canopy and a grassy median being erroneously bound by a single segment. These errors require post-processing to correct.

Using ArcGIS Pro's Pixel Editor to Refine Classified Results

When this research was conducted (using ArcGIS Pro version 2.6.3), Pixel Editor had a functional bug related to the recalculation of the thematic raster's statistics that resulted in the corruption or deletion of the raster being refined when saving your edits. When attempting to use a file geodatabase raster, this research found a considerable increase in critical errors resulting in lost data. This research found that by conducting all refining on the .tif file only and saving every 5-10 minutes of refining, the number of critical errors were significantly reduced.

Training Sample Collection and Imagery Classification

Rather than attempting to collect an excess of training samples in one single round of sample collection, this research found that by conducting multiple rounds of training sample collection and image classification separately for each image, the process of fine tuning each image's classified output was more manageable by a single person. In each round, only a small number of training samples were added before re-classifying as to avoid errors due to oversampling.

This process was started by collecting ~50 pure samples per major class (less prevalent classes like exposed soil can get away with fewer samples) and classifying the image. Then, following a preliminary assessment of the results, the number of samples were increased in under-represented classes, and the number of poor quality or biased samples were reduced in over-represented classes, as suggested by the preliminary classification report generated by ArcGIS Pro's Image Classification geoprocessing tool. This research found that by conducting multiple rounds of training sample collection and image classification, a fewer number of pure training samples were needed to obtain accurate results.

Documented Challenges

Schema Changes Not Preserved

Schema files are used in the image classification process to tell the machine learning classifier the different names and unique IDs for each of the desired classes. The training sample dataset and the schema file are directly connected to each other within ArcGIS Pro. Therefore, if any edits to the schema are made after collecting training samples, this research found that by temporarily switching to a different sketch tool within the training samples manager window, any edits made to the schema are preserved and updated within the training samples dataset.

Error 999999: Unexpected Errors

In a preliminary assessment of the object-based workflow applied in this study, researchers had success in running the segment mean shift raster function on a small subset of the imagery and exporting the output to memory, rather than running the segment mean shift geoprocessing tool. Using the exported raster function segmented layer, a subset of the multispectral imagery, and a preliminary testing training samples dataset, a subset land cover dataset derived from object-based classification was obtained. However, when scaling up to an entire strip of imagery, attempting classification using the raster function derived segmented layer resulted in the process failing with an unexpected error. Although the true cause of this unexpected error was not directly identified by the researchers, it was determined that exporting the raster function version of the segmented strips of imagery did not create an indexing file, whereas the Segment Mean Shift geoprocessing tool does create an indexing file. It is plausible that running the classifier using the segment mean shift raster function export, which lacked an index file, may have caused the unexpected error when applied to larger datasets.

Error 003436: No Training Samples Found

On multiple occasions, immediately following the execution of the machine learning classifier, an error was triggered stating that no training samples were found, even though the training samples were in fact correctly loaded. This study found multiple plausible explanations for this error. First, when conducting object-based image classification, in navigating to the standalone training samples manager outside the image classification wizard in ArcGIS Pro, it is imperative that you select the segmented raster within the table of contents and not the physical multispectral image to be classified. If the image was selected instead, there would be no obvious sign of a problem until the machine learning classifier is executed. This is because when object based classification is selected within ArcGIS Pro, the machine learning classifier will specifically be looking for the spectral and spatial segment characteristics transferred from the segmented layer to the training samples as attributes during sample collection. If the multispectral image was selected and not the segmented layer, then the spectral and spatial characteristics needed to classify the image are not successfully transferred to the training samples.

Another plausible explanation for Error 003436 is that unlike ArcGIS Pro's standalone "Training Samples Manager", when collecting training samples within the image classification wizard, there is no way to save your training samples dataset. Most likely when collecting training samples within the image classification wizard, the samples are temporarily written to memory until the "next" button is clicked, which initiates the training samples to be saved.

However, when collecting a large number of training samples across a very large, high resolution multispectral image, it is possible that the training samples temporarily saved to memory are not saved effectively to the hard drive. This research found that when collecting training samples within the standalone training samples manager within ArcGIS Pro, which does have a

save and save as button, Error: 003436 did not occur, suggesting that the training samples were properly preserved.

CHAPTER 7

FUTURE DIRECTIONS AND CONCLUSION

Future Directions

To help reduce the rate at which our urban forest is converted to new urban spaces, this research recommends the City of Chattanooga establish a regular acquisition of fine resolution imagery, as maintaining an accurate and publicly shared map of the distribution of a city's urban forest canopy is a sure-fire way to enhance the inherent value of an urban forest in the eyes of local government and the community.

The research presented here is intended to serve as a model for any institution to reference when attempting to map urban forest distribution and model sequestered carbon, as the methods explained here may be applied to any city extent. For those researchers looking to apply any of the workflows as described here, a few details might be considered. First, as discovered in the fourth chapter of this research, as spatial resolution becomes finer, the strength of any predictive model based on spectral characteristics of forest canopy pixels will increase. With this in mind, applying high resolution imagery, like SkySat used in the fifth chapter of this research, is very likely to yield statistically significant results. Because SkySat imagery was acquired after the research in the fourth chapter was conducted, this research was not able to utilize SkySat as a source of predictive variables. Other research might consider acquiring SkySat imagery for this purpose.

As mentioned earlier in this manuscript, SkySat imagery requires tasking and is not open to view or download without a considerable financial investment. The process of tasking SkySat imagery begins with contacting a sales representative with Planet Labs and inquiring about SkySat imagery. You will eventually be directed to an online tasking portal to provide more details on the specific requirements of your data request.

Some of these requirements might include the boundary of your area of interest, the ideal window of time to obtain imagery, or specific time of day/solar zenith angle required for your research. Your request will be reviewed by Planet Labs, and you will be quoted accordingly. The number of images and each of the individual image boundaries will not be known prior to the onset of data collection, as the availability of a given satellite in the SkySat constellation may change through time. Once all SkySat imagery has been tasked, you will be able to download all imagery as a number of different pre-processed data products, such as pansharpened orthorectified imagery, top of atmosphere reflectance, and corrected surface reflectance products.

While it is true that SkySat imagery is an excellent data source for mapping urban tree canopy, due to the high cost of acquiring SkySat imagery, it is worth considering other sources of data.

One possible direction is the utilization of UAV imagery to map urban forest canopy distribution. UAV platforms are capable of collection both LiDAR and high resolution imagery with spatial resolution measured in centimeters or millimeters. However, there are a number of issues related to the use of UAV systems for this type of research. The first is the relatively small coverage area a UAV platform can visit at a time. Additionally, there are a number of legal limitations related to the airspace a drone is permitted to access. These limitation make scaling UAV-based research up to the city scale difficult.

Next, data obtained by UAVs require complex processing before they can be used in analyses. While UAV collects imagery and LiDAR, it is also carefully collecting global navigation satellite system information (GNSS) and inertial navigation system (INS) information.

Depending on whether a real-time kinematic (RTK) or post-processed kinematic (PPK) workflow is selected, the LiDAR/imagery data must be integrated with the GNSS and INS information. This process is complex and can require expensive software.

Specifically related to correlating multiple UAV images through time, because of the complex processing and calibration techniques needed to obtain a final mosaiced image, it can be difficult to derive imagery products that can be objectively and quantifiably correlated. This is a major consistency issue that hinders the wider application of UAV imagery for spatiotemporal analyses. For this reason, and due to their limited coverage area, spaceborne and aerial platforms are often selected over UAV platforms when mapping urban forest canopy at the city level.

Another plausible option that has the potential to significantly improve the accuracy of the obtained urban tree canopy map is the utilization of LiDAR. As mentioned earlier in this manuscript, LiDAR data can be difficult to obtain and is costly to task. However, the number of publicly available LiDAR datasets is increasing through time. Because LiDAR works to generate dense 3-D point clouds across a landscape, it is possible to obtain highly accurate 3D models of urban tree canopy distribution. More research is needed to test the application of LiDAR in mapping urban tree canopy at the city level.

Conclusions

In review of the research presented here, moderate resolution imagery sources, such as Landsat and Sentinel-2a, are excellent data sources for approximating broad land cover changes at the city-level. However, land cover change analyses using moderate resolution imagery are only as accurate as the sensor's spatial resolution, regardless of the obtained overall accuracy. As the spatial resolution of any remote sensor becomes coarser, the ability for the sensor to "see" the spectral identity of a single isolated or small cluster of urban trees quickly decreases. Therefore, to model sequestered carbon across an urban tree canopy using remote sensing principles and to effectively manage a city's urban tree canopy using geospatial data, fine resolution imagery, such as that captured by the SkySat constellation, should be sought. Once the hurdle of obtaining quality data has been obtained, the resulting high resolution land cover data products, will likely have great utility in several industries.

When developing a model to predict the carbon sequestered in urban forest biomass at a low cost and with relatively low time investment, rather than sampling within a random subset of urban forest, sampling across randomly placed points across the full extent of the urban tree canopy would likely yield more significant results, as the obtained training dataset would be more representative of the whole population.

The importance of maintaining high levels of sequestered carbon in temperate forest ecosystem is apparent. Forests are solely defined by the dominance of woody tree species with high levels of sequestered carbon, so to maintain high levels of sequestered carbon is to maintain natural populations of trees within temperate forest environments. Additionally, maintaining high levels of sequestered carbon in temperate forests has another environmental implication.

Maintaining urban forest health and integrity though time can increase the carbon sequestration potential and overall quality of temperate forest habitats. Additionally, through public engagement and increased awareness brought about by the sharing of the information obtained from the mapping of urban tree canopy and modeling of sequestered carbon with local governments and surrounding communities, it is possible to reduce the rate at which extant urban forests are converted to urban spaces into the future.

REFERENCES

- [1] Bradley CA, Altizer S. Urbanization and the ecology of wildlife diseases. *Trends in ecology & evolution*. 2007;22(2):95-102.
- [2] Elmqvist T, Zipperer W, Güneralp B. Urbanization, habitat loss, biodiversity decline: solution pathways to break the cycle. In, Seta, Karen; Solecki, William D; Griffith, Corrie A(eds) *Routledge Handbook of Urbanization and Global Environmental Change* London and New York: Routledge. 2016;2016:139-51.
- [3] Freeman PL, Schorr MS. Influence of watershed urbanization on fine sediment and macroinvertebrate assemblage characteristics in Tennessee Ridge and Valley Streams. *Journal of Freshwater Ecology*. 2004;19(3):353-62.
- [4] Hall J, Hossain AA. Mapping urbanization and evaluating its possible impacts on stream water quality in Chattanooga, Tennessee, using GIS and remote sensing. *Sustainability*. 2020;12(5):1980.
- [5] Rizwan AM, Dennis LY, Chunho L. A review on the generation, determination and mitigation of Urban Heat Island. *Journal of environmental sciences*. 2008;20(1):120-8.
- [6] Lorenz K, Lal R. *Carbon sequestration in forest ecosystems*: Springer; 2009.
- [7] Nowak DJ, Hoehn RE, Bodine AR, Greenfield EJ, O'Neil-Dunne J. Urban forest structure, ecosystem services and change in Syracuse, NY. *Urban Ecosystems*. 2016;19(4):1455-77.
- [8] Nowak DJ, Dwyer JF. Understanding the benefits and costs of urban forest ecosystems. *Urban and community forestry in the northeast*: Springer; 2007. p. 25-46.
- [9] Nowak DJ, Greenfield EJ. US urban forest statistics, values, and projections. *Journal of Forestry*. 2018;116(2):164-77.
- [10] Endreny TA. Strategically growing the urban forest will improve our world. *Nature communications*. 2018;9(1):1-3.
- [11] Li X, Chen WY, Sanesi G, Laforzezza R. Remote sensing in urban forestry: Recent applications and future directions. *Remote Sensing*. 2019;11(10):1144.
- [12] Myeong S, Nowak DJ, Duggin MJ. A temporal analysis of urban forest carbon storage using remote sensing. *Remote Sensing of Environment*. 2006;101(2):277-82.

- [13] Shahtahmassebi AR, Li C, Fan Y, Wu Y, Gan M, Wang K, et al. Remote sensing of urban green spaces: A review. *Urban Forestry & Urban Greening*. 2021;57:126946.
- [14] Kanniah K, Muhamad N, Kang C, editors. Remote sensing assessment of carbon storage by urban forest. *IOP Conference Series: Earth and Environmental Science*; 2014: IOP Publishing.
- [15] Ren Z, Zheng H, He X, Zhang D, Shen G, Zhai C. Changes in spatio-temporal patterns of urban forest and its above-ground carbon storage: Implication for urban CO₂ emissions mitigation under China's rapid urban expansion and greening. *Environment international*. 2019;129:438-50.
- [16] Watanabe MD, Ortega E. Ecosystem services and biogeochemical cycles on a global scale: valuation of water, carbon and nitrogen processes. *Environmental science & policy*. 2011;14(6):594-604.
- [17] Brandão M, Levasseur A, Kirschbaum MU, Weidema BP, Cowie AL, Jørgensen SV, et al. Key issues and options in accounting for carbon sequestration and temporary storage in life cycle assessment and carbon footprinting. *The International Journal of Life Cycle Assessment*. 2013;18(1):230-40.
- [18] Falkowski P, Scholes R, Boyle E, Canadell J, Canfield D, Elser J, et al. The global carbon cycle: a test of our knowledge of earth as a system. *science*. 2000;290(5490):291-6.
- [19] DePaolo DJ, Cole DR. Geochemistry of geologic carbon sequestration: an overview. *Reviews in Mineralogy and Geochemistry*. 2013;77(1):1-14.
- [20] Jensen JR. Remote sensing of the environment: An earth resource perspective 2/e: Pearson Education India; 2009.
- [21] Johnson MP. Correction: Photosynthesis. *Essays in Biochemistry*. 2017;61(4):429.
- [22] fao. Global forest resources assessment 2020—Key findings. Rome. 2020.
- [23] Kindermann G, Obersteiner M, Sohngen B, Sathaye J, Andrasko K, Rametsteiner E, et al. Global cost estimates of reducing carbon emissions through avoided deforestation. *Proceedings of the national Academy of Sciences*. 2008;105(30):10302-7.
- [24] Pan Y, Birdsey RA, Fang J, Houghton R, Kauppi PE, Kurz WA, et al. A large and persistent carbon sink in the world's forests. *science*. 2011;333(6045):988-93.
- [25] Zhu K, Song Y, Qin C. Forest age improves understanding of the global carbon sink. *Proceedings of the National Academy of Sciences*. 2019;116(10):3962-4.
- [26] Houghton R, Hall F, Goetz SJ. Importance of biomass in the global carbon cycle. *Journal of Geophysical Research: Biogeosciences*. 2009;114(G2).

- [27] Schimel DS. Terrestrial ecosystems and the carbon cycle. *Global change biology*. 1995;1(1):77-91.
- [28] Spicer ME, Mellor H, Carson WP. Seeing beyond the trees: a comparison of tropical and temperate plant growth forms and their vertical distribution. *Ecology*. 2020;101(4):e02974.
- [29] Tans PP, Fung IY, Takahashi T. Observational constraints on the global atmospheric CO₂ budget. *Science*. 1990;247(4949):1431-8.
- [30] Aryal PC, Aryal C, Bhusal K, Chapagain D, Dhamala MK, Maharjan SR, et al. Forest structure and anthropogenic disturbances regulate plant invasion in urban forests. *Urban Ecosystems*. 2022;25(2):367-77.
- [31] Canadell JG, Mooney H. Biological and ecological dimensions of global environmental change. *Encyclopedia of global environmental change* John Wiley, Chichester, UK. 2002:1-9.
- [32] Reich PB, Bolstad P. Productivity of evergreen and deciduous temperate forests. *Terrestrial global productivity Academic*, San Diego. 2001:245-83.
- [33] Malhi Y, Baldocchi D, Jarvis P. The carbon balance of tropical, temperate and boreal forests. *Plant, Cell & Environment*. 1999;22(6):715-40.
- [34] Williams GW. *The USDA Forest Service: the first century*: USDA Forest Service; 2000.
- [35] Germany DB, Referat Ö. Protecting the tropical forests: a high-priority international task. *Protecting the tropical forests: a high-priority international task*. 1990.
- [36] Heath LS, Kauppi PE, Burschel P, Gregor H-D, Guderian R, Kohlmaier GH, et al. Contribution of temperate forests to the world's carbon budget. *Water, Air, and Soil Pollution*. 1993;70(1):55-69.
- [37] Potapov P, Hansen M, Stehman SV, Pittman K, Turubanova S. Gross forest cover loss in temperate forests: Biome-wide monitoring results using MODIS and Landsat data. *Journal of Applied Remote Sensing*. 2009;3(1):033569.
- [38] Millar CI, Stephenson NL. Temperate forest health in an era of emerging megadisturbance. *Science*. 2015;349(6250):823-6.
- [39] Miller MD. The impacts of Atlanta's urban sprawl on forest cover and fragmentation. *Applied Geography*. 2012;34:171-9.
- [40] Seto KC, Sánchez-Rodríguez R, Fragkias M. The new geography of contemporary urbanization and the environment. *Annual review of environment and resources*. 2010;35(1):167-94.

- [41] Fornal-Pieniak B, Ollik M, Schwerk A. Impact of different levels of anthropogenic pressure on the plant species composition in woodland sites. *Urban Forestry & Urban Greening*. 2019;38:295-304.
- [42] Davis KL. The Role of "Sense of Place:" A Theoretical Framework to Aid Urban Forest Policy Decision-Making. 2011.
- [43] Nesbitt L, Hotte N, Barron S, Cowan J, Sheppard SR. The social and economic value of cultural ecosystem services provided by urban forests in North America: A review and suggestions for future research. *Urban Forestry & Urban Greening*. 2017;25:103-11.
- [44] Ordóñez-Barona C. How different ethno-cultural groups value urban forests and its implications for managing urban nature in a multicultural landscape: A systematic review of the literature. *Urban Forestry & Urban Greening*. 2017;26:65-77.
- [45] Livesley S, McPherson EG, Calfapietra C. The urban forest and ecosystem services: impacts on urban water, heat, and pollution cycles at the tree, street, and city scale. *Journal of environmental quality*. 2016;45(1):119-24.
- [46] Albiero-Júnior A, Venegas-González A, Rodríguez-Catón M, Oliveira JM, Longhi-Santos T, Galvão F, et al. Edge effects modify the growth dynamics and climate sensitivity of *Araucaria angustifolia* trees. *Tree-Ring Research*. 2020;76(1):11-26.
- [47] Garvey SM, Templer PH, Pierce EA, Reinmann AB, Hutyra LR. Diverging patterns at the forest edge: Soil respiration dynamics of fragmented forests in urban and rural areas. *Global Change Biology*. 2022;28(9):3094-109.
- [48] Morreale LL, Thompson JR, Tang X, Reinmann AB, Hutyra LR. Elevated growth and biomass along temperate forest edges. *Nature Communications*. 2021;12(1):1-8.
- [49] Alrababah M, Alhamad M, Bataineh A, Bataineh M, Suwaileh A. Estimating east Mediterranean forest parameters using Landsat ETM. *International Journal of Remote Sensing*. 2011;32(6):1561-74.
- [50] Boccoardo P, Giulio Tonolo F. Remote sensing role in emergency mapping for disaster response. *Engineering Geology for Society and Territory-Volume 5*: Springer; 2015. p. 17-24.
- [51] Castillo JAA, Apan AA, Maraseni TN, Salmo III SG. Estimation and mapping of above-ground biomass of mangrove forests and their replacement land uses in the Philippines using Sentinel imagery. *ISPRS Journal of Photogrammetry and Remote Sensing*. 2017;134:70-85.
- [52] Dewan AM, Yamaguchi Y. Land use and land cover change in Greater Dhaka, Bangladesh: Using remote sensing to promote sustainable urbanization. *Applied geography*. 2009;29(3):390-401.

- [53] Gonzalez P, Asner GP, Battles JJ, Lefsky MA, Waring KM, Palace M. Forest carbon densities and uncertainties from Lidar, QuickBird, and field measurements in California. *Remote Sensing of Environment*. 2010;114(7):1561-75.
- [54] Muukkonen P, Heiskanen J. Biomass estimation over a large area based on standwise forest inventory data and ASTER and MODIS satellite data: A possibility to verify carbon inventories. *Remote Sensing of Environment*. 2007;107(4):617-24.
- [55] Tomlinson CJ, Chapman L, Thornes JE, Baker C. Remote sensing land surface temperature for meteorology and climatology: A review. *Meteorological Applications*. 2011;18(3):296-306.
- [56] Zhang L, Shao Z, Liu J, Cheng Q. Deep learning based retrieval of forest aboveground biomass from combined LiDAR and landsat 8 data. *Remote Sensing*. 2019;11(12):1459.
- [57] Gleason CJ, Im J. A review of remote sensing of forest biomass and biofuel: options for small-area applications. *GIScience & Remote Sensing*. 2011;48(2):141-70.
- [58] Issa S, Dahy B, Ksiksi T, Saleous N. A review of terrestrial carbon assessment methods using geo-spatial technologies with emphasis on arid lands. *Remote Sensing*. 2020;12(12):2008.
- [59] Anderson JE, Plourde LC, Martin ME, Braswell BH, Smith M-L, Dubayah RO, et al. Integrating waveform lidar with hyperspectral imagery for inventory of a northern temperate forest. *Remote Sensing of Environment*. 2008;112(4):1856-70.
- [60] Gleason CJ, Im J. Forest biomass estimation from airborne LiDAR data using machine learning approaches. *Remote Sensing of Environment*. 2012;125:80-91.
- [61] Bourgoïn C, Blanc L, Bailly J-S, Cornu G, Berenguer E, Oszwald J, et al. The potential of multisource remote sensing for mapping the biomass of a degraded Amazonian forest. *Forests*. 2018;9(6):303.
- [62] Foody GM, Boyd DS, Cutler ME. Predictive relations of tropical forest biomass from Landsat TM data and their transferability between regions. *Remote sensing of environment*. 2003;85(4):463-74.
- [63] Astola H, Häme T, Sirro L, Molinier M, Kilpi J. Comparison of Sentinel-2 and Landsat 8 imagery for forest variable prediction in boreal region. *Remote Sensing of Environment*. 2019;223:257-73.
- [64] Zhang X, Friedl MA, Schaaf CB, Strahler AH, Hodges JC, Gao F, et al. Monitoring vegetation phenology using MODIS. *Remote sensing of environment*. 2003;84(3):471-5.
- [65] Soergel U. Review of radar remote sensing on urban areas. *Radar remote sensing of urban areas*: Springer; 2010. p. 1-47.

- [66] Sinha S, Jeganathan C, Sharma LK, Nathawat MS. A review of radar remote sensing for biomass estimation. *International Journal of Environmental Science and Technology*. 2015;12(5):1779-92.
- [67] Joyce KE, Belliss SE, Samsonov SV, McNeill SJ, Glassey PJ. A review of the status of satellite remote sensing and image processing techniques for mapping natural hazards and disasters. *Progress in physical geography*. 2009;33(2):183-207.
- [68] Rauste Y. Multi-temporal JERS SAR data in boreal forest biomass mapping. *Remote sensing of environment*. 2005;97(2):263-75.
- [69] Brown WM, Porcello LJ. An introduction to synthetic-aperture radar. *IEEE spectrum*. 1969;6(9):52-62.
- [70] Gallaun H, Zanchi G, Nabuurs G-J, Hengeveld G, Schardt M, Verkerk PJ. EU-wide maps of growing stock and above-ground biomass in forests based on remote sensing and field measurements. *Forest Ecology and Management*. 2010;260(3):252-61.
- [71] Soudani K, Le Maire G, Dufrêne E, François C, Delpierre N, Ulrich E, et al. Evaluation of the onset of green-up in temperate deciduous broadleaf forests derived from Moderate Resolution Imaging Spectroradiometer (MODIS) data. *Remote Sensing of Environment*. 2008;112(5):2643-55.
- [72] Wu C, Chen JM, Desai AR, Hollinger DY, Arain MA, Margolis HA, et al. Remote sensing of canopy light use efficiency in temperate and boreal forests of North America using MODIS imagery. *Remote Sensing of Environment*. 2012;118:60-72.
- [73] Cohen WB, Maersperger TK, Gower ST, Turner DP. An improved strategy for regression of biophysical variables and Landsat ETM+ data. *Remote Sensing of Environment*. 2003;84(4):561-71.
- [74] Dong T, Liu J, Qian B, He L, Liu J, Wang R, et al. Estimating crop biomass using leaf area index derived from Landsat 8 and Sentinel-2 data. *ISPRS Journal of Photogrammetry and Remote Sensing*. 2020;168:236-50.
- [75] Forkuor G, Dimobe K, Serme I, Tondoh JE. Landsat-8 vs. Sentinel-2: examining the added value of sentinel-2's red-edge bands to land-use and land-cover mapping in Burkina Faso. *GIScience & remote sensing*. 2018;55(3):331-54.
- [76] Frazier RJ, Coops NC, Wulder MA, Kennedy R. Characterization of aboveground biomass in an unmanaged boreal forest using Landsat temporal segmentation metrics. *ISPRS Journal of Photogrammetry and Remote Sensing*. 2014;92:137-46.
- [77] Gómez C, White JC, Wulder MA, Alejandro P. Historical forest biomass dynamics modelled with Landsat spectral trajectories. *ISPRS Journal of Photogrammetry and Remote Sensing*. 2014;93:14-28.

- [78] Gu C, Clevers JG, Liu X, Tian X, Li Z, Li Z. Predicting forest height using the GOST, Landsat 7 ETM+, and airborne LiDAR for sloping terrains in the Greater Khingan Mountains of China. *ISPRS Journal of Photogrammetry and Remote Sensing*. 2018;137:97-111.
- [79] Izadi S, Sohrabi H, Khaledi MJ. Estimation of coppice forest characteristics using spatial and non-spatial models and Landsat data. *Journal of Spatial Science*. 2022;67(1):143-56.
- [80] Tian X, Li Z, Su Z, Chen E, van der Tol C, Li X, et al. Estimating montane forest above-ground biomass in the upper reaches of the Heihe River Basin using Landsat-TM data. *International journal of remote sensing*. 2014;35(21):7339-62.
- [81] Wulder MA, White JC, Loveland TR, Woodcock CE, Belward AS, Cohen WB, et al. The global Landsat archive: Status, consolidation, and direction. *Remote Sensing of Environment*. 2016;185:271-83.
- [82] Zhu Z, Woodcock CE. Continuous change detection and classification of land cover using all available Landsat data. *Remote sensing of Environment*. 2014;144:152-71.
- [83] Hossain AA, Mathias C, Blanton R. Remote sensing of turbidity in the Tennessee River using Landsat 8 satellite. *Remote Sensing*. 2021;13(18):3785.
- [84] Baloloy AB, Blanco AC, Candido CG, Argamosa RJL, Dumalag JBLC, Dimapilis LLC, et al. Estimation of mangrove forest aboveground biomass using multispectral bands, vegetation indices and biophysical variables derived from optical satellite imagery: rapideye, planetscope and sentinel-2. *ISPRS Annals of Photogrammetry, Remote Sensing & Spatial Information Sciences*. 2018;4(3).
- [85] Evangelides C, Nobajas A. Red-Edge Normalised Difference Vegetation Index (NDVI705) from Sentinel-2 imagery to assess post-fire regeneration. *Remote Sensing Applications: Society and Environment*. 2020;17:100283.
- [86] Imran A, Khan K, Ali N, Ahmad N, Ali A, Shah K. Narrow band based and broadband derived vegetation indices using Sentinel-2 Imagery to estimate vegetation biomass. *Global Journal of Environmental Science and Management*. 2020;6(1):97-108.
- [87] Blaschke T. Object based image analysis for remote sensing. *ISPRS journal of photogrammetry and remote sensing*. 2010;65(1):2-16.
- [88] Ellis EA, Mathews AJ. Object-based delineation of urban tree canopy: Assessing change in Oklahoma City, 2006–2013. *Computers, Environment and Urban Systems*. 2019;73:85-94.
- [89] Walker JS, Briggs JM, editors. An object-oriented classification of an arid urban forest with true-color aerial photography. *Proceedings of the ISPRS Joint Conference*; 2005.
- [90] Maxwell AE, Strager MP, Warner TA, Ramezan CA, Morgan AN, Pauley CE. Large-area, high spatial resolution land cover mapping using random forests, GEOBIA, and

- NAIP orthophotography: Findings and recommendations. *Remote Sensing*. 2019;11(12):1409.
- [91] Dos Reis AA, Werner JP, Silva BC, Figueiredo GK, Antunes JF, Esquerdo JC, et al. Monitoring pasture aboveground biomass and canopy height in an integrated crop–livestock system using textural information from PlanetScope imagery. *Remote Sensing*. 2020;12(16):2534.
 - [92] Miller GJ, Morris JT, Wang C. Estimating aboveground biomass and its spatial distribution in coastal wetlands utilizing planet multispectral imagery. *Remote Sensing*. 2019;11(17):2020.
 - [93] Jog S, Dixit M, editors. Supervised classification of satellite images. 2016 Conference on Advances in Signal Processing (CASP); 2016: IEEE.
 - [94] Perumal K, Bhaskaran R. Supervised classification performance of multispectral images. arXiv preprint arXiv:10024046. 2010.
 - [95] Duda T, Canty M. Unsupervised classification of satellite imagery: choosing a good algorithm. *International Journal of Remote Sensing*. 2002;23(11):2193-212.
 - [96] Nijhawan R, Srivastava I, Shukla P, editors. Land cover classification using supervised and unsupervised learning techniques. 2017 international conference on computational intelligence in data science (ICCIDS); 2017: IEEE.
 - [97] Lemenkova P. ISO Cluster classifier by ArcGIS for unsupervised classification of the Landsat TM image of Reykjavík. *Bulletin of Natural Sciences Research*. 2021;11(1):29-37.
 - [98] Whiteside TG, Boggs GS, Maier SW. Comparing object-based and pixel-based classifications for mapping savannas. *International Journal of Applied Earth Observation and Geoinformation*. 2011;13(6):884-93.
 - [99] Pande-Chhetri R, Abd-Elrahman A, Liu T, Morton J, Wilhelm VL. Object-based classification of wetland vegetation using very high-resolution unmanned air system imagery. *European Journal of Remote Sensing*. 2017;50(1):564-76.
 - [100] Baatz M, Hoffmann C, Willhauck G. Progressing from object-based to object-oriented image analysis. *Object-Based Image Analysis*: Springer; 2008. p. 29-42.
 - [101] Dronovau I. The Potential of Remote Sensing to Improve Landscape Research and Monitoring at Under-Studied Spatial Scales. *Frameworks*. 2016.
 - [102] Bo S, Ding L, Li H, Di F, Zhu C. Mean shift-based clustering analysis of multispectral remote sensing imagery. *International Journal of Remote Sensing*. 2009;30(4):817-27.

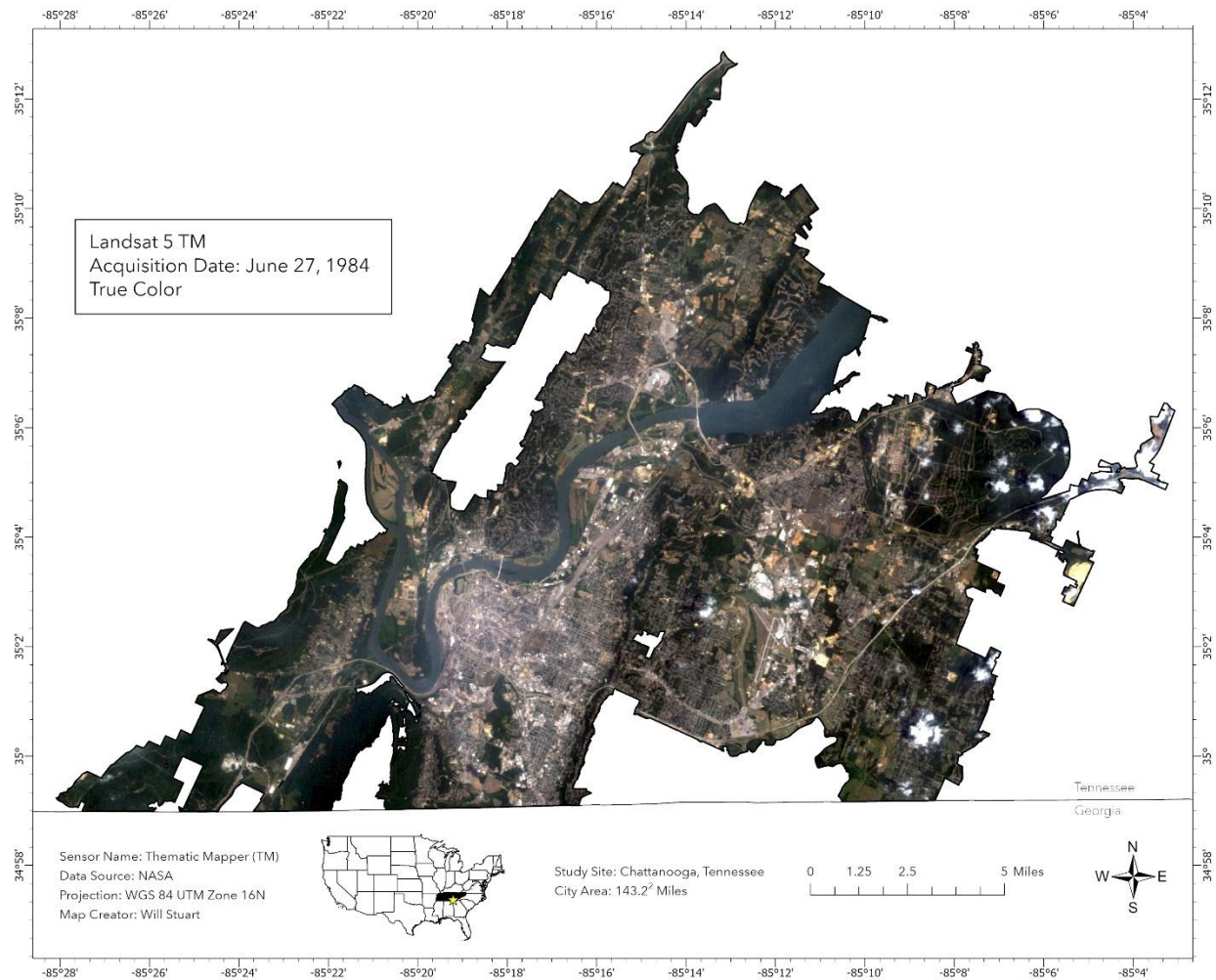
- [103] Michel J, Youssefi D, Grizonnet M. Stable mean-shift algorithm and its application to the segmentation of arbitrarily large remote sensing images. *IEEE Transactions on Geoscience and Remote Sensing*. 2014;53(2):952-64.
- [104] Wan F, Deng F, editors. Remote sensing image segmentation using mean shift method. *Advanced Research on Computer Education, Simulation and Modeling: International Conference, CESM 2011, Wuhan, China, June 18-19, 2011 Proceedings, Part II*; 2011: Springer.
- [105] Ma L, Li M, Ma X, Cheng L, Du P, Liu Y. A review of supervised object-based land-cover image classification. *ISPRS Journal of Photogrammetry and Remote Sensing*. 2017;130:277-93.
- [106] Huo L-Z, Boschetti L, Sparks AM. Object-based classification of forest disturbance types in the conterminous United States. *Remote Sensing*. 2019;11(5):477.
- [107] Thenkabail PS, Enclona EA, Ashton MS, Legg C, De Dieu MJ. Hyperion, IKONOS, ALI, and ETM+ sensors in the study of African rainforests. *Remote sensing of environment*. 2004;90(1):23-43.
- [108] Abdul-Hamid H, Mohamad-Ismail F-N, Mohamed J, Samdin Z, Abiri R, Tuan-Ibrahim T-M, et al. Allometric Equation for Aboveground Biomass Estimation of Mixed Mature Mangrove Forest. *Forests*. 2022;13(2):325.
- [109] Chave J, Andalo C, Brown S, Cairns MA, Chambers JQ, Eamus D, et al. Tree allometry and improved estimation of carbon stocks and balance in tropical forests. *Oecologia*. 2005;145(1):87-99.
- [110] Maulana SI, Wibisono Y, Utomo S. Development of local allometric equation to estimate total aboveground biomass in Papua tropical forest. *Indonesian Journal of Forestry Research*. 2016;3(2):107-18.
- [111] Picard N, Saint-André L, Henry M. Manual for building tree volume and biomass allometric equations: from field measurement to prediction. *Manual for building tree volume and biomass allometric equations: from field measurement to prediction*, FAO; Food and Agricultural Organization of the United Nations (2012). 2012.
- [112] Jenkins JC. Comprehensive database of diameter-based biomass regressions for North American tree species: United States Department of Agriculture, Forest Service, Northeastern ...; 2004.
- [113] McPherson EG, van Doorn NS, Peper PJ. Urban tree database and allometric equations. *Gen Tech Rep PSW-GTR-253* Albany, CA: US Department of Agriculture, Forest Service, Pacific Southwest Research Station 86 p. 2016;253.
- [114] Horler D, DOCKRAY M, Barber J. The red edge of plant leaf reflectance. *International journal of remote sensing*. 1983;4(2):273-88.

- [115] Rouse Jr J, Haas RH, Deering D, Schell J, Harlan JC. Monitoring the vernal advancement and retrogradation (green wave effect) of natural vegetation. 1974.
- [116] Gitelson AA, Kaufman YJ, Merzlyak MN. Use of a green channel in remote sensing of global vegetation from EOS-MODIS. *Remote sensing of Environment*. 1996;58(3):289-98.
- [117] Weier J, Herring D. Measuring Vegetation (NDVI/EVI) <http://earthobservatory.nasa.gov/Library/MeasuringVegetation>. Internet; 2007.
- [118] Feyisa K, Beyene S, Megersa B, Said MY, Angassa A. Allometric equations for predicting above-ground biomass of selected woody species to estimate carbon in East African rangelands. *Agroforestry Systems*. 2018;92(3):599-621.
- [119] Guerra-Hernández J, González-Ferreiro E, Monleón VJ, Faias SP, Tomé M, Díaz-Varela RA. Use of multi-temporal UAV-derived imagery for estimating individual tree growth in *Pinus pinea* stands. *Forests*. 2017;8(8):300.
- [120] Kamoske AG, Dahlin KM, Stark SC, Serbin SP. Leaf area density from airborne LiDAR: Comparing sensors and resolutions in a temperate broadleaf forest ecosystem. *Forest Ecology and Management*. 2019;433:364-75.
- [121] Slik J, Aiba SI, Brearley FQ, Cannon CH, Forshed O, Kitayama K, et al. Environmental correlates of tree biomass, basal area, wood specific gravity and stem density gradients in Borneo's tropical forests. *Global Ecology and Biogeography*. 2010;19(1):50-60.
- [122] G. Poley L, J. McDermid G. A systematic review of the factors influencing the estimation of vegetation aboveground biomass using unmanned aerial systems. *Remote Sensing*. 2020;12(7):1052.
- [123] Pham TD, Yokoya N, Xia J, Ha NT, Le NN, Nguyen TTT, et al. Comparison of machine learning methods for estimating mangrove above-ground biomass using multiple source remote sensing data in the red river delta biosphere reserve, Vietnam. *Remote Sensing*. 2020;12(8):1334.
- [124] Hall J. Mapping urban growth and investigating its potential impact on surface water quality in Chattanooga, Tennessee using GIS and remote sensing. 2019.
- [125] Hossain AA, Stuart W, Mies J, Brock-Hon A. Investigating Urban Heat Island Impact for the City of Chattanooga, Tennessee, Using GIS and Remote Sensing. *Journal: Handbook of Climate Change Mitigation and Adaptation*. 2021:1-35.
- [126] USGS. 3D Elevation Program 1-Meter Resolution Digital Elevation Model. 2020.
- [127] Bannari A, Morin D, Bonn F, Huete A. A review of vegetation indices. *Remote sensing reviews*. 1995;13(1-2):95-120.

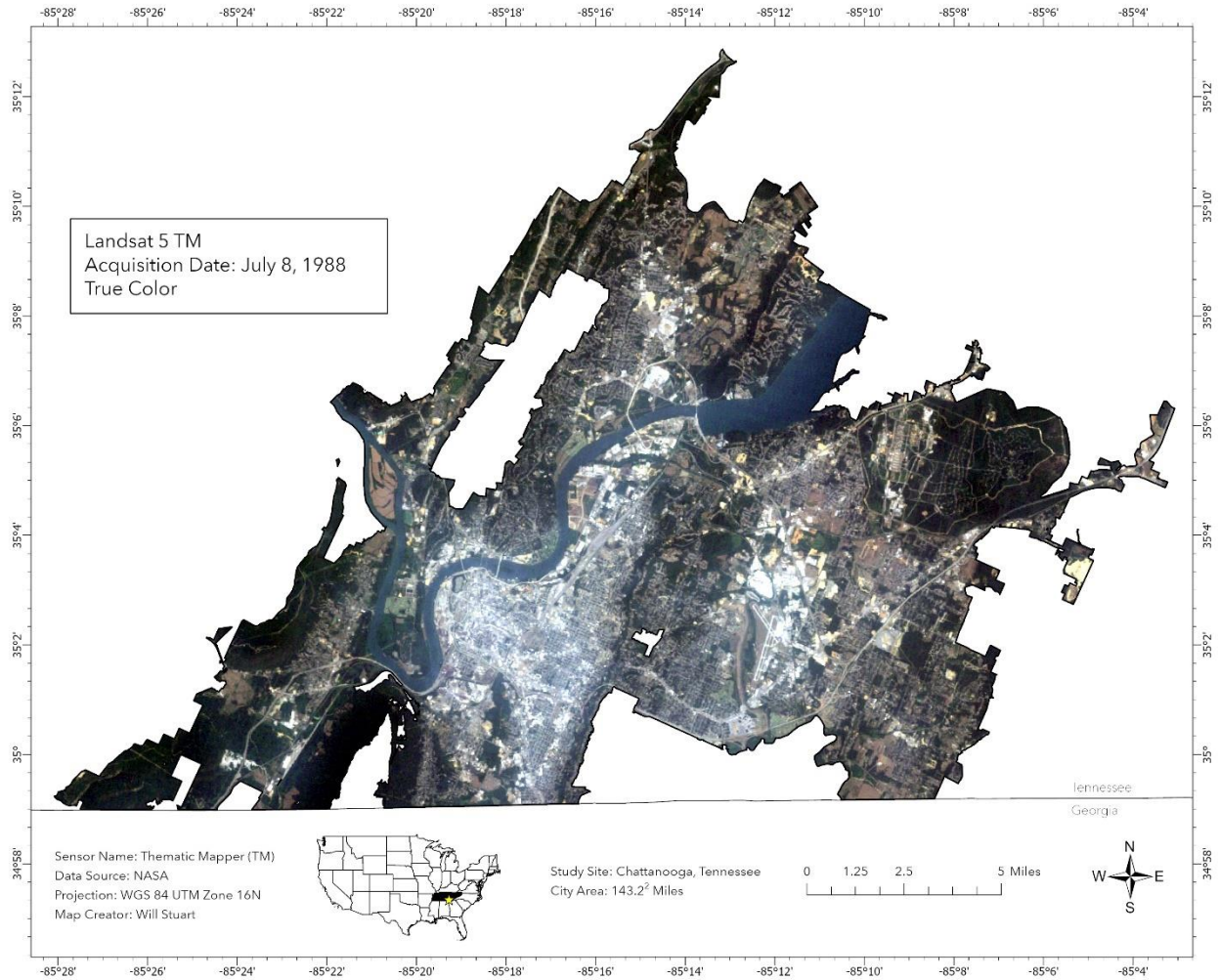
- [128] Huete A, Justice C, van Leeuwen W. MODIS vegetation index (MOD 13) algorithm theoretical basis document version 3. University of arizona. 1999;1200.
- [129] Huete AR. A soil-adjusted vegetation index (SAVI). Remote sensing of environment. 1988;25(3):295-309.
- [130] Lu L, Kuenzer C, Wang C, Guo H, Li Q. Evaluation of three MODIS-derived vegetation index time series for dryland vegetation dynamics monitoring. Remote Sensing. 2015;7(6):7597-614.
- [131] Shen G, Wang Z, Liu C, Han Y. Mapping aboveground biomass and carbon in Shanghai's urban forest using Landsat ETM+ and inventory data. Urban Forestry & Urban Greening. 2020;51:126655.
- [132] Terakunpisut J, Gajasen N, Ruankawe N. Carbon sequestration potential in aboveground biomass of Thong Pha Phum national forest, Thailand. Applied ecology and environmental research. 2007;5(2):93-102.
- [133] Tolunay D. Carbon concentrations of tree components, forest floor and understorey in young *Pinus sylvestris* stands in north-western Turkey. Scandinavian Journal of Forest Research. 2009;24(5):394-402.
- [134] Jenkins JC, Chojnacky DC, Heath LS, Birdsey RA. National-scale biomass estimators for United States tree species. Forest science. 2003;49(1):12-35.
- [135] Sedgwick P. Pearson's correlation coefficient. Bmj. 2012;345.
- [136] ESRI. Environmental Science Research Institute. ArcGIS Pro: Version 30. 2022.
- [137] Petit C, Lambin EF. Integration of multi-source remote sensing data for land cover change detection. International journal of geographical information science. 2001;15(8):785-803.
- [138] Chen B, Huang B, Xu B. Multi-source remotely sensed data fusion for improving land cover classification. ISPRS Journal of Photogrammetry and Remote Sensing. 2017;124:27-39.
- [139] Zhang J. Multi-source remote sensing data fusion: status and trends. International Journal of Image and Data Fusion. 2010;1(1):5-24.
- [140] Ghassemian H. A review of remote sensing image fusion methods. Information Fusion. 2016;32:75-89.
- [141] Shao Z, Cai J, Fu P, Hu L, Liu T. Deep learning-based fusion of Landsat-8 and Sentinel-2 images for a harmonized surface reflectance product. Remote Sensing of Environment. 2019;235:111425.

- [142] Page BP, Olmanson LG, Mishra DR. A harmonized image processing workflow using Sentinel-2/MSI and Landsat-8/OLI for mapping water clarity in optically variable lake systems. *Remote Sensing of Environment*. 2019;231:111284.
- [143] Lisiewicz M, Kamińska A, Stereńczak K. Recognition of specified errors of Individual Tree Detection methods based on Canopy Height Model. *Remote Sensing Applications: Society and Environment*. 2022;25:100690.

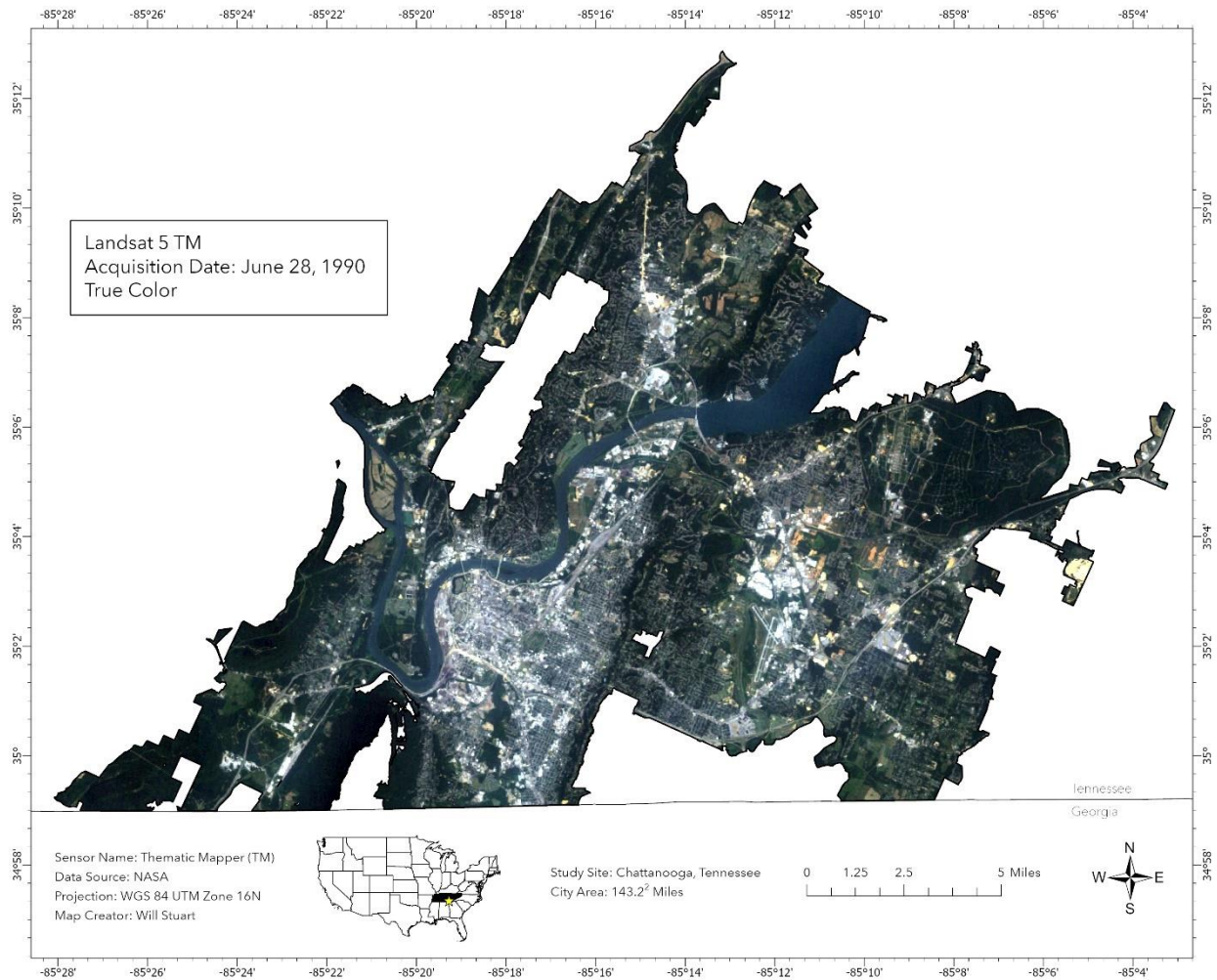
APPENDIX A
APPLICATION OF LANDSAT IMAGERY



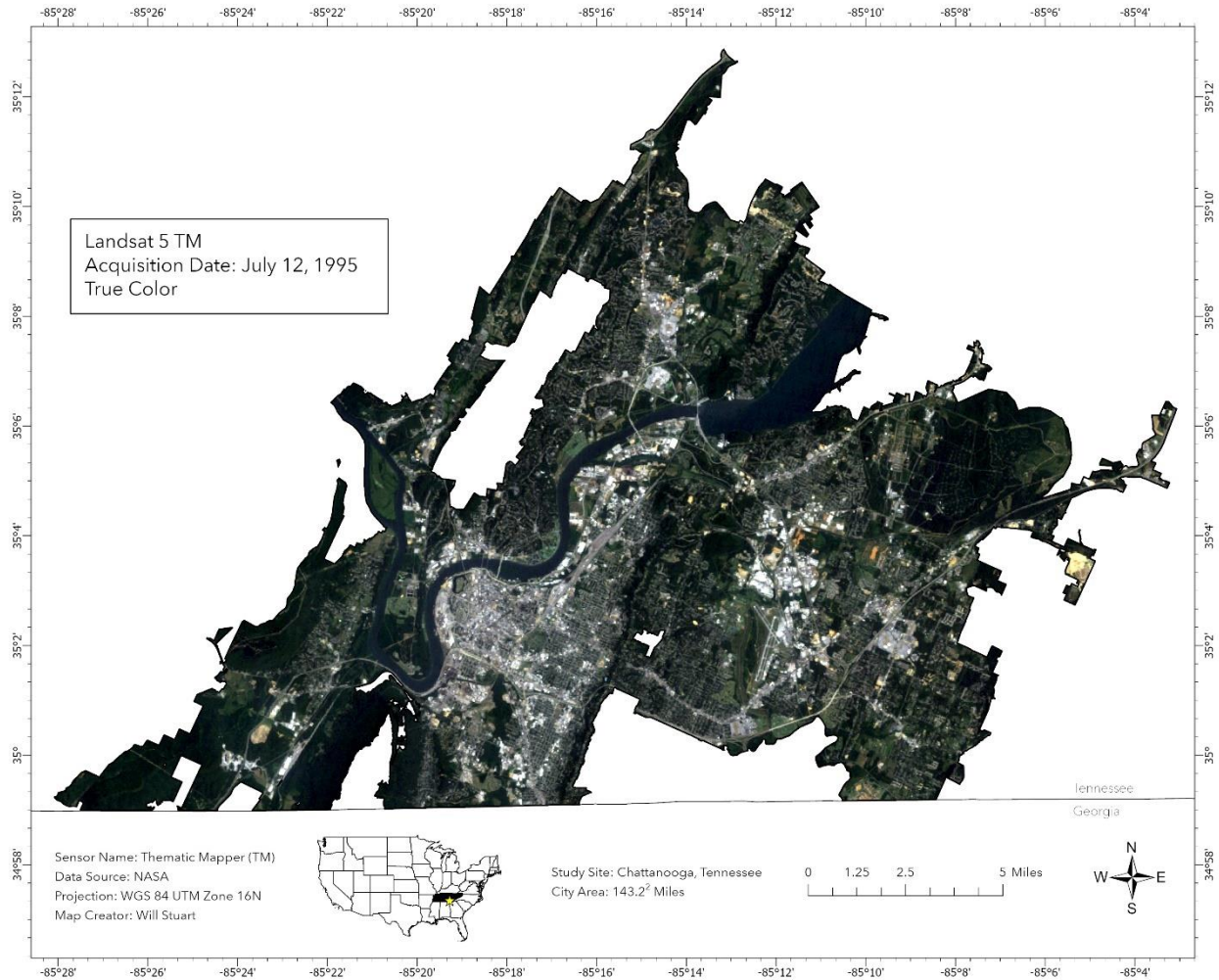
A1 True color Landsat 5 TM image captured June 27, 1984 across Chattanooga, TN.



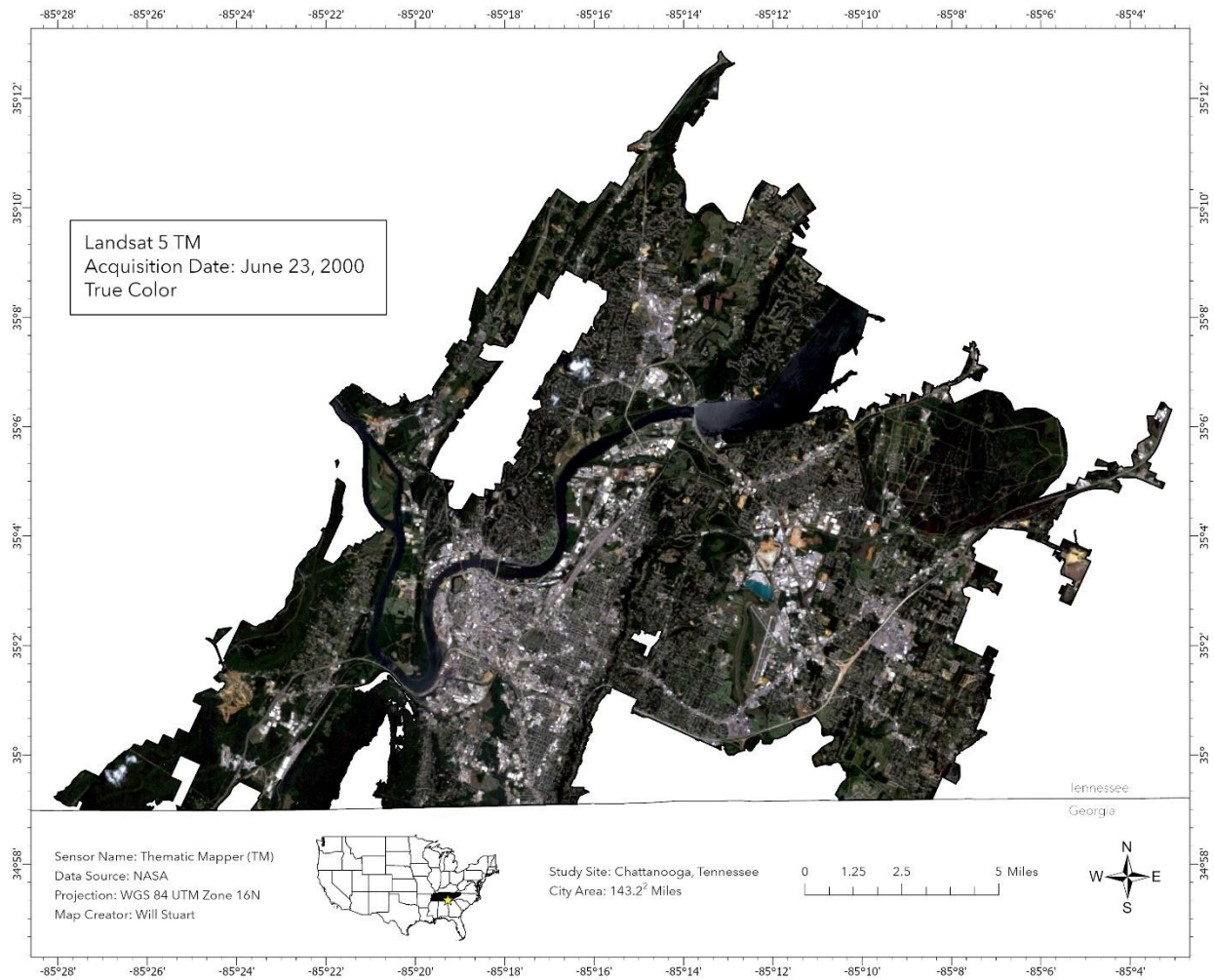
A2 True color Landsat 5 TM image captured July 8, 1984 across Chattanooga, TN.



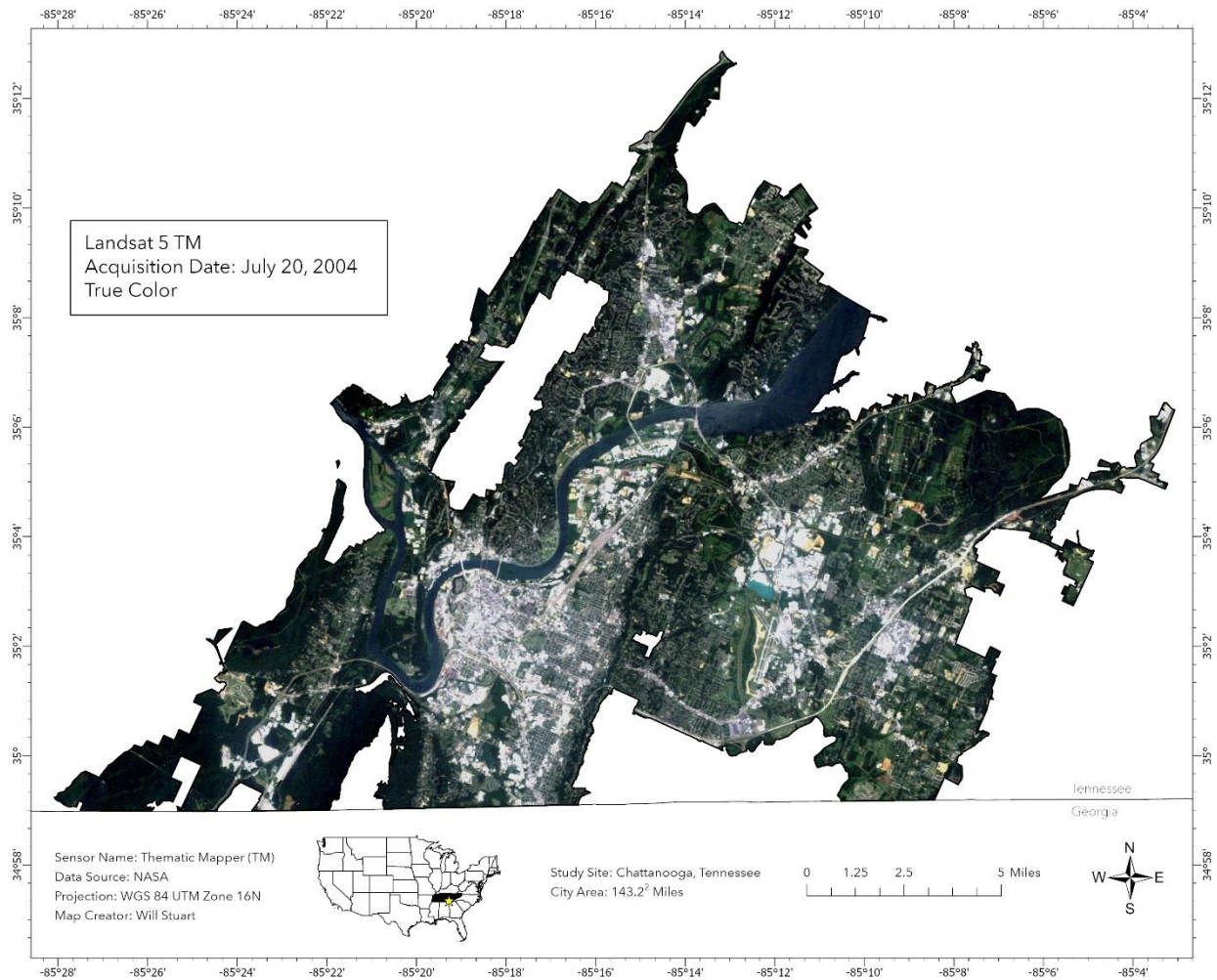
A3 True color Landsat 5 TM image captured June 28, 1990 across Chattanooga, TN.



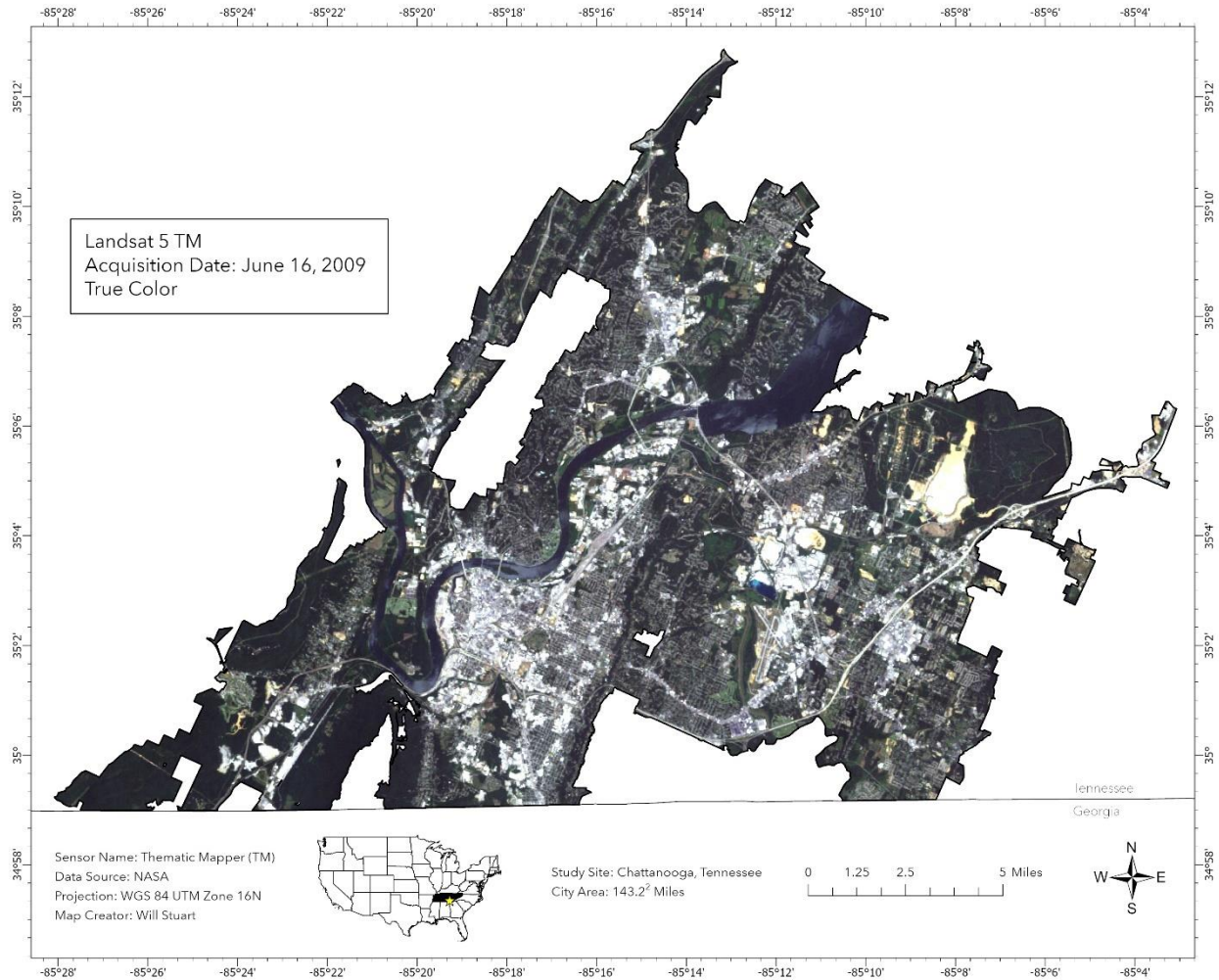
A4 True color Landsat 5 TM image captured July 12, 1995 across Chattanooga, TN.



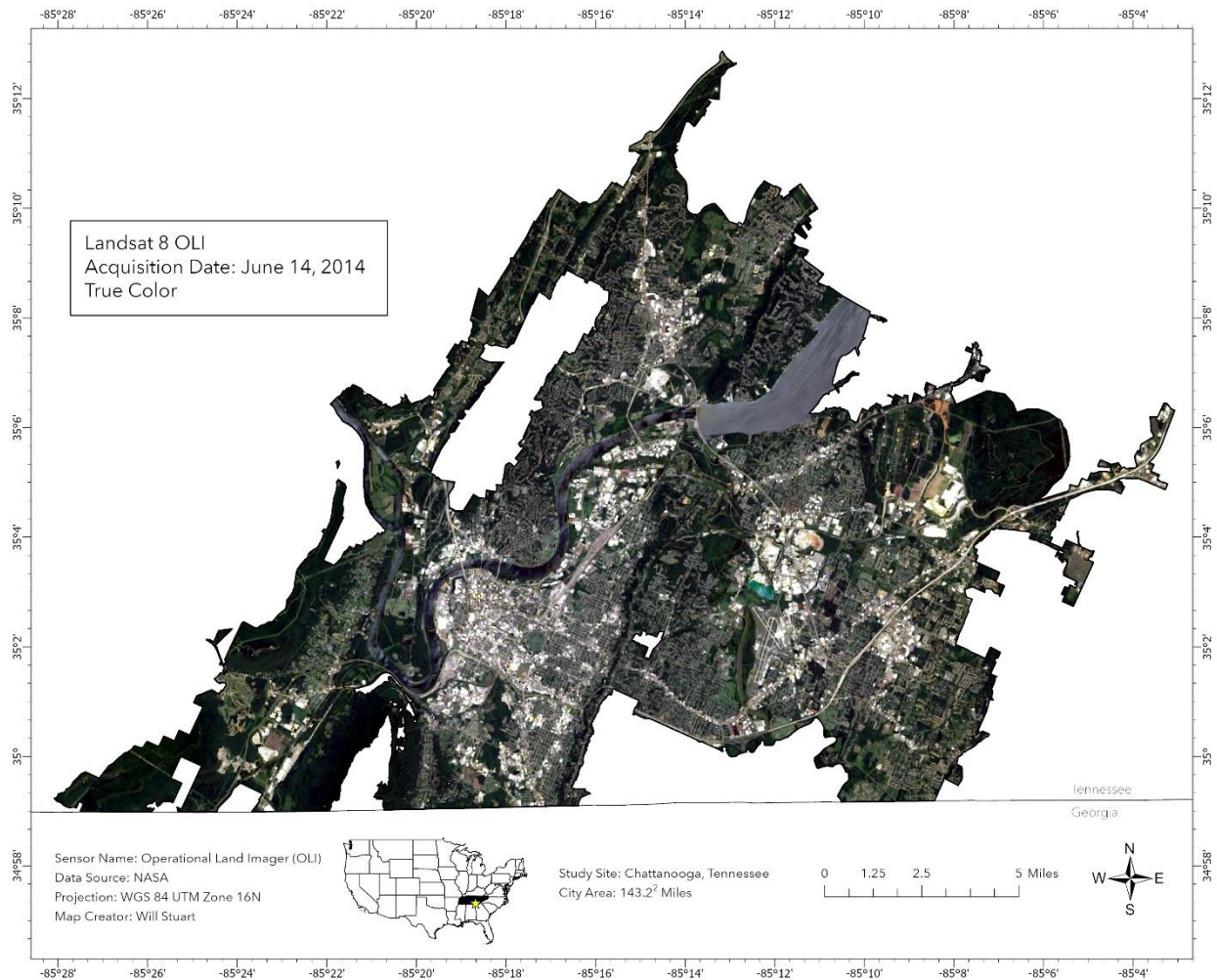
A5 True color Landsat 5 TM image captured June 23, 2000 across Chattanooga, TN.



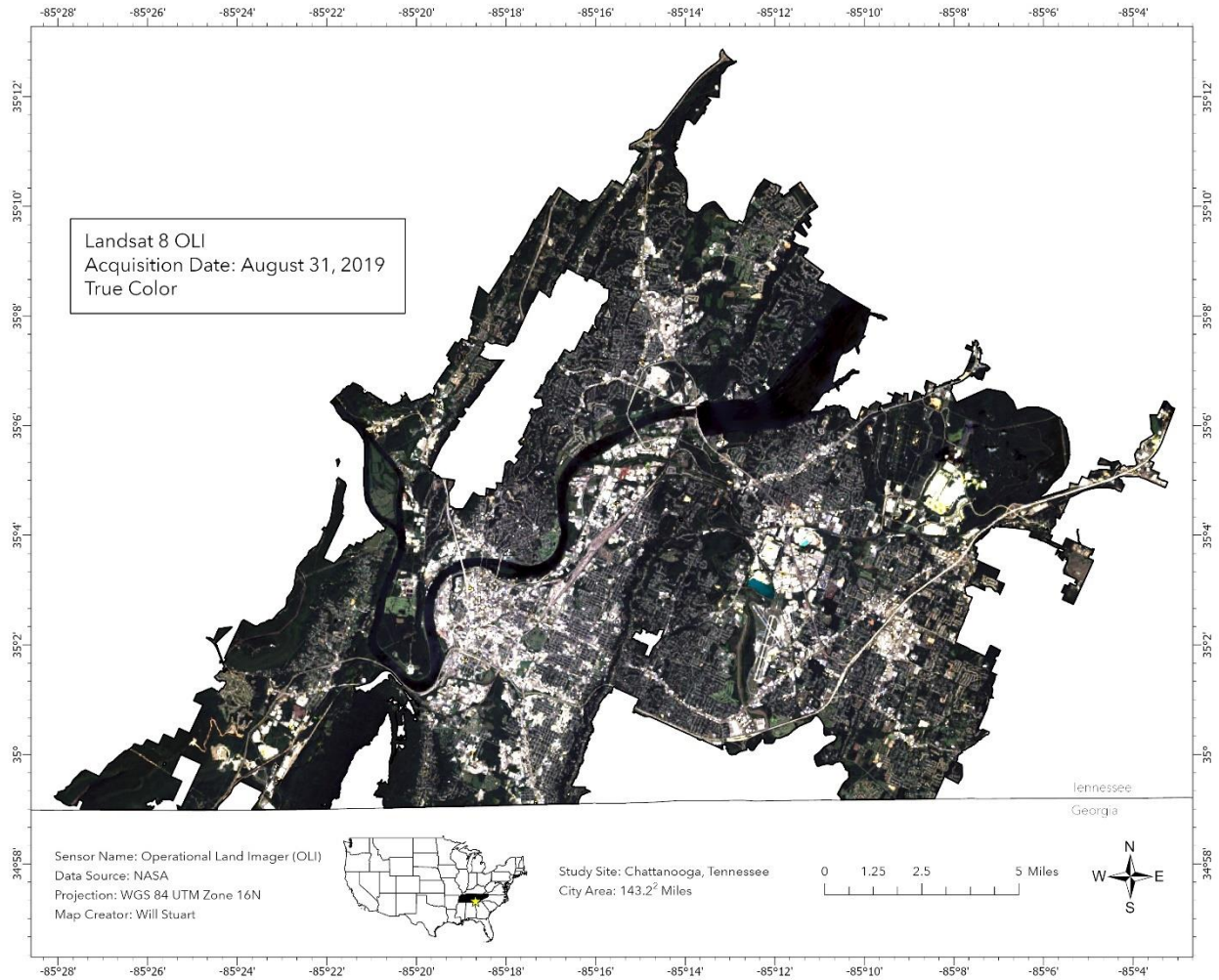
A6 True color Landsat 5 TM image captured July 20, 2004 across Chattanooga, TN.



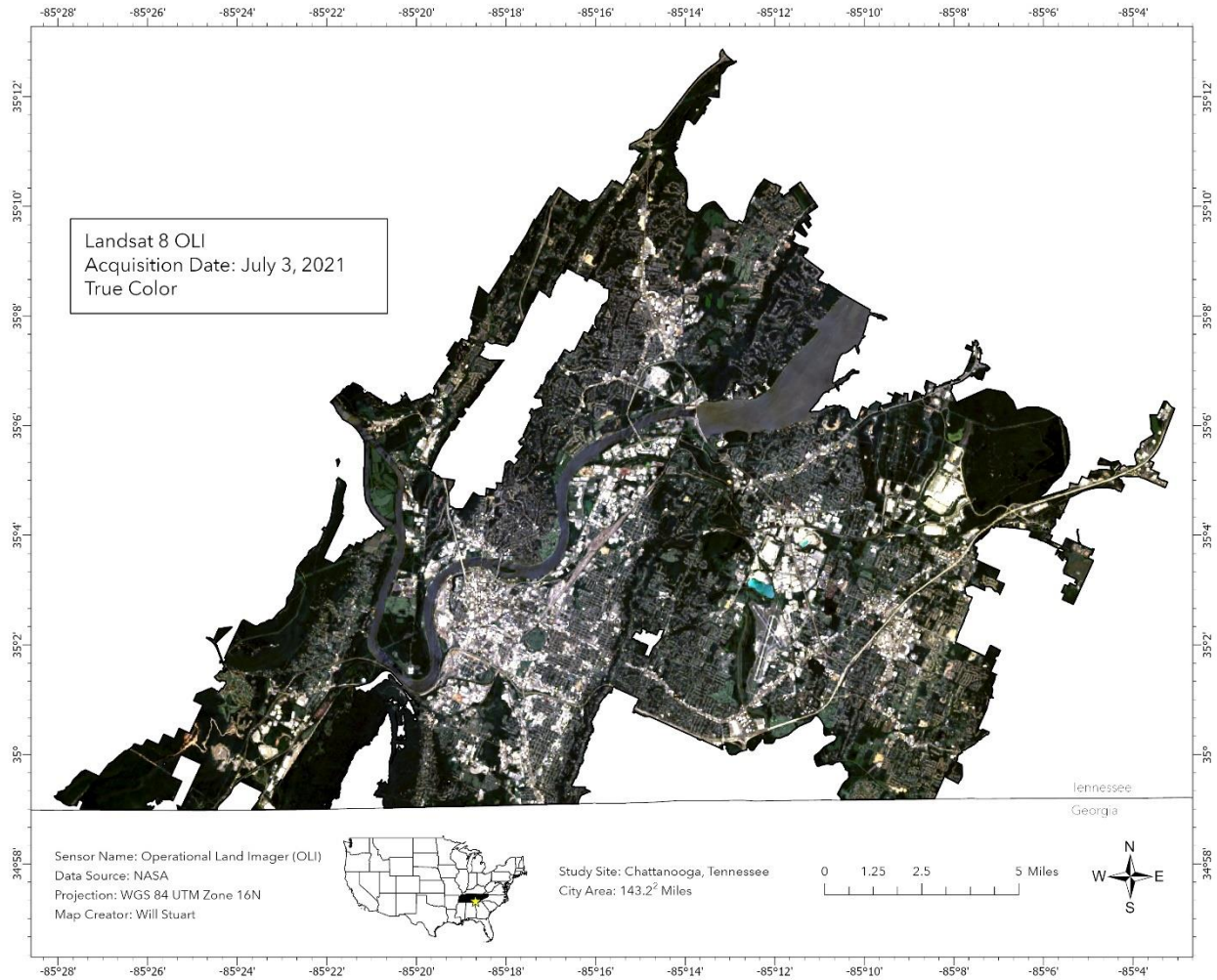
A7 True color Landsat 5 TM image captured June 16, 2009 across Chattanooga, TN.



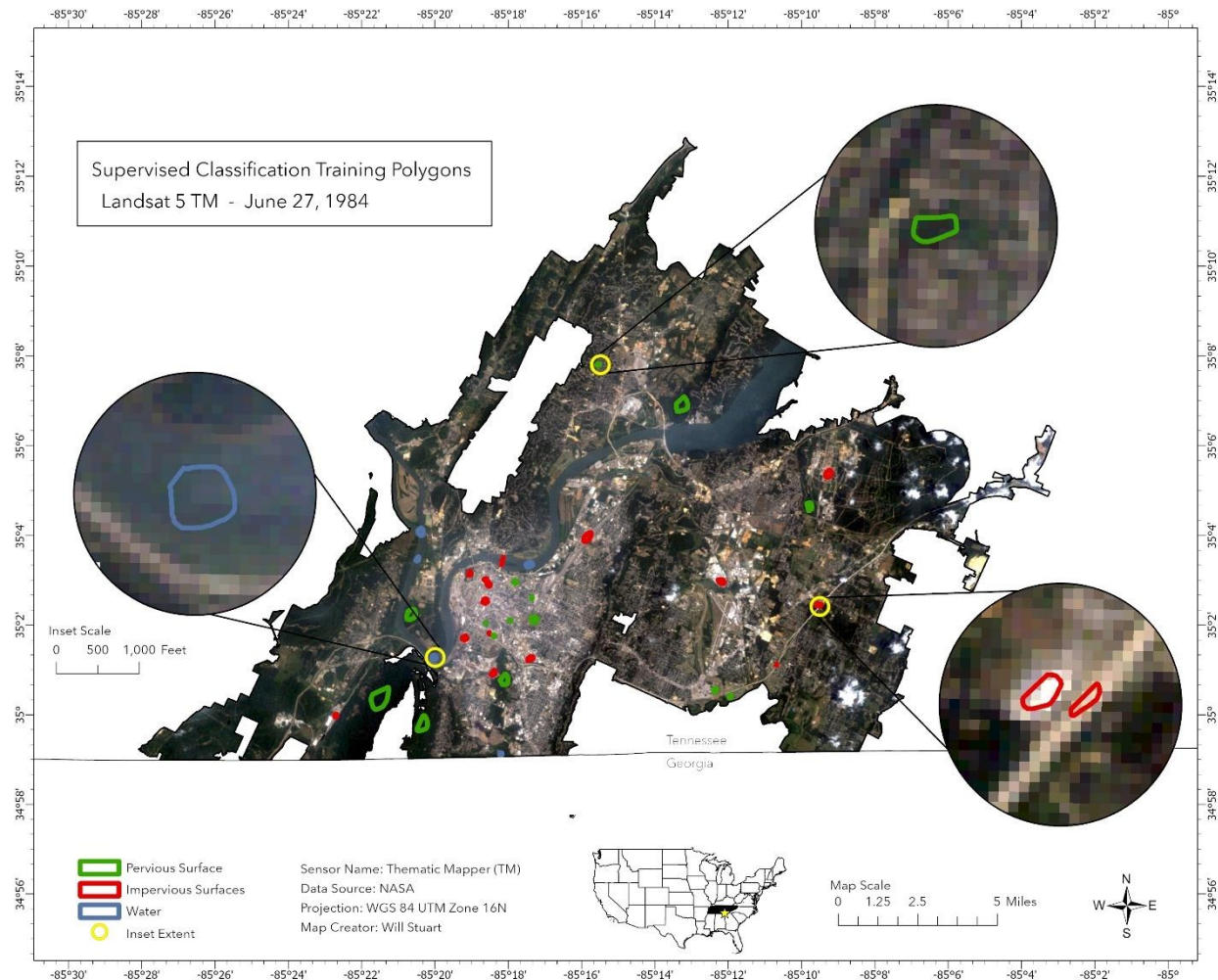
A8 True color Landsat 8 OLI image captured June 14, 2014 across Chattanooga, TN.



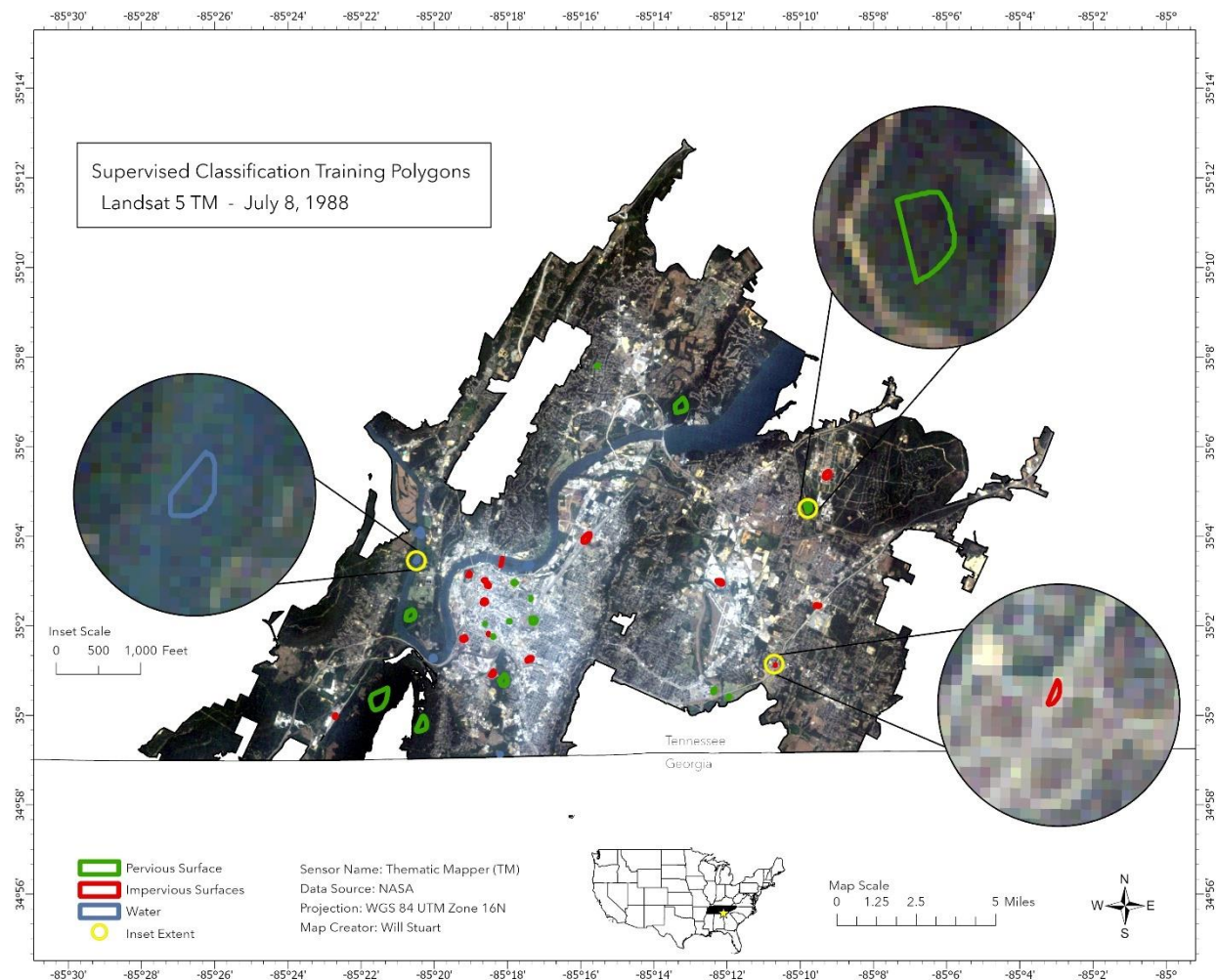
A9 True color Landsat 8 OLI image captured August 31, 2019 across Chattanooga, TN.



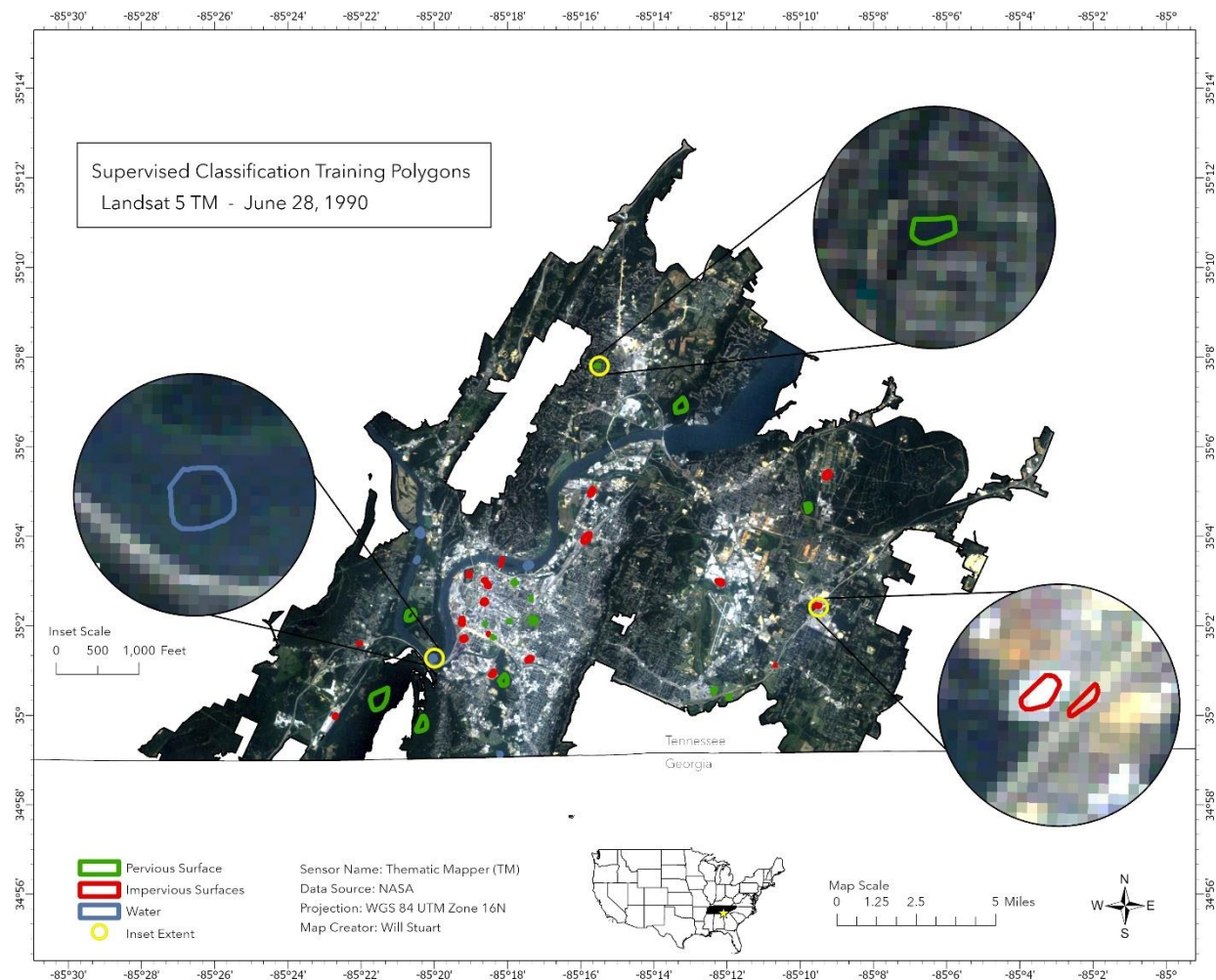
A10 True color Landsat 8 OLI image captured July 3, 2021 across Chattanooga, TN.



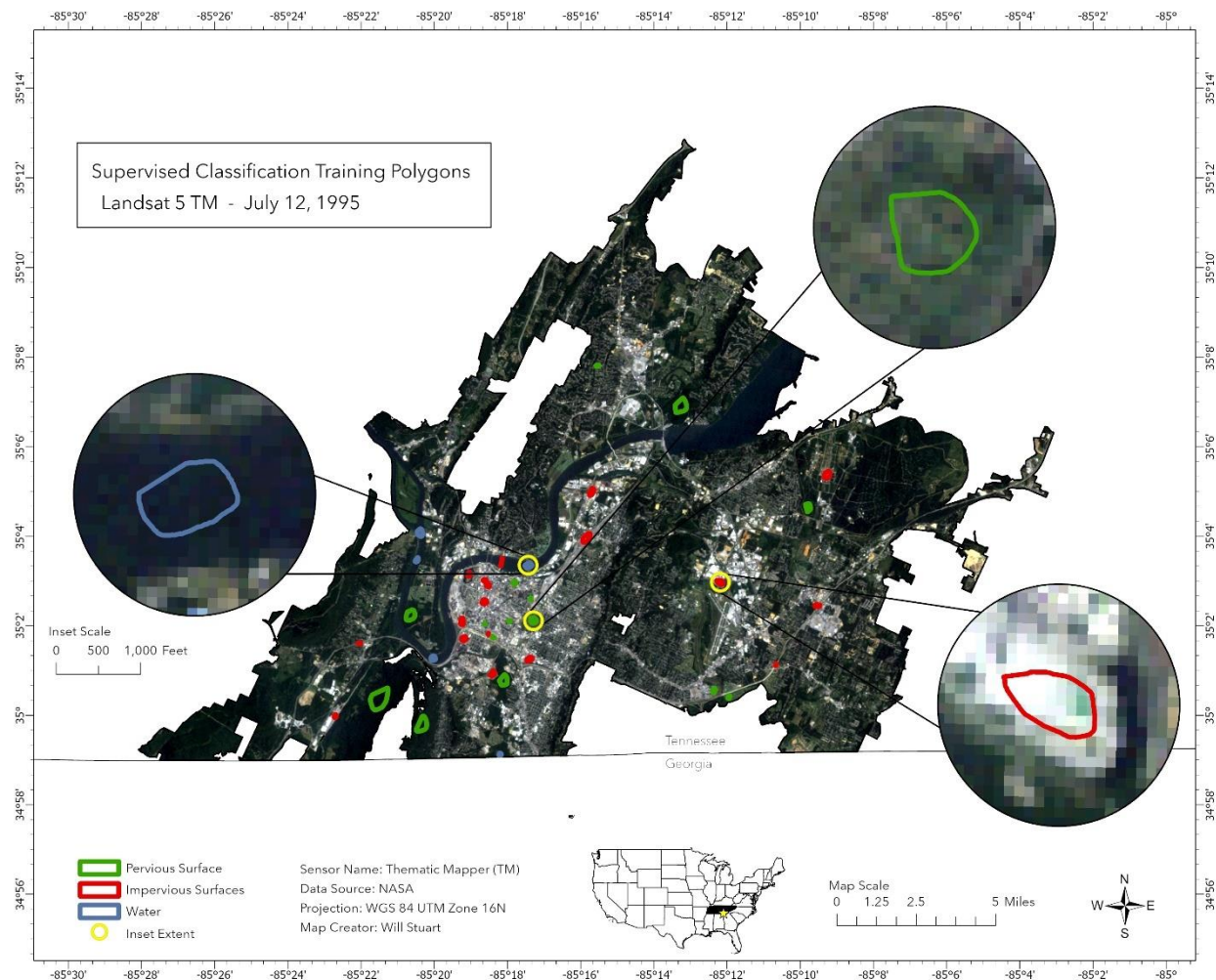
A11 Distribution of training polygons for supervised classification over true color Landsat 5 TM image captured June 27, 1984 across Chattanooga, TN.



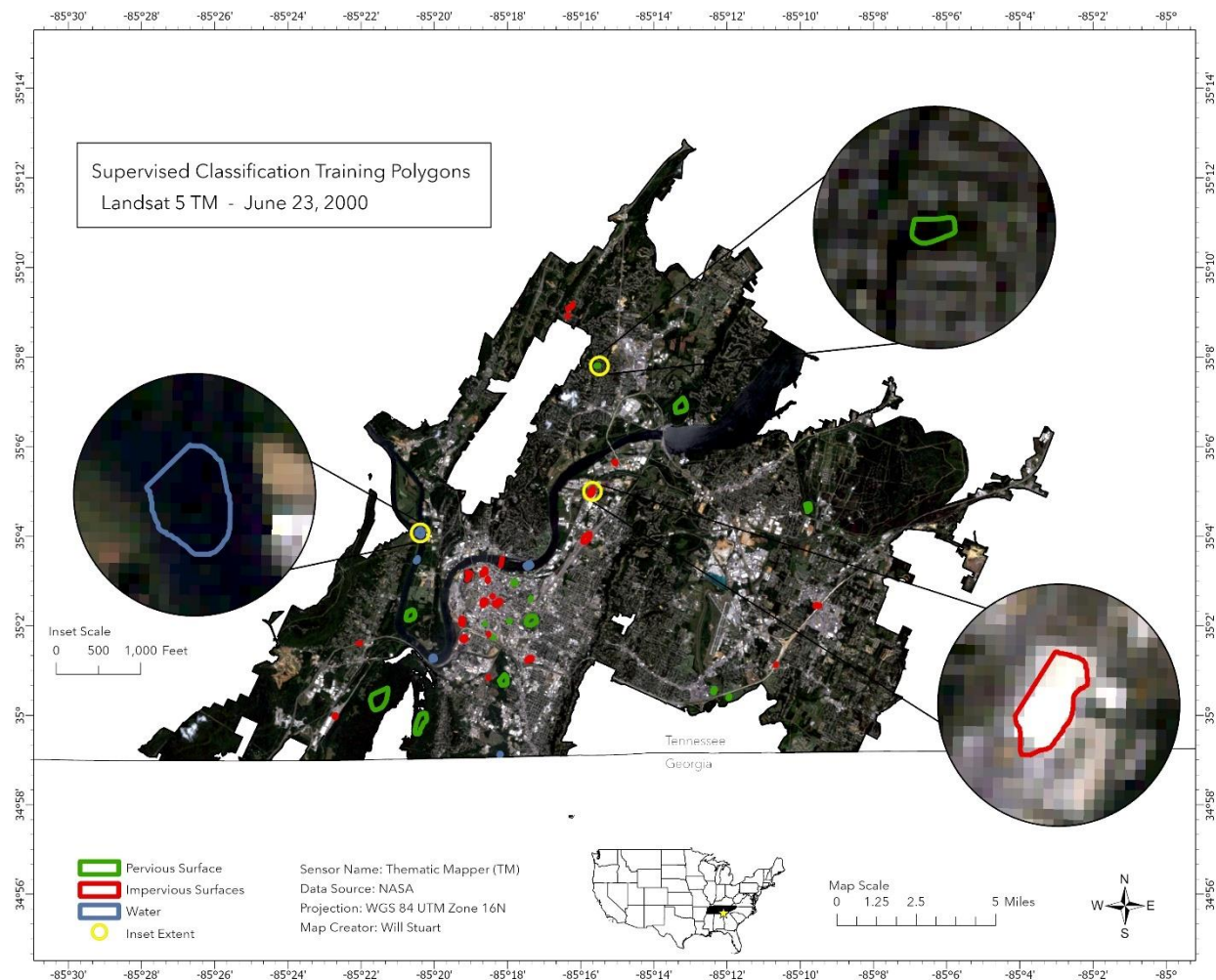
A12 Distribution of training polygons for supervised classification over true color Landsat 5 TM image captured July 8, 1984 across Chattanooga, TN.



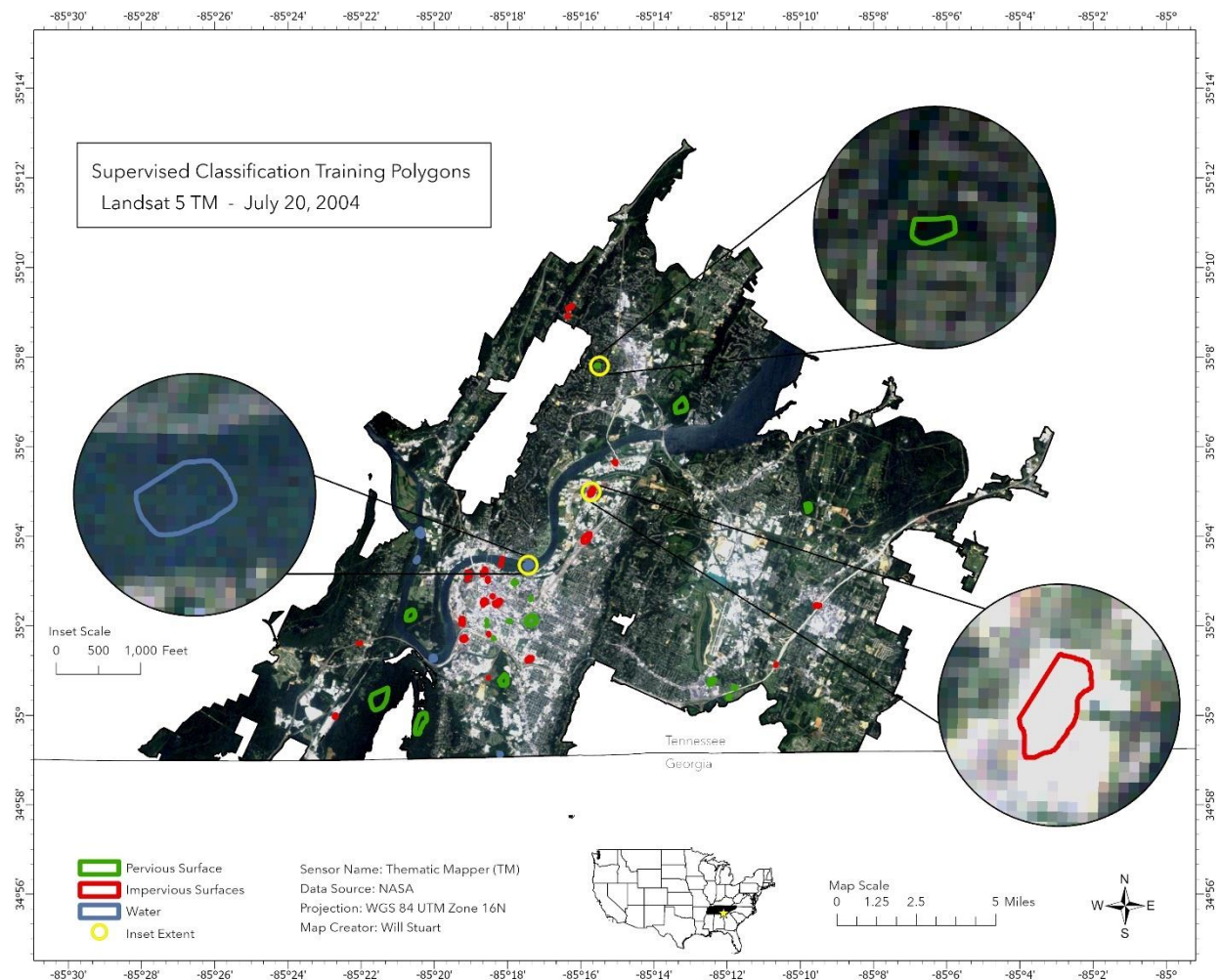
A13 Distribution of training polygons for supervised classification over true color Landsat 5 TM image captured June 28, 1990 across Chattanooga, TN.



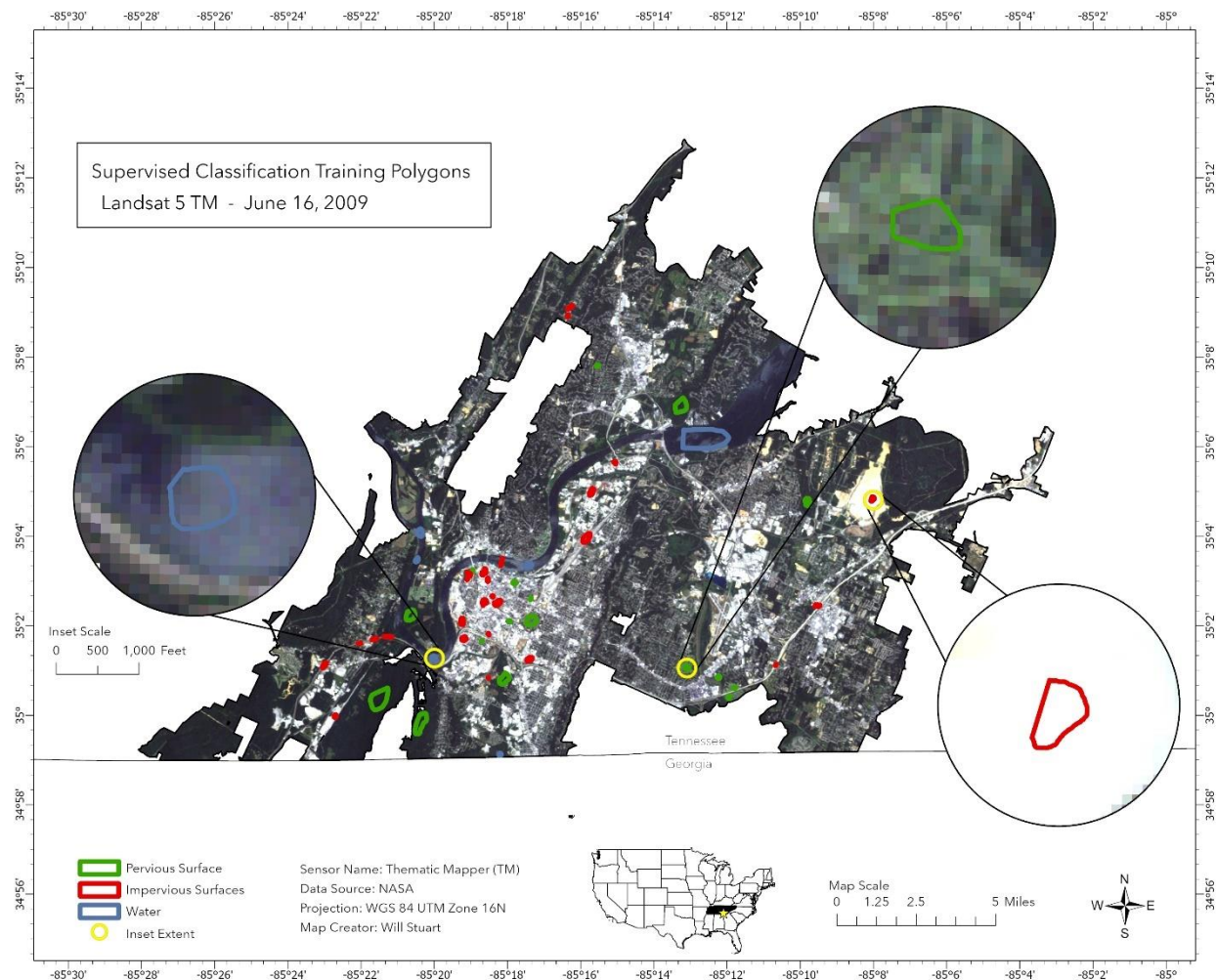
A14 Distribution of training polygons for supervised classification over true color Landsat 5 TM image captured July 12, 1995 across Chattanooga, TN.



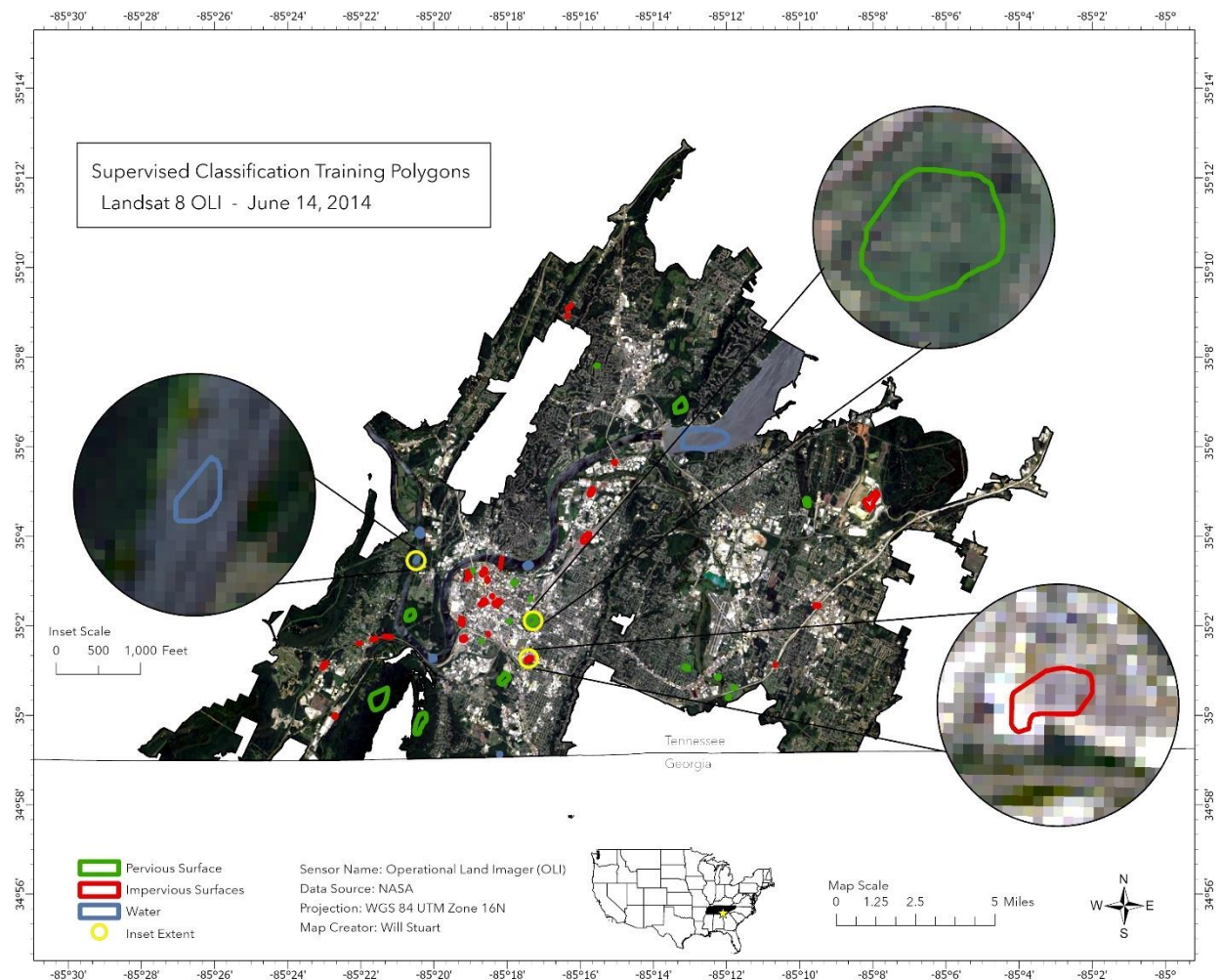
A15 Distribution of training polygons for supervised classification over true color Landsat 5 TM image captured June 23, 2000 across Chattanooga, TN



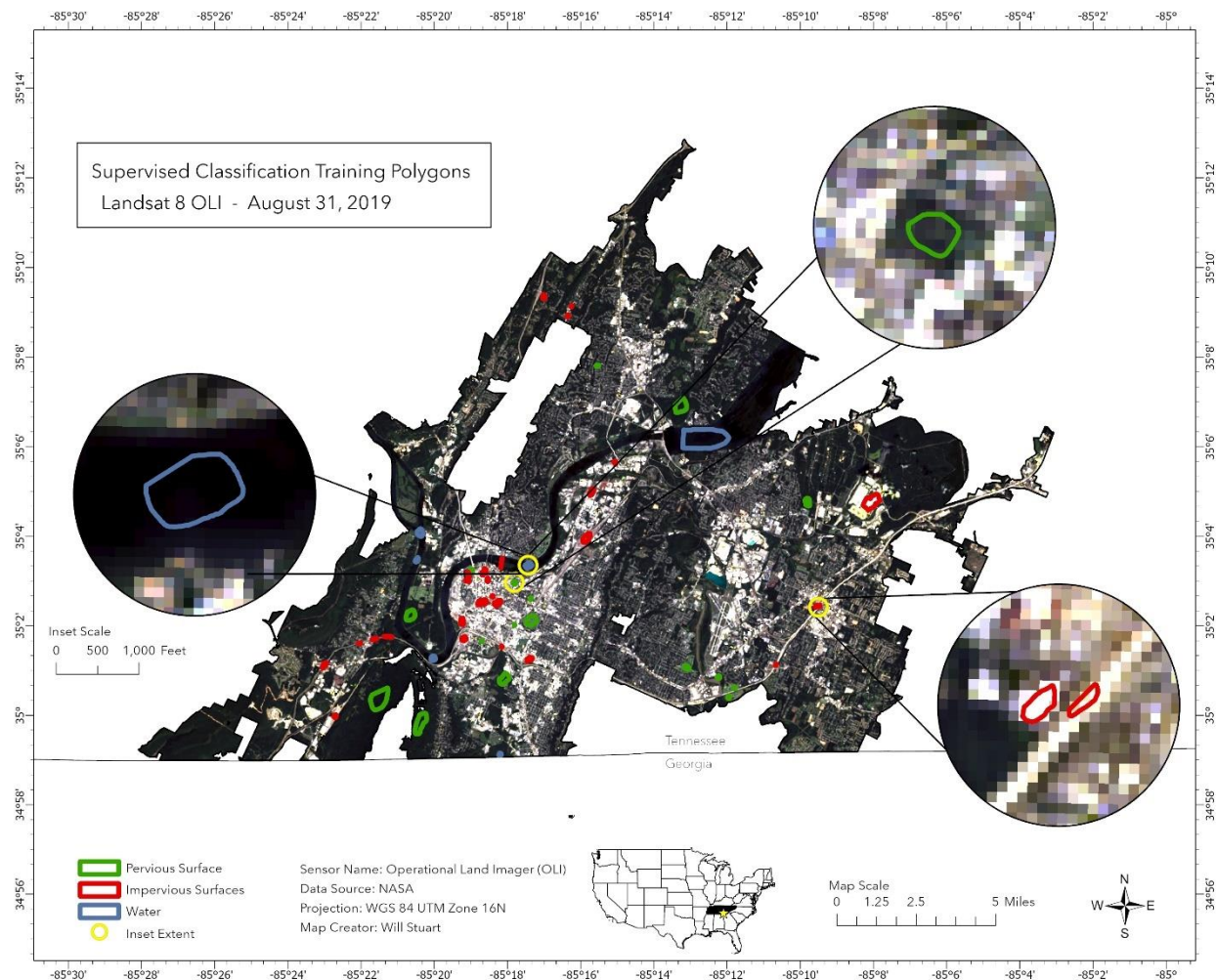
A16 Distribution of training polygons for supervised classification over true color Landsat 5 TM image captured July 20, 2004 across Chattanooga, TN.



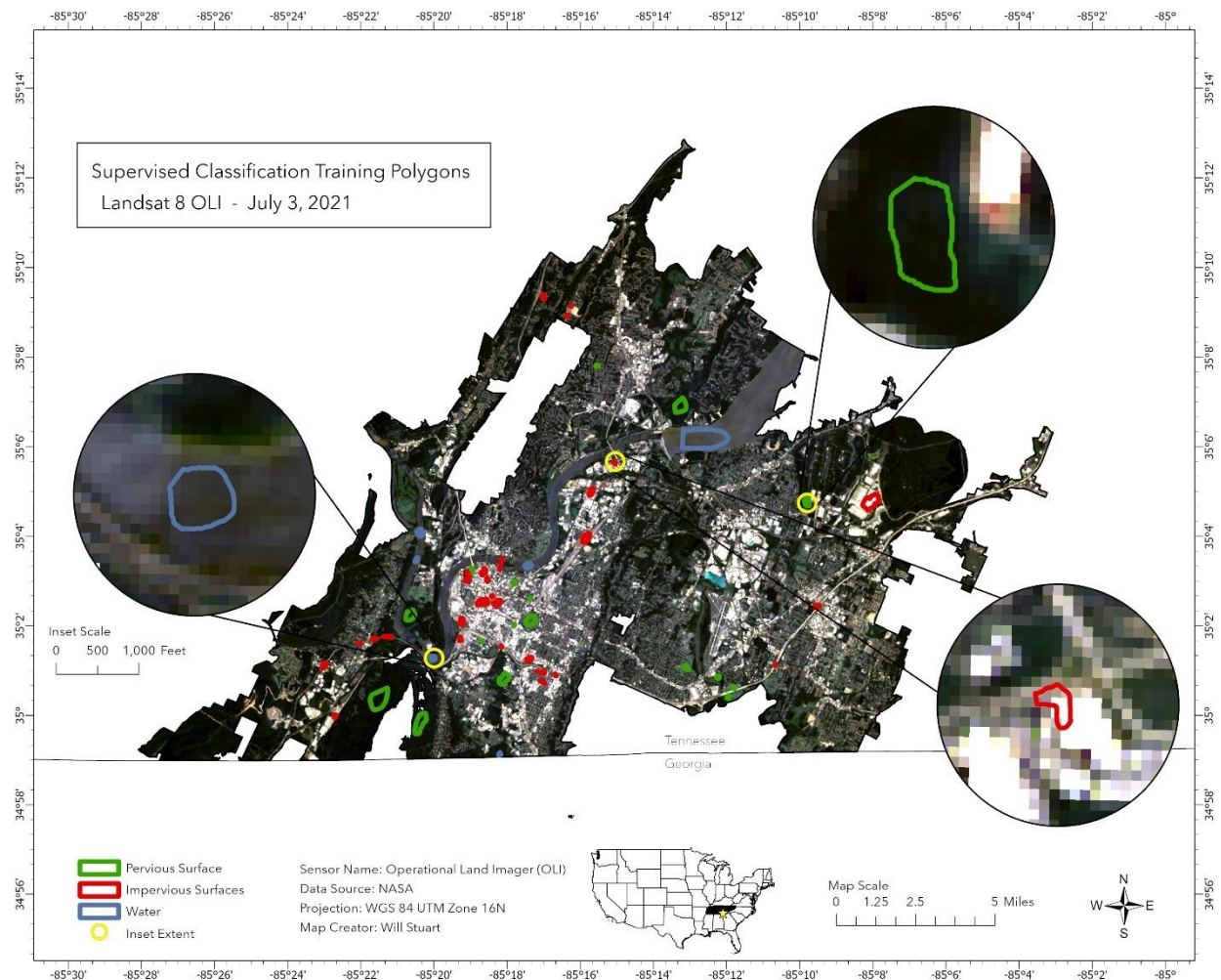
A17 Distribution of training polygons for supervised classification over true color Landsat 5 TM image captured June 16, 2009 across Chattanooga, TN.



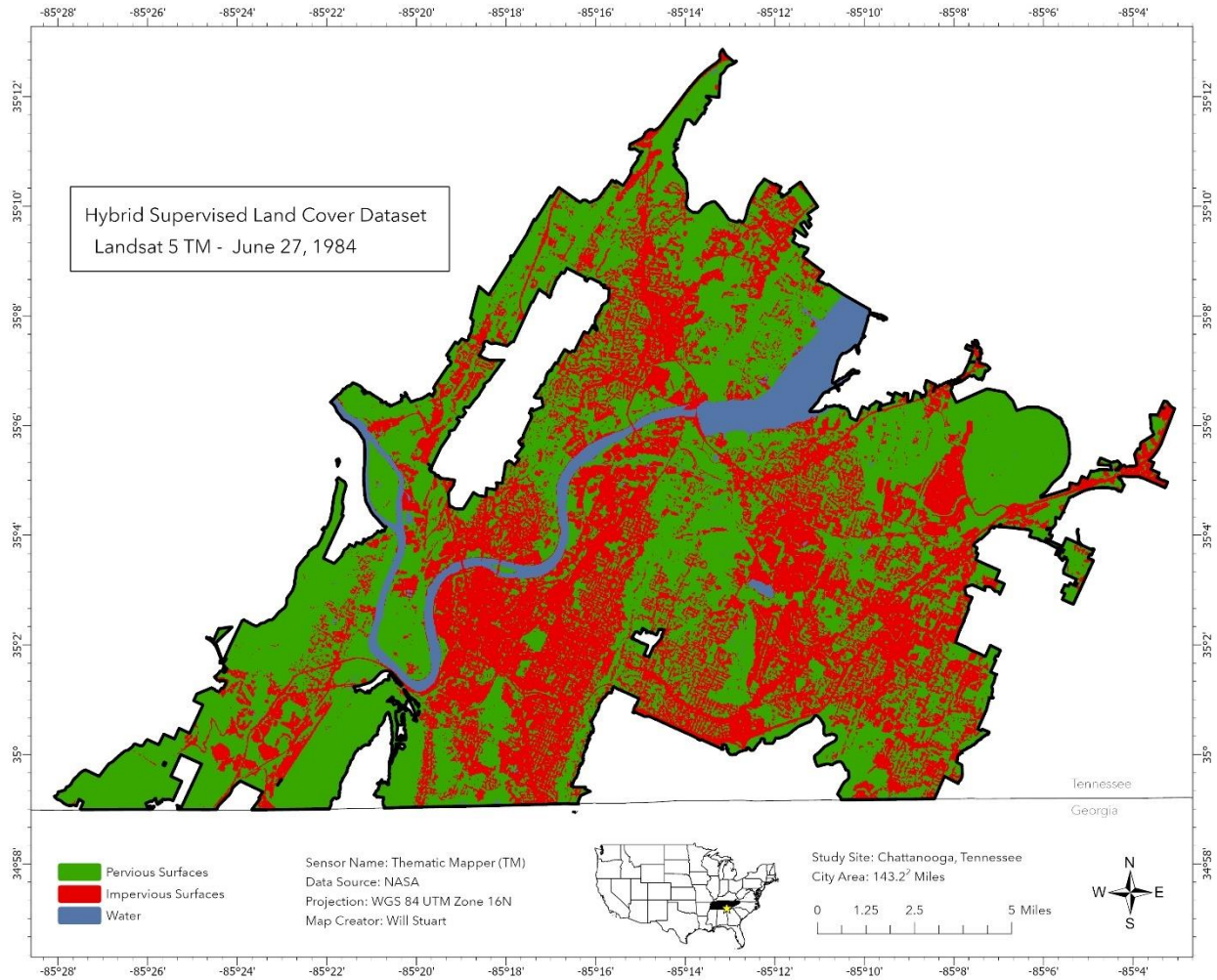
A18 Distribution of training polygons for supervised classification over true color Landsat 8 OLI image captured June 14, 2014 across Chattanooga, TN.



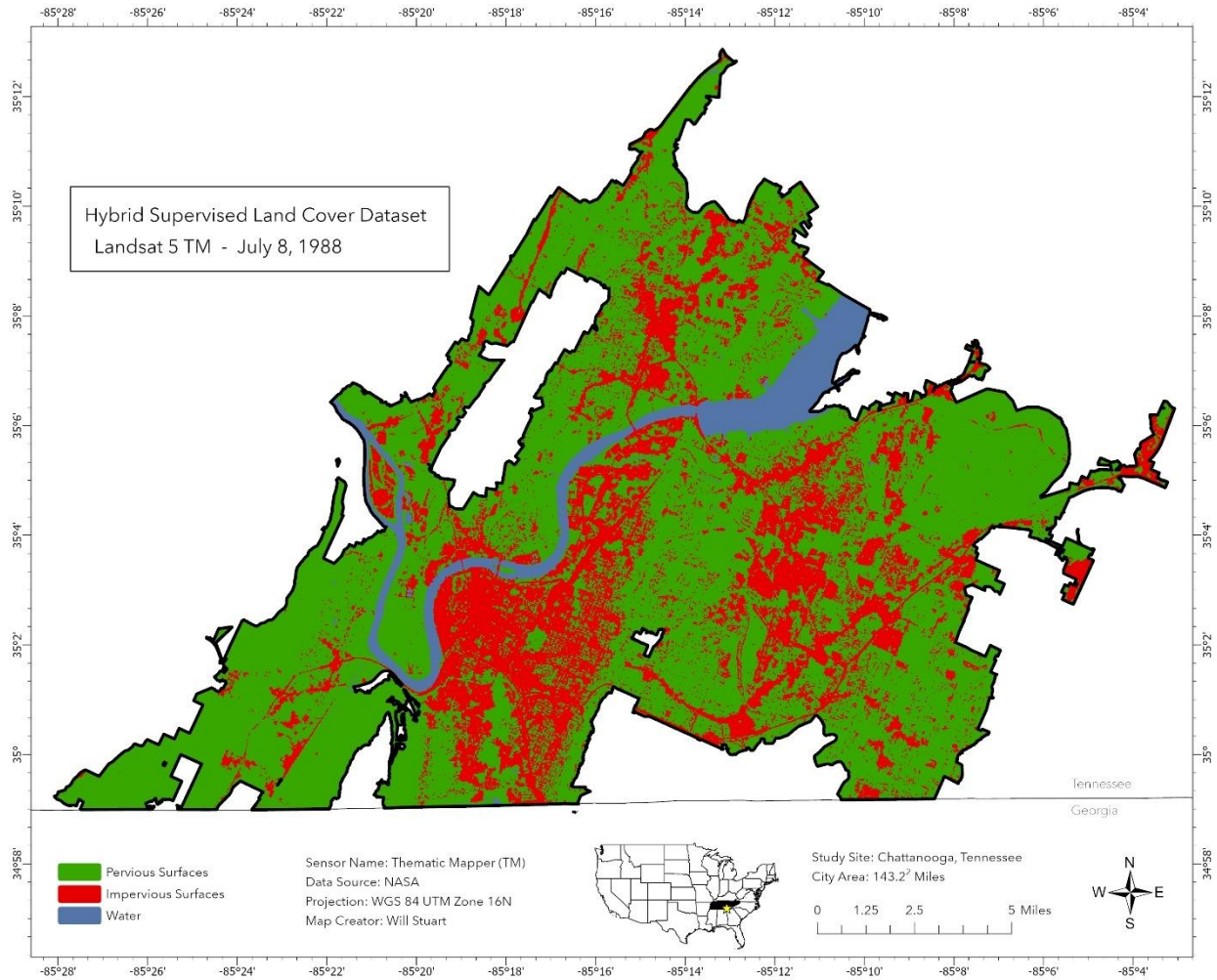
A19 Distribution of training polygons for supervised classification over true color Landsat 8 OLI image captured August 31, 2019 across Chattanooga, TN.



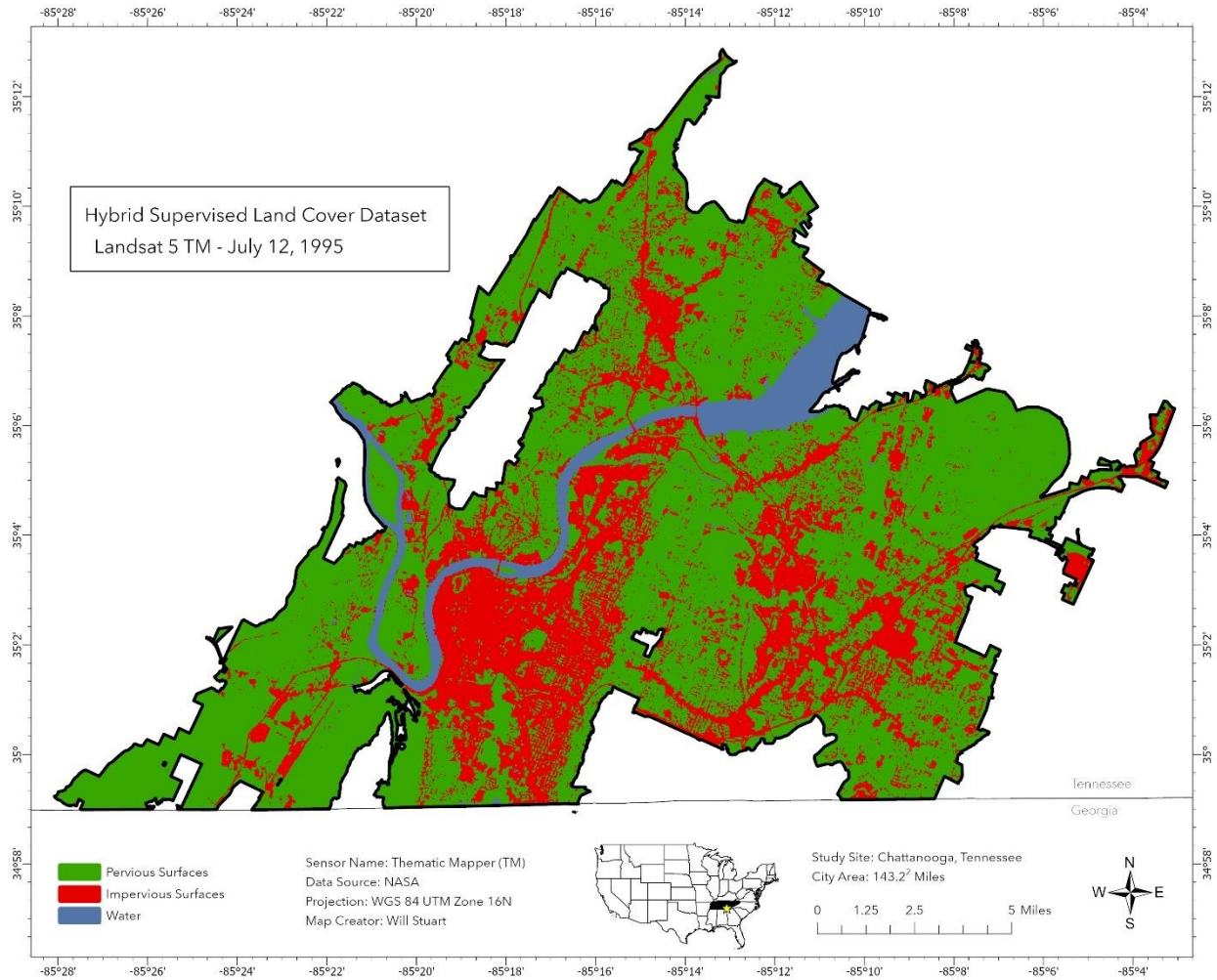
A20 Distribution of training polygons for supervised classification over true color Landsat 8 OLI image captured July 3, 2021 across Chattanooga, TN.



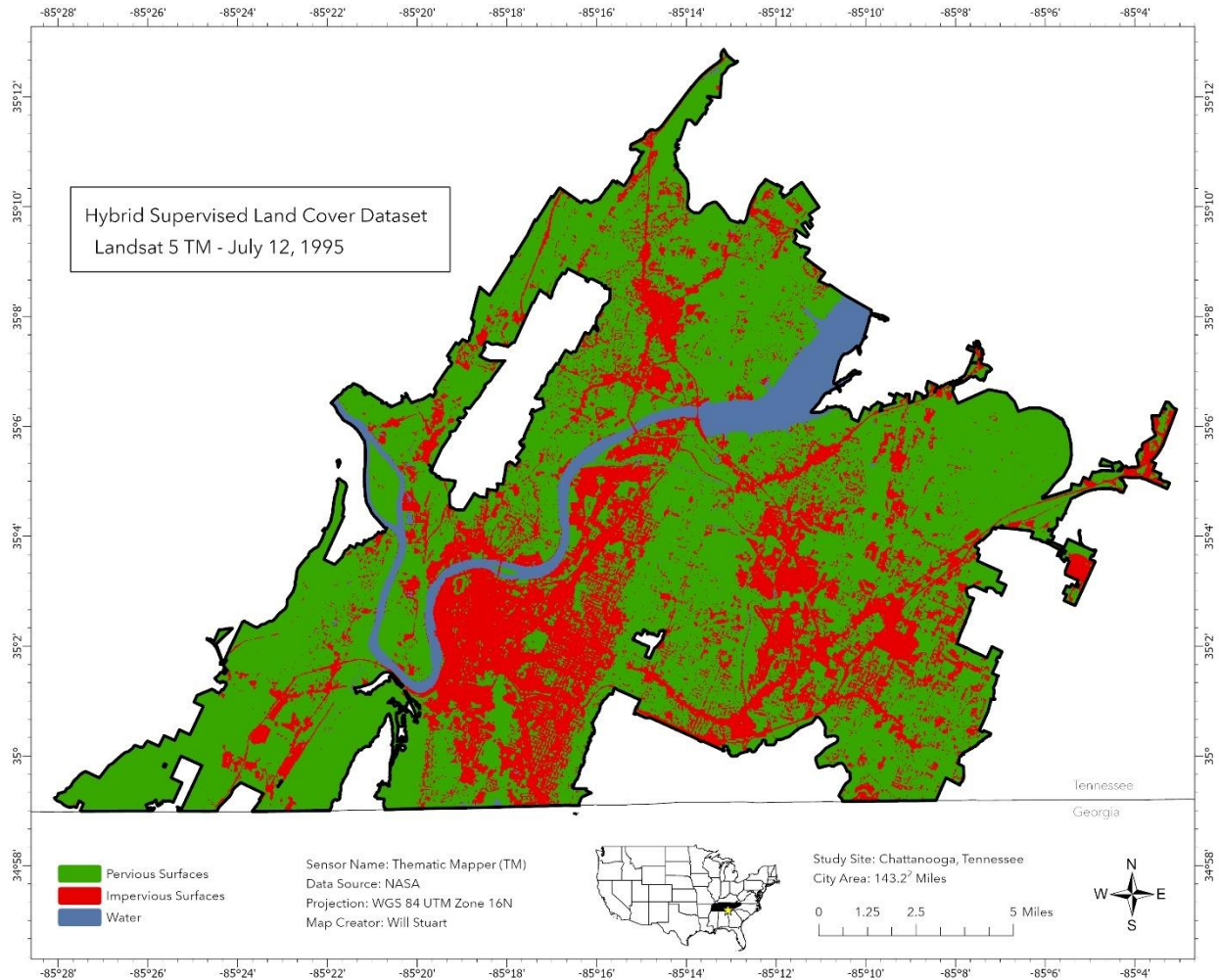
A21 3 Class thematic land cover map derived from the classification of a true color Landsat 5 TM image captured June 27, 1984 across Chattanooga, TN.



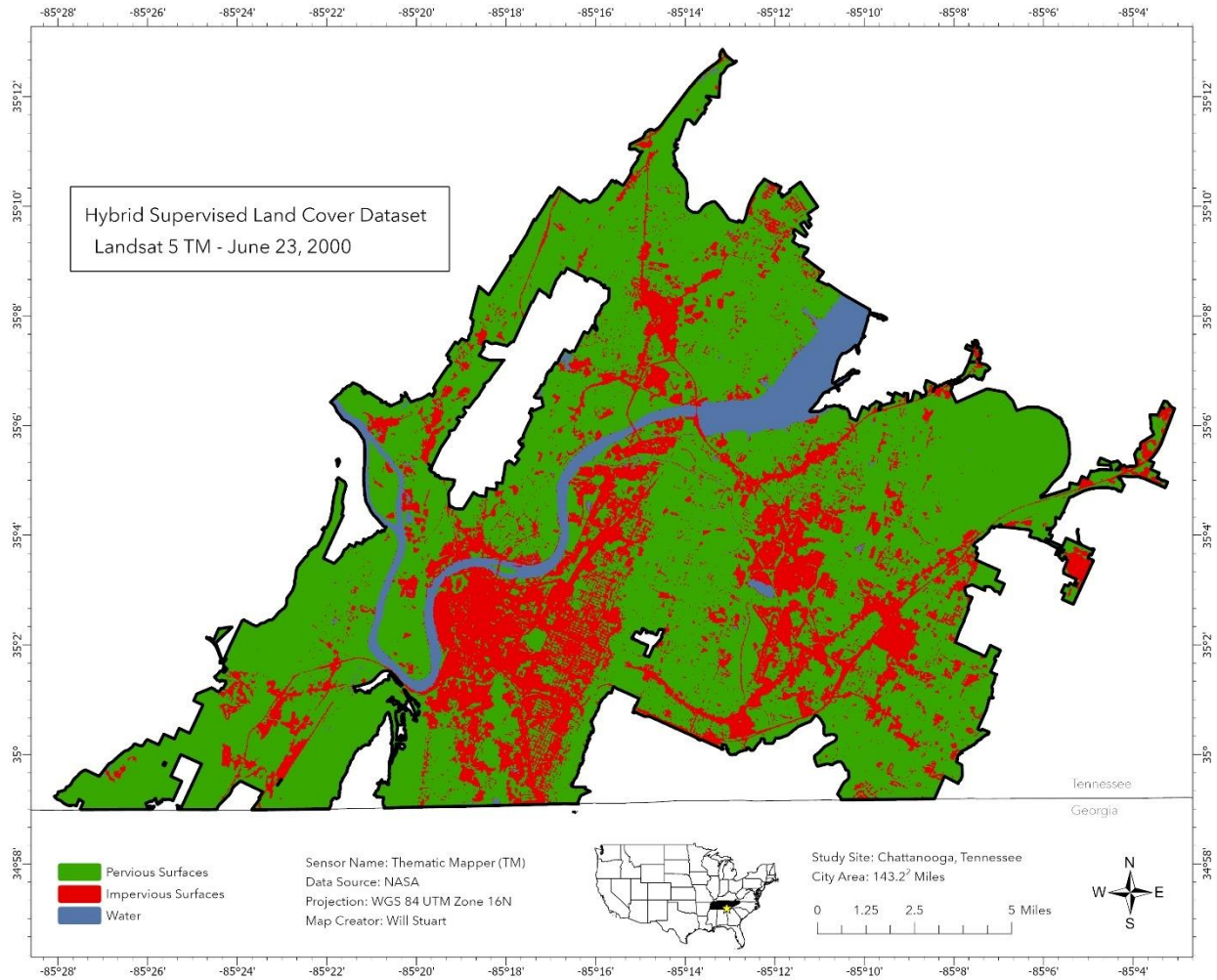
A22 3 Class thematic land cover map derived from the classification of a true color Landsat 5 TM image captured July 8, 1984 across Chattanooga, TN.



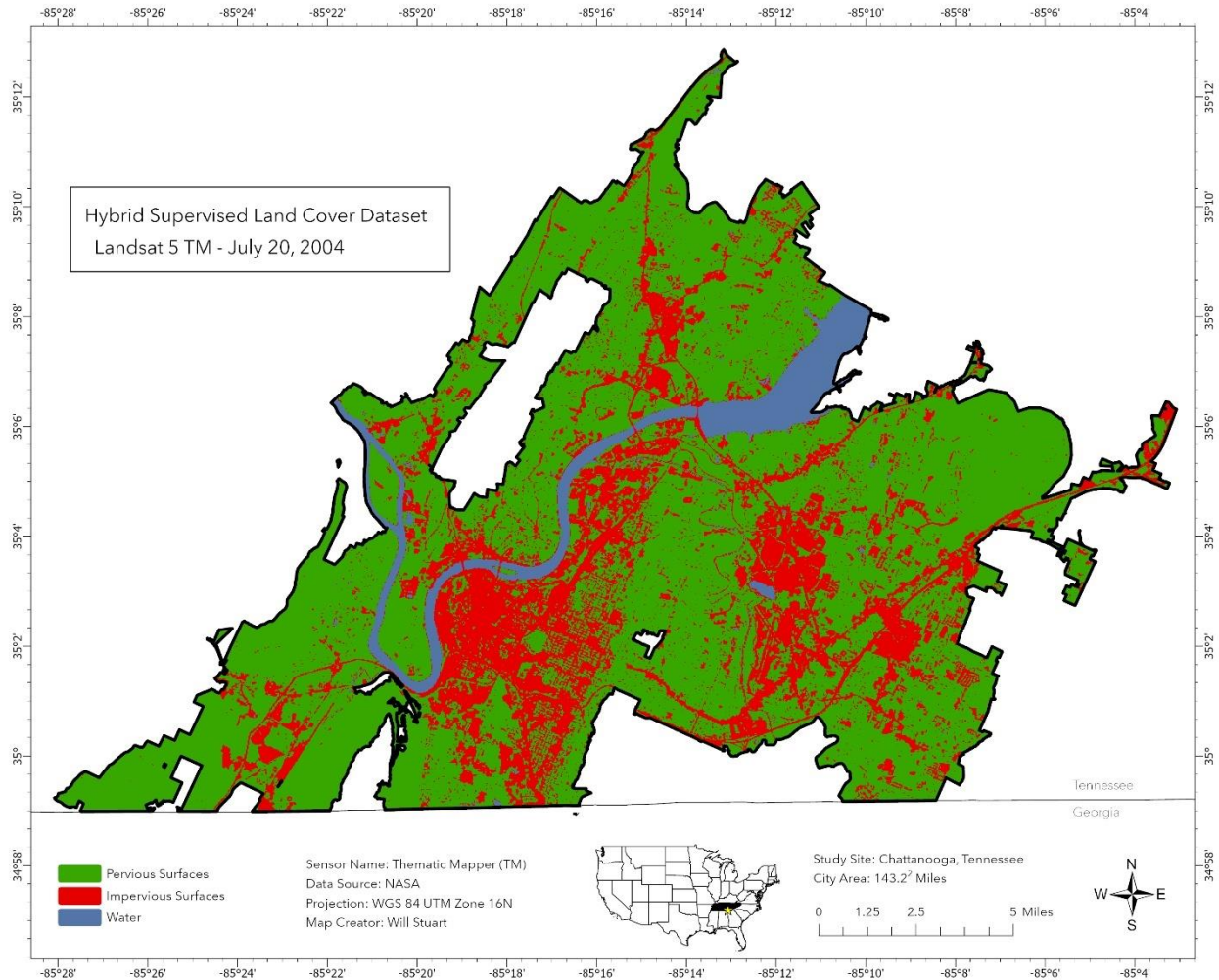
A23 3 Class thematic land cover map derived from the classification of a true color Landsat 5 TM image captured June 28, 1990 across Chattanooga, TN.



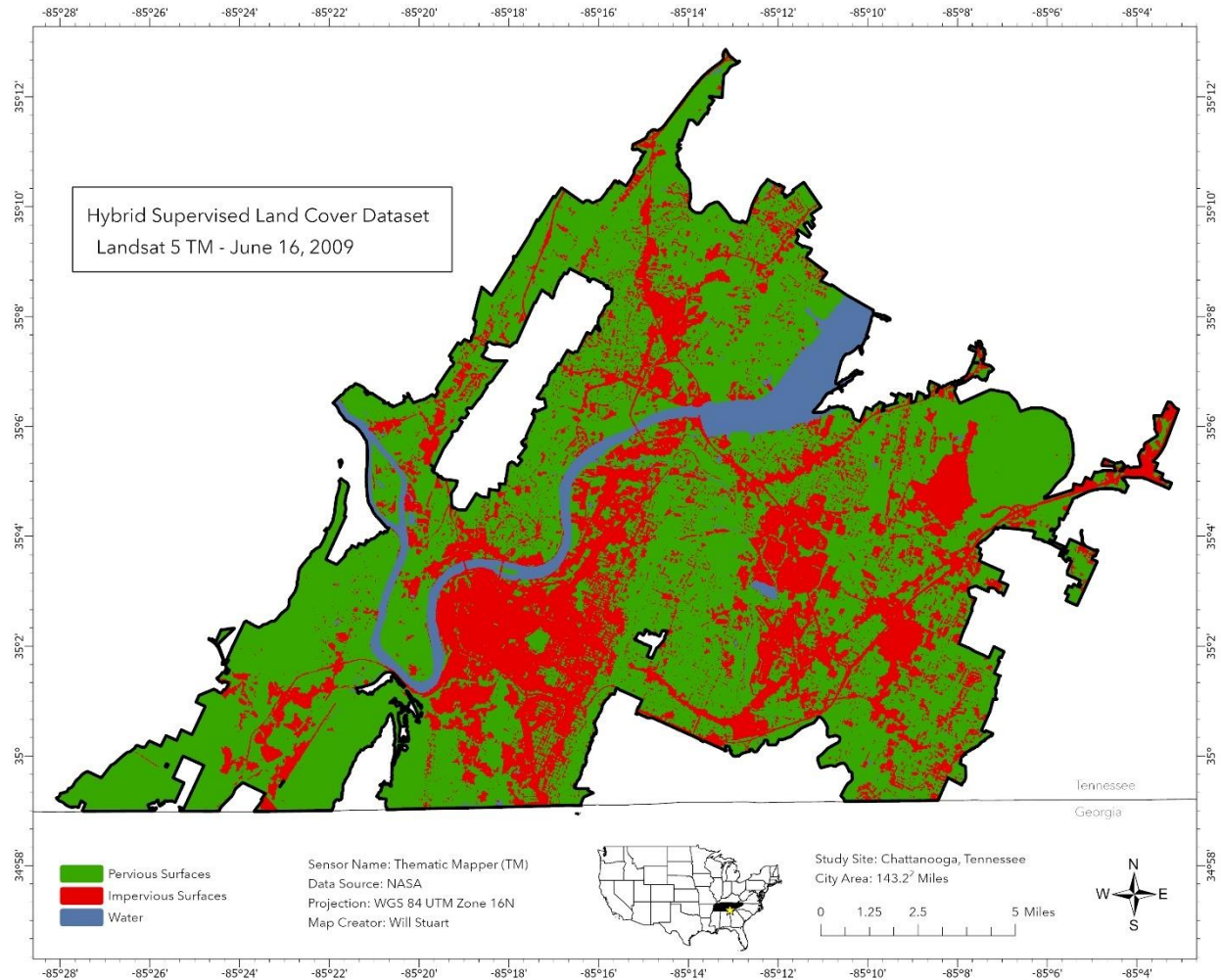
A24 3 Class thematic land cover map derived from the classification of a true color Landsat 5 TM image captured July 12, 1995 across Chattanooga, TN.



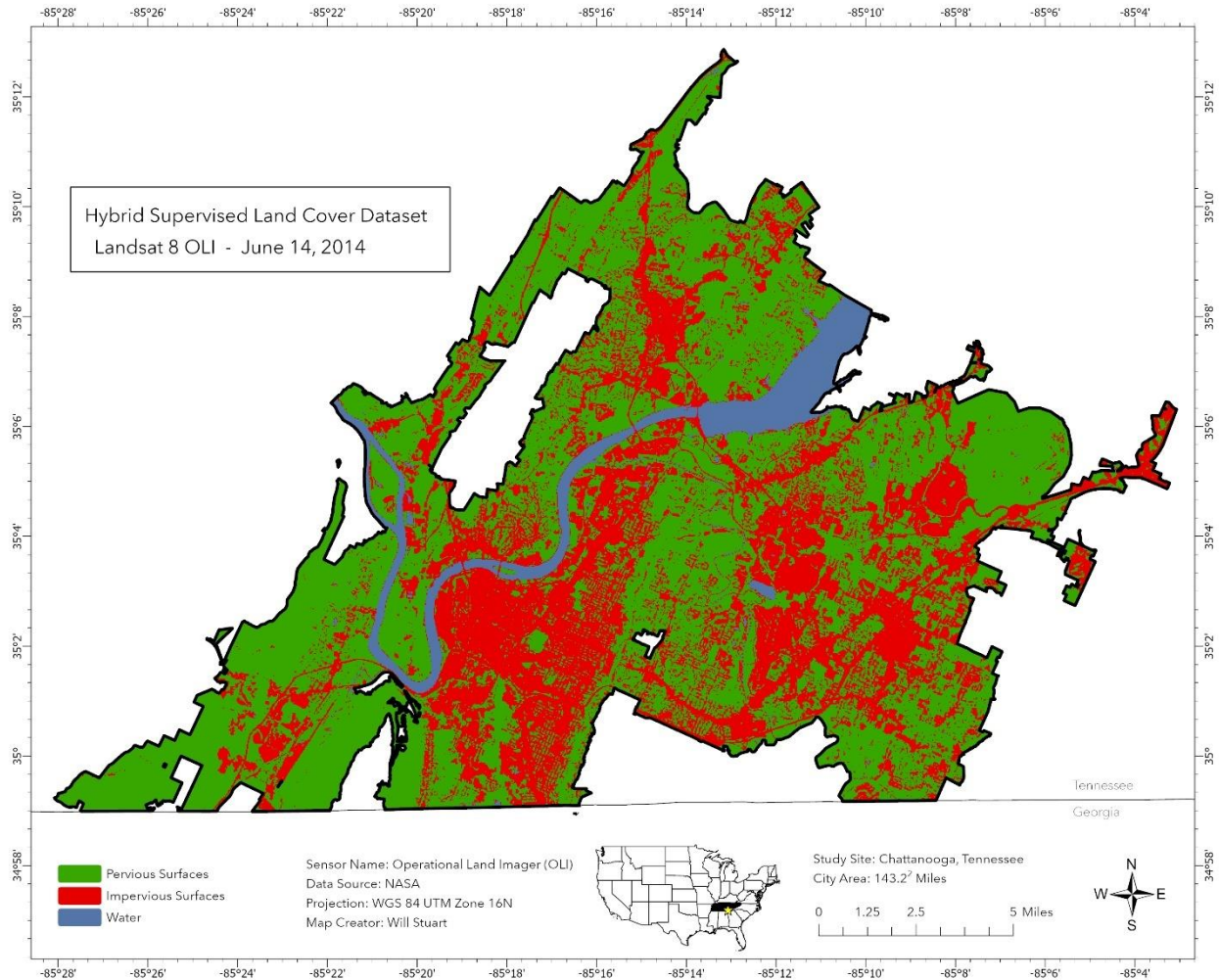
A25 3 Class thematic land cover map derived from the classification of a true color Landsat 5 TM image captured June 23, 2000 across Chattanooga, TN.



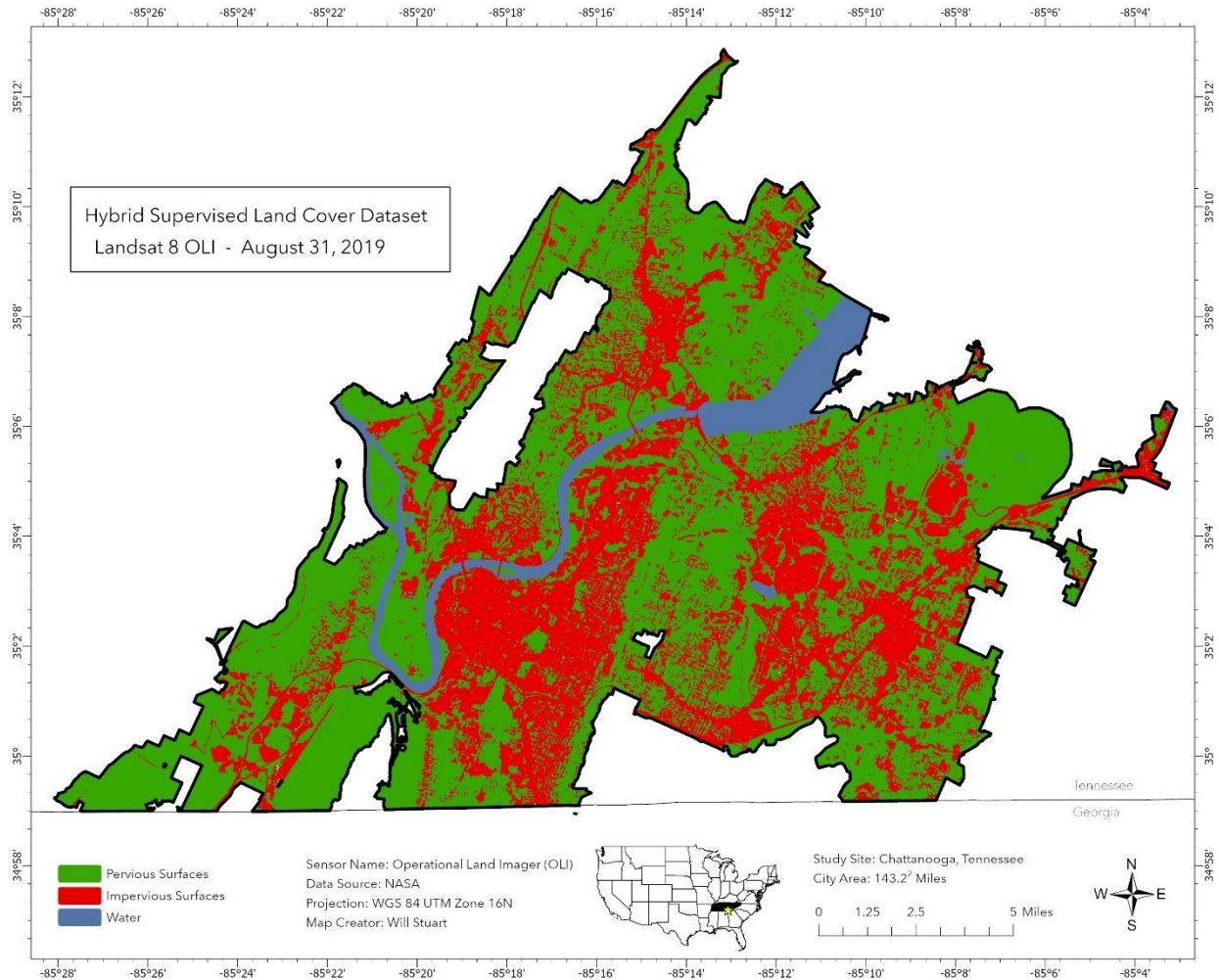
A26 3 Class thematic land cover map derived from the classification of a true color Landsat 5 TM image captured July 20, 2004 across Chattanooga, TN.



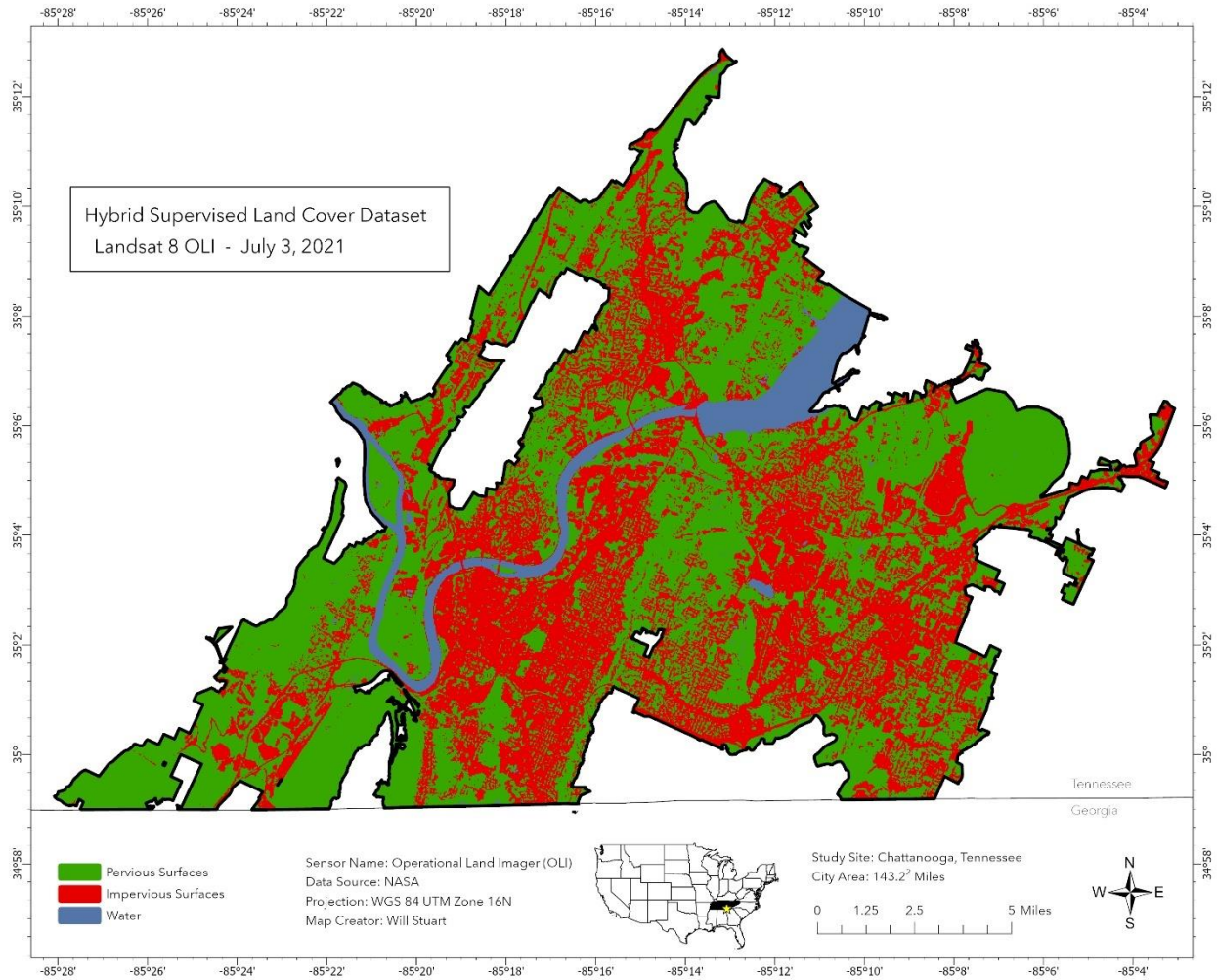
A27 3 Class thematic land cover map derived from the classification of a true color Landsat 5 TM image captured June 16, 2009 across Chattanooga, TN.



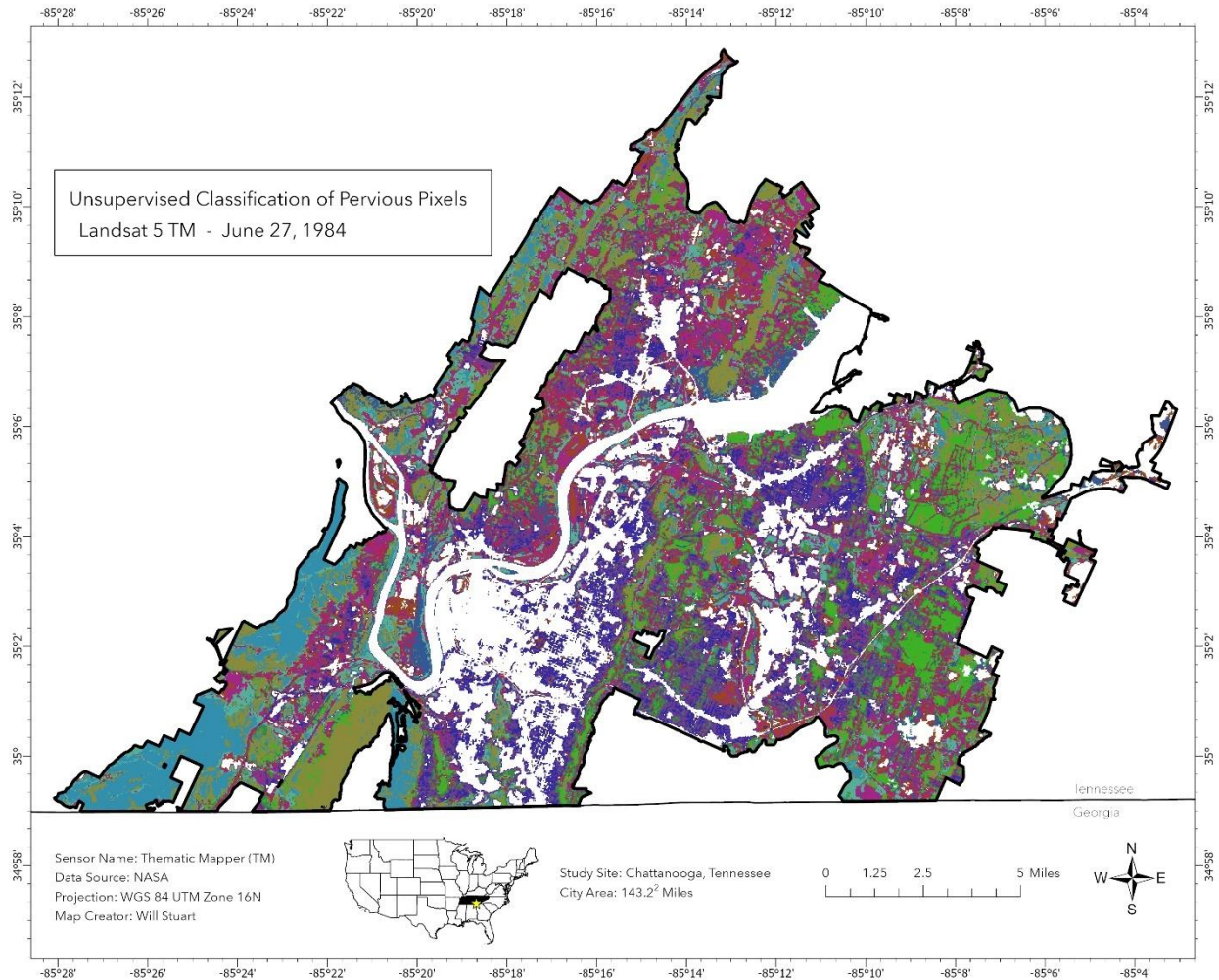
A28 3 Class thematic land cover map derived from the classification of a true color Landsat 8 OLI image captured June 14, 2014 across Chattanooga, TN.



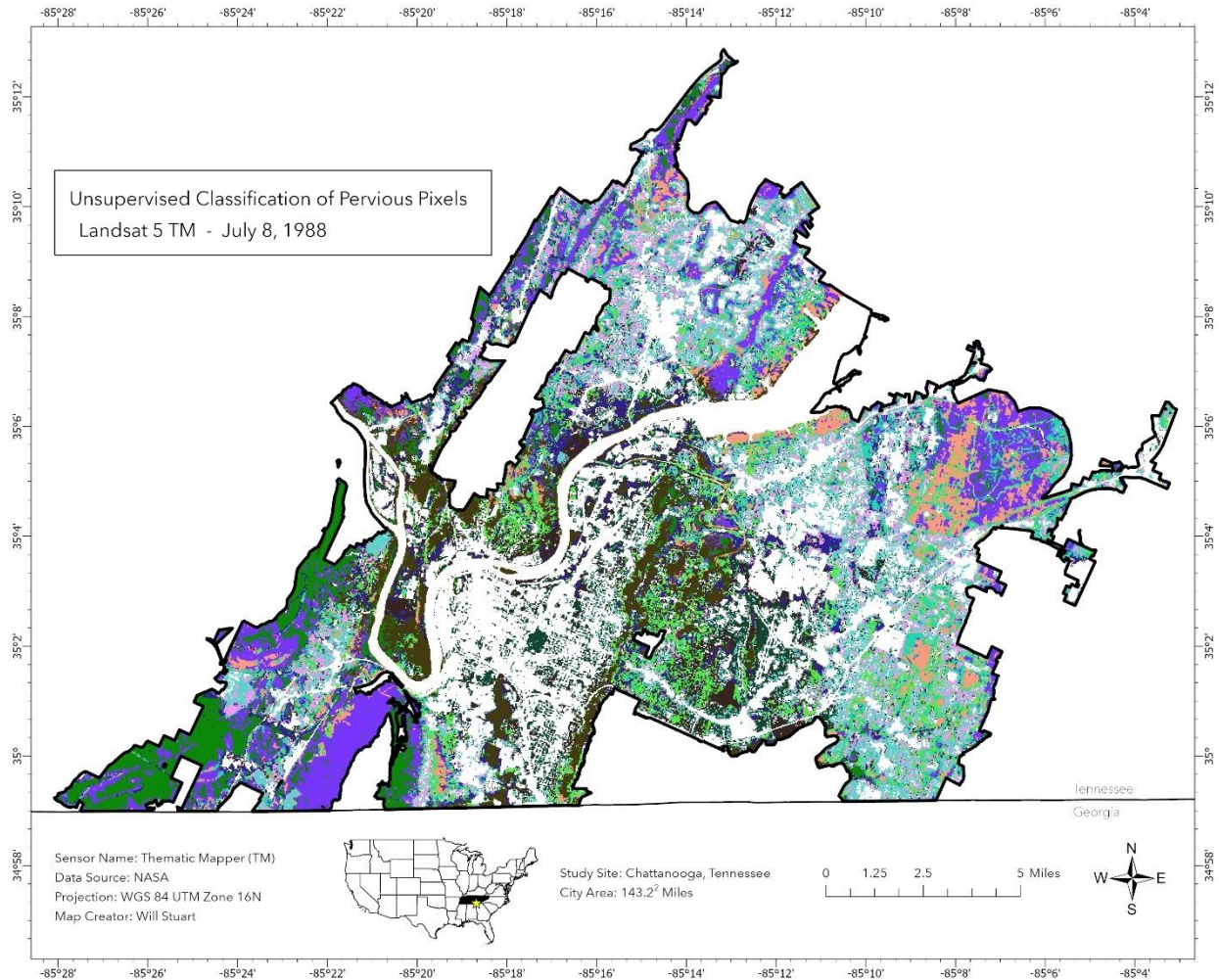
A29 3 Class thematic land cover map derived from the classification of a true color Landsat 8 OLI image captured August 31, 2019 across Chattanooga, TN.



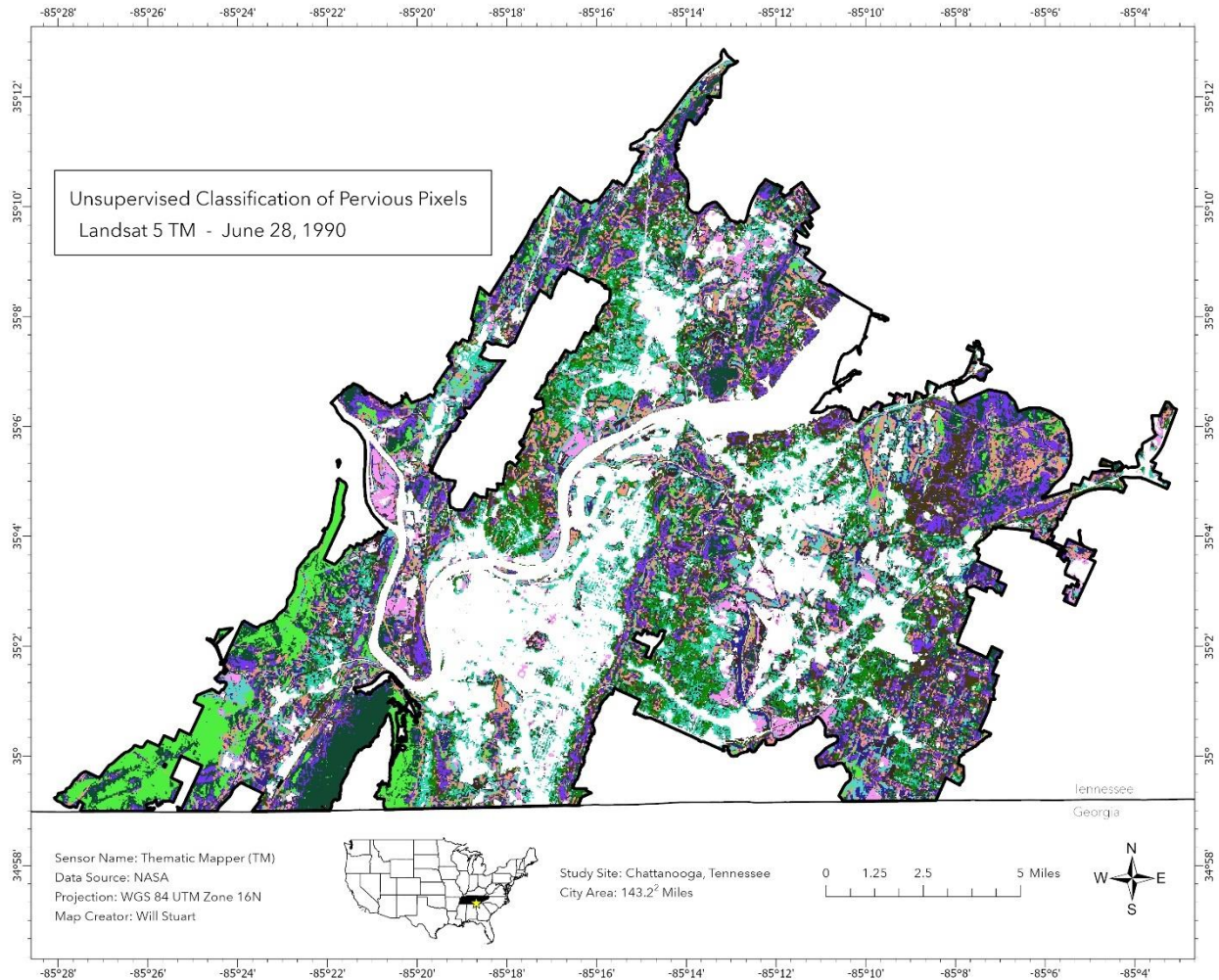
A30 3 Class thematic land cover map derived from the classification of a true color Landsat 8 OLI image captured July 3, 2021 across Chattanooga, TN.



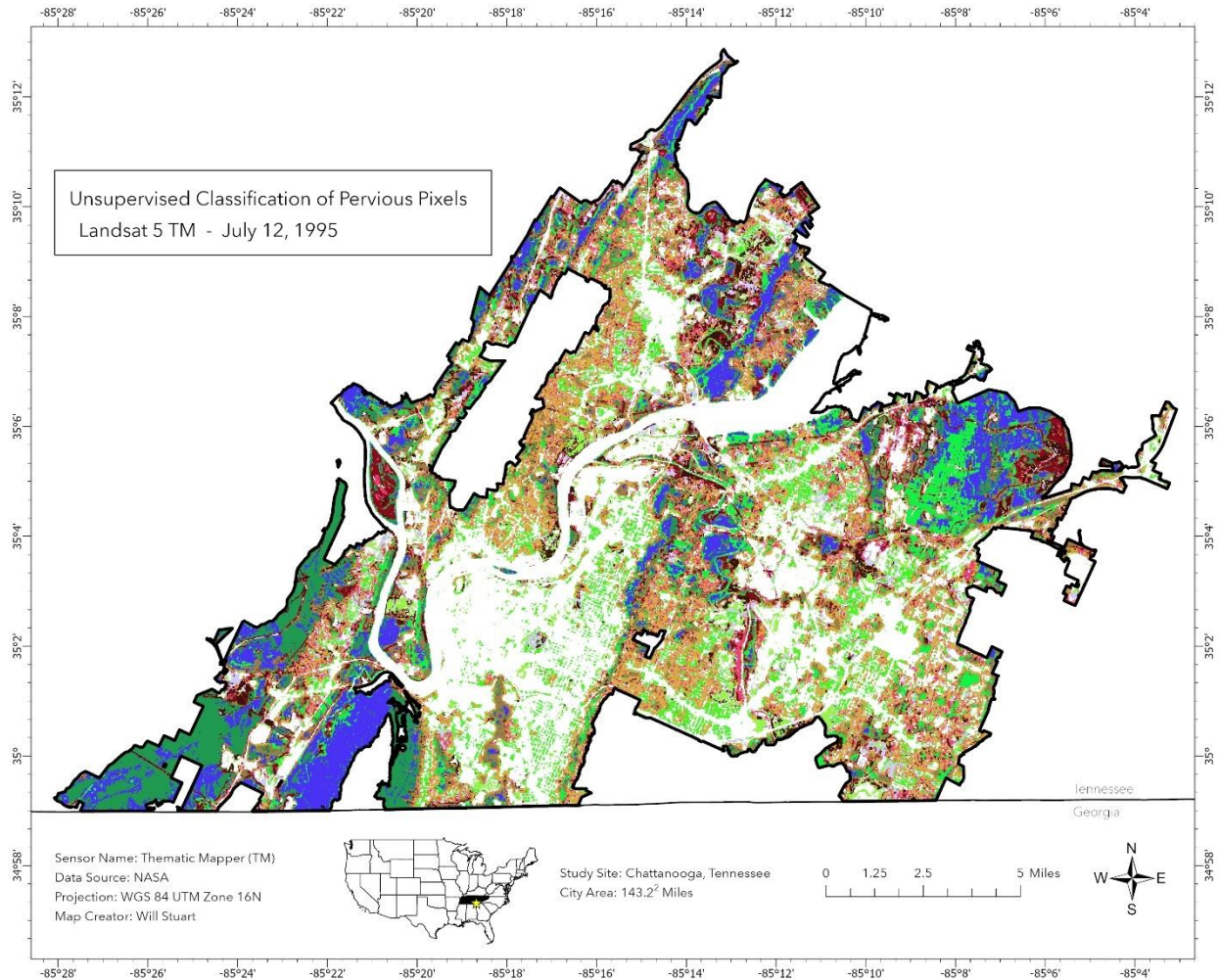
A31 Land cover output consisting of 10 spectrally distinct classes of pervious pixels following unsupervised classification of pervious pixels extracted from true color Landsat 5 TM image captured June 27, 1984 across Chattanooga, TN.



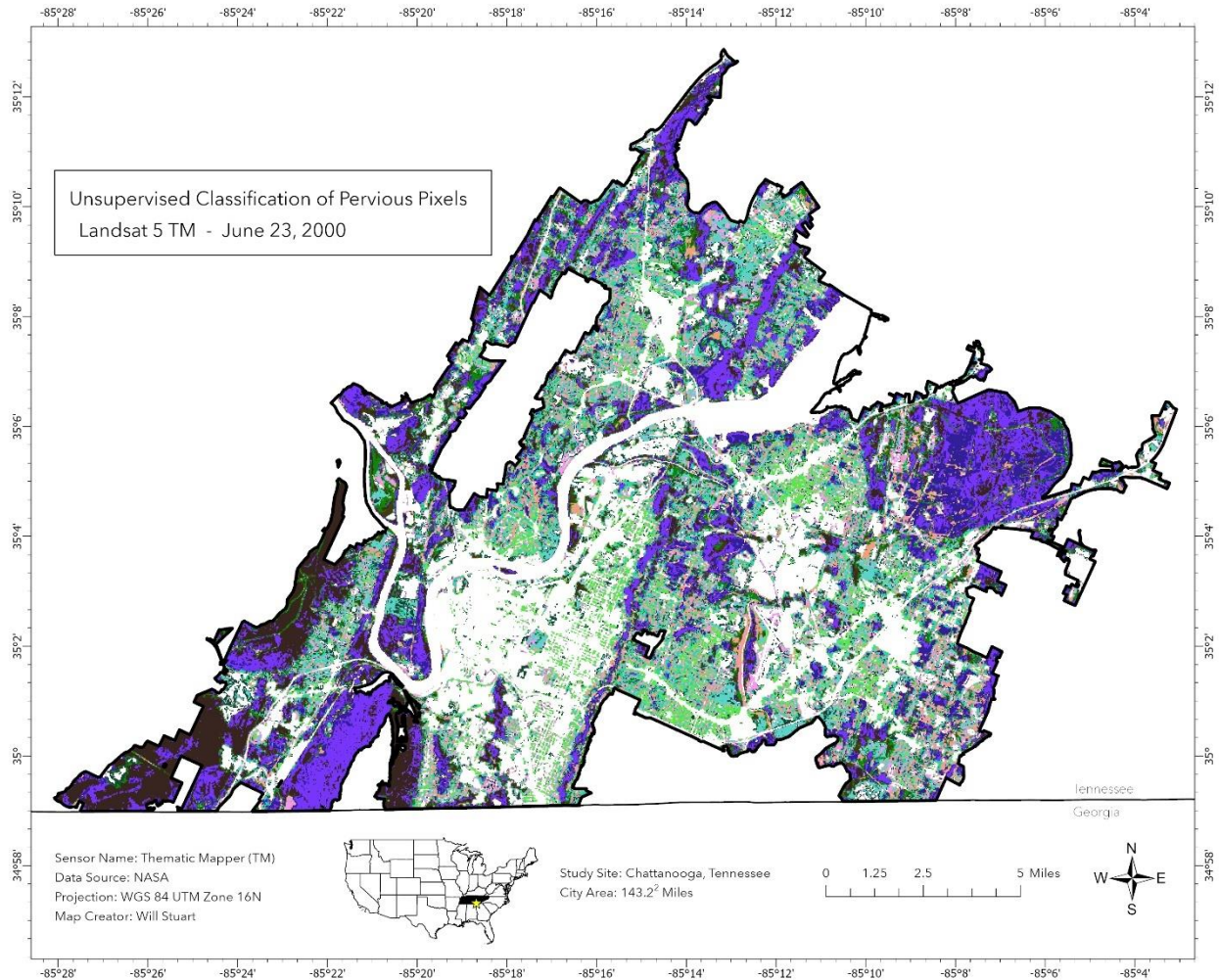
A32 Land cover output consisting of 10 spectrally distinct classes of pervious pixels following unsupervised classification of pervious pixels extracted from true color Landsat 5 TM image captured July 8, 1988 across Chattanooga, TN.



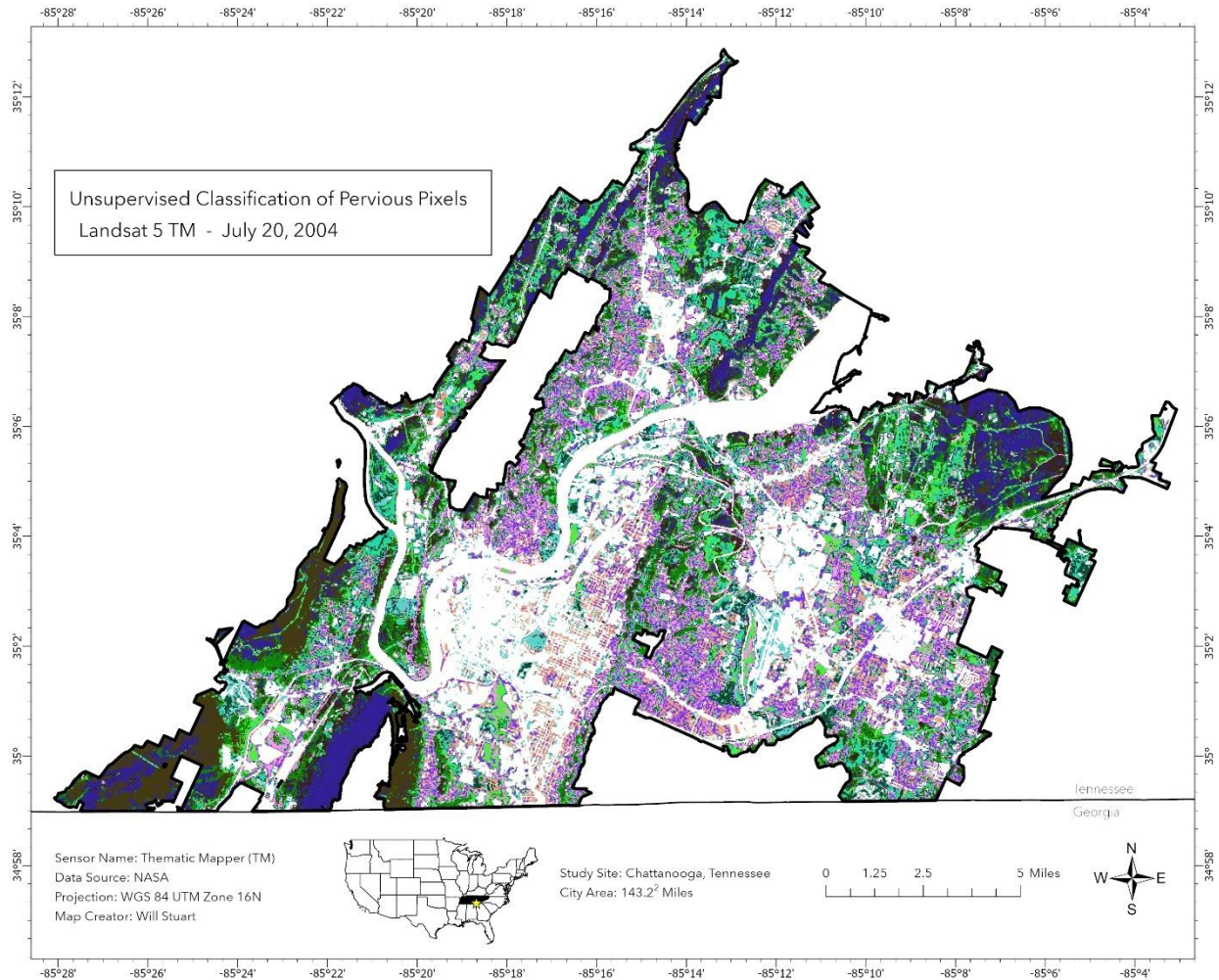
A33 Land cover output consisting of 10 spectrally distinct classes of pervious pixels following unsupervised classification of pervious pixels extracted from true color Landsat 5 TM image captured June 28, 1990 across Chattanooga, TN.



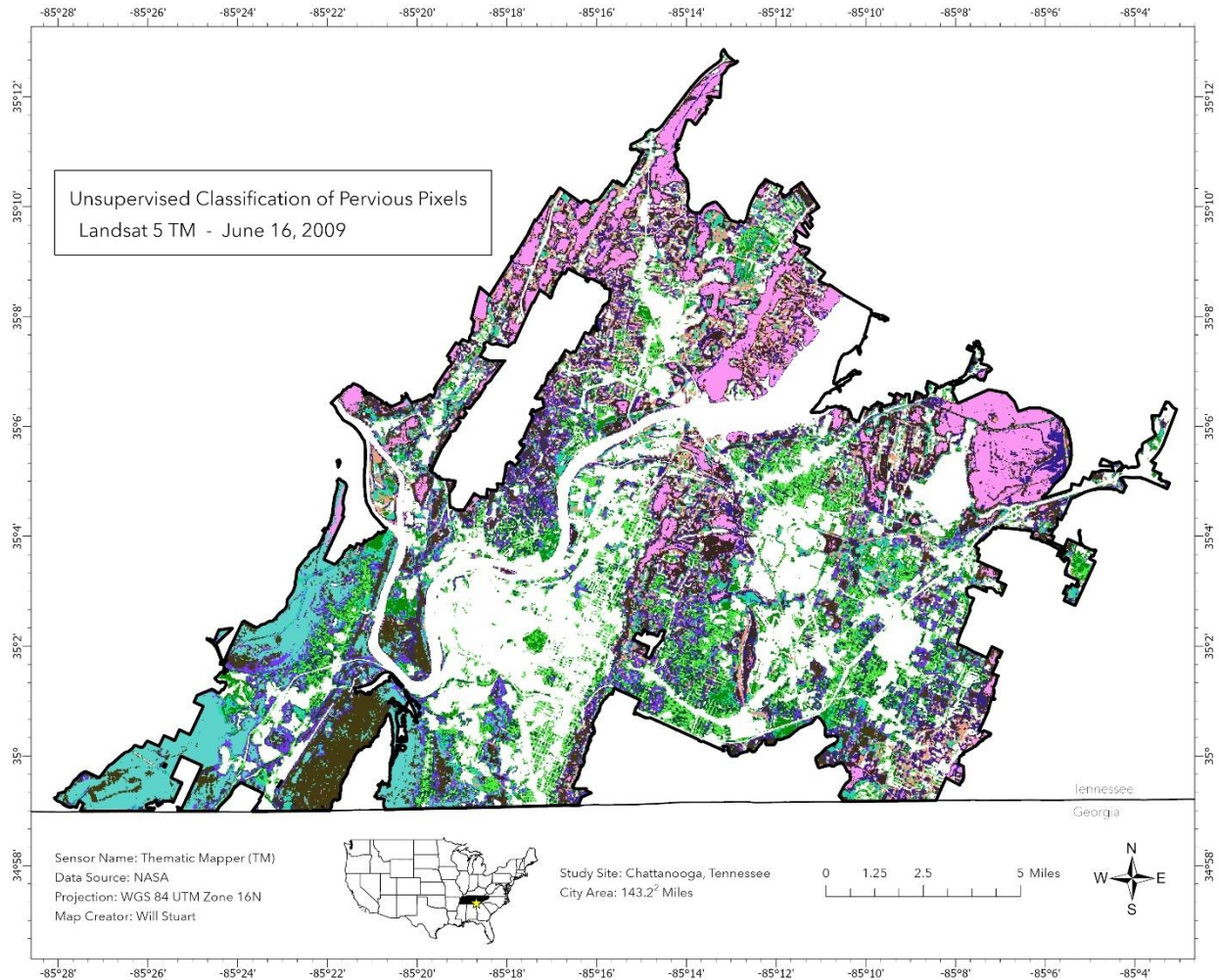
A34 Land cover output consisting of 10 spectrally distinct classes of pervious pixels following unsupervised classification of pervious pixels extracted from true color Landsat 5 TM image captured July 12, 1995 across Chattanooga, TN.



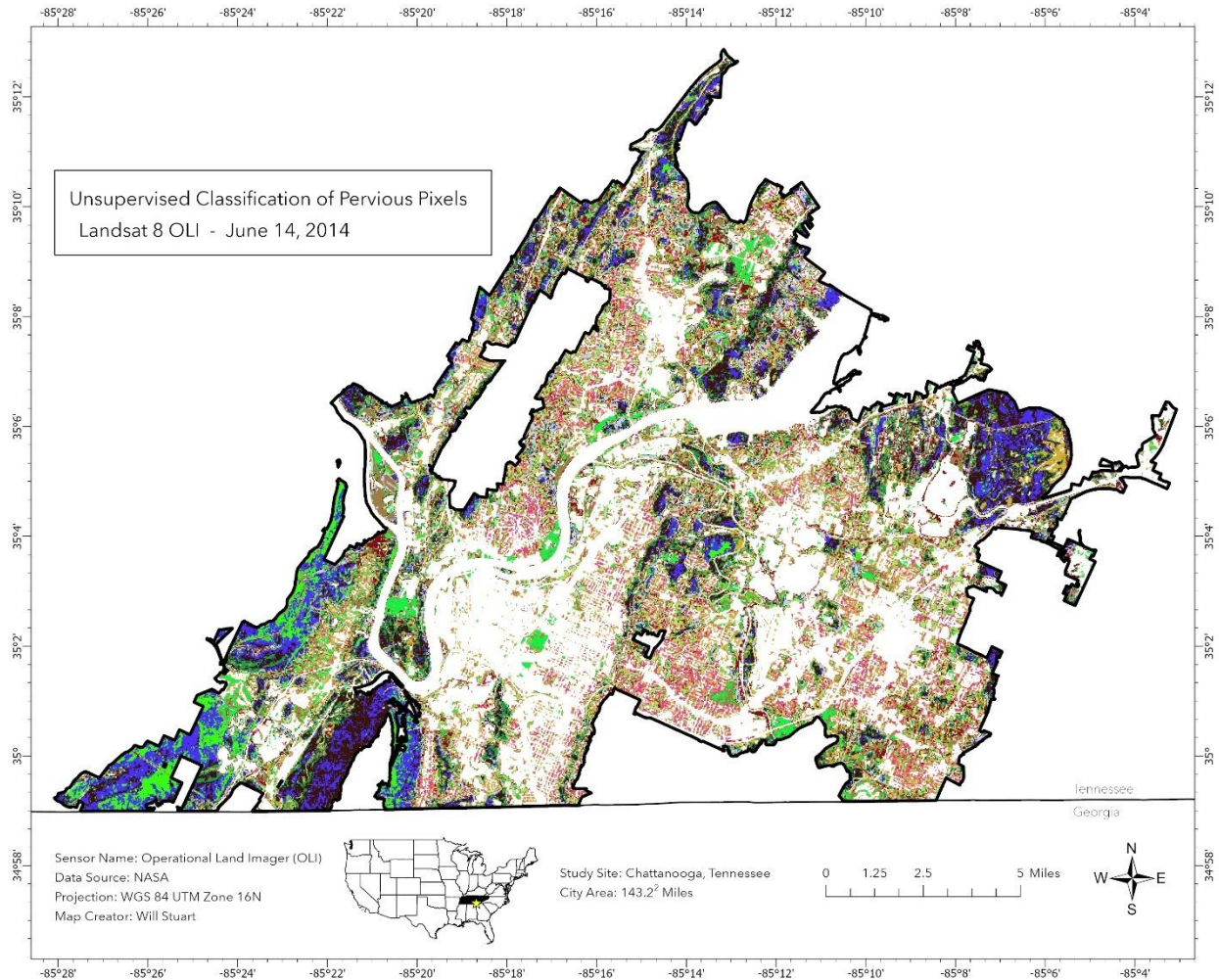
A35 Land cover output consisting of 10 spectrally distinct classes of pervious pixels following unsupervised classification of pervious pixels extracted from true color Landsat 5 TM image captured June 23, 2000 across Chattanooga, TN.



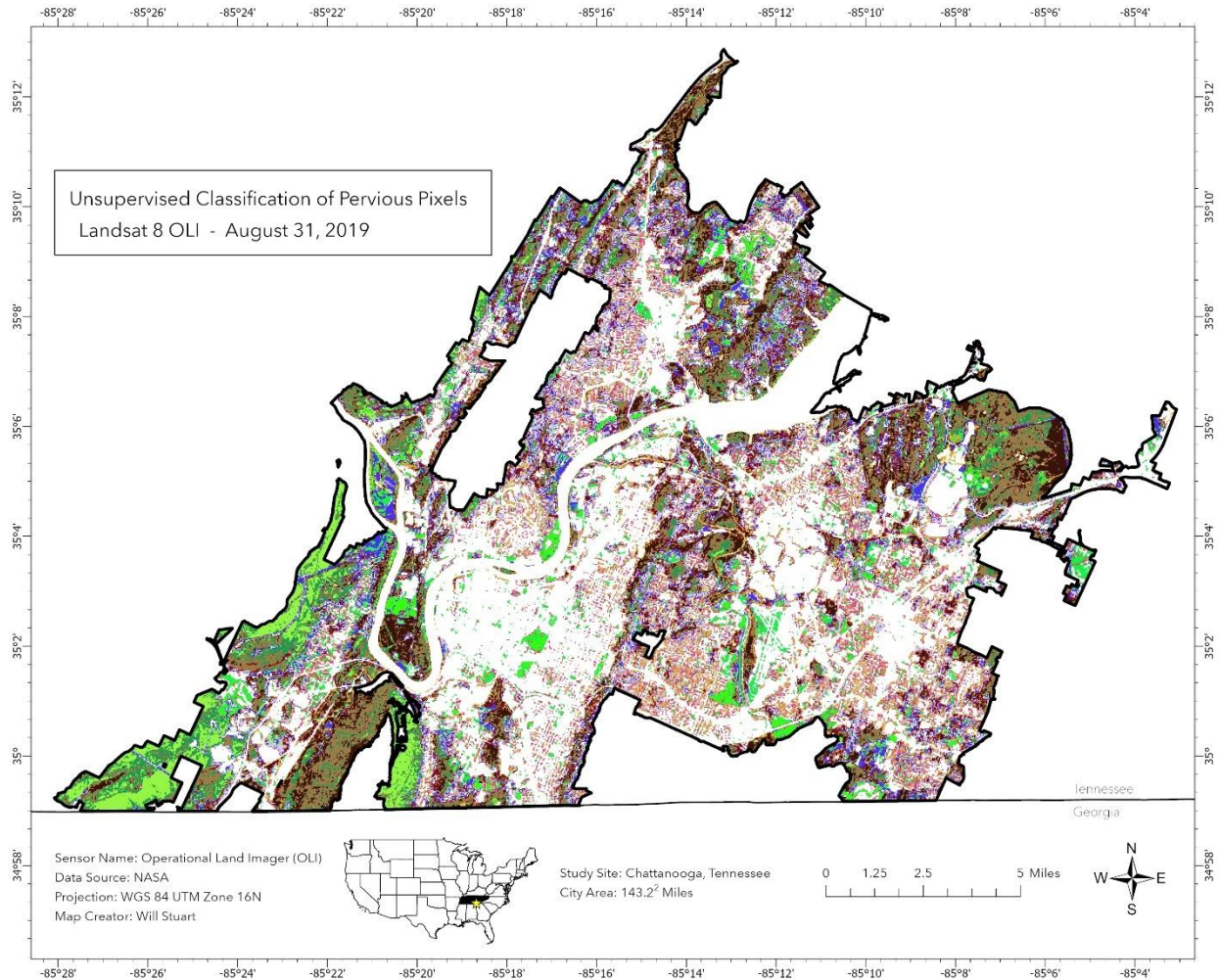
A36 Land cover output consisting of 10 spectrally distinct classes of pervious pixels following unsupervised classification of pervious pixels extracted from true color Landsat 5 TM image captured July 20, 2004 across Chattanooga, TN.



A37 Land cover output consisting of 10 spectrally distinct classes of pervious pixels following unsupervised classification of pervious pixels extracted from true color Landsat 5 TM image captured June 16, 2009 across Chattanooga, TN.



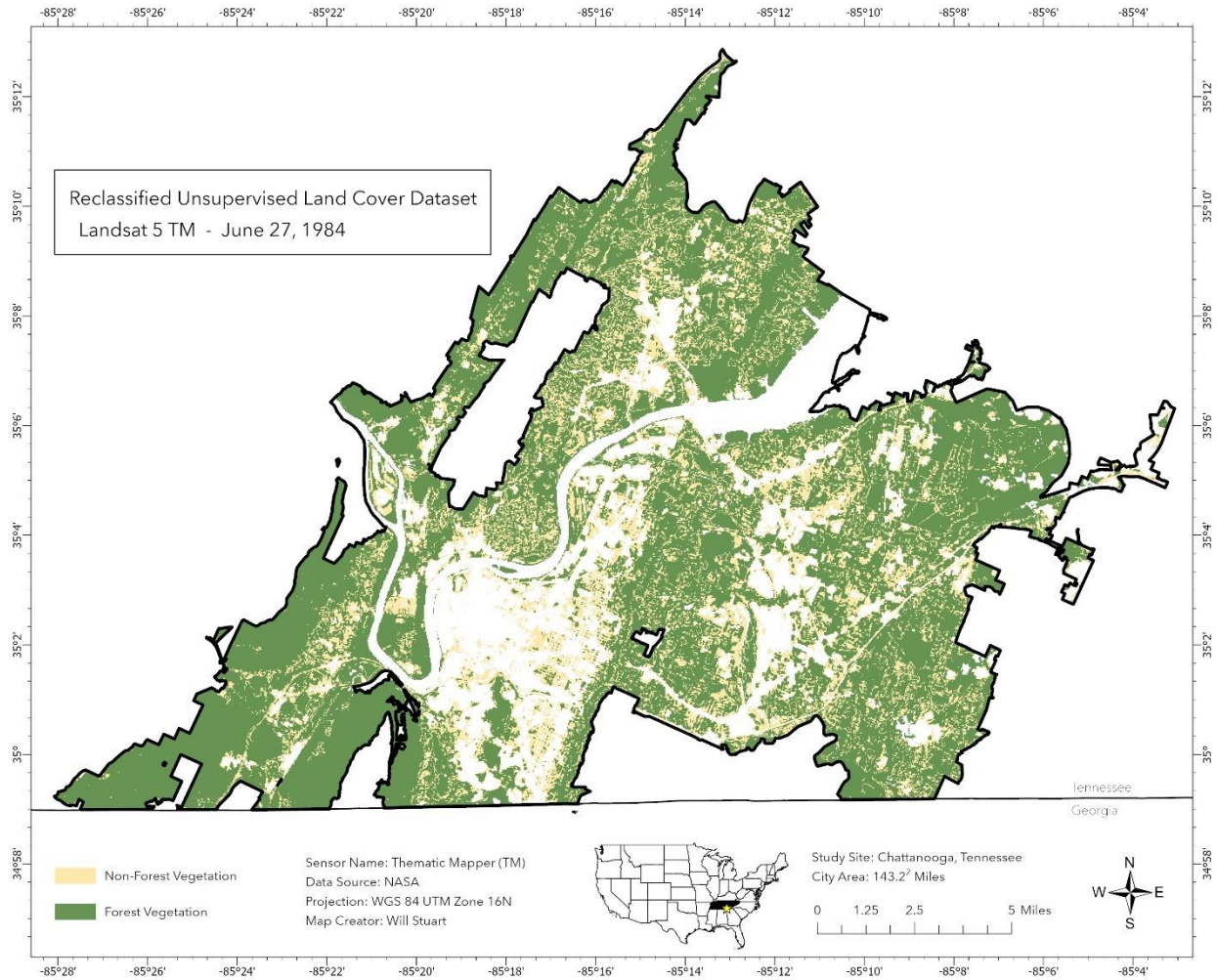
A38 Land cover output consisting of 10 spectrally distinct classes of pervious pixels following unsupervised classification of pervious pixels extracted from true color Landsat 8 OLI image captured June 14, 2014 across Chattanooga, TN.



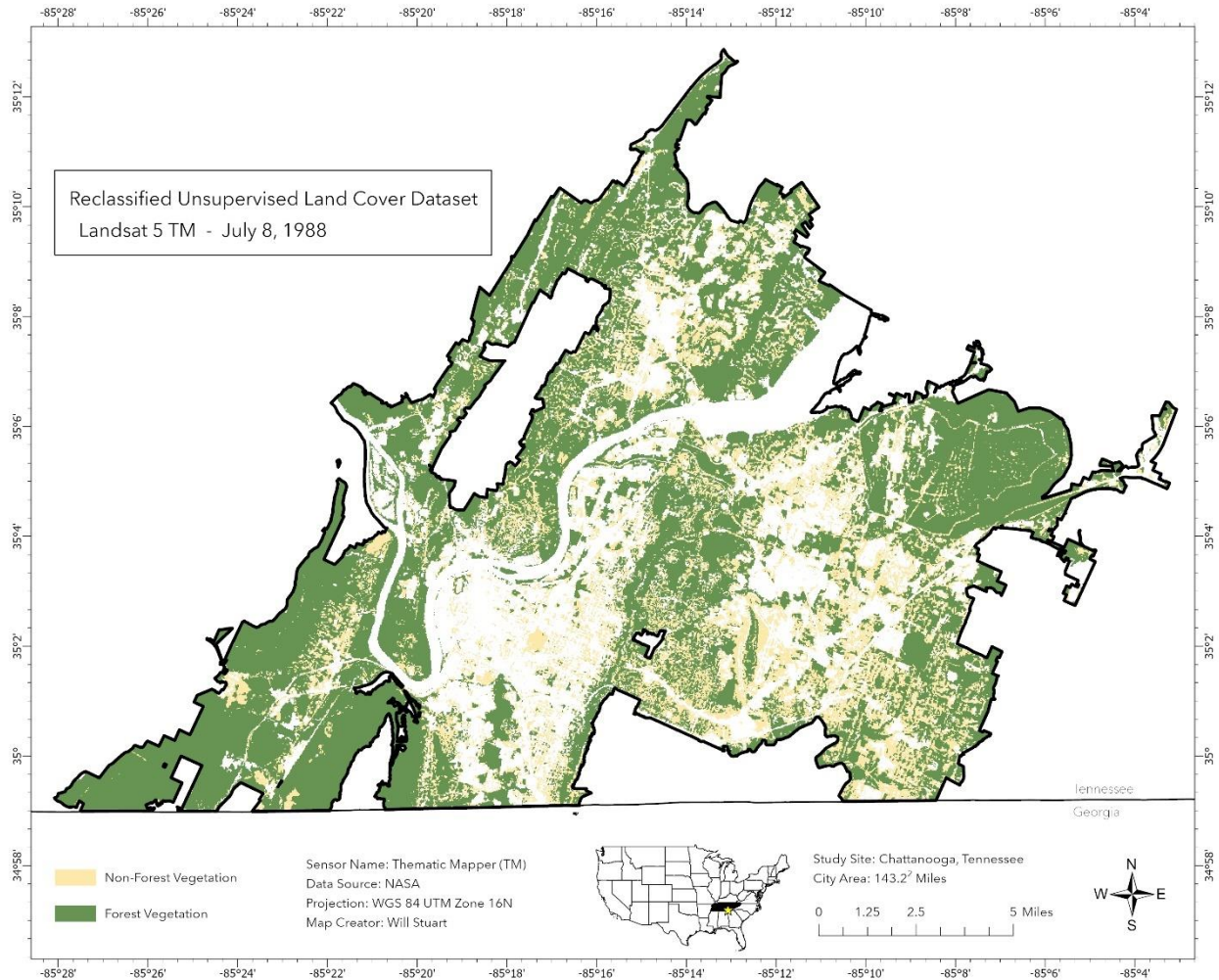
A39 Land cover output consisting of 10 spectrally distinct classes of pervious pixels following unsupervised classification of pervious pixels extracted from true color Landsat 8 OLI image captured August 31, 2019 across Chattanooga, TN.



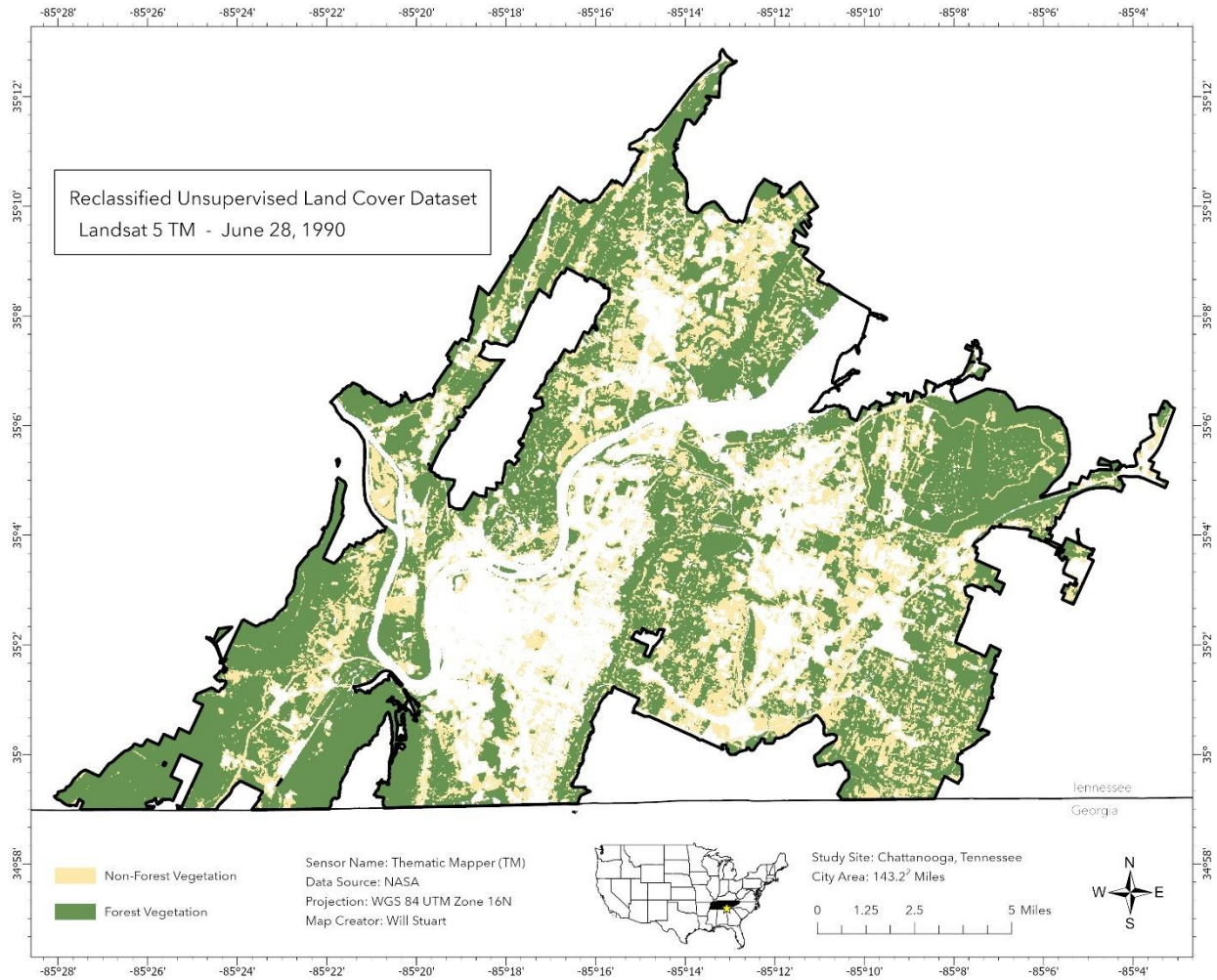
A40 Land cover output consisting of 10 spectrally distinct classes of pervious pixels following unsupervised classification of pervious pixels extracted from true color Landsat 8 OLI image captured July 3, 2021 across Chattanooga, TN.



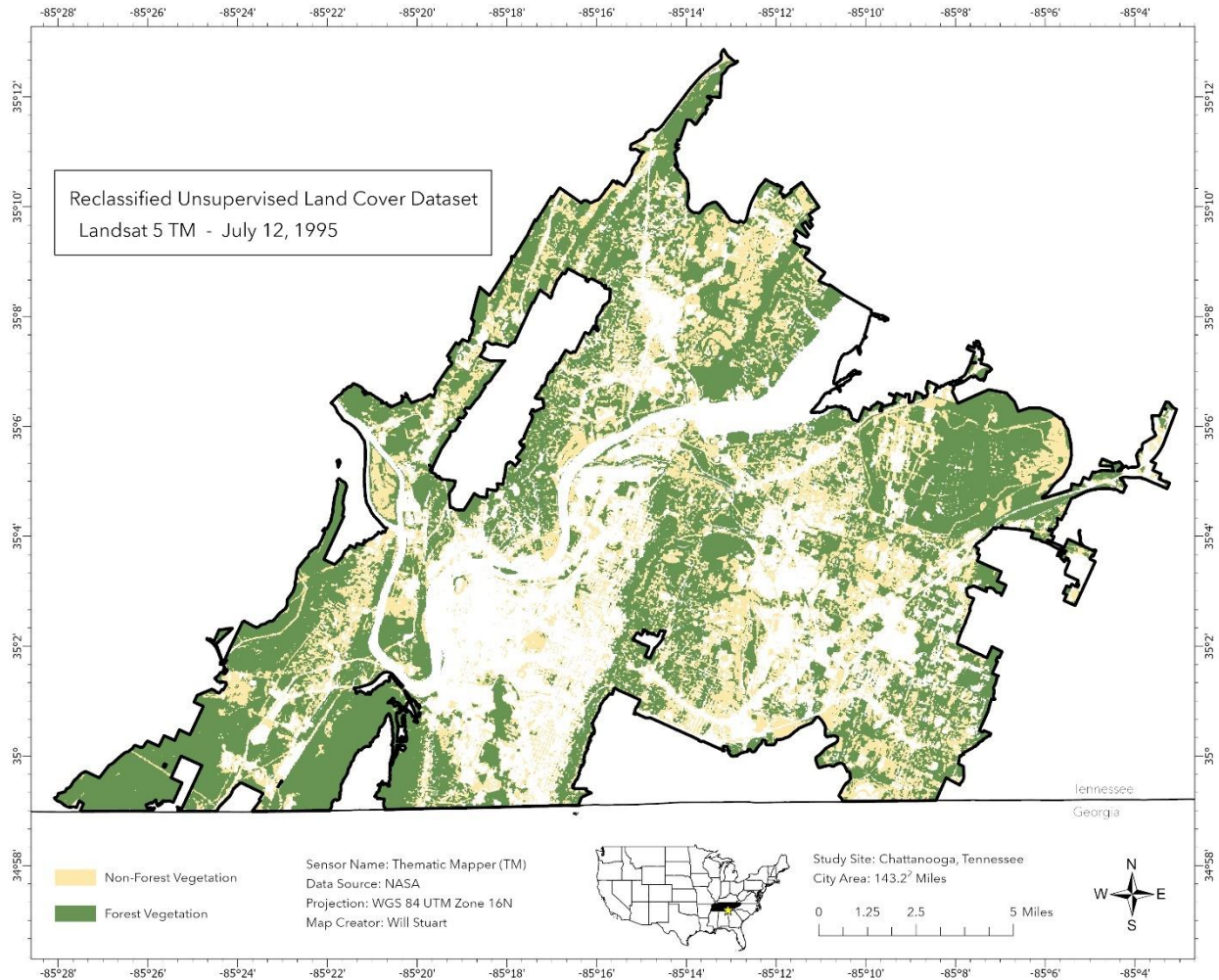
A41 Manual reclassification of 10 spectrally distinct classes of pervious pixels into Forest and Non-Forest Vegetation. Derived from true color Landsat 5 TM image captured June 27, 1984 across Chattanooga, TN.



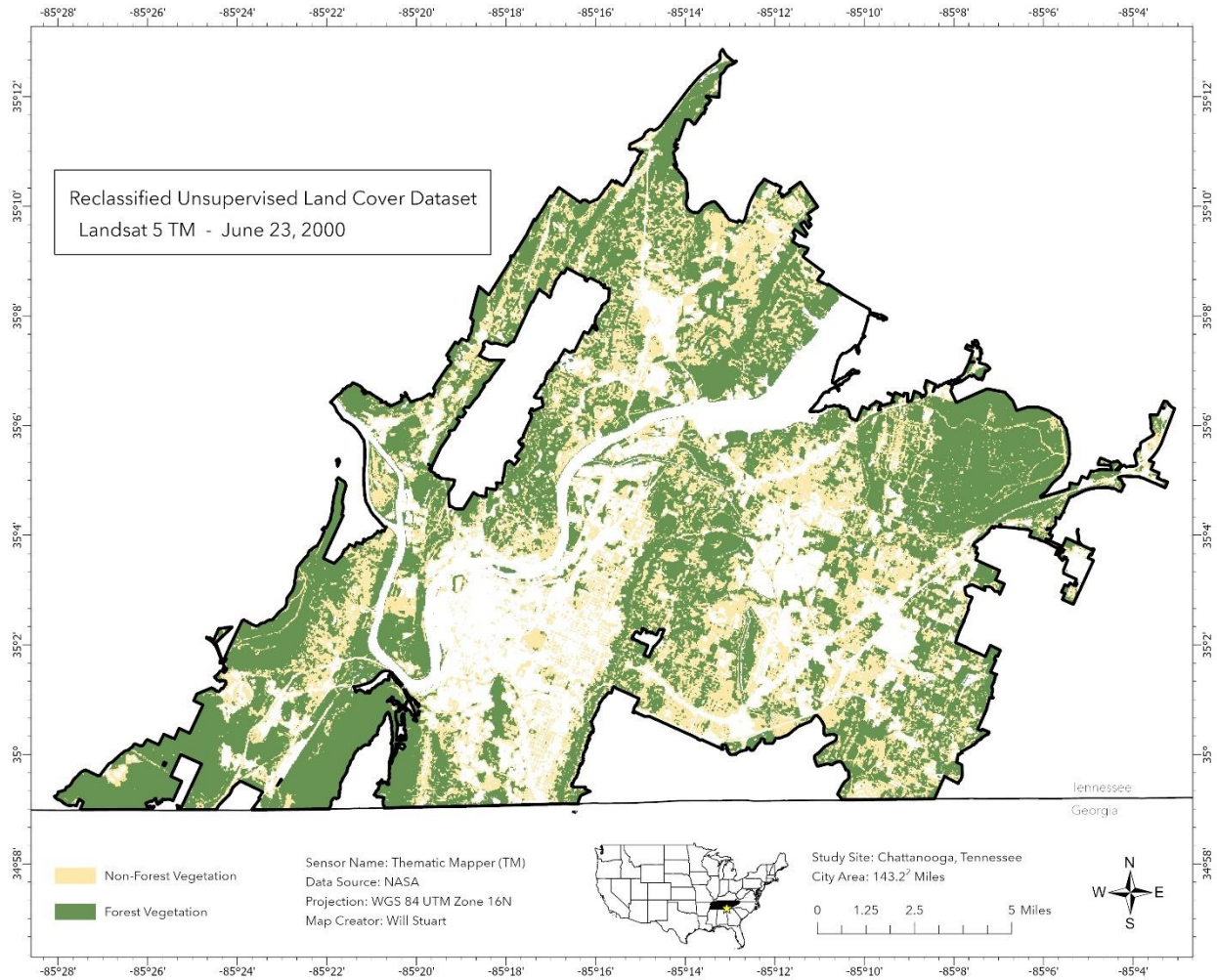
A42 Manual reclassification of 10 spectrally distinct classes of pervious pixels into Forest and Non-Forest Vegetation. Derived from true color Landsat 5 TM image captured July 8, 1984 across Chattanooga, TN.



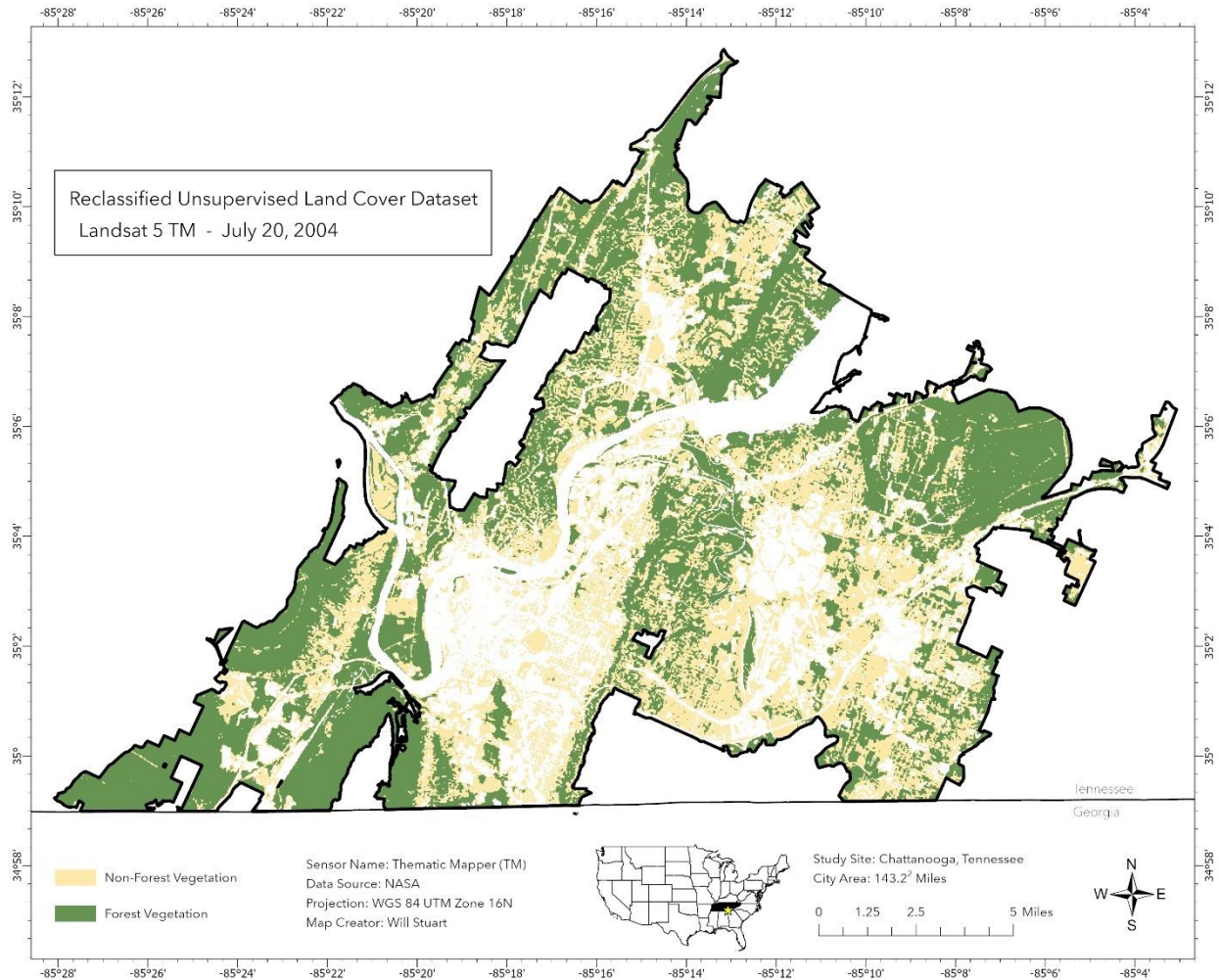
A43 Manual reclassification of 10 spectrally distinct classes of pervious pixels into Forest and Non-Forest Vegetation. Derived from true color Landsat 5 TM image captured June 28, 1990 across Chattanooga, TN.



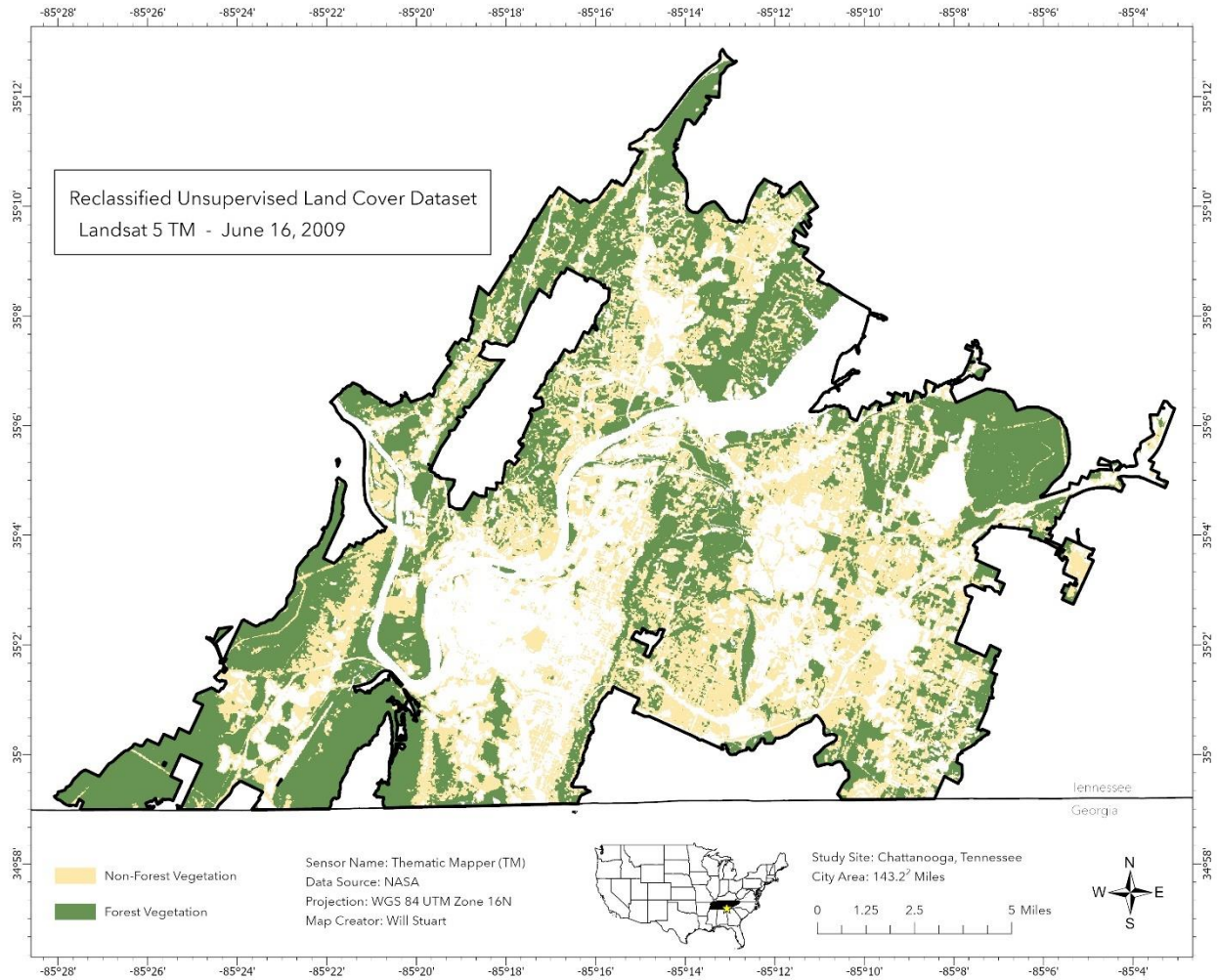
A44 Manual reclassification of 10 spectrally distinct classes of pervious pixels into Forest and Non-Forest Vegetation. Derived from true color Landsat 5 TM image captured July 12, 1995 across Chattanooga, TN.



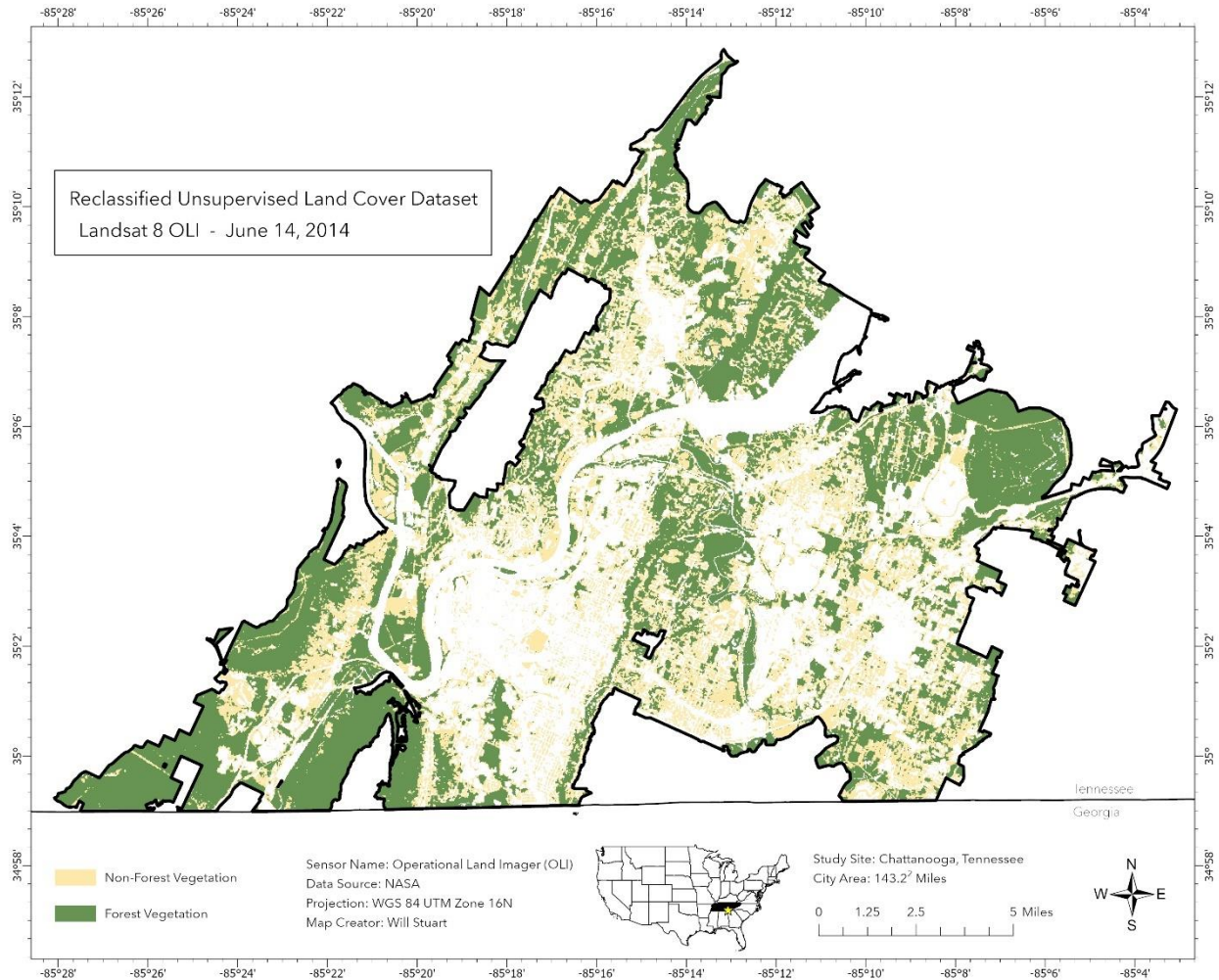
A45 Manual reclassification of 10 spectrally distinct classes of pervious pixels into Forest and Non-Forest Vegetation. Derived from true color Landsat 5 TM image captured June 23, 2000 across Chattanooga, TN.



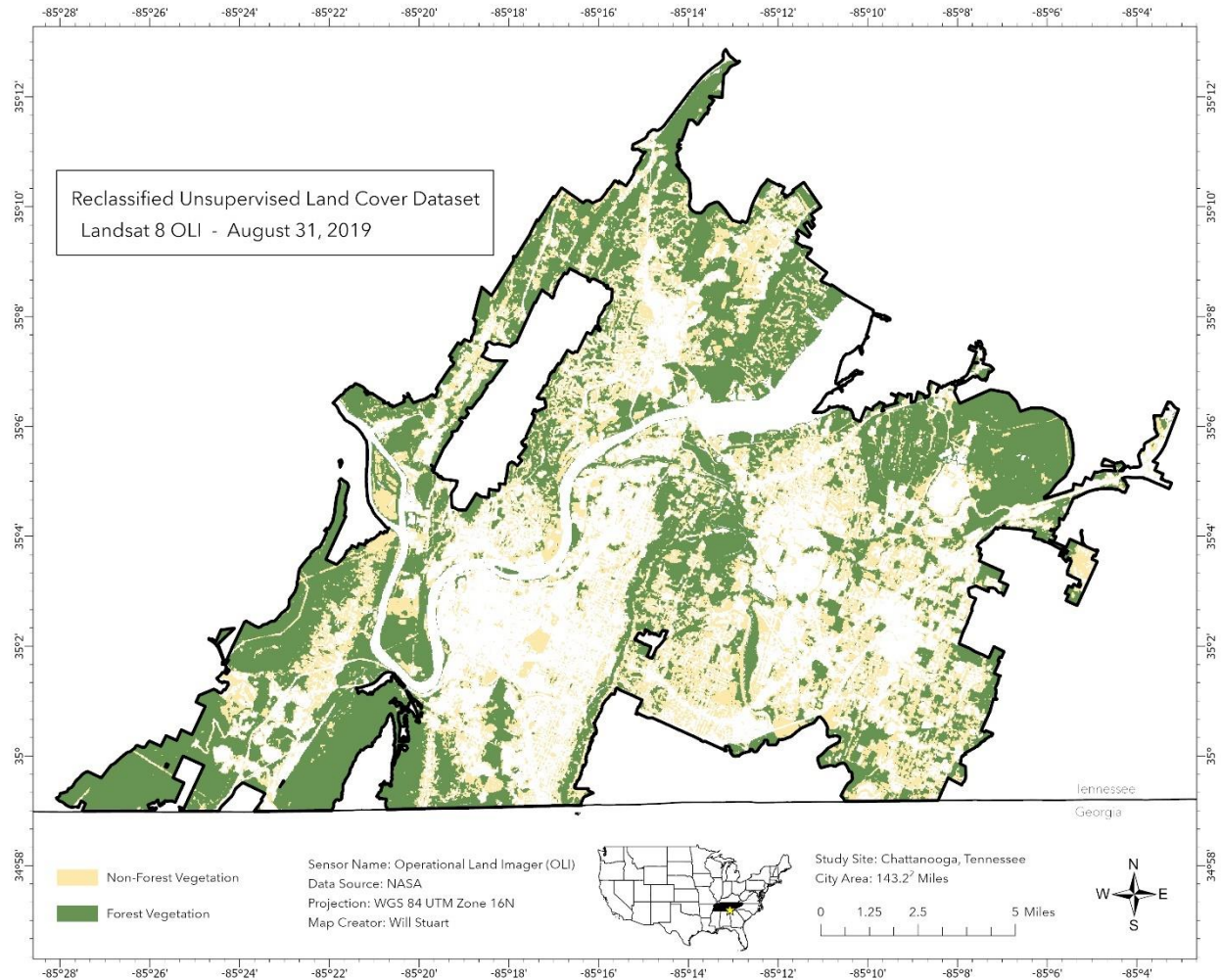
A46 Manual reclassification of 10 spectrally distinct classes of pervious pixels into Forest and Non-Forest Vegetation. Derived from true color Landsat 5 TM image captured July 20, 2004 across Chattanooga, TN.



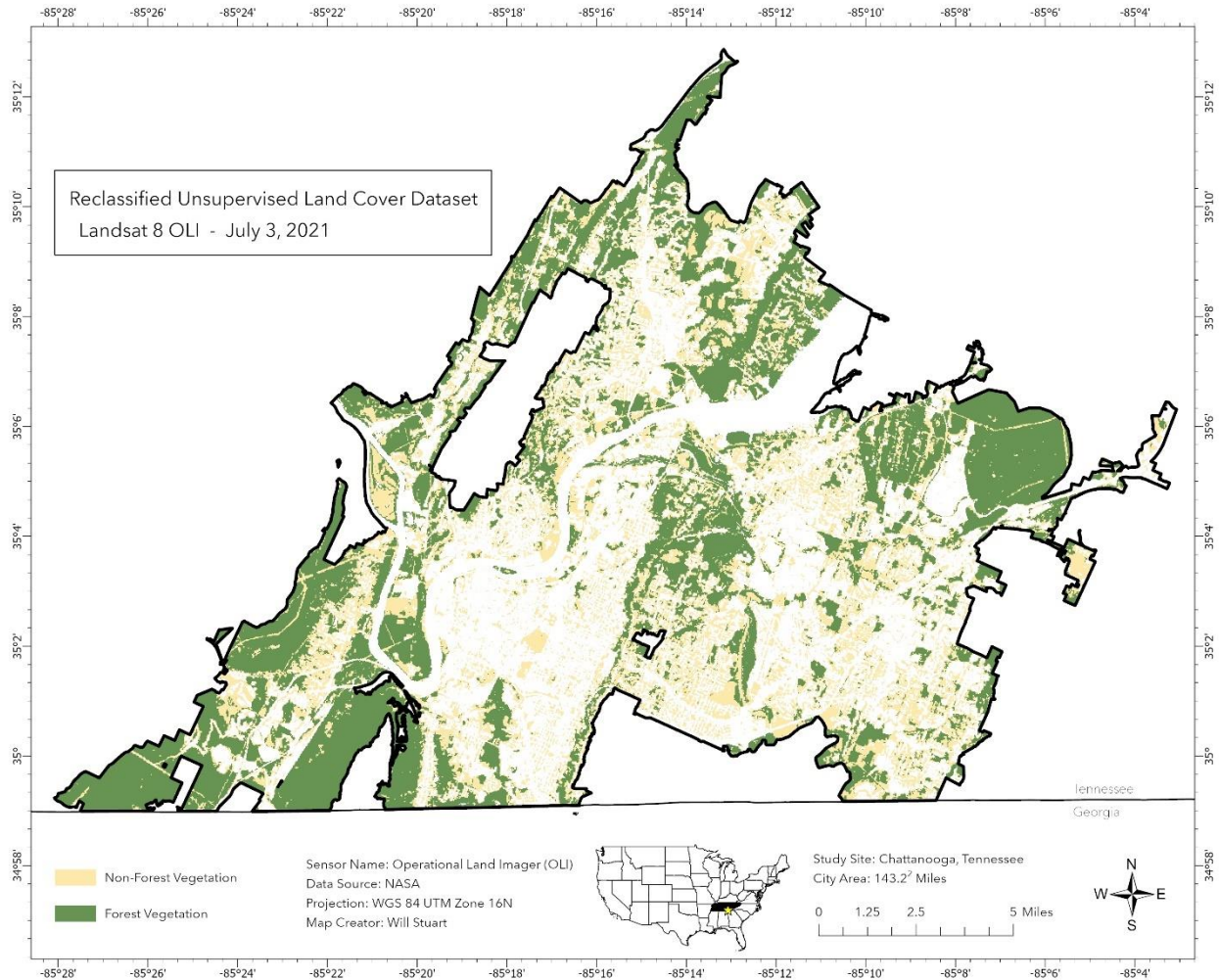
A47 Manual reclassification of 10 spectrally distinct classes of pervious pixels into Forest and Non-Forest Vegetation. Derived from true color Landsat 5 TM image captured June 16, 2009 across Chattanooga, TN.



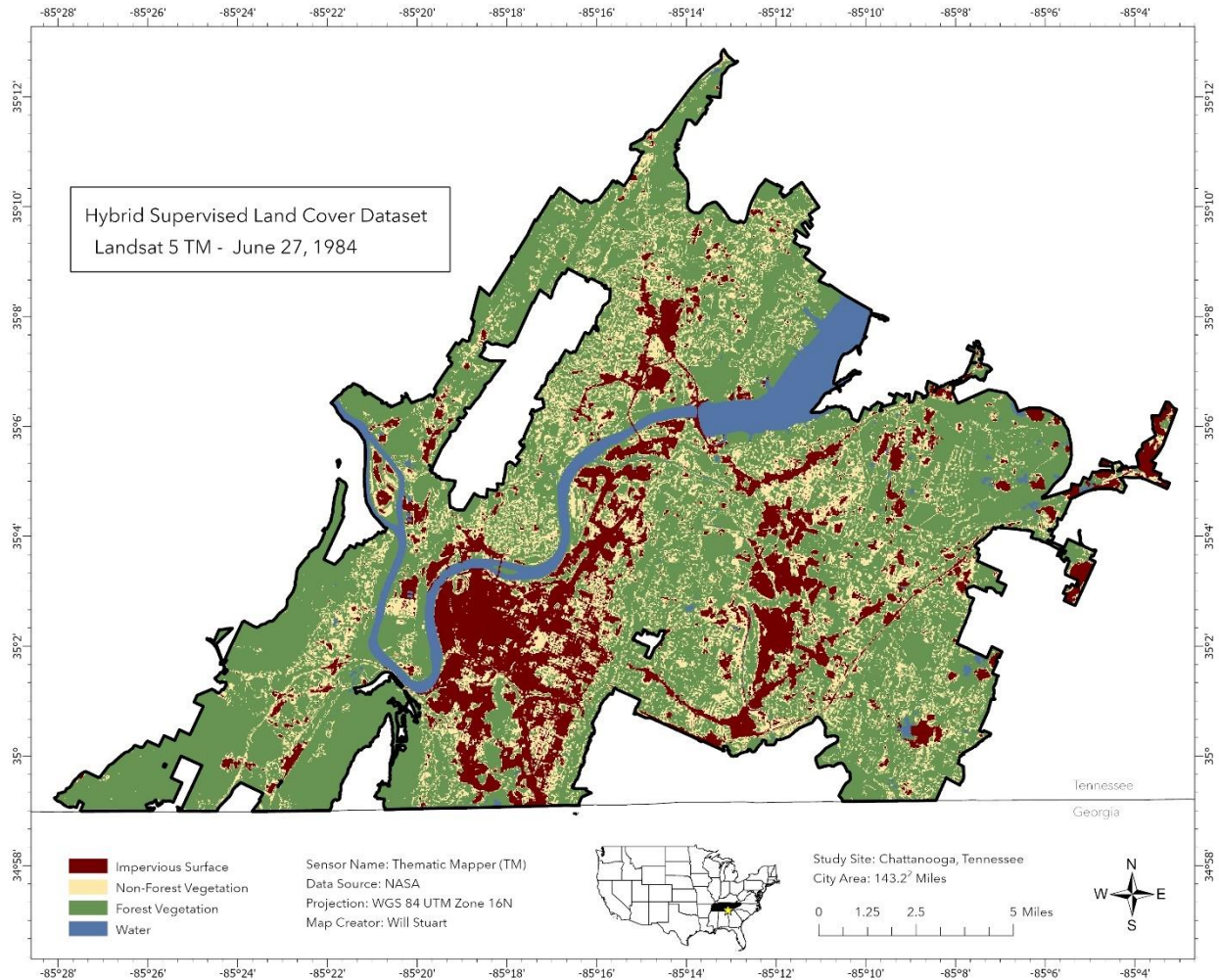
A48 Manual reclassification of 10 spectrally distinct classes of pervious pixels into Forest and Non-Forest Vegetation. Derived from true color Landsat 8 OLI image captured June 14, 2014 across Chattanooga, TN.



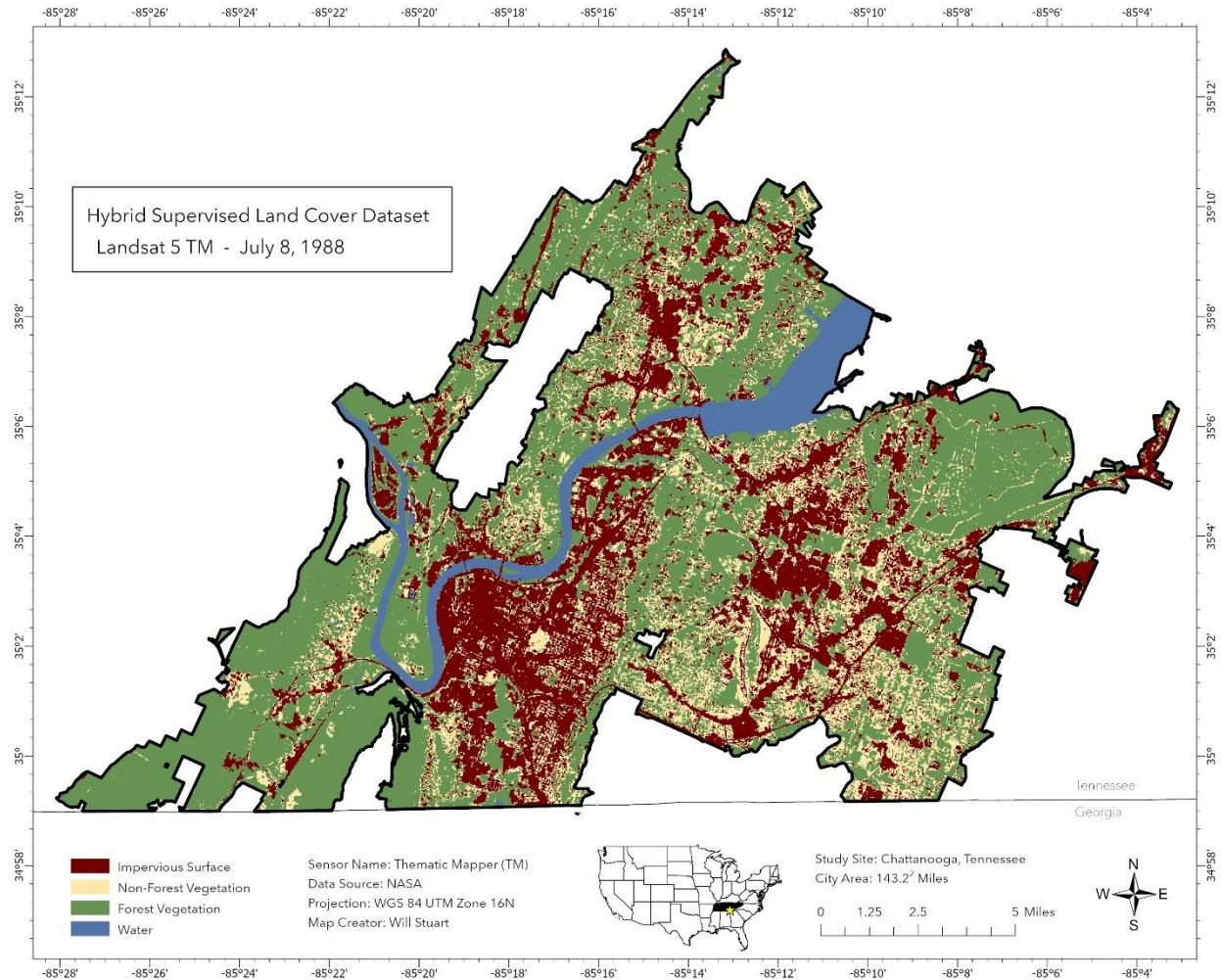
A49 Manual reclassification of 10 spectrally distinct classes of pervious pixels into Forest and Non-Forest Vegetation. Derived from true color Landsat 8 OLI image captured August 31, 2019 across Chattanooga, TN.



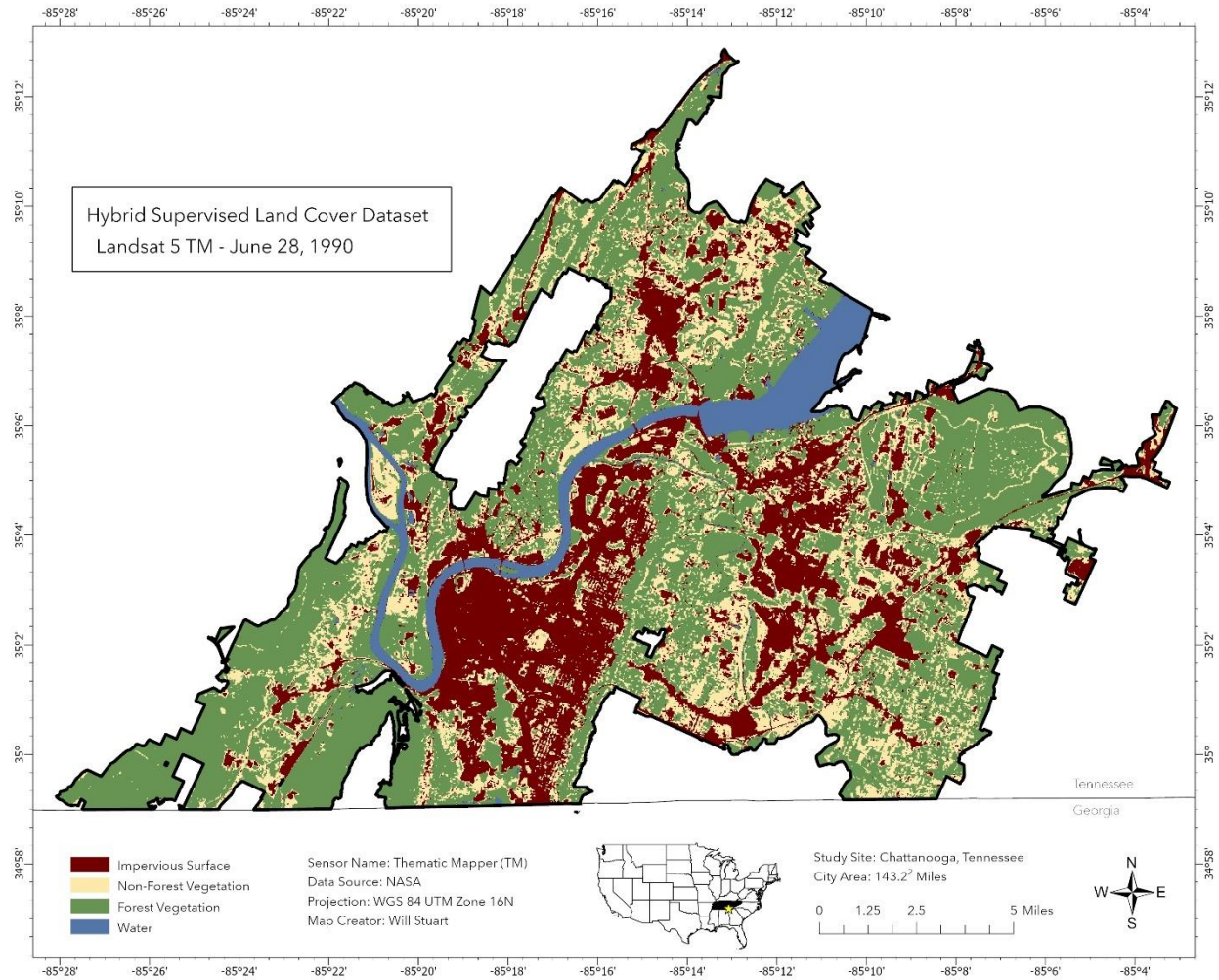
A50 Manual reclassification of 10 spectrally distinct classes of pervious pixels into Forest and Non-Forest Vegetation. Derived from true color Landsat 8 OLI image captured July 3, 2021 across Chattanooga, TN.



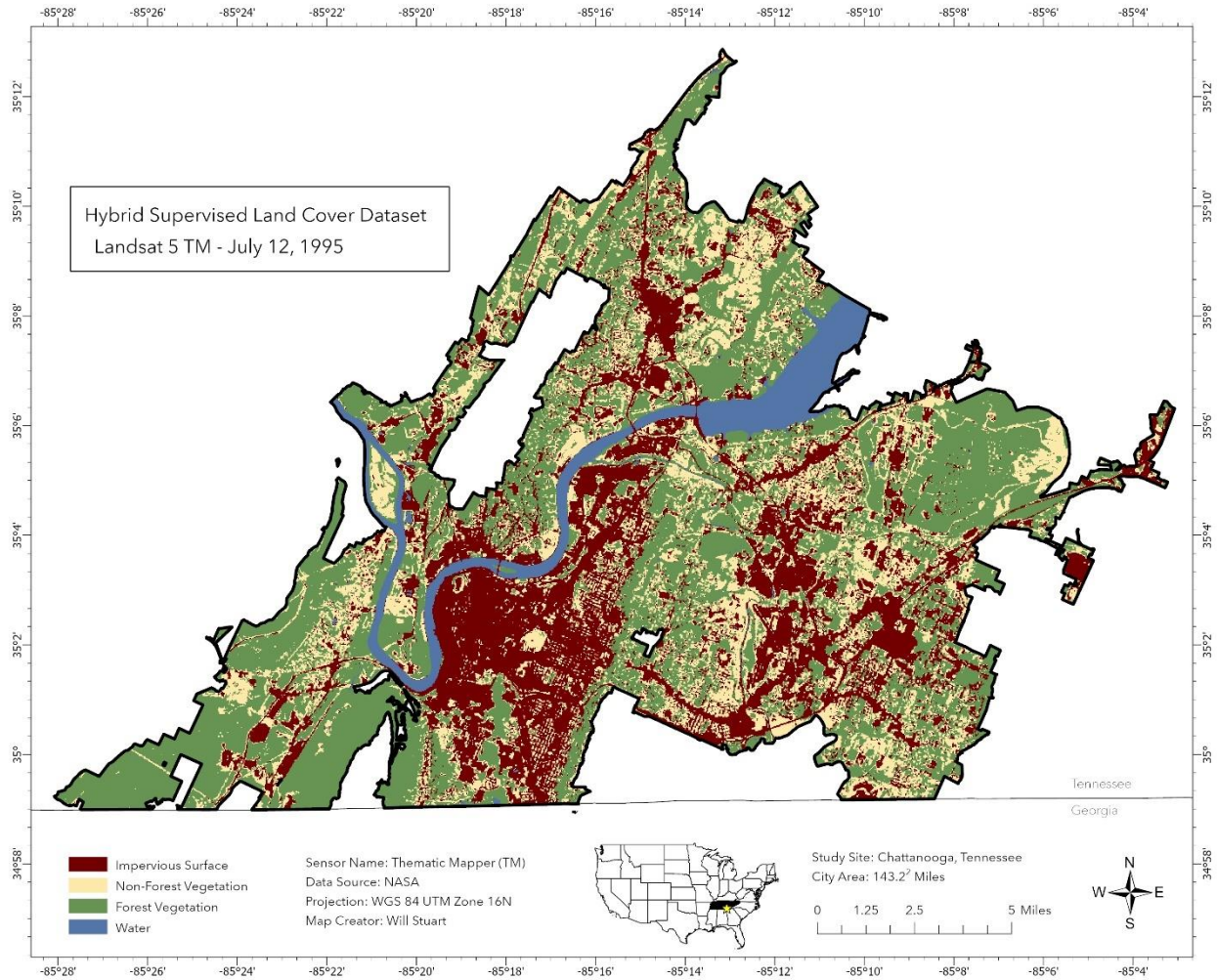
A51 Final 4 class thematic land cover map derived from the supervised hybrid classification of a Landsat 5 TM image captured June 27, 1984 across Chattanooga, TN.



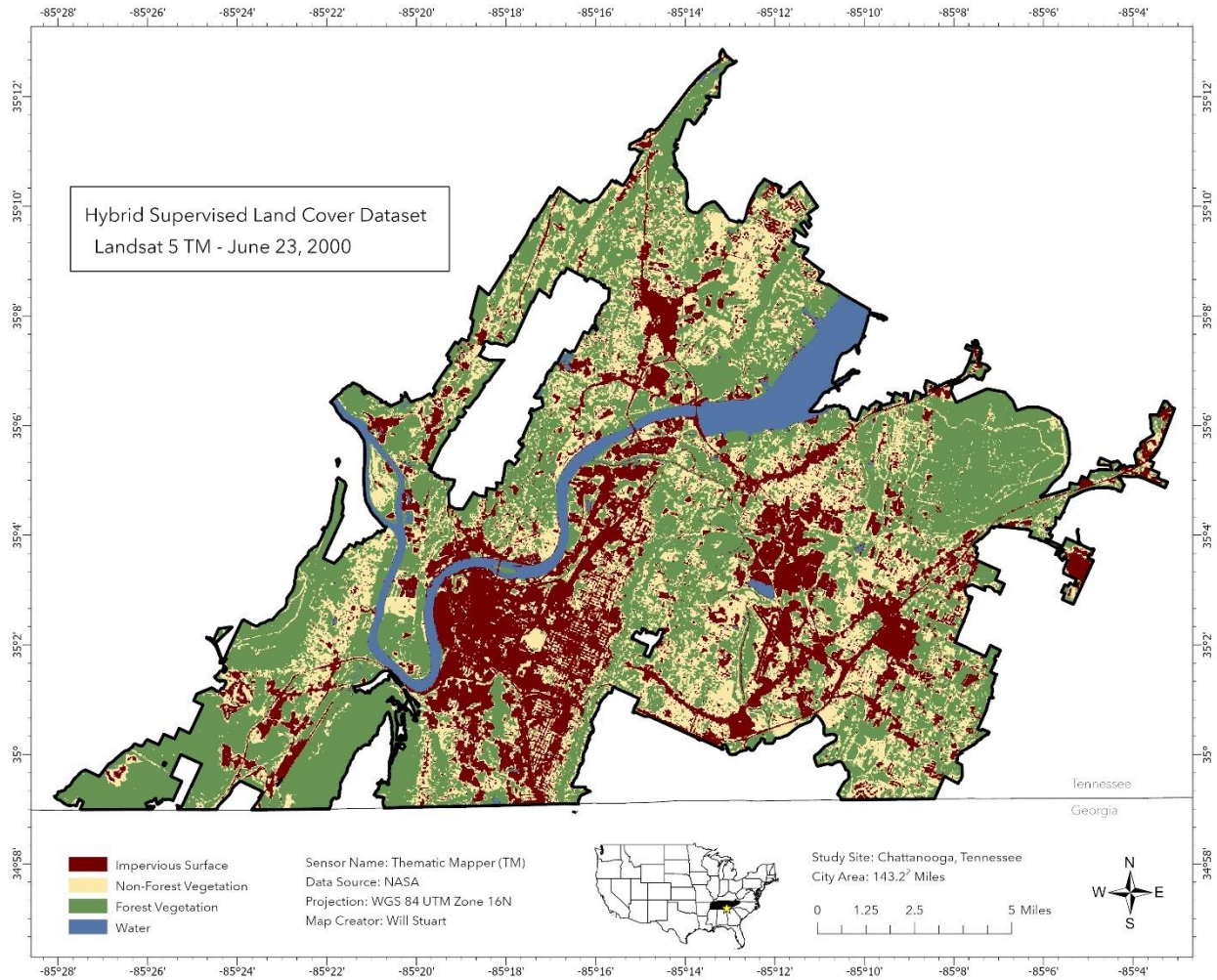
A52 Final 4 class thematic land cover map derived from the supervised hybrid classification of a Landsat 5 TM image captured July 8, 1988 across Chattanooga, TN.



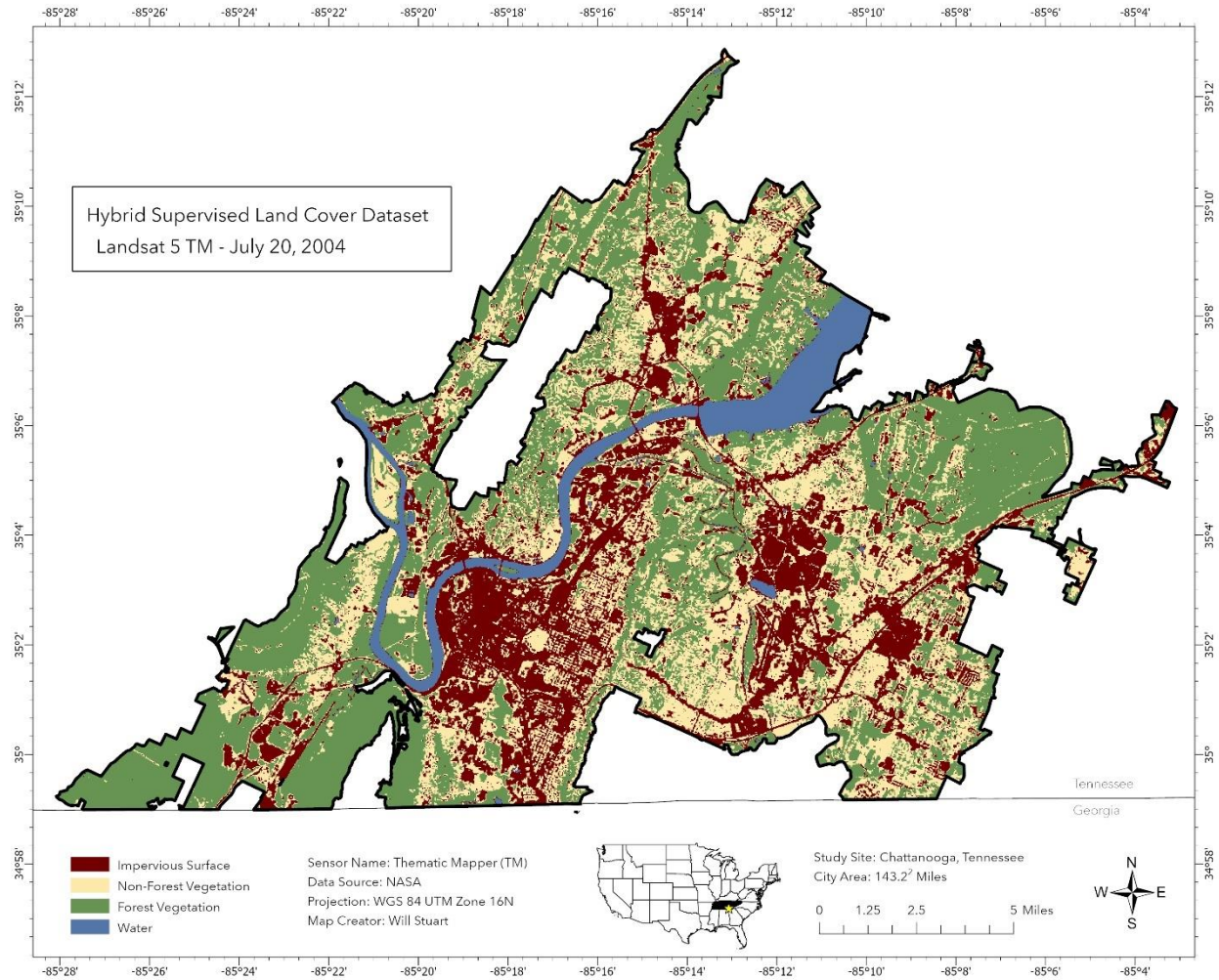
A53 Final 4 class thematic land cover map derived from the supervised hybrid classification of a true color Landsat 5 TM image captured June 28, 1990 across Chattanooga, TN.



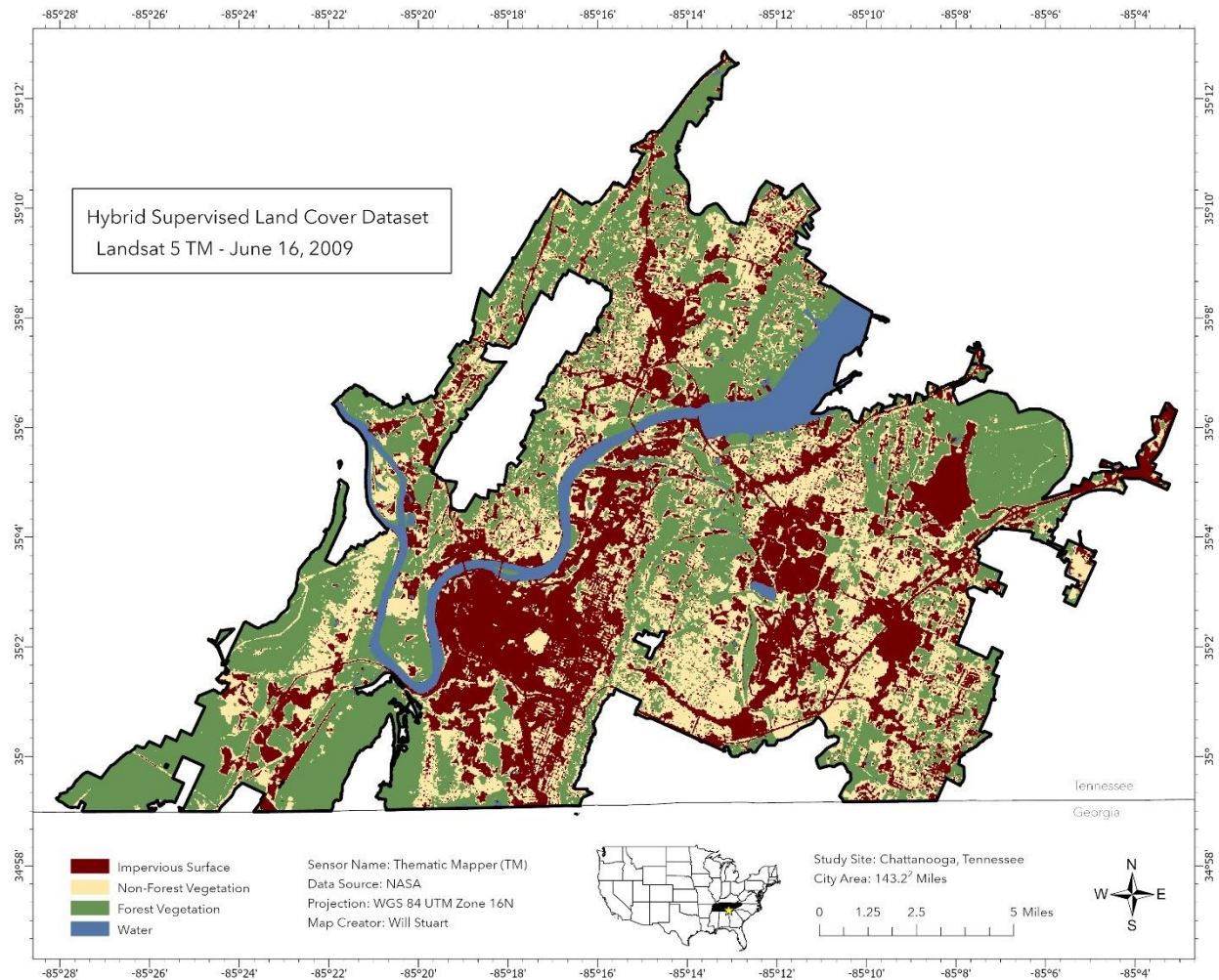
A54 Final 4 class thematic land cover map derived from the supervised hybrid classification of a true color Landsat 5 TM image captured July 12, 1995 across Chattanooga, TN.



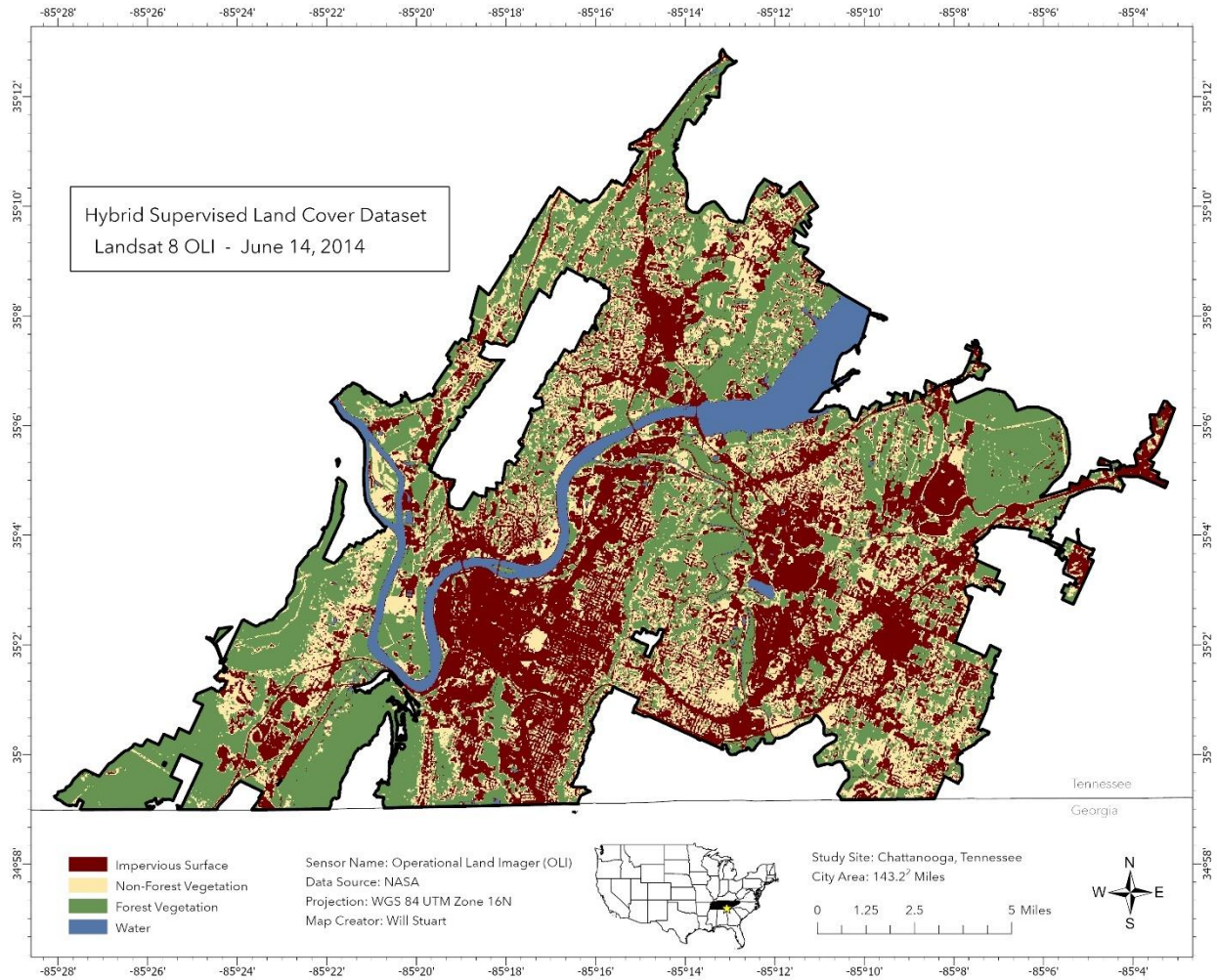
A55 Final 4 class thematic land cover map derived from the supervised hybrid classification of a true color Landsat 5 TM image captured June 23, 2000 across Chattanooga, TN.



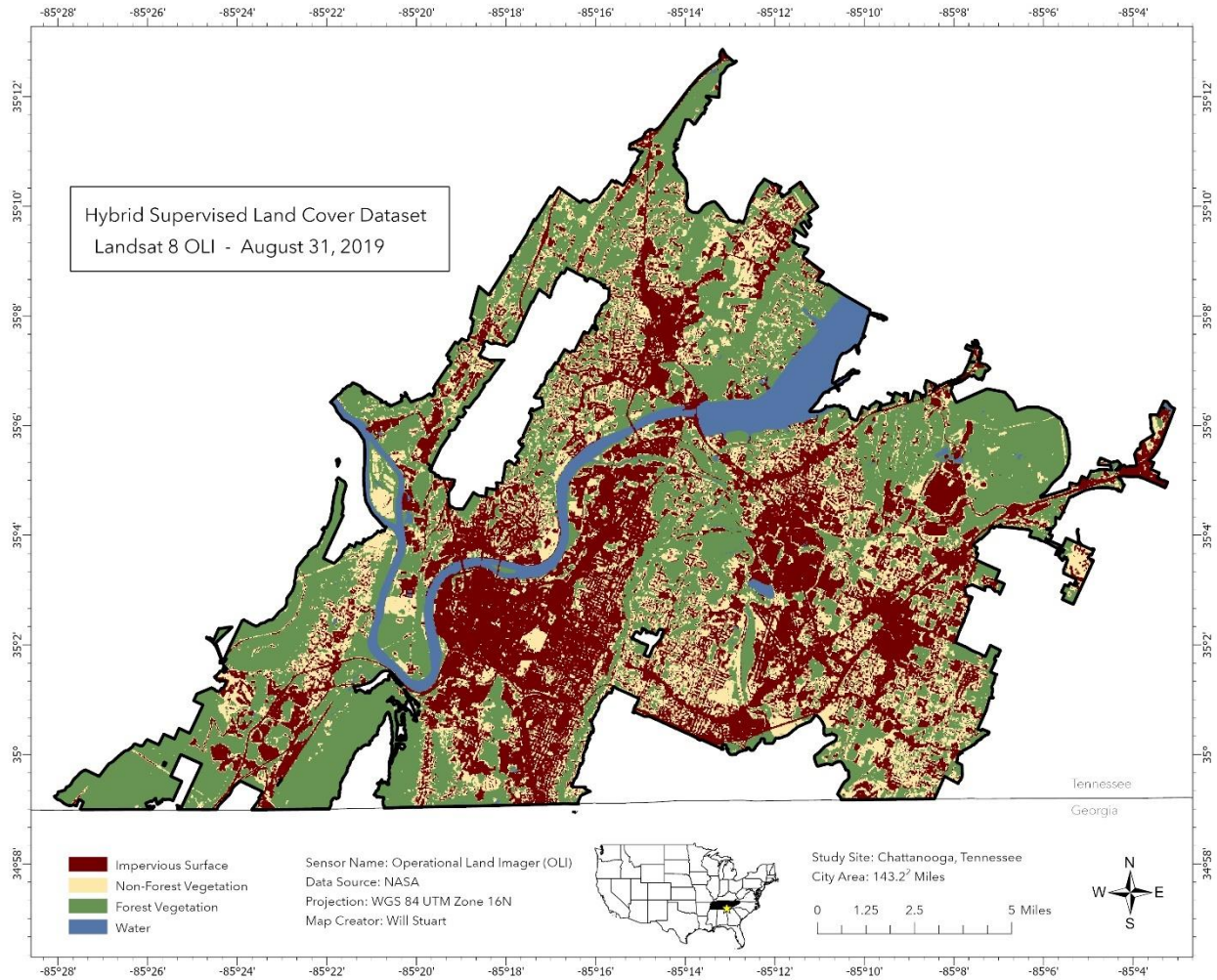
A56 Final 4 class thematic land cover map derived from the supervised hybrid classification of a true color Landsat 5 TM image captured July 20, 2004 across Chattanooga, TN



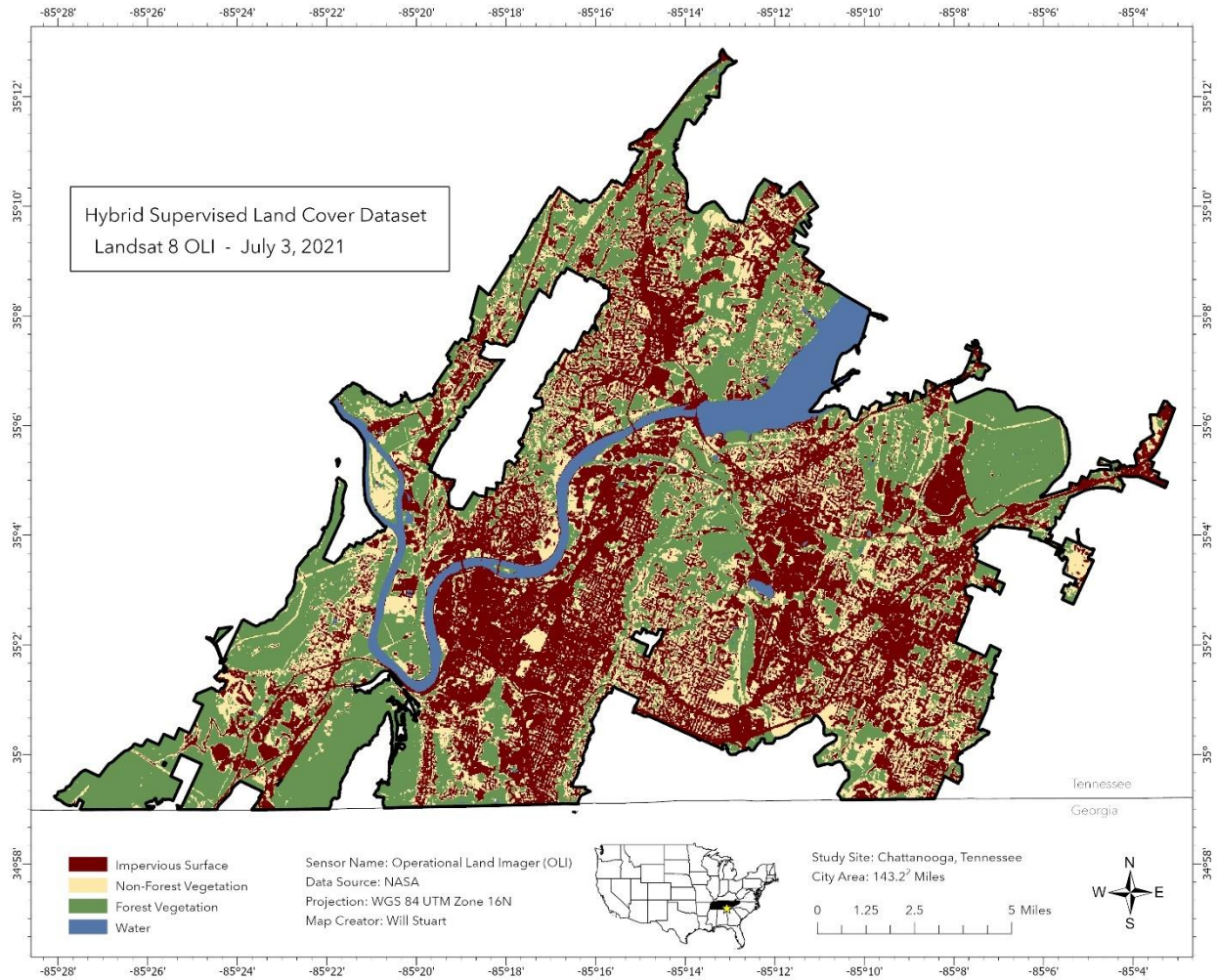
A57 Final 4 class thematic land cover map derived from the supervised hybrid classification of a true color Landsat 5 TM image captured June 16, 2009 across Chattanooga, TN.



A58 Final 4 class thematic land cover map derived from the supervised hybrid classification of a true color Landsat 8 OLI image captured June 14, 2014 across Chattanooga, TN.



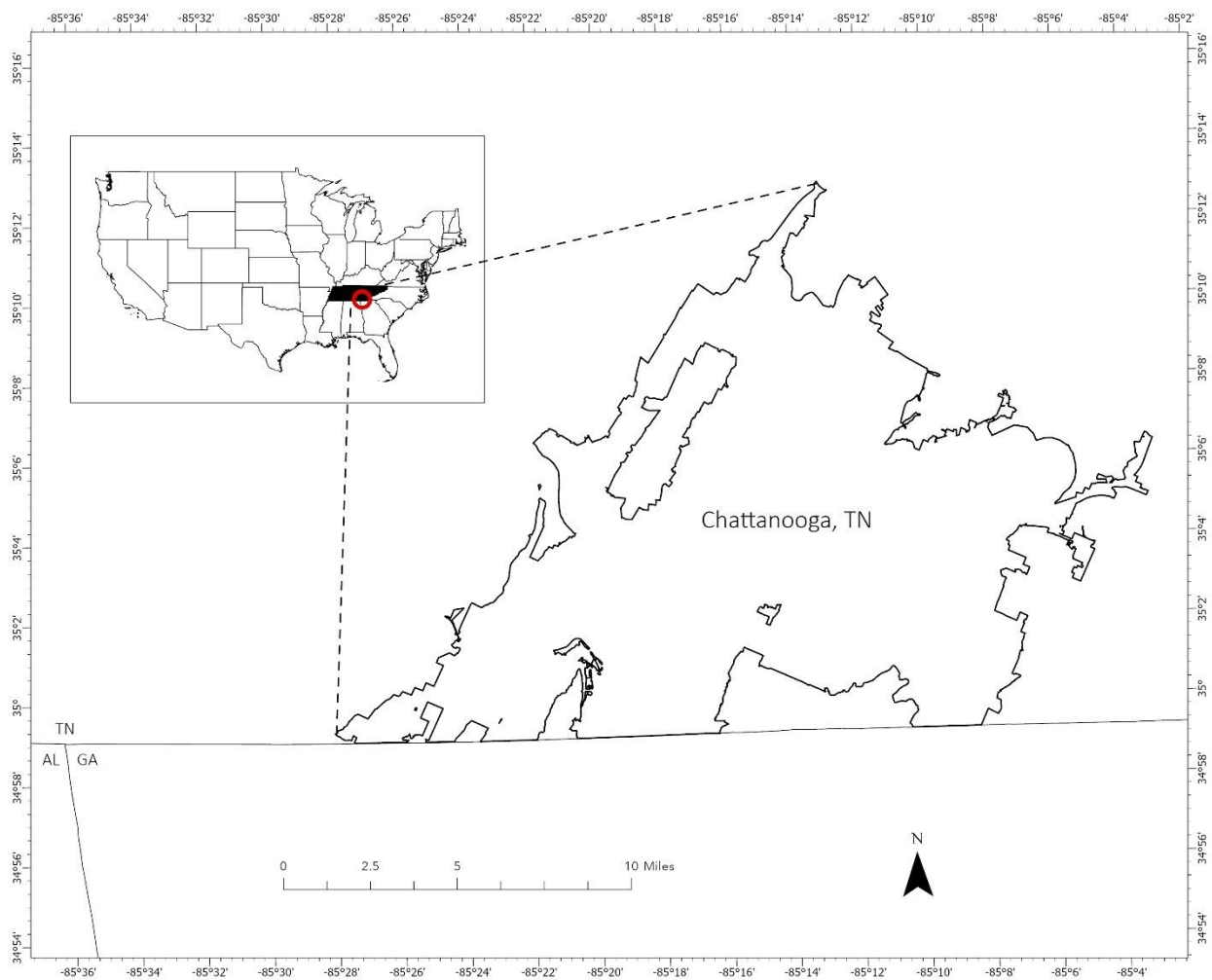
A59 Final 4 class thematic land cover map derived from the supervised hybrid classification of a true color Landsat 8 OLI image captured August 31, 2019 across Chattanooga, TN.



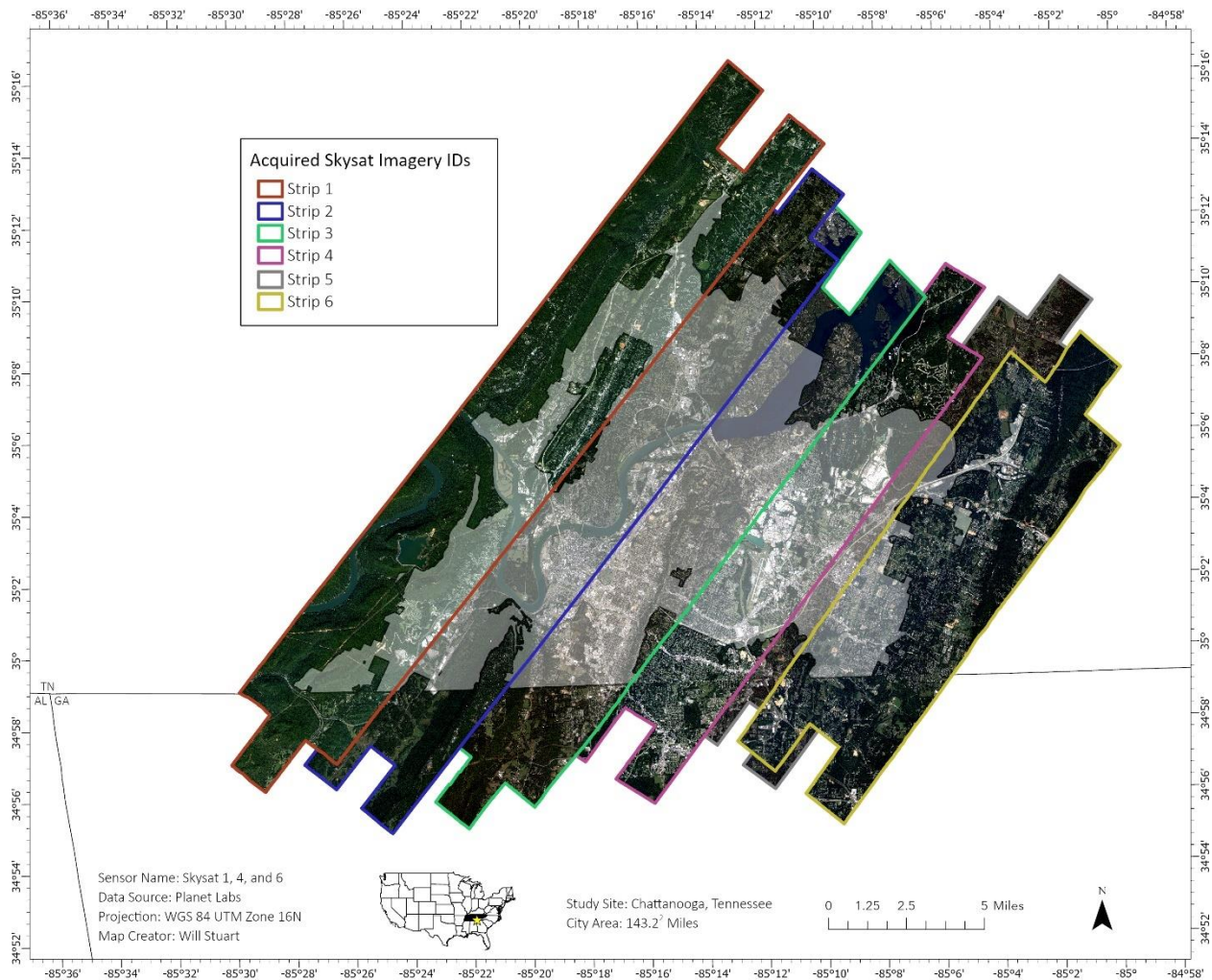
A60 Final 4 class thematic land cover map derived from the supervised hybrid classification of a true color Landsat 8 OLI image captured July 3, 2021 across Chattanooga, TN.

APPENDIX B

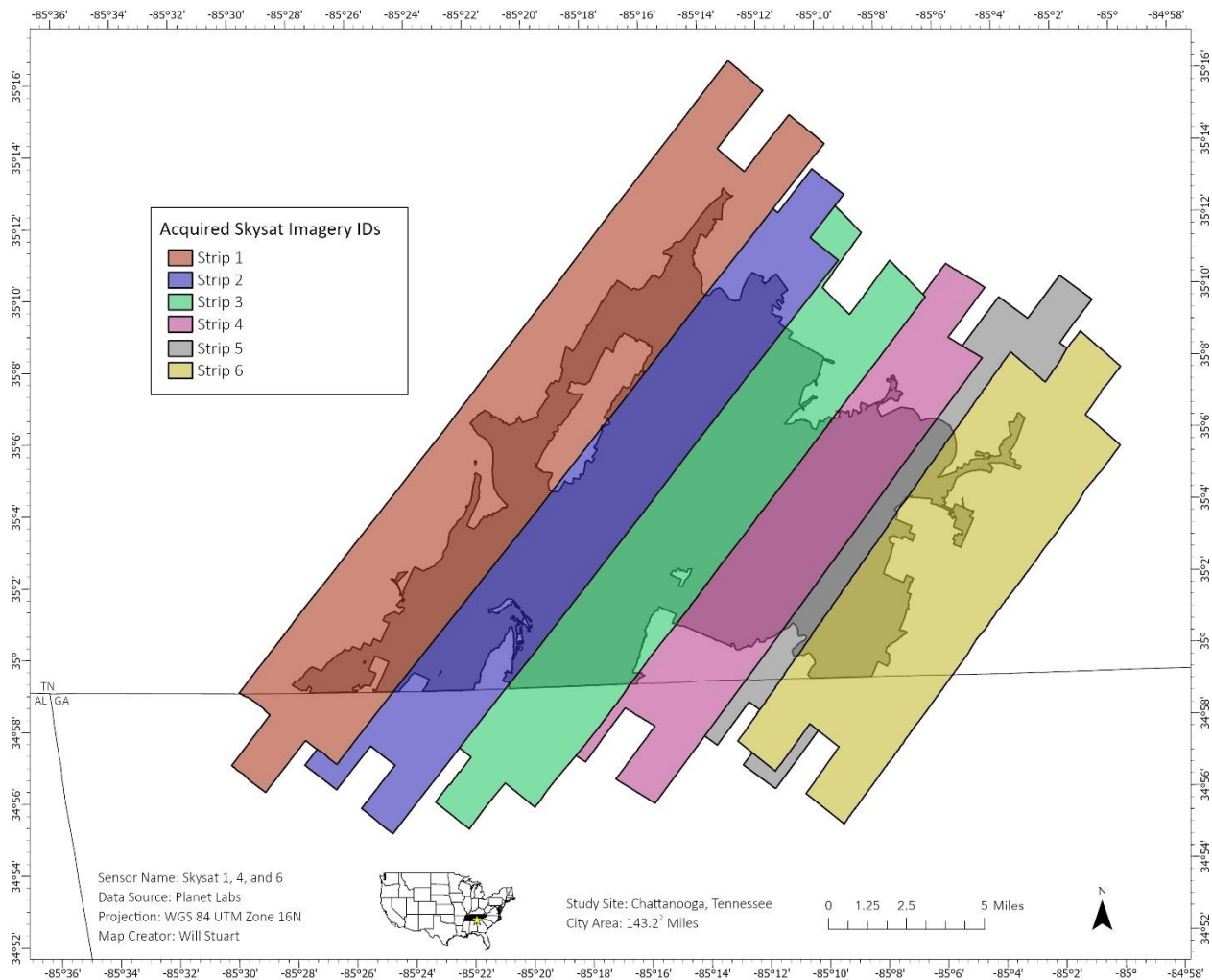
APPLICATION OF SKYSAT IMAGERY



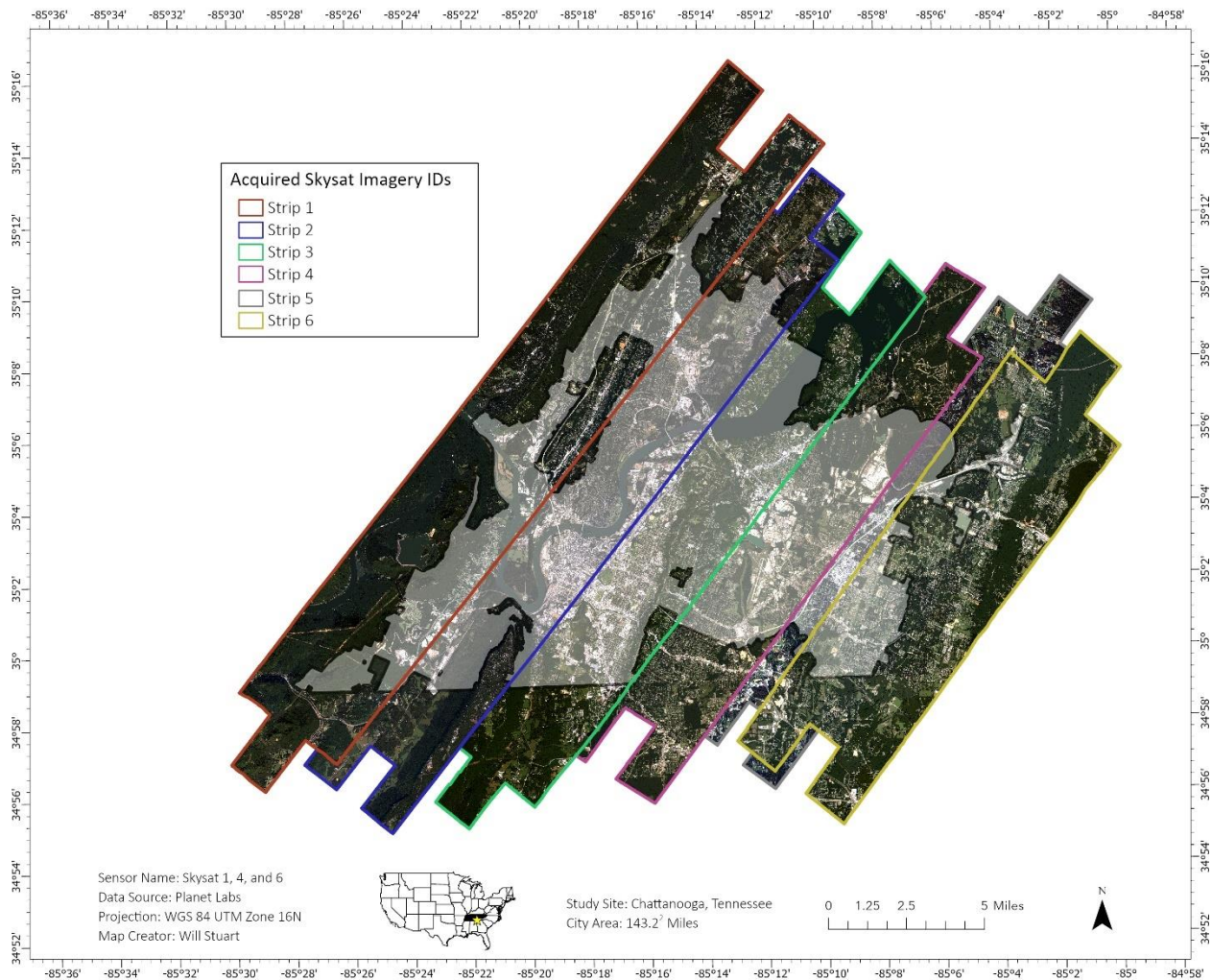
B1 Study site map for SkySat research. The study site boundary is the City of Chattanooga, Tennessee.



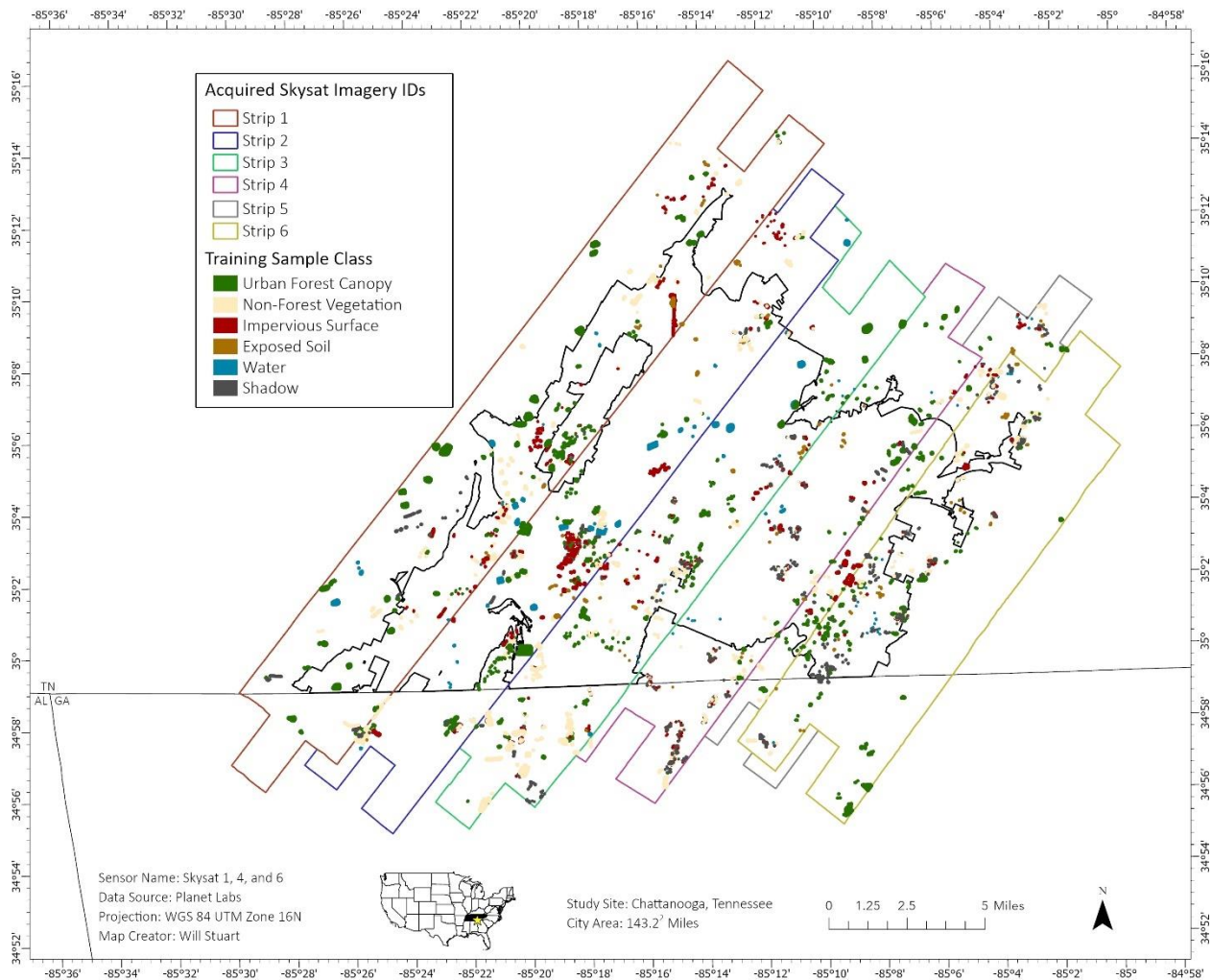
B2 Footprint boundary and true color SkySat imagery acquired.



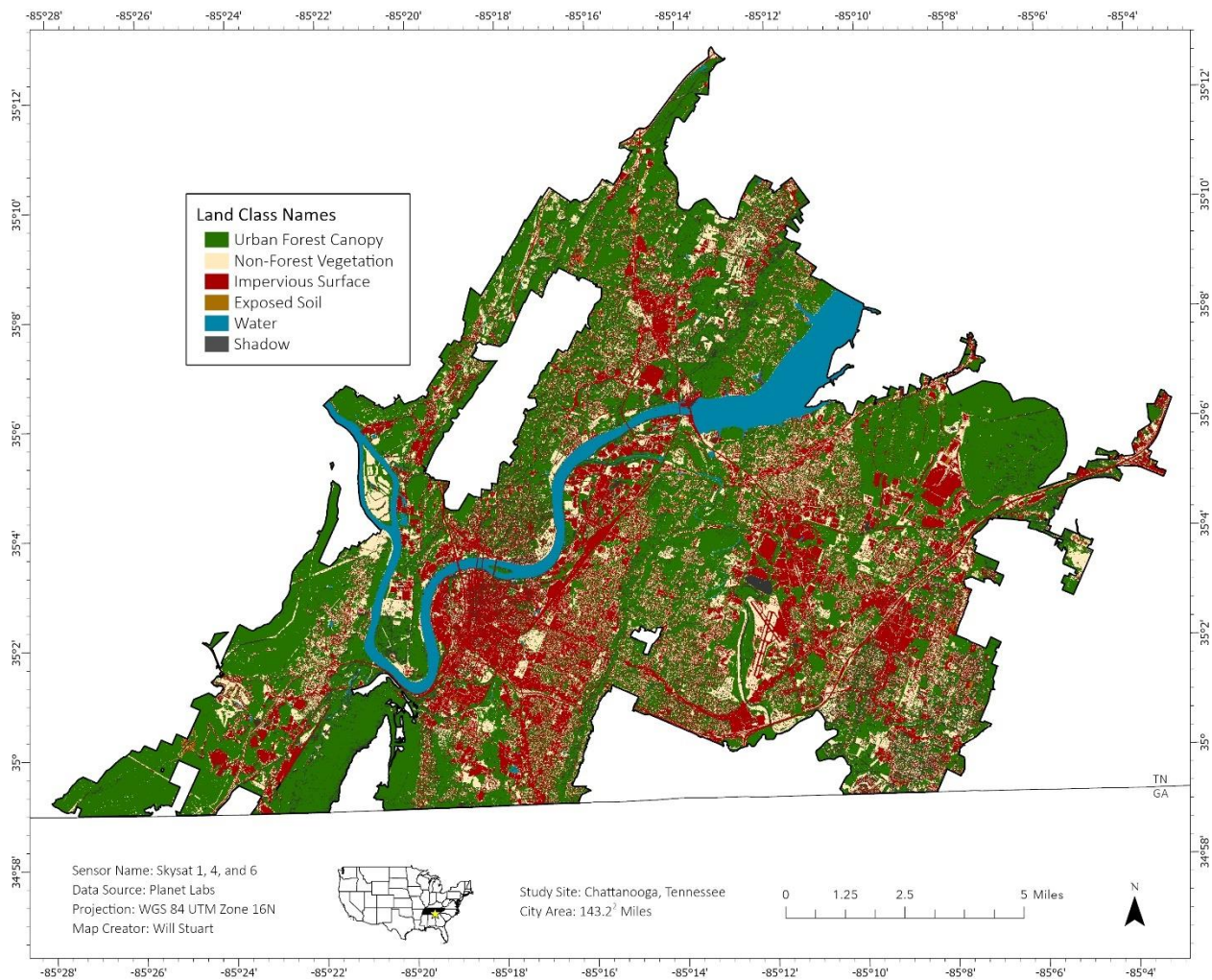
B3 Footprint of tasked SkySat imagery. Both pansharpened orthomosaics and surface reflectance products were obtained.



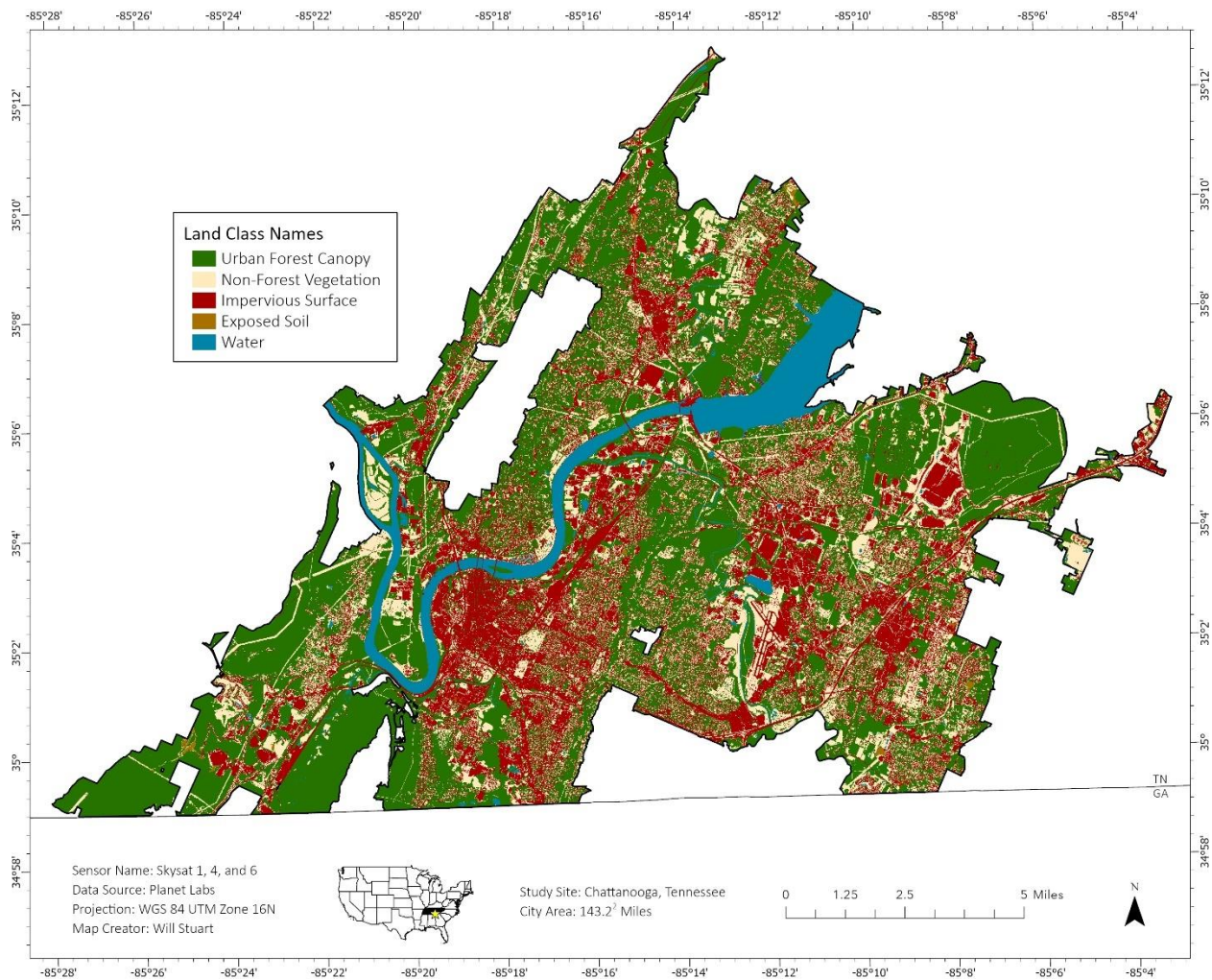
B4 Footprint boundary, study site boundary, and segmented true color SkySat rasters.



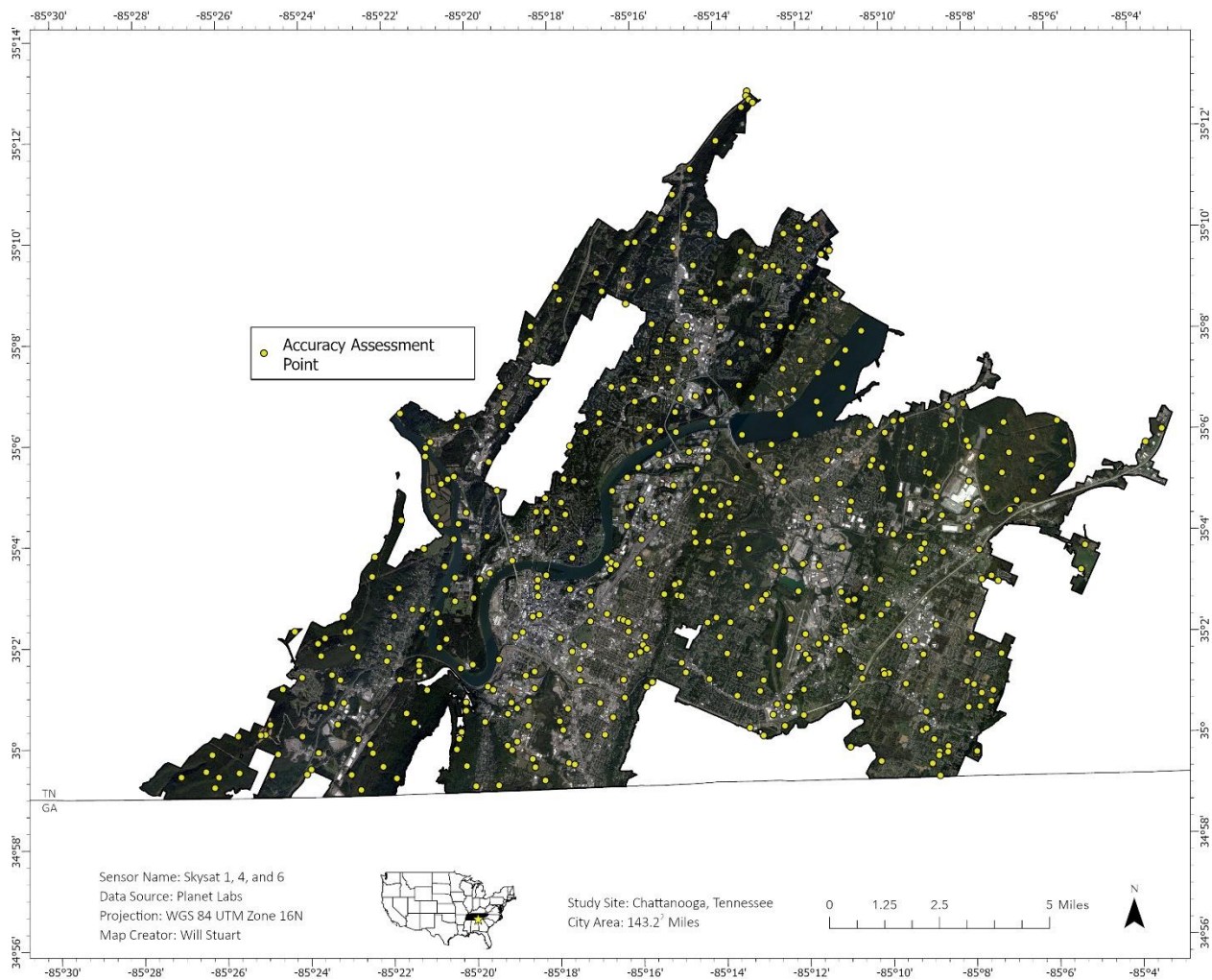
B5 Training samples collected across segmented SkySat imagery to support object-based classification. All training samples were collected within ArcGIS Pro's Training Sample Manager.



B6 Final unrefined high resolution (50 cm) land cover dataset derived from SkySat imagery.



B7 Final unrefined high resolution (50 cm) land cover dataset derived from SkySat imagery.



B8 500 randomly distributed points used for the accuracy assessment of the final unrefined high resolution land cover dataset.



B9 500 randomly distributed points used for the accuracy assessment of the final refined high resolution land cover dataset.

VITA

Will Stuart is currently a master's candidate in the Environmental Science program at the University of Tennessee at Chattanooga. He earned his B.S. in Environmental Science, with a focus in Earth, Atmosphere, and Geologic Resources. In addition to his academic achievements, Will has served as a lab instructor for Environmental Science and teaching assistant for Introduction to GIS for Geoscientists at UTC. His research experiences include geologic-based field studies across the US desert southwest, research concerning the topography and microclimate of the Cumberland Plateau, and the integration of GIS and remote sensing techniques to model the carbon sequestered in the trees across Chattanooga's urban forest. Current research is utilizing satellite imagery to accurately and rapidly map Chattanooga's forest lands, quantify how the extent of forest lands have changed through time, and to model the carbon these forests have sequestered in their biomass in order to help inform future sustainable development initiatives in the City of Chattanooga. He is excited to continue conducting GIS-empowered spatial analyses to further the conservation of Chattanooga's culturally, recreationally, and ecologically valued natural resources.